Heavy-Ion Performance of the LHC and Future Colliders

Von der Fakultät für Mathematik, Informatik und Naturwissenschaften der RWTH Aachen University zur Erlangung des akademischen Grades einer Doktorin der Naturwissenschaften genehmigte Dissertation

vorgelegt von

Master of Science
Michaela Schaumann

aus Bad-Neuenahr Ahrweiler

Berichter: Univ.-Prof. Dr. rer. nat. Achim Stahl
Univ.-Prof. Mei Bai, PhD
John M. Jowett, PhD

Tag der mündlichen Prüfung: 29.04.2015

Contents

1. Introduction

In 2008 the Large Hadron Collider (LHC) and its experiments started operation at the European Center of Nuclear Research (CERN) in Geneva with the main aim of finding or excluding the Higgs boson. Only four years later, on the 4th July 2012, the discovery of a Higgs-like particle was proven and first published by the two main experiments ATLAS and CMS in [1] and [2].

Even though proton–proton (p-p) collisions are the main operation mode of the LHC, it also acts as an heavy-ion collider. Here, the term "heavy-ion collisions" refers to the collision between fully stripped nuclei.

While the major hardware system of the LHC is compatible with heavy-ion operation, the beam dynamics and performance limits of ion beams are quite different from those of protons. Because of the higher mass and charge of the ions, beam dynamic effects like intra-beam scattering (IBS) and radiation damping are stronger. Also the electromagnetic cross-sections in the collisions are larger, leading to a significantly faster intensity decay and thus shorter luminosity lifetimes.

As the production cross-sections for various physics processes under study of the experiments are still small at energies reachable with the LHC and because the heavy-ion run time is limited to a few days per year, it is essential to obtain the highest possible collision rate, e.g. maximise the instantaneous luminosity, in order to obtain enough events and therefore low statistical errors.

Within this thesis, the past performance of the LHC in lead-lead (Pb-Pb) collisions, at a centre-of-mass energy of 2.76 TeV per colliding nucleon pair, is analysed and potential luminosity limitations are identified. Tools are developed to predict future performance and techniques are presented to further increase the luminosity. Finally, a perspective on the future of high energy heavy-ion colliders is given.

In the history of particle accelerators, the LHC is only the third storage ring colliding nuclei. High energy heavy-ion physics has only been performed with colliding beams since 2000, and today only two heavy-ion colliders are operational worldwide [3]. Apart from the Intersecting Storage Rings (ISR) [4] at CERN, which only briefly collided light ions in 1977, the Relativistic Heavy Ion Collider (RHIC) [5] at the Brookhaven National Laboratory (BNL) is the only other collider performing nucleus-nucleus collisions[1].

In high energy nucleus-nucleus collisions the interactions between quarks and gluons, described in the theory of Quantum Chromo Dynamics (QCD), are studied. Quarks

[1] RHIC has operated since 2000 in several modes, using different particle species, up to date: copper (Cu), gold (Au), uranium (U), deuterons and spin-polarised protons.

always occur in a bound state due to the confinement, forming barons ans mesons. However, QCD predicts that microseconds after the Big Bang, when the universe was extremely hot and dense, quarks and gluons could form a new state of matter, the so-called Quark-Gluon-Plasma (QGP). In order to understand not only the evolution of the universe, but also basic properties of matter, e.g., how hadrons are formed, knowledge of the structure and the dynamics of the QGP is required. An extremely high energy density in a large enough volume is required to create the QGP. Creating this high energy density in the laboratory is only possible in high energy heavy-ion collisions. The goal is to explore the largest possible region of the QCD matter phase diagram (temperature vs. baryon chemical potential) in order to experimentally obtain the properties of the QGP.

Already at RHIC a wide range of energies and species could be scanned [6,7]. RHIC reaches a centre-of-mass energy per colliding nucleon pair of up to $\sqrt{s_{\mathrm{NN}}} = 200\,\mathrm{GeV}$. First results from Pb-Pb collisions at the LHC at nearly 14 times higher energy confirm the physics picture derived from RHIC data [7–9], while accessing a new area in the high temperature regime of the nuclear matter phase diagram.

The LHC heavy-ion programme started in 2010 and is scheduled for about one month per operational year. Two modes of operation are covered: collisions between two beams of fully stripped lead ions ($^{208}\mathrm{Pb}^{82+}$), referred to as Pb-Pb operation, and between a lead nucleus and a proton beam (p-Pb). While Pb-Pb operation was included in the conceptual design of the LHC from an early stage, p-Pb collisions were not originally considered. A maximum beam energy of 2.76 TeV/nucleon is foreseen, yielding a center-of-mass energy of 1.15 PeV or $\sqrt{s_{\mathrm{NN}}} = 5.5\,\mathrm{TeV}$/nucleon. Heavy-ion collisions are provided in three interaction points (IP), where in IP2 the ALICE detector is installed, an experiment dedicated to heavy-ion physics. The two multi-purpose detectors, ATLAS and CMS, are located in IP1 and IP5, respectively. Under nominal conditions a peak luminosity of $\mathcal{L} = 1 \times 10^{27}\,\mathrm{cm}^{-2}\mathrm{s}^{-1}$ is to be reached. At the time of writing, three main heavy-ion runs and the p-Pb pilot run (very first p-Pb collisions in the LHC) had been performed at about half of the nominal energy[2]

1. Nov.-Dec. 2010: Pb-Pb collisions at $3.5Z$ TeV beam energy [10–12],
2. Nov.-Dec. 2011: Pb-Pb collisions at $3.5Z$ TeV beam energy [13],
3. 12.-13. Sep. 2012: p-Pb pilot run at $4Z$ TeV beam energy [14],
4. Jan.-Feb. 2013: p-Pb collisions at $4Z$ TeV beam energy [15].

This thesis was conducted from the end of 2011 until the beginning of 2015. During this time I participated in the commissioning, data taking and machine development sessions concerning the heavy-ion runs between 2011 and 2013. The analysis of the performance during these past runs is presented in Chapter 4 and was partly published

[2] As the bending of particles in a magnetic field depends on their charge, rather than their mass (see Chapter 2.1.1), the beam energy is quoted in units of Z eV, where Z is the charge number of the ion ($Z = 82$ for Pb). This approximation only holds for highly relativistic beams, as they are used in the LHC.

in Ref. [13]. A large spread of bunch properties is specific to the LHC lead ion operation. The reasons for this effect are investigated. I have analysed beam data of the 2011 Pb-Pb and the 2013 p-Pb run on the injection plateau and during collisions to understand the beam parameter and luminosity evolution throughout the operating cycle. The influence of effects such as IBS and luminosity "burn-off" are studied by performing tracking simulations, using the so-called Collider Time Evolution (CTE) program. Systematic simulations are performed to benchmark the simulation code against LHC heavy-ion data.

In heavy-ion collisions electromagnetic processes can change the charge or mass state of the participating ions, creating secondary beams emerging from the IP that impact in a superconducting magnet further downstream. These secondary beams carry a significant power. The risk of magnet quenches increases with the beam energy and the luminosity. The secondary beam losses can therefore become a limiting factor for the luminosity, if the operation of the accelerator is substantially perturbed by quenches. Chapter 7 is dedicated to these secondary beams. Observations made in last Pb-Pb run are discussed. During this run, a technique to temporarily mitigate the risk of quenches with orbit bumps was experimentally verified and the detailed analysis of this experiment is presented. The permanent installation of collimators in the dispersion suppressor to absorb the secondary beams is also briefly addressed.

During the Long Shut-down 1 (LS1) the LHC has been prepared to run at nominal energies. The next heavy-ion run is planned to be Pb-Pb at the end of 2015 at $6.5Z$ TeV, only slightly below the nominal beam energy. In general, it is foreseen to have a p-Pb run about every third year, while in the remaining runs Pb-Pb data is to be taken. A major upgrade of the ALICE detector is planned during the second long shut-down (LS2) [16]. Afterwards, ALICE would like to collect data at peak rates of up to 6 or 7 times the nominal peak luminosity. The main contribution to increasing the luminosity must come from an upgrade of the heavy-ion injector chain [17, 18], which is being prepared in the scope of the LHC Injector Upgrade (LIU) project [19]. Possibilities, limits and estimates to improve the heavy-ion luminosity from within the LHC are the main topic of this thesis.

Based on the observed performance, I derived a semi-empirical model to make detailed predictions for future runs, presented in Chapter 5 and also published in Ref. [20]. This model parametrises the differences in the intensity and luminosity from bunch to bunch as observed in 2011 and combines it with tracking simulations of a set of typical bunches, to obtain the parameter evolution over a fill. In this way, the total luminosity evolution, the integrated luminosity in a fill of average length, and following that, the expected integrated luminosity per 30 days run, are estimated in Chapter 6 and Refs. [20, 21]. The model takes into account higher single bunch intensities and new filling schemes, which are foreseen after the planned upgrades of the injector chain during LS2 (2018-2019).

The luminosity is proportional to the intensities and the emittances of the colliding bunches, which are both defined by the injectors. As was already successfully shown in RHIC [22–26], a stochastic cooling system could reduce the emittance far below its

initial value, such that more luminosity can be integrated over the same time interval, while the initial intensity is used more efficiently. In Chapter 8, I present a first feasibility study for stochastic cooling in the LHC and evaluate the potential benefit and effort for heavy-ion operation. Abstracts of this study are also published in Refs. [27, 28].

After the discovery of the Higgs boson, the expectations to find new physics beyond the standard model are high. However, it is likely that even higher energies will be required to fully explore the discoveries, which stimulates the interest in a larger circular collider. A substantial increase in collision energy is only possible with a larger tunnel. Therefore, the study of a future circular high energy hadron collider (FCC-hh), based on a new tunnel of 80 to 100 km circumference, which would allow centre-of-mass energies up to 100 TeV in proton-proton collisions, was launched recently [29, 30]. The performance of a potential heavy-ion operation of this collider is addressed in Chapter 9. In this setup, the LHC is assumed to be the last injector before the FCC and its current injector performance is taken as a conservative but robust baseline for Pb-Pb and p-Pb collisions. Proton-proton operation is also briefly discussed, assuming the official FCC p-p parameters [29]. This work is published in Ref. [31].

Preceding the analysis chapters, a short introduction to the relevant background in accelerator physics and the LHC itself is given in Chapter 2 and 3. A global summary of the results compiled in this thesis and an outlook are presented in Chapter 10.

Additional work I performed slightly outside the scope of this thesis, concerning the influence of IBS on HL-LHC proton beams, is published in Refs. [32–34].

2. Heavy Ions in The Large Hadron Collider

2.1. Fundamentals of Accelerator Physics

In this chapter a brief introduction to the fundamental principles of accelerator physics relevant in the scope of this thesis is given. For further details the reader should be directed to, e.g., Refs. [35–37].

2.1.1. Accelerator Components and Coordinate System

For the guidance and focussing of high energy charged particles in an accelerator, usually magnetic fields are used[1]. If a particle is defected in a magnetic field, the Lorentz and the centripetal force are always equal. This defines the curvature, ρ, of a particle with the charge q and momentum p in the magnetic field B, from which the so-called *beam rigidity*, $B\rho$, can be derived:

$$B\rho = \frac{p}{q}. \tag{2.1}$$

The beam rigidity determines the dipole strength and bending radius needed to keep a particle with a given energy and charge on a circular path. This leads to one of the fundamental design criteria for circular accelerators: with B limited by the technological development, the size of an accelerator increases with the increasing maximum particle energy to be reached.

A particle accelerator is built in a way that an ideal reference particle (i.e. a particle with design momentum, $p = p_0$, $x = y = 0$, $x' = y' = 0$) follows the so-called *design orbit*, which generally is meant to pass through the centres of the main magnetic elements. It is convenient to use a co-moving coordinate system to describe the beam motion relative to the design orbit, known as Frenet-Serret coordinate system, illustrated in Fig. 2.1.

Because of the large number of particles per bunch, it is unavoidable that some particles have a different momentum, an offset or an angle to the design orbit. The focussing force of quadrupoles is required to avoid beam losses and keep the particles

[1] In general, also electric fields would be available for this purpose, but it is difficult to produce them with the required strength.

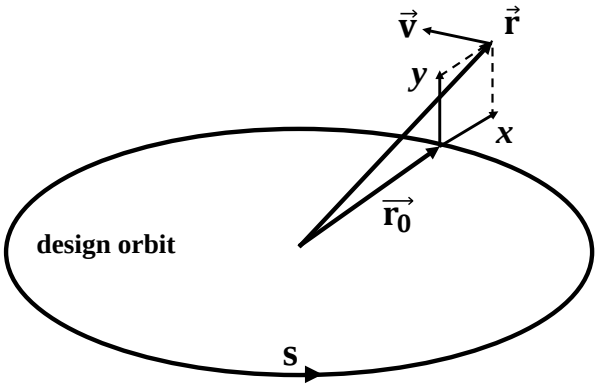

Figure 2.1.: Frenet-Serret coordinate system used for circular accelerators. $\mathbf{r_0}(s)$ describes the design orbit. $\hat{\mathbf{x}}$, $\hat{\mathbf{y}}$ and $\hat{\mathbf{s}}$ build the basis of the coordinate system. Any transverse position of the beam particles can be expressed by $\mathbf{r}(s) = \mathbf{r_0}(s) + x\hat{\mathbf{x}} + y\hat{\mathbf{y}}$, where x and y are the betatron coordinates, describing the horizontal and vertical offset from the design orbit.

close to the central trajectory. The transverse field components of a quadrupole increase linearly with the distance from the centre and vanish in the centre of the magnet. Unfortunately, the focussing force of the quadrupole magnetic field in one plane, is defocussing in the perpendicular plane. In order to obtain an overall focussing effect, focussing and defocussing elements have to be alternated. One of the most common sequences in the design of accelerators is the so-called *FODO-cell*, which is introduced in Section 2.2.2 on the example of the arc cells used in the LHC.

2.1.2. Linear Betatron Motion

This section discusses the influence of linear lattice elements (dipoles and quadrupoles) on the transverse motion of particles.

Hill's Equation

Under the assumption of a closed-orbit, a periodic quadrupole strength $k(s) = k(s + L)$ with L as the length of one period, a constant horizontal dipole bending radius of ρ_0 and neglecting vertical bending, the transverse motion of a particle in the magnetic structure of an accelerator can be described by a second order homogeneous differential equation, the so-called Hill's equation [35]

$$z''(s) + K_z(s)z(s) = 0, \tag{2.2}$$

with $z = x, y$ and

$$K_x(s) = \frac{1}{\rho_0^2(s)} - k(s) \tag{2.3}$$
$$K_y(s) = k(s). \tag{2.4}$$

The solution of Eq. 2.2 is given in phase-amplitude form as

$$z(s) = A\sqrt{\beta(s)}\cos(\phi(s) + \phi_0) \tag{2.5}$$
$$z'(s) = -\frac{A}{\sqrt{\beta(s)}}[\alpha(s)\cos(\phi(s) + \phi_0) + \sin(\phi(s) + \phi_0)], \tag{2.6}$$

where A and ϕ_0 are constants of integration and determined by initial conditions. Equations (2.5) and (2.6) describe an oscillation around the closed orbit, the so-called *betatron oscillation*, with a position-dependent amplitude of $A\sqrt{\beta(s)}$. The function $\beta(s)$ is called the amplitude or β-function and related to the phase advance $\phi(s)$ as

$$\phi(s) = \int_0^L \frac{ds}{\beta(s)}, \tag{2.7}$$

and $\alpha \equiv -\frac{1}{2}d\beta(s)/ds$. The β-function has no analytical solution and has to be evaluated numerically. The total number of betatron oscillations per turn is referred to as *tune*.

Expressing A in terms of z and z' yields:

$$\gamma z^2 + 2\alpha z z' + \beta z'^2 = A^2 = 2J = \text{const.} \tag{2.8}$$

where α, β and $\gamma \equiv (1+\alpha^2)/\beta$ are also called *Courant-Snyder functions*. Equation 2.8 describes an ellipse in the (z,z')-phase-space with an area of $A^2\pi$, as displayed in Fig. 2.2. The area enclosed by the ellipse is a constant of motion in absence of non-conservative forces such as intra-beam scattering. The constant A^2 is referred to as the *Courant-Snyder invariant*, which is also equal to twice the action, J, of the Hamiltonian leading to Eq. 2.2 [36].

Definition of the Beam Emittance

The Courant-Snyder invariant describes the amplitude of a single particle, while for an ensemble of particles the RMS emittance is defined as

$$\epsilon_{z,\text{RMS}} = \sqrt{\langle z^2\rangle\langle z'^2\rangle - \langle z z'\rangle^2}. \tag{2.9}$$

Here the $\langle\rangle$ indicate the expectation value of the bracketed quantity over the whole ensemble. $\langle z^2\rangle = \sigma_z$ corresponds to the beam size and $\langle z'^2\rangle = \sigma_{z'}$ to the beam diver-

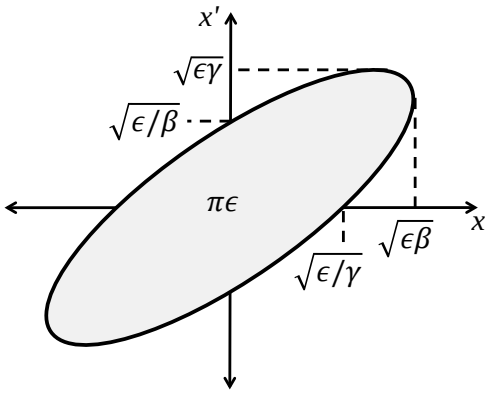

Figure 2.2.: Phase-space ellipse.

gence, which are, analogously to the single particle definition (compare Fig. 2.2), given by

$$\sigma_z = \sqrt{\beta_z \epsilon_{z,\mathrm{RMS}}} \qquad \sigma_{z'} = \sqrt{\gamma_z \epsilon_{z,\mathrm{RMS}}}. \tag{2.10}$$

During acceleration the emittance is adiabatically damped, because the longitudinal, but not the transverse, momentum component is increased. In order to obtain an energy invariant quantity the *normalised emittance*

$$\epsilon_{n,z,\mathrm{RMS}} = \epsilon_{z,\mathrm{RMS}} \sqrt{\gamma^2 - 1} \tag{2.11}$$

is introduced, where γ is the relativistic Lorentz factor. In this form, the normalised emittance is proportional to the area in the (z,p_z)-phase-space, where p_z is the component of the total momentum, p, in z-direction.

In this thesis, all values for the emittance refer to the RMS emittance of a particle ensemble. The index "RMS" will be omitted in the following: $\epsilon_{z,\mathrm{RMS}} \equiv \epsilon_z$, for either the horizontal or vertical geometric emittance. If both transverse emittances are assumed equal, or if it is referred to the transverse emittance in general, the symbol ϵ_{xy} or simply ϵ might be used. A similar notation is used for the normalised emittances: $\epsilon_{n,z}$, $\epsilon_{n,xy}$, ϵ_n.

Off-Momentum Motion and Dispersion Function

Particles having momenta different by Δp from the design momentum will travel on trajectories given by

$$z(s) = z_\beta(s) + D_z(s)\frac{\Delta p}{p}, \tag{2.12}$$

where $z_\beta(s)$ is the betatron oscillation of Eq. 2.5 and $D_z(s)$ is the *dispersion function*. $D_z(s)$ is the solution of an inhomogeneous Hill's equation [38]. The dispersion is a periodic function, $D_z(s) = D_z(s + L)$, with L as the length of one period, and describes

in first order a displacement of the closed orbit. Accordingly, $z_\beta(s)$ describes in case of $\Delta p/p \neq 0$ the betatron motion around the new closed orbit $D_z(s)\frac{\Delta p}{p}$. Dispersion originates from the influence of the particle's momentum on the curvatures of its trajectory in a magnetic field. Thus, dispersion is mainly generated in the arc dipoles. The beam is bent in the horizontal plane, introducing $D_x(s)$, while the vertical dispersion is in general very small.

This implies that particles with different momentum follow paths of different length. The ratio of the relative change in path length, $\Delta C_{\text{ring}}/C_{\text{ring}}$, to the relative difference in momentum, $\Delta p/p$, is evaluated by the *momentum compaction factor*

$$\alpha_c = \frac{\Delta C_{\text{ring}}/C_{\text{ring}}}{\Delta p/p} = \frac{1}{C_{\text{ring}}} \oint \frac{D_x(s)}{\rho_0} ds, \tag{2.13}$$

where C_{ring} is the circumference of the accelerator and ρ_0 the bending radius. In a circular accelerator this leads to a difference in revolution time $T = 1/f = C_{\text{ring}}/v$, where v the velocity of the circulating particle:

$$\frac{\Delta T}{T_0} = \frac{\Delta C_{\text{ring}}}{C_{\text{ring}}} - \frac{\Delta v}{v} = \left(\alpha_c - \frac{1}{\gamma^2}\right)\frac{\Delta p}{p} = \eta \frac{\Delta p}{p} \tag{2.14}$$

$$\eta = \alpha_c - \frac{1}{\gamma^2} = \frac{1}{\gamma_T^2} - \frac{1}{\gamma^2}. \tag{2.15}$$

with $T_0 = 1/f_{\text{rev}}$ the revolution time of the synchronous particle, $\gamma_T \equiv \sqrt{1/\alpha_c}$ is called the *transition-γ*, corresponding to a transition energy of $\gamma_T mc^2$, and η is the so-called *phase-slip-factor*.

2.1.3. Longitudinal Motion

In general, the beam is accelerated in an RF cavity with an sinusoidal field, $V(\phi) = V_{\text{RF}} \sin(\phi)$, where V_{RF} is the maximum RF voltage and $\phi = \omega_{\text{RF}} t$ is the RF phase, with ω_{RF} as the angular RF frequency and t as the time. For acceleration $\sin(\phi) > 0$ is required. A reference particle with $\Delta p/p = 0$ should see the same accelerating field ($\phi = \phi_s$) at each passage, thus the RF frequency must be a multiple of the revolution frequency

$$f_{\text{RF}} = h f_{\text{rev}}, \tag{2.16}$$

where h is the so-called *harmonic number*. A particle with $\Delta p/p \neq 0$ arrives due to its different revolution frequency (see Eq. 2.14) at a slightly different RF phase. Hence, it sees a different acceleration voltage compared to the synchronous particle and gains a different amount of energy per passage, as illustrated in Fig. 2.3. In order to obtain a stable longitudinal motion, a particle with $\Delta p/p < 0$ must gain more energy than the synchronous particle and vice versa.

In the linear approximation of small RF phase shifts ($\Delta\phi = \phi - \phi_s$) for off-momentum

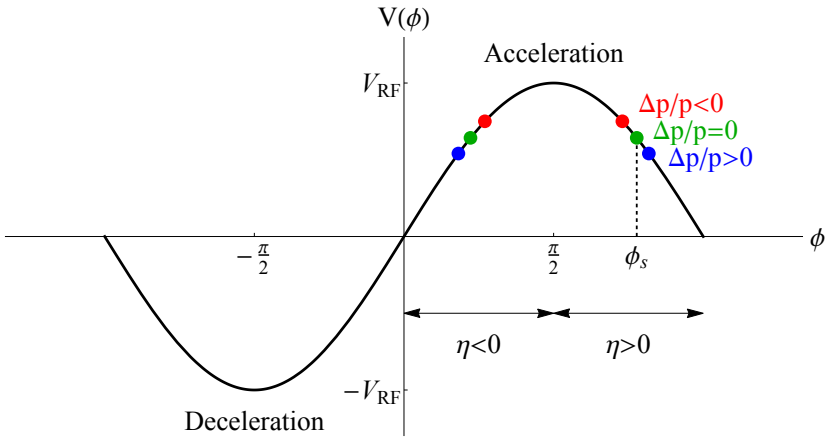

Figure 2.3.: Phase focussing of the RF system.

particles, the synchrotron motion can be described by a damped harmonic oscillator

$$\Delta\ddot{\phi} + 2\alpha_s\Delta\dot{\phi} + \omega_s^2\Delta\phi = 0, \tag{2.17}$$

where $\omega_s = 2\pi f_s$ is the oscillation frequency, referred to as *synchrotron frequency*, and α_s is the damping constant, also called damping decrement, which corresponds to the radiation damping rates that will be discussed in Section 2.5.2. The synchrotron frequency is given by

$$f_s = f_{\text{rev}}\sqrt{-\frac{hZeV_{\text{RF}}\eta\cos(\phi_s)}{2\pi\beta_{\text{rel}}E_b}}, \tag{2.18}$$

with η as the phase-slip-factor, Z the charge number of the particles, E_b the energy of the synchronous particle and $\beta_{\text{rel}} = v/c$. From Eq. 2.18 it is clear that a stable motion can only exist if $\eta\cos(\phi_s) < 0$.

The region of stable motion in the (ΔE, ϕ)-phase-space is enclosed by the so-called *separatrix*. The area inside the separatrix, where stable motion is possible, is called *RF-bucket* or simply bucket. More details can for example be found in [35].

2.2. LHC Collider Layout

2.2.1. Global Structure

The LHC has an eight-fold symmetry, it is constructed out of eight sections (octant) featuring the same structure, see Fig. 2.4. The dipole magnets provide the bending of the beam to its circular orbit, therefore they are located in eight *arcs*. The arcs are separated by *long straight sections* (LSS), the so-called *interaction regions* (IR). The symmetry point (middle) of the IR is called the *interaction point* (IP). The eight

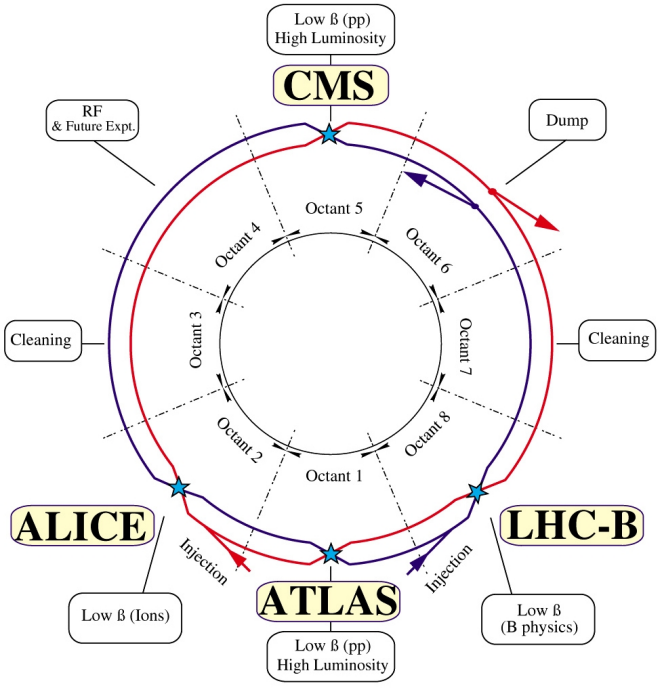

Figure 2.4.: LHC layout. Plot taken from [39].

IRs host the four physics experiments ATLAS (A Toroidal LHC ApparatuS) in IP1, ALICE (A Large Ion Collider Experiment) in IP2, CMS (Compact Muon Solenoid) in IP5 and LHCb (Large Hadron Collider beauty) in IP8, the accelerating cavities (IP4), the beam dump (IP6) and the collimation system (IP3 and IP7). The two equally charged beams counter rotate around the ring in two separated beam pipes. *Beam 1* (B1) is injected in IR2 and circulates clockwise, while *Beam 2* (B2) is injected in IR8 and travels anti-clockwise. The two beams need to be brought together into a common vacuum chamber to make them collide at the detectors, marked with a blue star in Fig 2.4.

2.2.2. Arc Cells

The eight arcs are built by repeating a common structure called *FODO-cell*, see Fig. 2.5. Six main dipoles (green) per cell are used to bend the particles on their circular orbit, while two quadrupoles take care of the beam focusing. By construction a horizontal focusing (F) quadrupole is defocusing (D) in the vertical plane, therefore one needs to locate a second quadrupole rotated by 90° some distance behind the first one to correct for this behaviour. Since in a separated function lattice, the dipoles do not in first order contribute to the focusing (zero focusing = 0), a "F0D0"-cell is built. One LHC FODO-cell is $L_c = 106.9\,\mathrm{m}$ long, and each arc consists of 23 regular cells.

Because of for instance mechanical tolerances and limited pole width of the magnets,

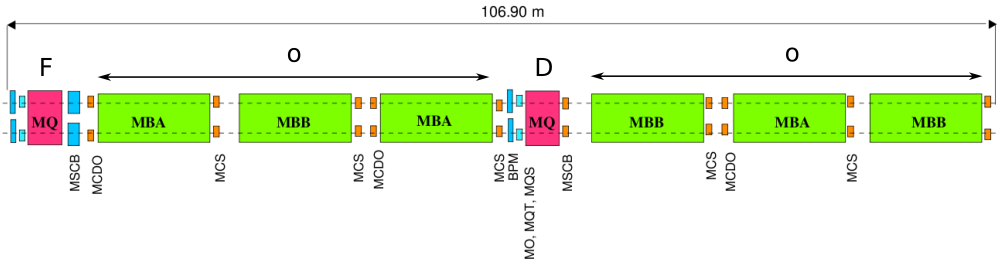

Figure 2.5.: LHC FODO-Cell, showing schematically the structure within the arcs. The main dipoles (green) and quadrupoles (red) are equipped with higher order correctors (sextupoles, octupoles and decapoles, orange), sextupoles for chromaticity correction are shown in dark blue, Beam Position Monitors (BPM) in light blue. For the naming convention see Section 2.2.3. Plot taken from [40].

all possible multipole fields are present in an accelerator and higher order multipole magnets are used for precise corrections of the particle trajectories. The main bending magnets and quadrupoles are equipped with sextupoles, octupoles and decapoles, schematically indicted in Fig. 2.5.

2.2.3. LHC naming convention

Each element installed in the LHC tunnel has its individual identification, constructed following a special convention. This section summarises the most relevant ideas of this convention as used in the LHC MADX [41] sequence.

The first letter indicates the type of element (magnet, beam instrumentation device, collimator etc.), see Table 2.1. For magnets (M) the second letter indicates its order (bending, quadrupole, sextupole, octupole) or its duty (e.g., correction). In case of beam instrumentation devices, the name is usually an acronym, but always starts with the letter B. Collimators are identified by the initial letter T for “Target”.

This initial element type description is followed by a dot and the location inside the ring, which is identified by the cell number (a cell is usually defined between two main quardupoles) to the left (L) or right (R) of the given IP. For example, the main quadrupole MQ.11R5, is located in the eleventh cell to the right of IP5. In case there is more than one element of the same type within one cell, the cell number is preceded by a counting letter (A, B, C, etc.), e.g., MB.B8L1 is second main dipole in the eighth cell left of IP1. Even though the LHC has a two-in-one magnet design, the two beams must be identified individually and a “.B1” or “.B2” is appended to the name.

Initial Letters	
M	Magnet
B	Beam instrumentation device
T	Collimator
Element Types	
MB	Bending Magnet, Dipole
MQ	Quadrupole
MS	Sextupole
MO	Octupole
MC	Corrector, can be an higher order or orbit corrector
Other Acronyms	
R	Right
L	Left
H	Element acts in the horizontal plane
V	Element acts in the vertical plane

Table 2.1.: LHC element naming convention.

2.3. Heavy-Ion Beams for the LHC

2.3.1. Design Parameters

During heavy-ion operation of the LHC, lead-lead (Pb-Pb, fully stripped $^{208}\mathrm{Pb}^{82+}$) and proton-lead (p-Pb) collisions are performed. The p-Pb operation mode was not originally considered in the design report, but first conducted in 2012 (p-Pb pilot run [14]).

With the nominal magnetic field of 8.33 T in the dipole magnets, the ions will have a beam energy of $7Z\,\mathrm{TeV} = 2.76A\,\mathrm{TeV} = 574\,\mathrm{TeV}$ (traditionally often written as 2.76 TeV/nucleon)[2]. In 2011, the LHC ran at only half of the nominal beam energy. A nominal peak luminosity of $\mathcal{L} = 1 \times 10^{27}\,\mathrm{cm}^{-2}\mathrm{s}^{-1}$ is reached. In order to compare this luminosity to proton-proton (p-p) or p-Pb operation, the nucleon-pair luminosity

$$\mathcal{L}_{\mathrm{NN}} = A_{\mathrm{ion},1} A_{\mathrm{ion},2} \mathcal{L} = 4.3 \times 10^{31}\,\mathrm{cm}^{-2}\mathrm{s}^{-1} \tag{2.19}$$

is to be considered, where A_{ion} is the atomic mass number of the nucleus in Beam 1 or 2.

The most important parameters for nominal Pb-Pb operation are listed in Table 2.2, extracted from the LHC design report [42]. Some aspects of ion beams are similar to proton beams and where possible the parameter list for heavy-ion operation is kept close to the one for protons. For instance, the nominal emittance of $\epsilon_n = 1.5\,\mu\mathrm{m}$ for

[2] Of course the exact proportionality holds only for momentum, not energy but is an excellent approximation at the LHC. In the following, the beam energy will frequently be quoted in units of Z eV, where Z is the charge number of the ion ($Z = 82$ for Pb).

Parameter	**Unit**	**Injection**	**Collision**
Lead ion energy	[TeV]	36.9	574
Lead ion energy/nucleon	[TeV]	0.18	2.76
Relativistic gamma factor		190.5	2963.5
Number of ions per bunch		$7. \times 10^7$	
Number of bunches		592	
Transverse normalised emittance	[μm]	1.4	1.5
Longitudinal emittance	[eVs/charge]	0.7	2.5
RMS bunch length	[cm]	9.97	7.94
RMS energy spread	[10^{-4}]	3.9	1.1
Peak RF voltage	[MV]	8	16
Longitudinal IBS emit. growth time	[h]	3.0	7.7
Transverse IBS emit. growth time	[h]	6.5	13
Longitudinal emit. rad. damp. time	[h]	23749	6.3
Transverse emit. rad. damp. time	[h]	47498	12.6
β-function at IP2	[m]	10.0	0.5
Total cross-section	[b]	-	515
Peak luminosity	[$\mathrm{cm}^{-2}\mathrm{s}^{-1}$]	-	1.0×10^{27}

Table 2.2.: LHC nominal Pb-Pb parameters [42].

the ion bunches has been chosen such that the same geometric beam size as for nominal proton bunches, at energies equivalent to the same magnetic dipole field, is obtained. In this way, basic aperture considerations will be the equivalent, if also the operational beam sizes are similar.

2.3.2. The Heavy-Ion Injector Chain

The remanence of the dipole magnets imposes a minimum (and maximum) current to guarantee the desired field quality. Therefore, the minimum energy a particle must have at injection is proportional to the minimum field strength available in a given accelerator. Moreover, it is desired to always achieve the highest injection energy possible to avoid beam instabilities, limiting the intensity. To reach the LHC injection energy of 450 ZGeV, the particles have to pass through a chain of pre-accelerators. The complete CERN accelerator complex (status 2013), which has evolved over the years since CERN was founded to reach higher and higher particle energies, is shown in Fig. 2.6.

The source (not displayed in the graphic) provides lead ions with a charge of $q = +29e$. These are accelerated up to an kinetic energy of 4.2 MeV/nucleon and stripped to $q = +54e$ in the *Radio Frequency Quadrupole (RFQ)* and *LINAC3*. Several LINAC3 pulses are accumulated and transformed into two dense bunches in the *Low Energy Ion Ring (LEIR)*. With the kinetic energy of 72 MeV/nucleon the ions

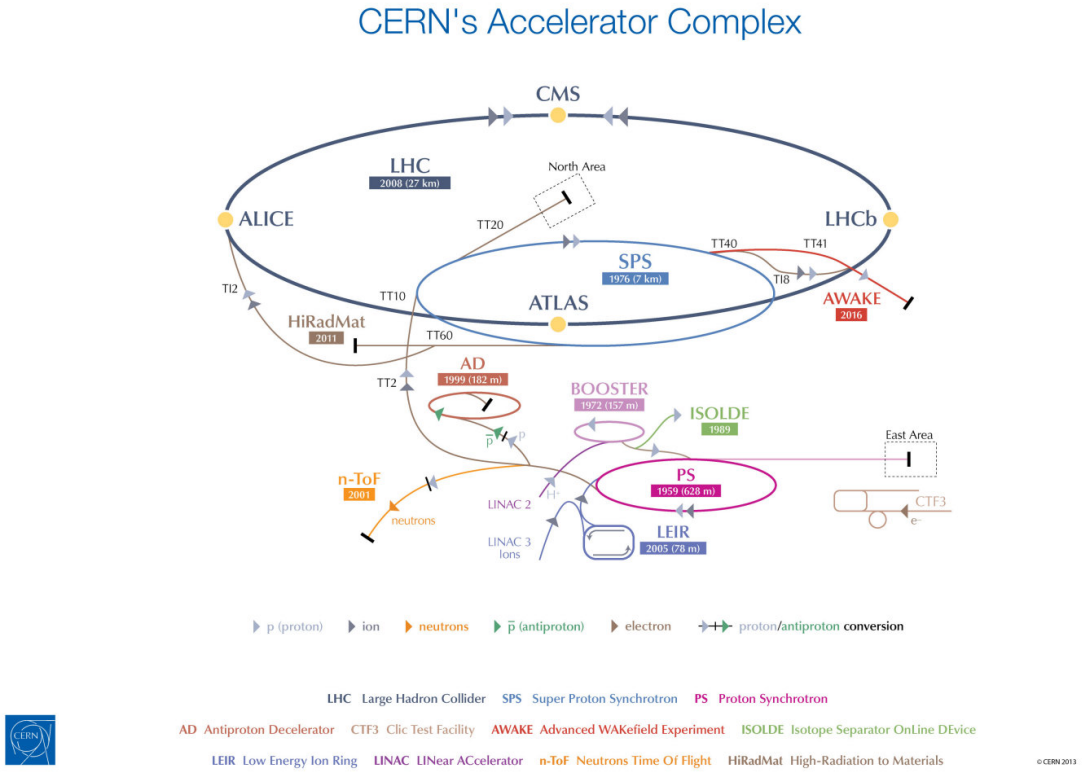

Figure 2.6.: CERN accelerator complex, not to scale. Plot taken from [39].

are transferred to the *Proton Synchrotron (PS)*, where the bunches are accelerated to 5.9 GeV/nucleon. Depending on the filling scheme, several shots from LEIR might be accumulated in the PS to form a so-called *batch*. In the transfer line to the *Super Proton Synchrotron (SPS)* the remaining electrons are stripped off ($q = +82$). In the SPS the final LHC *train* structure is defined. The complete train, composed of several batches, is ramped up to $E_b = 450Z\,\mathrm{GeV} = 177\,\mathrm{GeV/nucleon}$ and transferred to the *Large Hadron Collider (LHC)*. In the LHC several SPS-trains are accumulated to form the full *beam* of up to 592 bunches in the nominal filling scheme.

2.3.3. Filling Schemes

The different lengths of the accelerators in the injector chain imply that the whole beam of several hundred bunches cannot be injected into the LHC at once. At each stage, several pulses have to be accumulated from the previous stage, filling the available circumference, before acceleration and transfer to the next stage. In this way, the bunch trains become longer from one stage to the next and finally build the full LHC beam.

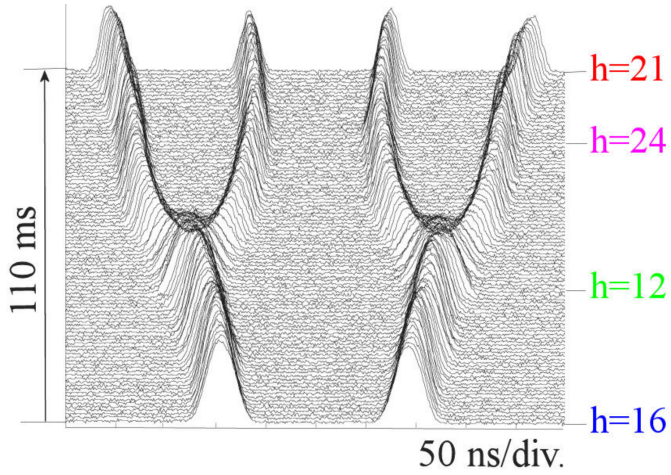

Figure 2.7.: Simulation of batch expansion and bunch splitting in the PS on the example of the nominal scheme. Plot taken from [46].

The production of the LHC beam in the subsequent stages of the injector chain is explained in the following on the examples of the nominal [43] and the 2011 filling scheme.

The Nominal Filling Scheme for Heavy Ions

This filling scheme foresees 592 bunches per LHC beam, which are spaced by 100 ns. Six LINAC3 pulses are injected into LEIR, where each pulse is accumulated over 70 turns under continuous electron cooling [44, 45]. The coasting beam is captured on harmonic $h = 2$, separating the particles into two bunches.

In the PS, the LEIR bunches are injected in two successive $h = 16$ buckets spaced by 130 ns. On a 370 MeV/nucleon intermediate energy plateau, a so-called *batch expansion* is performed, increasing the spacing between the two bunches by progressively decreasing the harmonic number from $h = 16$ over 14 to 12. Each bunch is split in two, while going from $h = 12$ to $h = 24$. The four bunches now sit in consecutive $h = 24$ buckets. A second batch expansion from $h = 24$ to $h = 21$ obtains a spacing close to 100 ns. The full process is visualised in the simulated mountain range display in Fig. 2.7. Details on the RF modifications performed in the PS and the principle of batch extension and bunch splitting can be found in [46, 47].

After acceleration to extraction energy, a final rebucketing to $h = 169$ is performed to precisely set a distance between bunches that corresponds to SPS buckets [46]. A batch of 4 bunches spaced by 100 ns is extracted to the SPS.

In order to optimise the space in the LHC and to provide all experiments with a similar number of collisions, it is necessary to fabricate trains with various numbers of bunches. In case of the nominal filling scheme, one train of 32, three trains of 48 and eight trains of 52 bunches are delivered to the LHC to build a beam of 592 bunches.

For this, either 8, 12 or 13 PS-injections are accumulated in the SPS before acceleration and extraction to LHC. The minimum spacing between batches is determined by the rise time of the SPS injection kicker, which requires 225 ns to reach its full strength. The minimum spacing between trains is determined by the LHC injection kicker, which has a rise time of 900 ns.

The large number of injections per SPS cycle determines the bulk time needed to fill the LHC. The PS would require about 2.4 s to process the beam it receives from LEIR. However, LEIR can only deliver fresh beam every 3.6 s, lengthening the PS cycle to this value. The SPS injection plateau has thus a length of $n_{\mathrm{PS}} \times 3.6\,\mathrm{s} + t_0$, where n_{PS} in is the number of batches taken form the PS per train and $t_0 \approx 1.3\,\mathrm{s}$ is additional time required to prepare the injections and acceleration. In practice, it is complicated to load an individual cycle sequence for each value of n_{PS}, hence the sequence prepared for $n_{\mathrm{PS}} =$ maximum is always used. For shorter trains, bunches that are not required are rejected before injection. This leads to a SPS cycle length, which is equivalent to the minimum time between injections to the LHC, of about 55.2 s. This result is obtained by calculating the length of the injection plateau: $13 \times 3.6\,\mathrm{s} + 1.3\,\mathrm{s} = 48.1\,\mathrm{s}$, and adding the length of the remaining cycle (ramp, flat top, ramp down and end of the cycle) of about 7.1 s [48].

It is unlikely that the nominal filling scheme will be used. Instead there are a few other scenarios, requiring batch extension or compression and bunch splitting, that are considered. Upgrades of the PS RF system and the SPS injection kicker to smaller rise times would allow the reduction of the spacing between bunches and batches. The filling schemes, considering these upgrades and the benefit for the luminosity, are discussed in Chapter 6.

The 2011 Filling Scheme

Since it is important for the analysis of the 2011 ion run, presented in Chapter 4, the filling scheme used is described briefly.

The unexpected high beam losses during RF capture in LEIR, which are observed since the early commissioning of the machine with high intensity beam [49] are still under investigation [50] and limit the achievable bunch intensity in the PS and downstream machines. If these LEIR bunches were split in the PS, the single bunch intensity would be low and the overall luminosity outcome would be reduced compared to unsplit bunches. Since the experience with high single bunch intensities, around $N_b = 1.12 \times 10^8$, in variations of the "Early" filling scheme [42] during the first Pb-Pb run in 2010 [10,11] were good, the nominal filling scheme described above, was modified for the 2011 Pb-Pb run, as sketched in Fig. 2.8.

The main difference is the absence of the bunch splitting in the PS. The arriving LEIR beam undergoes a batch expansion as foreseen, but when changing from $h = 12$ to $h = 24$ a rebucketing instead of a bunch splitting is performed, creating an arrangement with a free bucket between the two bunches. The remaining part of the PS cycle is the same as for the nominal scheme. A batch of two bunches spaced by 200 ns is extracted

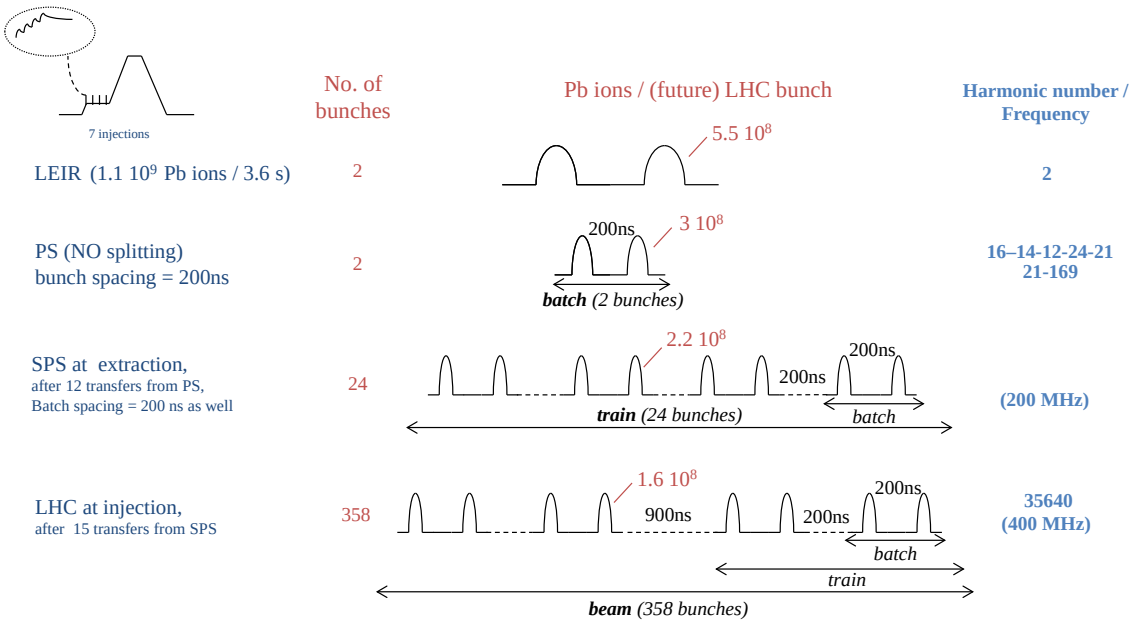

Figure 2.8.: Schematic sketch of the production of the 2011 LHC Pb-Pb filling scheme with 358 bunches. Courtesy of D. Manglunki.

to the SPS. Twelve such two-bunch-batches are accumulated in the SPS to form a train of 24 bunches.

In 2011, the batch spacing in the SPS could be reduced to 200 ns (instead of the nominal 225 ns) and trains with equally spaced bunches could be provided. This was possible because the SPS kicker consists of four modules, which can be ramped independently. With the optics used in 2011 and the reduced magnetic rigidity compared to protons (17.07 GeV/c/charge), the kick strength of the first three modules was sufficient to guide the arriving lead beam on the circular orbit. The three modules used have a faster rise time compared to the fourth one, which is the strongest. Thus, it was possible to reduce the total rise time by 25 ns.

This procedure is repeated 15 times per LHC beam, with one train missing the last batch, summing up to 358 bunches per beam.

2.3.4. The Operational Cycle

The operation of the LHC is organised in a sequence of operational modes, linked to the main accelerator activity. The modes used in every standard fill are “injection”, “prepare ramp”, “ramp”, “flattop”, “squeeze”, “adjust”, “stable beams”, “beam dump”, “ramp down” and “cycling” [51], whereas the last three modes are without circulating beam. A standard cycle is shown in Fig. 2.9: the beam energy (black) and intensity of Beam 1 (red) and Beam 2 (blue) is plotted and the phases of the beam modes are indicated.

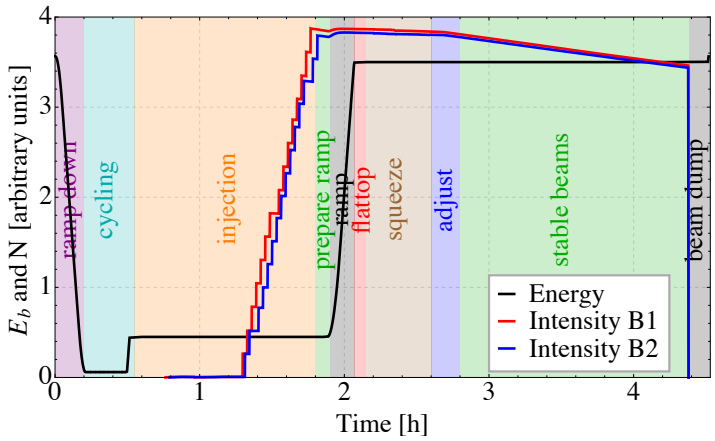

Figure 2.9.: Standard LHC operational cycle.

A fill starts with the injection of the beam. The current in the magnets is set to a value corresponding to a proton beam energy of 450 GeV. First a single so-called *pilot bunch* with low intensity is injected to check all settings before high intensity beam arrives. Trains are injected according to a predefined filling scheme equal or similar to the ones described in Section 2.3.3. When the injection process is finished, the energy ramp is prepared and the beam energy is increased (ramp). Once the flattop (maximum) energy is reached and the pre-squeeze checks are completed, the β^*-squeeze is initiated, reducing the β-function in the IPs to achieve high luminosities. In the following mode "adjust", the beams are brought into collisions. "Stable beams" declares that the beam setup is finished and that the situation is safe for the experiments to switch on their detectors. In general, the machine stays in "stable beams" as long as possible for the experiments to collect physics data. When the intensity has decayed so much that a re-fill becomes necessary, or a potentially dangerous situation is detected, the beams are dumped and the "ramp down" in initiated. A pre-cycle follows, it resets the history of the magnets and prepares for a new injection. One pass through all beam modes is called a *cycle*. Each cycle is identified by a number, the *fillnumber*.

2.4. Luminosity

The quantity that measures the ability of a particle accelerator to produce the required number of interactions is the *luminosity*, $\mathcal{L}$. It represents the proportionality factor between the number of produced events per unit of time, $\mathrm{d}R/\mathrm{d}t$, and the production cross-section of the considered reaction, σ_c:

$$\frac{\mathrm{d}R}{\mathrm{d}t} = \sigma_c \mathcal{L}. \tag{2.20}$$

The total cross-section, $\sigma_{c,\mathrm{tot}}$, in Pb-Pb collisions is dominated by electromagnetic processes, removing particles from the beam. This leads to a very rapid decay of the initial intensity and luminosity, which is called *burn-off*. At $E_b = 7Z\,\mathrm{TeV}$, $\sigma_{c,\mathrm{tot}}$ is about 515 b. The individual contributions are discussed in Section 2.5.4.

The luminosity is calculated from the beam parameters and is given in units of $\mathrm{cm}^{-2}\mathrm{s}^{-1}$. In the specific case of a circular collider and when the particle density distribution can be approximated by a Gaussian, the time-dependent luminosity of two colliding beams is given by:

$$\mathcal{L}(t) = \frac{N_{b1}(t)N_{b2}(t)f_{\mathrm{rev}}k_b}{2\pi\sqrt{\sigma_{x1}^2(t)+\sigma_{x2}^2(t)}\sqrt{\sigma_{y1}^2(t)+\sigma_{y2}^2(t)}} \times F(\sigma_s(t),\theta_c), \tag{2.21}$$

where N_{bi} is the bunch intensity of Beam i ($i = 1, 2$), f_{rev} is the revolution frequency, k_b the number of colliding bunch pairs[3], σ_{xi} and σ_{yi} are the RMS transverse beam-sizes in the horizontal and vertical direction, respectively. The factor $F \leq 1$ captures the geometric luminosity reduction due to the hourglass effect with bunch length, σ_s, and a (half-)crossing angle, θ_c [38].

In the approximation of equal distributions for both beams, $N_b = N_{b1} = N_{b2}$, $\sigma_x = \sigma_{x1} = \sigma_{x2}$, $\sigma_y = \sigma_{y1} = \sigma_{y2}$ and $F = 1$, Eq. (2.21) simplifies to

$$\mathcal{L} = \frac{N_b^2 f_{\mathrm{rev}} k_b}{4\pi\sigma_x\sigma_y} = \frac{N_b^2 f_{\mathrm{rev}} k_b \gamma}{4\pi\epsilon_n\beta^*}, \tag{2.22}$$

where for the second equality round beams, $\sigma_{xy} = \sigma_x = \sigma_y$, and $\sigma_{xy}^2 = \epsilon_n\beta^*/\gamma$ were used. With ϵ_n as the normalised transverse emittance, β^* as the β-function at the IP and γ as the relativistic Lorentz factor. Note that the luminosity linearly scales with energy, due to the adiabatically damped beam sizes during acceleration.

The time-integrated luminosity is denoted as

$$\mathcal{L}_{\mathrm{int}} = \int \mathcal{L}(t)dt. \tag{2.23}$$

2.4.1. Crossing Angle Considerations

The factor F in Eq. (2.21) represents the geometrical overlap of the two particle distributions, which can be equal to one, when the two distributions are perfectly overlapping, or smaller than one in case of collisions with a crossing angle, offsets, hourglass effect, non-Gaussian beam profile and/or non-zero dispersion at the collision point [52].

[3] $k_b \leq n_b$, with n_b as the number of bunches per beam.

The reduction factor due to a non-zero crossing angle is given by

$$F = 1/\sqrt{1 + \left(\frac{\theta_c \sigma_s}{\sqrt{\epsilon_n \beta^*/\gamma}}\right)^2}, \tag{2.24}$$

where θ_c is the half-crossing angle and σ_s is the RMS bunch length, assuming equal beam parameters for both beams and in both planes [40].

Collisions of heavy nuclei can be central (full overlap) or peripheral (partial overlap). In peripheral collisions only a few protons and neutrons participate in the collisions, the remaining fraction of the two colliding ions is broken up into so-called spectator nucleons, flying along the beam line. The ALICE experiment uses a Zero Degree Calorimeter (ZDC)[53] to detect the energy of these spectator nucleons in order to determine the overlap region of the two colliding nuclei. The ZDCs are located 115 m away from the IP on both sides, exactly along the beam line. For a good measurement, it is crucial that all spectator nucleons hit the detector. To ensure this, the half-crossing angle in IP2 has to be below θ_c <60 μrad, otherwise to many neutrons would get lost in the aperture of other elements installed in between the main ALICE detector and the ZDCs.

Fortunately, the relatively low intensities and the large bunch spacing of the ion beams lead to weak beam-beam effects (see Section 2.5.3 and [52]), which do not themselves impose a minimum separation under nominal conditions. However, zero crossing angle would lead to additional head-on beam-beam encounters, reducing the beam lifetime and distorting the ZDC measurement. Therefore, a minimum crossing angle is required, leading to only a small reduction of the luminosity in ALICE.

In proton operation the intensities are much higher and the bunch spacing is reduced, therefore a crossing angle is required. Even though, the insertion of a crossing angle eliminates all unwanted head-on collisions, it leads to the so-called long-range interactions. In long-range interactions the bunches do not cross each other, but still feel the electromagnetic forces from the bunches of the opposite beam. When the separation is large enough, these long-range encounters should be weak. To save commissioning time at the beginning of the ion run, the optics settings, including the relatively large crossing angles, in ATLAS and CMS are adopted from proton operation.

2.5. Beam Dynamic Effects

2.5.1. Intra-Beam Scattering

Multiple small-angle Coulomb scattering between charged particles of the same bunch, the so-called *intra-beam scattering* (IBS) [54], results in energy exchange between the three planes. This does not only lead to a re-distribution; in case the collision transfers momentum from the transverse to the longitudinal plane, the change in momentum

leads to a change in the motion of the particle: $u = u_\beta + D_u \Delta p/p$, with $u = x, y$, the dispersion $D_u \neq 0$ and u_β as the u-position due to betatron oscillation, introducing transverse emittance growth. In a circular accelerator, dispersion is unavoidably created by dipoles in the horizontal plane. However, the vertical dispersion is usually small and so is the vertical emittance growth due to IBS. Vertical dispersion only occurs because of magnet errors or displacements, introducing a dipole component in the magnetic field acting on the vertical plane. This effect is orders of magnitudes smaller than in the horizontal plane and can be corrected. Moreover, IBS can lead to particle losses, if particles travelling close to the separatrix scatter and the change in longitudinal momentum is large enough that they leave the bucket. This effect is called *debunching*. For the LHC, the particle loss rate due to debunching is small.

Formalism and Scaling

Several formalisms are available describing the physical effects derived by Piwinski, Bjorken and Mitingwa, Bane, Nagaitsev or Wei [55–59], based on different assumptions and suitable for different situations. In Piwinski's formalism the IBS emittance growth rates, α_{IBS}, are determined with the following equations [60]:

$$\alpha_{\mathrm{IBS},s} = \left\langle A_{\mathrm{p}} \frac{\sigma_h^2}{\sigma_p^2} f(a,b,q) \right\rangle \tag{2.25}$$

$$\alpha_{\mathrm{IBS},x} = \left\langle A_{\mathrm{p}} \left[f\left(\frac{1}{a}, \frac{b}{a}, \frac{q}{a}\right) + \frac{D_x^2 \sigma_h^2}{\sigma_x^2} f(a,b,q) \right] \right\rangle \tag{2.26}$$

$$\alpha_{\mathrm{IBS},y} = \left\langle A_{\mathrm{p}} \left[f\left(\frac{1}{b}, \frac{a}{b}, \frac{q}{b}\right) + \frac{D_y^2 \sigma_h^2}{\sigma_y^2} f(a,b,q) \right] \right\rangle \tag{2.27}$$

with

$$A_{\mathrm{p}} = \frac{2 r_0^2 c N_b}{64 \pi^2 \beta_{\mathrm{rel}}^3 \gamma^4 \epsilon_x \epsilon_y \sigma_s \sigma_p} \tag{2.28}$$

$$\frac{1}{\sigma_h^2} = \frac{1}{\sigma_p^2} + \frac{D_x^2}{\sigma_x^2} + \frac{D_y^2}{\sigma_y^2} \tag{2.29}$$

$$a = \frac{\sigma_h \beta_x}{\gamma \sigma_x}, \quad b = \frac{\sigma_h \beta_y}{\gamma \sigma_y}, \quad q = \sigma_h \beta_{\mathrm{rel}} \sqrt{\frac{2d}{r_0}} \tag{2.30}$$

where $D_{x,y}$ is the horizontal and vertical dispersion, σ_s, σ_p and $\sigma_{x,y}$ are the RMS bunch length, relative momentum spread and transverse beam sizes, $\beta_{x,y}$ are the β-functions, $\epsilon_{x,y} = \sigma_{x,y}^2/\beta_{x,y}$ are the transverse geometric emittances, d quotes the smaller of the horizontal and vertical beam radii. The classical particle radius, r_0, relates to the classical proton radius, r_{p0}, as $r_0 = Z^2/A_{\mathrm{ion}} r_{p0}$, with Z and A_{ion} as the charge and

mass number of the ion. The function f is given by:

$$f(a,b,q) = 8\pi \int_0^1 \left\{ 2\ln\left[\frac{q}{2}\left(\frac{1}{P}+\frac{1}{Q}\right)\right] - 0.577\ldots \right\} \frac{1-3u^2}{PQ}\mathrm{d}u \tag{2.31}$$

where

$$P^2 = a^2 + (1-a^2)u^2 \tag{2.32}$$
$$Q^2 = b^2 + (1-b^2)u^2. \tag{2.33}$$

The IBS growth rates in Eq. (2.25) to (2.27) are proportional to the factor A_p given in Eq. (2.28). This factor gives an indication of the scaling and quantities most important for the IBS strength. Equation 2.28 scales inversely with the energy[4], meaning the IBS growth is strongly suppressed at higher energies. On the other hand, the rates increase with bunch intensity and decrease with growing emittances ($\alpha_\mathrm{IBS} \propto N_b/(\epsilon_x\epsilon_y\sigma_s\sigma_p)$), implying that the higher the bunch brightness, desired for luminosity production, the stronger the IBS. A third relevant proportionality is the relation to r_0, which depends on the particles' mass and charge ($\alpha_\mathrm{IBS} \propto Z^2/A_\mathrm{ion}$), hence the effect is stronger for heavy ions compared to protons.

The remaining factors in Eq. (2.25) to (2.27) are complicated and depend mainly on lattice parameters, like the dispersion and β-functions, and the beam divergences in all dimensions.

In general, the local IBS growth rates, introduced by each element in the lattice (with their local dispersion and β-functions), are determined separately around the ring with Eq. (2.25) to (2.27). They have to be combined to obtain the usually quoted *total IBS growth rate* in units of time.

In a simplified formalism J. Wei derived analytical equations for the IBS emittance growth rates of hadron beams [59], provided that the lattice of the accelerator mainly consists of regular cells. For full coupling between the horizontal and vertical motion, the growth rates average in the transverse dimension. For round beams ($\epsilon = \epsilon_x = \epsilon_y$) and if the motion is fully coupled, Wei's formulae for the IBS emittance growth rates are

$$\alpha_{\mathrm{IBS},x,y} = \frac{C_1 N_b}{\sigma_s \epsilon^2 \sqrt{\epsilon + C_2\sigma_p^2}} \tag{2.34}$$
$$\alpha_{\mathrm{IBS},s} = \frac{C_3\,\epsilon}{\sigma_p^2}\alpha_{\mathrm{IBS},x,y}, \tag{2.35}$$

[4]Since the emittances shrink during acceleration, $\epsilon_{n,xy} = \epsilon_{xy}\gamma$, and $\sigma_p = \Delta p/p \propto 1/\gamma$.

where C_1, C_2 and C_3 are constant for a given fill:

$$C_1 = \frac{5\sqrt{2}cZ^4r_{p0}^2}{8A_{\text{ion}}^2\gamma^5\beta_{\text{rel}}^3}\frac{2D_x^2\gamma^2-\beta_x(\beta_x+\beta_y)}{\beta_x\sqrt{\beta_x+\beta_y}} \tag{2.36}$$

$$C_2 = \frac{D_x^2}{\beta_x} \tag{2.37}$$

$$C_3 = \frac{4\gamma^2\beta_x}{2D_x^2\gamma^2-\beta_x(\beta_x+\beta_y)}. \tag{2.38}$$

In this form, the longitudinal and transverse growth rates are directly related.

Beam Evolution

If the emittance evolution is dominated by IBS, its growth is given by the differential equation:

$$\alpha_{\text{IBS},i} = \frac{1}{\epsilon_i}\frac{d\epsilon_i}{dt}, \tag{2.39}$$

where $\alpha_{\text{IBS},i}$ is the IBS growth rate of plane $i = x, y, s$. Assuming a constant and positive rate, Eq. (2.39) describes an exponential growth of the geometric emittance

$$\epsilon_i(t) = \exp(\alpha_{\text{IBS},i}t) + \text{const.} \tag{2.40}$$

In general, $\alpha_{\text{IBS},i}$ varies with time, since it strongly depends on the beam parameters.

The emittance is influenced also by other effects like radiation damping (see Section 2.5.2), quantum excitation, various noise effects etc. that have to be taken into account in Eq. (2.39) by introducing additional terms corresponding to the specific growth/decay times of the considered effects. To obtain expressions for the evolution of the emittances and the number of particles per bunch, a system of four coupled ordinary differential equations (ODE) has to be solved:

$$\frac{1}{\epsilon_x}\frac{d\epsilon_x}{dt} = \alpha_{\text{IBS},x}(N_b,\epsilon_x,\epsilon_y,\epsilon_s) - \alpha_{\text{rad},x} + \alpha_{\text{coll},x}(N_b,\epsilon_x,\epsilon_y,\epsilon_s) + \ldots \tag{2.41}$$

$$\frac{1}{\epsilon_y}\frac{d\epsilon_y}{dt} = \alpha_{\text{IBS},y}(N_b,\epsilon_x,\epsilon_y,\epsilon_s) - \alpha_{\text{rad},y} + \alpha_{\text{coll},y}(N_b,\epsilon_x,\epsilon_y,\epsilon_s) + \ldots \tag{2.42}$$

$$\frac{1}{\epsilon_s}\frac{d\epsilon_s}{dt} = \alpha_{\text{IBS},s}(N_b,\epsilon_x,\epsilon_y,\epsilon_s) - \alpha_{\text{rad},s} + \ldots \tag{2.43}$$

$$\frac{1}{N_b}\frac{dN_b}{dt} = -\alpha_{\text{IBS},N}(N_b,\epsilon_x,\epsilon_y,\epsilon_s) - \alpha_{\mathcal{L}}(N_b,\epsilon_x,\epsilon_y,\epsilon_s) - \ldots \tag{2.44}$$

where $\alpha_{\text{IBS},N}$ and $\alpha_{\mathcal{L}}$ are the inverse instantaneous lifetimes from debunching and luminosity production[5]. The emittance growth rate caused by core depletion in the collisions is denoted $\alpha_{\text{coll},i}$, with $i = x, y$ [61]. The minus signs indicate that the associated

[5]If the beams are not colliding: $\alpha_{\mathcal{L}} = 0$.

processes lead to damping or particle losses.

2.5.2. Radiation Damping

A charge undergoing acceleration will radiate energy in form of electromagnetic waves. Therefore, a charged particle travelling in a storage ring will radiate energy, when it is bent on its circular orbit. This radiation is called synchrotron radiation. Because of the average energy loss into synchrotron radiation in a circular accelerator, radiation damping occurs. The transverse and longitudinal emittances are damped like $A_i = A_{0,i}e^{-\alpha_{\mathrm{rad},i}t}$, where $i = x, y, s$, with the radiation emittance damping rates $\alpha_{\mathrm{rad},i}$ [38]:

$$\alpha_{\mathrm{rad},s} = 2E_b^3 \frac{C_\alpha}{C_{\mathrm{ring}}} \mathcal{I}_2 \left(2 + \frac{\mathcal{I}_{4,x} + \mathcal{I}_{4,y}}{\mathcal{I}_2}\right) \tag{2.45}$$

$$\alpha_{\mathrm{rad},x} = 2E_b^3 \frac{C_\alpha}{C_{\mathrm{ring}}} \mathcal{I}_2 \left(1 - \frac{\mathcal{I}_{4,x}}{\mathcal{I}_2}\right) \tag{2.46}$$

$$\alpha_{\mathrm{rad},y} = 2E_b^3 \frac{C_\alpha}{C_{\mathrm{ring}}} \mathcal{I}_2 \left(1 - \frac{\mathcal{I}_{4,y}}{\mathcal{I}_2}\right) \tag{2.47}$$

where E_b is the particle's energy, $C_\alpha = r_0 c/(3(m_{\mathrm{ion}}c^2)^3)$ and C_{ring} is the circumference of the accelerator. The damping partition numbers, J_i, are defined as

$$J_x = 1 - \frac{\mathcal{I}_{4,x}}{\mathcal{I}_2}, \quad J_y = 1 - \frac{\mathcal{I}_{4,y}}{\mathcal{I}_2}, \quad J_s = 2 + \frac{\mathcal{I}_{4,x} + \mathcal{I}_{4,y}}{\mathcal{I}_2}. \tag{2.48}$$

Following the Robinson theorem [38], the sum of the damping partition numbers of the three planes $i = x, y, s$ is constant:

$$\sum_i J_i = 4. \tag{2.49}$$

The radiation integrals $\mathcal{I}$ are given by

$$\mathcal{I}_2[\mathrm{m}^{-1}] = \oint \kappa^2 ds \tag{2.50}$$

$$\mathcal{I}_{4,x}[\mathrm{m}^{-1}] = \oint [\kappa^2 \kappa_x D_x + 2\kappa_x (k D_x + \underline{k} D_y)] ds \tag{2.51}$$

$$\mathcal{I}_{4,y}[\mathrm{m}^{-1}] = \oint [\kappa^2 \kappa_y D_y + 2\kappa_y (\underline{k} D_x - k D_y)] ds \tag{2.52}$$

$$\mathcal{I}_{6,x}[\mathrm{m}^{-1}] = \oint (k D_x + \underline{k} D_y)^2 ds \tag{2.53}$$

$$\mathcal{I}_{6,y}[\mathrm{m}^{-1}] = \oint (\underline{k} D_x - k D_y)^2 ds, \tag{2.54}$$

where k, $\underline{k}$ are the strengths of normal and skew quadrupoles, respectively, D_{xy} is the dispersion function in the corresponding plane, $\kappa_{xy} \equiv 1/\rho_{xy}$ with ρ_{xy} as the horizontal or vertical curvature[6], $\kappa^2 = (\kappa_x^2 + \kappa_y^2)$.

For an isomagnetic ring with separated function magnets and $D_y = 0$ the integrals simplify to

$$\mathcal{I}_2 \approx \frac{2\pi}{\rho_0} \tag{2.55}$$

$$\mathcal{I}_{4,x} \approx 2\pi \frac{D_x}{\rho_0^2} \ll \mathcal{I}_2 \tag{2.56}$$

$$\mathcal{I}_{4,y} \approx 0. \tag{2.57}$$

Equation (2.56) is approximated, since D_x is in the order of a few metres, while the bending radius $\rho_0 = p/(qB)$ is in the order of several kilometres. Inserting Eq. (2.55) to (2.57) into Eq. (2.45) to (2.47) yields

$$\alpha_{\mathrm{rad},s} \approx 2E_b^3 C_\alpha \frac{4\pi}{\rho_0 C_{\mathrm{ring}}} \tag{2.58}$$

$$\alpha_{\mathrm{rad},x} \approx 2E_b^3 C_\alpha \frac{2\pi}{\rho_0 C_{\mathrm{ring}}} \tag{2.59}$$

$$\alpha_{\mathrm{rad},y} \approx 2E_b^3 C_\alpha \frac{2\pi}{\rho_0 C_{\mathrm{ring}}}. \tag{2.60}$$

These equations do not depend on the beam parameters. The strongest dependence is on the third power of the energy, the machine size and the particle type. It is worth pointing out that in this approximation the longitudinal damping is twice as fast as in the transverse planes:

$$\alpha_{\mathrm{rad},s} = 2\alpha_{\mathrm{rad},x} = 2\alpha_{\mathrm{rad},y}. \tag{2.61}$$

2.5.3. Beam-Beam

The two beams travel in separated beam pipes. Only in the interaction regions they pass through a common pipe to bring them into collisions in the local experiment. In these regions of interaction the beams exert electromagnetic forces on each other, the so-called *beam-beam force*. The effects of the beam-beam force manifest themselves in very different ways. They can, for example, lead to instabilities followed by particle losses and emittance growth. Especially during the passage of one bunch through the other in the IP, during a so-called *head-on* interaction, these forces can be very strong. In a simplified picture, each single particle of one bunch receives a kick from the opposite beam and is deflected by a certain angle. In a linear approximation this kick acts as a quadrupole lens and thus introduces a tune shift, which can be approximated

[6] $\rho_x \equiv \rho_0$ is the bending radius of the accelerator, in the LHC $\rho_y = 0$.

with the linear beam-beam parameter ξ [38]:

$$\xi_{i,u} = \frac{N_{b,j} r_{p0} Z_i Z_j \beta^*}{2\pi A_{\mathrm{ion},i} \gamma_i \sigma_{j,u} (\sigma_{j,u} + \sigma_{j,v})}, \tag{2.62}$$

where the beam receiving the kick is labelled with i and the beam exerting the force is labelled j. u and v describe the two transverse planes. r_{p0} is the classical proton radius, Z and A_{ion} the charge and atomic mass number of the corresponding beams, σ the beam size in the corresponding plane.

For equal and round beams Eq. (2.62) simplifies to

$$\xi = \frac{N_b r_0 \beta^*}{4\pi\gamma\sigma^2} = \frac{N_b r_0}{4\pi\epsilon_n}, \tag{2.63}$$

with r_0 as the classical radius of the considered particle and ϵ_n the normalised emittance. As is easy to see, this equation only depends on the beams themselves and is independent of energy and lattice parameters. Equations (2.62) and (2.63) describe the tune shift introduced due to one head-on collision per turn, if the beams collide in more than one place, ξ has to be multiplied by the number of experiments in which the investigated bunch is colliding.

The beam-beam tune shift can be a limiting factor for the luminosity, since, if it becomes too large, the particles could cross resonances and get lost. If this is the case, the intensities have to be reduced, the emittances blown-up or a crossing angle introduced to force the tune shift below its limit, consequently the luminosity will be reduced simultaneously.

Only during operation it does become certain where the beam-beam limit of a collider exactly is. For the p-p operation in the LHC, for instance, a beam-beam limit of 0.015 was expected, based on Sp$\bar{\mathrm{p}}$S experience. Nevertheless, the tune shifts achieved in p-p in dedicated experiments exceeded the nominal value by almost a factor of 5 and the value reached in normal operation by already a factor of 2 [62].

2.5.4. Secondary Beams Emerging from the Collisions

Electromagnetic Processes In the collision of two fully stripped ions a variety of processes, leading to fragmentation and particle production, occur. If the impact parameter b [63] is smaller than twice the nuclear electric radius R, inelastic hadronic interactions take place. These are usually the most desired for physics analysis of the experiments. For $b > 2R$, the interactions are specified as ultraperipheral, where the intense Lorentz-contracted fields of the nuclei can be represented as a pulse of virtual photons [64], which collide.

Ultraperipheral electromagnetic interactions dominate the total cross-section during heavy-ion collisions and cause the initial intensity to decay rapidly [65]. The most

important interactions in Pb collisions are Bound-Free Pair-Production (BFPP)

$$^{208}\mathrm{Pb}^{82+} +^{208}\mathrm{Pb}^{82+} \longrightarrow^{208}\mathrm{Pb}^{82+} +^{208}\mathrm{Pb}^{81+} + \mathrm{e}^{+} \tag{2.64}$$

and Electromagnetic Dissociation (EMD)

$$^{208}\mathrm{Pb}^{82+} +^{208}\mathrm{Pb}^{82+} \longrightarrow^{208}\mathrm{Pb}^{82+} +^{207}\mathrm{Pb}^{82+} + \mathrm{n}. \tag{2.65}$$

Reaction (2.64) describes electron capture to one of the nuclei, which will be called BFPP1 hereafter. The next order reaction, when two electrons are captured by one of the nuclei, is called BFPP2, etc. A similar naming convention is applied to EMD, where Eq. (2.65) characterises EMD1.

Deviation from Main Beam These interactions change the charge state or mass of one of the colliding ions and thus its magnetic rigidity, creating a secondary beam emerging from the collision point [66]. The magnetic rigidity is defined in Eq. (2.1). If the mass of an ion is changed by $A \to A_0 + \Delta A$ and the charge state by $Z \to Z_0 + \Delta Z$, its rigidity becomes $B\rho(1+\delta)$. The fractional deviation δ from the main beam, with A_0 and Z_0, is given to a very good approximation[7] by [66]

$$\delta \approx \frac{Z_0(A_0 + \Delta A)}{A_0(Z_0 + \Delta Z)}(1 + \delta_p) - 1, \tag{2.66}$$

taking into account a central relative momentum offset, δ_p, of the beam. In the Pb-Pb collisions discussed here, $\delta_p = 0$ is assumed. The secondary beams will follow dispersive orbits according to their magnetic rigidity. However, their momentum deviation lies outside the acceptance of the ring, resulting in an impact on the beam screen in a localised position (depending on the lattice) around a superconducting magnet downstream of the interaction point (IP), as sketched in Fig. 2.10. The secondary beam's horizontal orbit, with respect to the central orbit, is given by δ times the locally generated dispersion, d_x, since the IP. Thus, the impact position is given by the first point where the horizontal aperture $A_x \leq d_x\delta$, unless δ is small enough that the secondary beam goes through the arc. This occurs on each side of every IP where ions collide.

The secondary beam trajectories on the example of Beam 1 right of IP2 are shown in Fig. 2.11. The (a) horizontal and (b) vertical beam envelopes were tracked with MADX, using the nominal optics configuration at $E_b = 7Z\,\mathrm{TeV}$ and $\beta^* = 0.5\,\mathrm{m}$, assuming a normalised emittance of $\epsilon_n = 1.5\,\mu\mathrm{m}$. The main beam is displayed with its 10σ envelope (blue in (a), light red in (b)), while the 1σ envelopes are shown for the BFPP1 (red), BFPP2 (orange), EMD1 (light green) and EMD2 (dark green) beams.

Dispersion is mainly generated by dipoles in the horizontal plane, therefore the secondary beams are significantly separated only in the horizontal plane (top picture), while they travel along with the main beam in the vertical plane. The straight section

[7] neglecting the increments of the mass excess

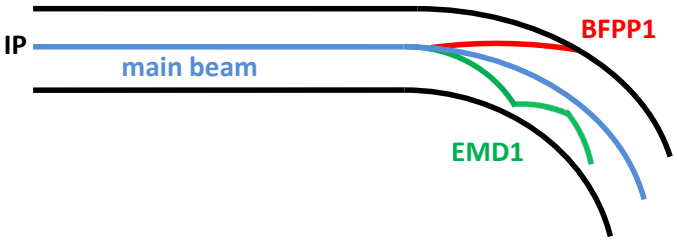

Figure 2.10.: Sketch of the separation of the secondary beams from the main beam in the curved beam pipe inside bending magnets.

	BFPP		**EMD**			**Hadronic**
Symbole	$\sigma_{\mathrm{c,BFPP1}}$	$\sigma_{\mathrm{c,BFPP2}}$	$\sigma_{\mathrm{c,EMD1}}$	$\sigma_{\mathrm{c,EMD2}}$	$\sum \sigma_{\mathrm{c,EMD}}$	$\sigma_{\mathrm{c,hadron}}$
Reference	[67]	[68]	[66]			[69]
Cross-section [b]	281	0.006	96	29	226	8

Table 2.3.: Cross-sections for electromagnetic interactions in Pb-Pb collisions at $E_b = 7Z$ TeV.

directly behind the IP (between $s = 0$ and ∼250 m) does not feature many dipoles. The only bending magnets installed here are the ones responsible for separating Beam 1 and 2 after the collision and some correctors. Thus, the trajectories of the secondary beams are mostly overlaid with the main beam. The first section of the arc connected to the IR is called dispersion suppressor (DS), since, as its name suggests, a special arrangement of bending and focusing magnets takes care to eliminate the dispersion, created by the dipoles in the arc, to be zero at the IP. At the entrance of the DS the secondary beams start to diverge from the main beam. The BFPP beams will impact in the beam screen inside a superconducting dipole about 100 m further downstream, while the EMD beams are deflected less and travel on dispersive trajectories parallel to the main beam until the momentum collimation section in IR3, where they are absorbed by the collimators (see Section 7.2.3).

Interaction Cross-Sections The rate of particle removal from the beam is directly proportional to the interaction cross-section, see Eq. (2.20). Table 2.3 summarizes the cross-sections for the dominating electromagnetic processes at $E_b = 7Z$ TeV in Pb-Pb collisions.

Of all electromagnetic interactions, changing the charge-to-mass ratio of at least one of the participating ions, BFPP1 is the reaction with the highest probability. A calculation to estimate the BFPP1 cross-section is described in Ref. [67]. The parametrization

$$\sigma_{\mathrm{c,BFPP1}} \approx Z_1^5 Z_2^2 \sum_i (A_i \log\gamma + B_i) \tag{2.67}$$

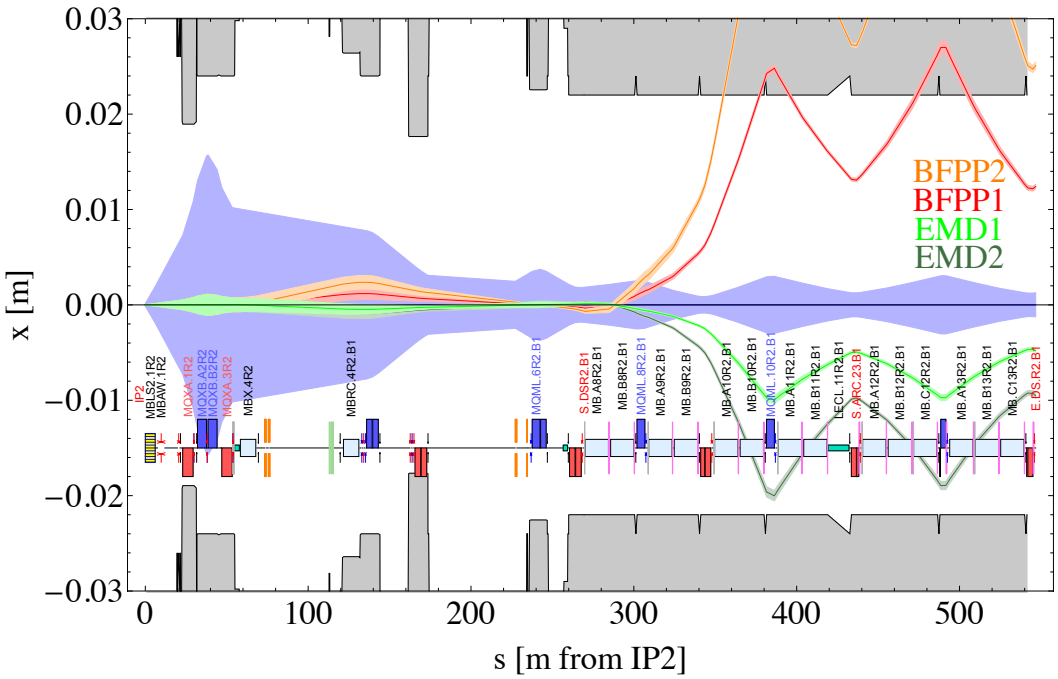

(a) Horizontal plane.

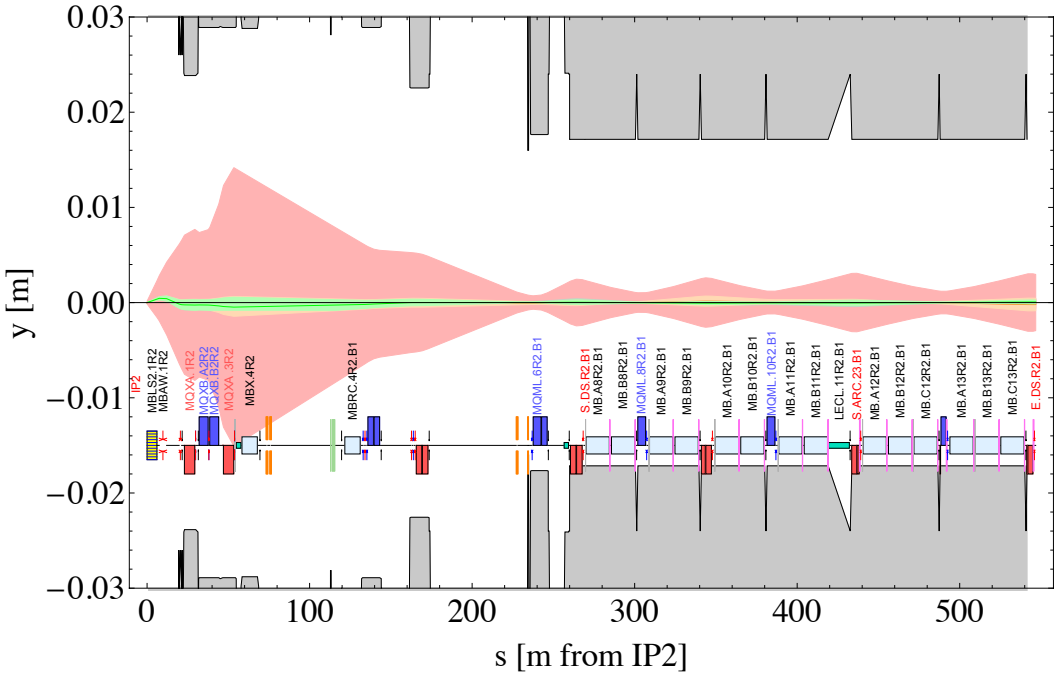

(b) Vertical plane.

Figure 2.11.: Beam envelopes of main (10σ) and secondary (1σ) beams right of IP2 in the (a) horizontal and (b) vertical plane. The gray areas on the top and bottom indicate the aperture, the boxes in the lower third of the plots show the main beam line elements.

can be used, where the electron is captured by nucleus 1, with the charge number Z_1. The sum is taken over the atomic shells i and γ is the relativistic Lorentz factor of the ion. Values for A_i, B_i are given in Ref. [67]. The uncertainty on $\sigma_{\mathrm{c,BFPP1}}$ given in Table 2.3 is estimated to about 20% [66, 67]. The probabilities of higher order BFPP interactions, i.e., capturing two or more electrons, leading to a charge state of $\leq 80^+$, is much smaller, and as Table 2.3 states, almost negligible in the sum over all cross-sections relevant for particle removal. EMD cross-sections were estimated by using the Monte Carlo program FLUKA [70] in Ref. [66] using [71]. In case of EMD, the higher order interactions are still highly probable and contribute to the total EMD cross-section, $\sigma_{\mathrm{c,EMD}}$, which includes all decay channels. Inelastic hadronic interactions, which are usually the main object of study of the experiments, have only a rather moderate cross-section compared to the electromagnetic processes.

The total event cross-section, $\sigma_{c,\mathrm{tot}}$, is given by the sum over the cross-sections of all possible interactions removing particles from the beam in collision (burn-off); at $E_b = 7Z\,\mathrm{TeV}$ the total Pb-Pb cross-section is thus given by

$$\begin{aligned} \sigma_{c,\mathrm{tot}}(7Z\,\mathrm{TeV}) &= \sigma_{c,\mathrm{BFPP}} + \sigma_{c,\mathrm{EMD}} + \sigma_{c,\mathrm{hadron}} \\ &\approx 281\,\mathrm{b} + 226\,\mathrm{b} + 8\,\mathrm{b} = 515\,\mathrm{b}. \end{aligned} \tag{2.68}$$

The particle losses from BFPP and EMD processes dominate the decay of intensity and luminosity, because of their high cross-sections.

The total cross-section at the 2011 beam energy of $E_b = 3.5Z\,\mathrm{TeV}$ is determined by a combination of recent measurements and calculations: Ref. [72] states the measured EDM + hadronic cross-section as $\sigma_{c,\mathrm{EDM+had.}} = 195.6\,\mathrm{b}$, with a maximal systematic uncertainty of about 12%. The BFPP cross-section was calculated to $\sigma_{c,\mathrm{BFPP}} = 253.6\,\mathrm{b}$ with the aid of Ref. [67], where the exact uncertainty of the method is not given, but the predictions are expected to be reliable. Thus, the total cross-section evaluates to

$$\sigma_{\mathrm{c,tot}}(3.5Z\,\mathrm{TeV}) \approx 449\,\mathrm{b}, \tag{2.69}$$

with an uncertainty of several percent.

Deposited Beam Power Following Eq. (2.20), the production rate of a considered reaction is given by the product of its cross-section with the instantaneous luminosity, thus changes during the fill. Nevertheless, the magnets would suffer from a continuous high exposure. The risk of quenching a superconducting magnet and long-term damage, due to these losses, is high. The power, P, in these secondary beams can be calculated as the production rate times the particle energy:

$$P = \sigma_c \mathcal{L} E_b. \tag{2.70}$$

For the nominal peak luminosity and at $E_b = 7Z\,\mathrm{TeV}$, the power in the BFPP1 beam, having the highest intensity and damage potential, evaluates to

$$P = 26\,\mathrm{W}. \tag{2.71}$$

In 2001 it was first pointed out that these secondary beams could potentially quench superconducting magnets [73]. When theoretical studies confirmed this danger in 2003 [74–76], it was already too late to implement required changes to the lattice before the start of the LHC. Owing to the predictable loss location, it was proposed to install collimators in the cryogenic dispersion suppressor regions around the experiments, specifically positioned to absorb the high power secondary beams. It is foreseen to install these collimators around IP2 in the second long shut-down (LS2). However, after LS1 these collimators will not yet be installed, but the beam energy will be increased from $4Z\,\mathrm{TeV}$, as in 2012 and 2013, to $6.5Z\,\mathrm{TeV}$. Luminosities in the order of the design value will be reached (see Chapter 6.3) and quenches provoked by secondary beam losses are likely. Using orbit bumps to spread out the loss peak over a larger area and to move the impact point to a less vulnerable location, was proposed in Ref. [66] as a technique for temporary mitigation (see Chapter 7.3).

Chapter 7 presents a detailed discussion of the measured secondary beam losses in 2011, including the analysis of a test, using an orbit bump to move the BFPP1 beam right of IP5 out of the dipole of impact and into the connecting empty cryostat. Potential DS collimator positions are as well presented.

3. Measurement and Simulation Techniques

In this thesis theoretical calculations are performed and compared to measured data. This chapter introduces the simulation codes and beam diagnostic devices used for these purposes.

3.1. Simulation Codes

3.1.1. Introduction to CTE

The Collider Time Evolution (CTE) Program [77], originally written by Mike Blaskiewicz, Roderik Bruce and Tom Mertens, is a simulation program to track two bunches of macro-particles in time in a collider. The code is constructed of subroutines, which act on the bunches on a turn-by-turn basis. Each subroutine represents an operation mode or a physical process changing the particles' coordinates.

The simulation treats two individual bunches with different horizontal and vertical beam sizes, number of particles and bunch lengths. Synchrotron and betatron motion, IBS, radiation damping and quantum excitation is taken into account. Several methods are available to determine the emittance growth rates from IBS. Luminosity production in collisions can be simulated for several individual IPs with defined crossing angles and β^*-values. If desired, β^*-levelling can restrict the maximum luminosity until the virtual value has fallen below the limit, or the minimum β^*-value is reached. It is possible to introduce a second RF system to modulate the main one. Additionally, stochastic cooling in three planes can be studied as described in [23, 78].

Via an input file, the user is able to describe the desired beam and machine properties, like beam shape, particle type, particles per bunch, horizontal and vertical emittances, bunch length, RF voltage, tunes and other necessary parameters. A complete list of the required input parameters can be found in Appendix A. To improve the simulation time for a given beam storage time, it is possible to choose the number of real turns corresponding to one turn in the simulation and the number of macro-particles representing the desired number of real particles. The program provides the possibility to individually switch on or off the implemented physical process and to choose if special operation modes (e.g. β^*-levelling) are used during the present simulation run.

CTE simulations are used extensively within the scope of this thesis, especially in Chapters 4 to 6, to analyse the beam and luminosity evolution during the past runs

and to make predictions for the upcoming operation.

3.1.2. Introduction to MADX

The MADX (Methodical Accelerator Design, version 10) program is a general purpose accelerator and lattice design program. As the successor of MAD-8, MADX is developed and maintained at CERN, featuring several additions and extensions to comply with the LHC requirements. The MAD scripting language is de facto the standard to describe particle accelerators, simulate beam dynamics and optimize beam optics.

One of the main objectives is to define and compute the desired machine properties. The calculation of the optics parameters to obtain the linear beam optics that correspond to the chosen lattice elements, is another main task. The simulation of possible machine imperfections and their influence on the beam dynamics can be included in the calculation. In order to perform these calculations, MADX features many predefined functions, options and parameters. A full documentation of the program can be found in Ref. [41].

3.2. Instrumentation

During operation several beam parameters, like intensity, transverse position, tune and beam size, are under constant review to be able to monitor the beam behaviour and to apply corrections, if necessary. This is important for the optimisation and safety of the machine but also to provide the experiments with the highest luminosity possible. To obtain the necessary information from the beam, several devices for beam diagnostics and instrumentation are needed. Because of the complexity of the LHC not all instruments can be discussed in the scope of this thesis, the ones used to collect the data analysed here will be mentioned briefly. Note that Refs. [40, 62] collect and describe the primarily used detectors in more detail. All instruments discussed are located in IR4. All data presented in this thesis, except the wire scans, is automatically and continuously acquired by the devices and saved to the logging database, where it can easily be accessed at any time.

3.2.1. Intensity Measurement

The beam current is one of the most important quantities for the operation of a particle accelerator. It is one of the first parameter to be checked for the accelerator functionality and to prevent particle losses. Many different devices can be used for this purpose, but for a continuous measurement of the beam current during operation a non-destructive device is needed. The LHC uses a measurement method based on the detection of the magnetic field carried by the beam, a so-called current transformer.

The Fast Beam Current Transformers (FBCTs) installed in the LHC are capable of performing bunch-by-bunch measurements by integrating the charge of each bunch.

By summing over all bunches, they also provide information about the total beam intensity. Its functionality is explained in [79, 80].

3.2.2. Transverse Beam Profile Measurement

Equation (2.10) states the relation of the transverse emittance to the beam size. Hence, in order to get information about ϵ_{xy}, the RMS beam radius (transverse beam size) has to be measured at one position in the ring, where the corresponding β-function, β_{xy}, is known. The β-function could be taken from optics calculations, or be measured [81, 82].

Wire Scanner

A wire scanner (WS) consists of a thin wire that is moved across the beam. By doing so, the beam interacts with the wire material and a flux of high energy secondary particles can be detected (e.g., in a scintillator) several metres downstream of the wire. Plotting the count-rate of the detector against the wire position, describes the transverse beam profile. Since the wire has to pass the beam, this is a destructive instrument. However, the disturbance of the beam is very small.

Although, the wire material is very heat resistant, the scanners cannot be used in the operation with many bunches and at high energies. This is because of two reasons: the wire material can only withstand a certain amount of energy deposition before it breaks and secondly, due to the produced secondary particles, the first downstream magnet could quench during a scan. The wire scanners are meant to be used for the cross calibration of other emittance measurement devices, like the Beam Synchrotron Radiation Telescope (BSRT) and the Beam Gas Ionisation (BGI) monitor, or for a small number of bunches at injection energy. Nevertheless, the wire scanners have been extensively used from an early stage on to monitor the beam size and calculate the emittance.

Each LHC beam is equipped with two wire scanners in both horizontal and vertical planes. One is available for operation and the other one intended as a fully functional back-up. Acquisition is possible in two different modes: the standard full beam mode and the bunch-by-bunch mode. For more information see [79, 80, 83, 84].

Beam Synchrotron Radiation Telescope

The Beam Synchrotron Radiation Telescope (BSRT) provides a non-destructive and continuous measurement of the beam sizes in the transverse planes. The device uses the synchrotron light produced by the beam, when the particles are bent in a dipole.

The BSRT is built to measure light in the visible range. One (D3) of the four dipoles responsible to widen the separation of the beams at the RF cavities in IR4, is used by the BSRT as the main light source above 2 TeV. Below 2 TeV the emitted light

leaves the visible spectrum and an additional superconducting undulator was installed to obtain enough light for a beam profile measurement at injection energy [85,86]. The D3 magnet also separates the photon beam from the primary beam, such that the light can be extracted several metres behind the magnet and be processed by an optical system below the beam pipe.

The BSRT can either provide an average over the whole beam or a bunch-by-bunch measurement. However, in the bunch-by-bunch mode one bunch has to be measured after the other, which leads to long intervals without measuring a given bunch when scanning all bunches in the beam [87].

A calibration of the BSRT signals with the wire scanners is required to obtain the absolute value of the beam size. This is obtained in a dedicated fill with only a few single bunches. Wire scans are taken throughout the cycle, while BSRT data is acquired automatically. From the discrepancy between the BSRT and the wire scanner measurements, correction factors are derived [62], which are saved to the logging database to provide easy access to the emittance values. The calibration has to be repeated at the beginning of each run and in case certain settings of the system have to be changed.

The energy emitted in synchrotron light is proportional the fourth power of the particle's energy and inversely proportional to the forth power of the particle's mass [37]. This means that the beam size measurement works better at high energies and that protons can be seen earlier than heavy-ions. In fact, the lead bunches do not emit enough light at injection energy for a single bunch measurement. Integration over several circulating bunches is necessary to collect enough light for a measurement. Only during the ramp the single Pb bunches become visible for the BSRT.

In the 2011 Pb-Pb run (see Chapter 4), the data taken during the calibration fill was contradictory and the extraction of correction factors failed. Unfortunately, there was no time to repeat the measurements and the BSRT had to be left uncalibrated for the whole run. This implies that the absolute value of the emittance was unknown for long periods of the run. Nevertheless, relative values are believed to be reliable also without calibration.

3.2.3. Longitudinal Beam Profile Measurement

The Beam Quality Monitor (BQM) [88] measures the bunch lengths and filling pattern in the LHC. The BQM consists of a pickup, measuring the wall current induced by the beam, that allows the observation of the longitudinal beam profile [79]. The Full Width Half Maximum (FWHM) of the measured signal is determined. The original bunch profile is assumed to be Gaussian, thus the RMS bunch length, σ_s (σ width of the Gaussian), is related to the measured FWHM as $\text{FWHM} = 2\sqrt{2\ln 2}\sigma_s = 2.35\sigma_s$. By convention the 4σ bunch length is saved to the logging database.

In the process of determining the FWHM, the location of the profile's peak is extracted, which is essential to verify the filling pattern during the injection process. During the energy ramp, the BQM feeds back the bunch length to control the longitu-

dinal emittance blow-up.

3.2.4. Luminosity Measurement

The luminosity data presented in the thesis is the official online luminosity published by ALICE, ATLAS or CMS. Both the full beam values and the data acquired for single bunches were used.

3.2.5. Measurement of Beam Losses

Particles with a large divergence from the main beam might impact in the beam pipe and deposit their energy in the superconducting coils leading to temperature increase, possible magnet quenches and damage. A beam loss detection system [40,89], consisting of about 3600 ionization chambers, is installed at likely or critical loss locations around the LHC ring. For protection and prevention the Beam Loss Monitors (BLM) trigger the beam dump via the beam interlock system, whenever beam losses above a certain value are detected. These dump thresholds are defined by the quench limits [90–93] of the superconducting magnets. In addition, loss data is used as a diagnostic tool for the machine setup and operational verifications of, for example, the collimation system.

BLMs are installed on both sides of the outer shell of the cryostat, in order to distinguish between beam losses from both beams.

3.2.6. Schottky Pickup

A Schottky detector system is able to perform a non-destructive and precise measurement of several beam parameters, like revolution frequency, momentum distribution, tune, transverse emittance and chromaticity. Such devices use the so-called Schottky noise to obtain a frequency spectrum from which the mentioned parameters can be calculated. Schottky noise is produced by statistical fluctuations of a current, created by a finite number of charge carriers. Details on the formation of Schottky noise and the principle of Schottky pickups can be found in Ref. [79, 80].

A single particle creates a delta-signal when it passes the detector once per turn. Since it travels with a constant revolution frequency, f_{rev}, the Fourier transformation of this current is a line spectrum with peaks at all harmonics of f_{rev}. The momentum spread within a (coasting) beam of N particles leads to a slightly different revolution frequency for each particle, creating fluctuations of the current (Schottky noise). In the frequency spectrum the lines for a single particle evolve into frequency bands with a finite width, which corresponds to the spread in the revolution frequency. The width of the bands increases with the harmonic number, but since the total power within a band is constant, the hight must decrease.

The described signal is modulated by the transverse betatron oscillation: two mirroring sidebands appear around each harmonic of the longitudinal Schottky frequency

spectrum. These are spaced by $\Delta f = 2 f_{\mathrm{rev}} q$, where q is the non-integer part of the tune, providing an easy measurement of the incoherent value of the tune without influencing the beam [80].

For bunched beams, the longitudinal synchrotron oscillation of bunches inside their bucket causes additional sidebands to each harmonic line. From the distance between the maxima the synchrotron frequency can be determined. If betatron motion is present, the betatron sidebands are also modulated. A quite complex spectrum is observed [79, 80].

In the LHC a 4.8 GHz slotted waveguide structure Schottky pickup is used [94]. It has an aperture of 60×60 mm and is 1.5 m long. This device is capable of bunch-by-bunch measurements. Four pickups are installed near point 4 in a normal conducting straight section, one per plane and beam. The transverse sensitivity is designed to peak at 4.8 GHz, since this is a multiple integer number of the 40 MHz revolution frequency of the 25 ns bunch spacing under nominal conditions.

In case of stochastic cooling, discussed in Chapter 8, a Schottky pickup measures the properties of the betatron sidebands (for transverse cooling), which are related to the spread of the transverse particle positions, i.e., the beam size. Further downstream a kicker corrects the measured average particle offset in order to gradually reduce the emittance of the beam.

4. Analysis of the 2011 and 2013 Heavy-Ion Runs

In this chapter the analysis of the 2011 Pb-Pb and partly the 2013 p-Pb run is presented. The reasons for the typically observed differences between lead bunches are discussed. The distributions of the bunch properties and luminosities between the years are studied and the beam evolutions at the injection plateau and during collisions are compared to tracking simulations. The focus of this thesis lies on Pb-Pb collisions, therefore only the lead bunch parameters at injection and before the start of collisions are considered for 2013. Finally, the goodness of fit between the simulation code and the measured data of many bunches and fills from 2011 is addressed. Parts of this work were presented at the International Particle Accelerator Conference 2013 [13].

4.1. Bunch-by-Bunch Differences

In Chapter 2.3.2 it was discussed that the lead ions have to pass several pre-accelerators before they are injected into the LHC. At each stage, a certain number of bunches will be accumulated from the previous accelerator before their energy ramp and transfer to the next stage. The bunches injected earliest have to wait at the low injection energy, where they are strongly affected by dynamic effects, like IBS ($\propto \gamma^{-3}$) and space charge. Since these effects lead to emittance growth and particle losses, significant bunch-by-bunch differences between early and late injected bunches are introduced. The filling scheme used in 2011 implied that this effect happens mainly in the SPS, while forming trains, and in the LHC, while forming the whole beam.

4.1.1. After Injection into LHC

Figure 4.1 shows the bunch intensity (top) and length (middle) as a function of the bunch number within one train (left) and along the beam (right), directly after each train was injected into the LHC. The data shown was measured in Fill 2342 during the 2011 Pb-Pb run. Each block of points in the right plot corresponds to one train of 24 bunches. The statistical error on successive single bunch measurements is too small to be resolved in the plots. As discussed in Chapter 2.3.3, each train is constructed in the SPS out of 12 PS-injections with 2 bunches each (except for the 4^{th} train of Beam 2 and the 12^{th} train of Beam 1, which miss the last batch). 15 trains form the full LHC beam. The position of the trains is ordered by their time of injection and

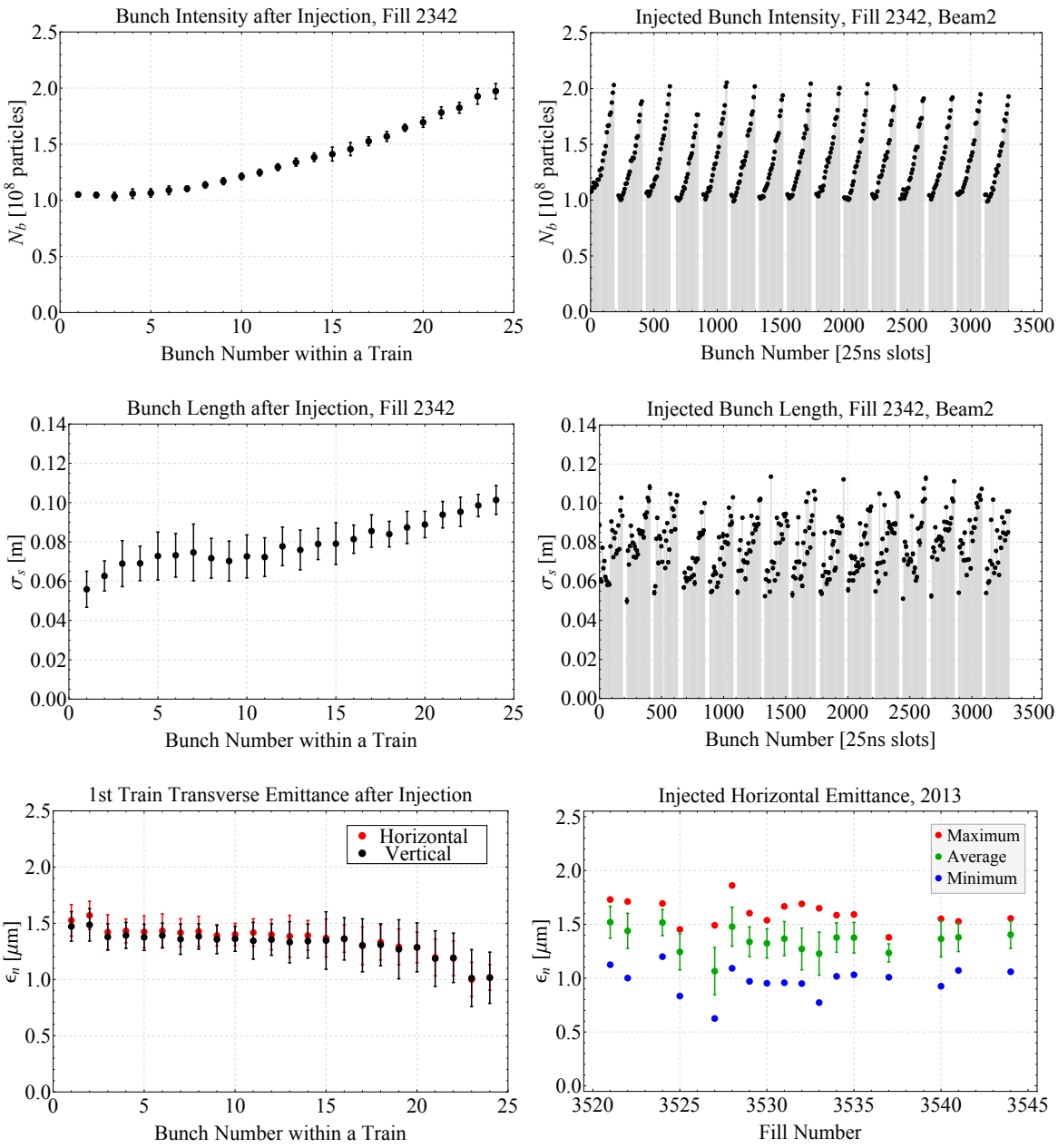

Figure 4.1.: Injected bunch-by-bunch Pb beam properties. Top - Bottom: intensity, bunch length, normalised emittance. Data shown as a function of the bunch number within one train (left) and along the beam (right, for intensity and bunch length) on the example of Fill 2342 measured during 2011 Pb-Pb run. The bottom right plot shows the evolution of the Pb normalised emittance of the first injected train through the 2013 p-Pb run.

the first bunch is always injected at position 0. Therefore, the bunch number gives an indication of when a certain bunch was produced with respect to the others.

A clear increase in intensity, N_b, from the first to the last bunch of each train is observable, where the bunches follow a defined curve within their trains (to be analysed in detail in Chapter 5.2). The head of the train has lost about half of its intensity during the accumulation of bunches, resulting in a run average of $N_b = (1.24 \pm 0.30) \times 10^8$ injected ions per bunch.

A similar pattern is imprinted on the bunch length, σ_s, but less pronounced and with a larger random spread compared to N_b. The run average determines to $\sigma_s = (8.1 \pm 1.4)$ cm. With a total energy of 1404 GeV $= 17.1Z$ GeV, corresponding to $\gamma = 7.3$, at the injection plateau of the SPS, the ions are below transition ($\gamma_T(\text{SPS}) = 22.8$). Below transition the longitudinal dynamics are very different from the situation above transition. Particularly important for this analysis is the fact that the longitudinal IBS growth rate for ions is negative, i.e., damping the longitudinal emittance, at injection in the SPS. Measurements have shown that the predicted IBS damping of σ_s is too weak to explain the observed shrinkage [95]. The responsible effect(s) for the additional damping could not clearly be identified so far. Nevertheless, the data seems to follow a "Touschek like" [96] behaviour, which could as well indicate RF noise or space charge contributions. This longitudinal damping is the reason for the reduced bunch length of the trains' leading bunches.

In the LHC the transverse beam size can be measured with the Beam Synchrotron Radiation Telescope (BSRT) [85, 86], by monitoring the size of the synchrotron radiation light cone emitted by the beam, and the Wire Scanners (WS) [80, 97], by flying a thin carbon wire through the beam and measuring the secondary particles produced in a scintillator. A wire scan is a beam perturbing measurement technique, which can lead to small particle losses and emittance blow-up. Unfortunately, data acquisition and/or calibration issues lead to difficulties in the interpretation of the BSRT data taken in 2011. Moreover, the wire scanners are not meant to be used continuously, but only for rare measurements with low stored beam energy and for cross-calibration of other emittance measurement devices, like the BSRT. Therefore, the emittance data collected in 2011 is very limited and not sufficient to perform a complete statistic analysis. In the scope of this thesis, we launched a dedicated emittance measurement campaign to study the bunch-by-bunch emittance of trains delivered to the LHC in the second half of the 2013 p-Pb run. The wire scanners are sensitive devices and the beam intensity has to be below a safety limit to avoid burning the wire during the scan or dumping the beam because of the particle losses produced. The stored energy of one 24-bunch Pb train is low enough to allow a beam size measurement and it was possible to scan the first Pb train in many fills directly after injection.

The results are shown in the bottom plots of Fig. 4.1. The average horizontal and vertical normalised emittances, ϵ_n, over all trains measured is shown on the left as a function of the bunch number. The evolution of the train's bunch average (green) through the run is displayed on the right. The red and blue points indicate the bunches with the highest and lowest emittance, respectively, the green error bars give the stan-

dard deviation within the train.

The single bunch emittances along the train (left) show that the dimensions in the horizontal and vertical plane are similar, i.e. the beams are close to being round. The data available from 2011, however, shows a tendency to flatter beams with a larger horizontal emittance. The 2-bunch-PS-batch structure is still clearly observable, with equal emittances within former PS-batches. The spread within a train is in the order of the standard deviation between injections. The average emittance between bunches and injections lies slightly below the nominal value at $\epsilon_n = (1.3 \pm 0.2)\,\mu$m.

If all the phenomena in the SPS (and the upstream machines) are reproducible, the distribution of bunch parameters is the same in each LHC train at its injection. The left plots of Fig. 4.1 show average values of the bunches at equivalent positions in the trains. The standard deviations of all injections considered are indicated as the errorbars. As suggested by the plots on the right side, the reproducibility of the intensity is very good, a relative error of around 3% is observed. In contrast to this, a relative error of around 20% is measured for the bunch length and the emittances.

This spread mainly originates in LEIR. While the bunch intensity is defined by the amount injected from LINAC3, beam properties like the transverse and longitudinal emittances are defined by the electron cooling in LEIR [98]. The position and properties of the electron beam used for cooling has significant influence on the cooling efficiency and shape of the ion beam [99]. Fluctuations in the stability of the cooling therefore impose the largest contribution to the spread observed in the LHC. Moreover, due to an unexplained instability during RF capture [50], the bunch intensities extracted from LEIR can vary significantly. If the bunch properties become too bad, batches are rejected to maintain a constant quality of the LHC trains. The batch extension (or compression) done in the PS to obtain the desired bunch spacing, is adiabatic and does not disturb the bunch conditions considerably. However, bunch splitting in the PS, required for future filling schemes (see Chapter 6), is a major perturbation and would also introduce a large dispersion between bunches.

4.1.2. At Top Energy (Beginning of Collisions)

After the last train is injected, the beams are accelerated to their final energy, in 2011 to $E_b = 3.5Z\,$TeV, and brought into collisions. The argument of the long dwell times and long exposure to strong dynamic effects at injection energy also holds for the trains delivered to LHC. The effect on the intensity and emittances is less pronounced, because of the higher energy compared to the SPS, but visible.

In collisions, Eq. 2.21 gives the full dependency of the luminosity on the beam properties and by defining the effective normalised emittance[1] as

$$\tilde{\varepsilon}_n = \frac{\gamma}{\beta^*}\sqrt{\sigma_{x1}^2 + \sigma_{x2}^2}\sqrt{\sigma_{y1}^2 + \sigma_{y2}^2} \tag{4.1}$$

[1]For equal and round beams ($\sigma = \sigma_{x1} = \sigma_{x2} = \sigma_{y1} = \sigma_{y2}$) the effective normalised emittance, $\tilde{\varepsilon}_n$, is equal to the usual normalised emittance defined as $\epsilon_n = \sigma^2\gamma/\beta$.

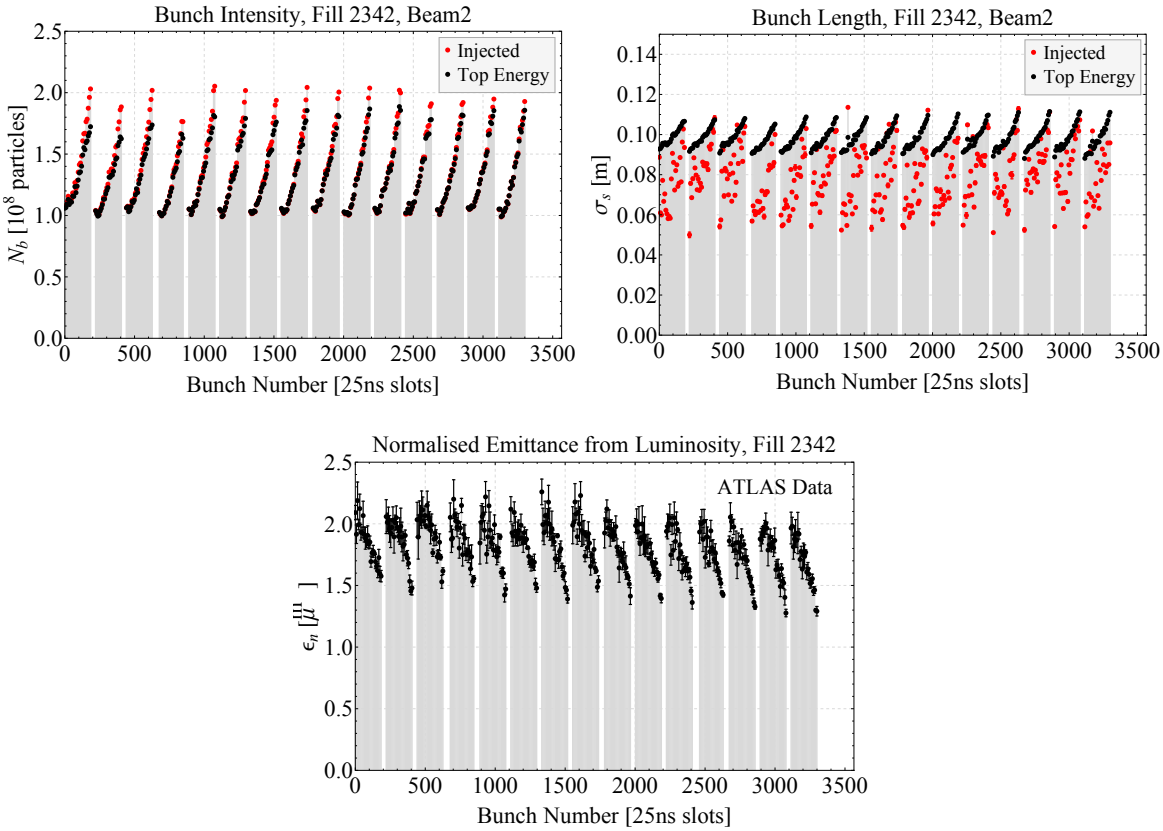

Figure 4.2.: Initial Pb-beam properties bunch-by-bunch at the beginning of collisions. Top: intensity (left), bunch length (right), bottom: effective emittances calculated from luminosity, intensity and bunch length data, on the example of Fill 2342 measured during 2011 Pb-Pb run.

an estimate of the emittance can be calculated from the measurements of $\mathcal{L}_b$, N_b and σ_s, implying that result can only give one common value for both beams and both transverse planes. The measurement of one quantity cannot provide separate information about four independent quantities.

For the moment the beams were brought into collisions (black) in Fill 2342, Fig. 4.2 presents N_b (top left), σ_s (top right) and $\tilde{\varepsilon}_n$ (bottom) as a function of the bunch number. The errorbars show the statistic uncertainty between successive measurements over the first couple of minutes in collisions. N_b and σ_s measurements are very accurate and only show a very small dispersion between consecutive acquisitions, which cannot be resolved in the plot. The bunch-by-bunch measurement of the luminosity on the other hand is very noisy, resulting in a larger error, which is the main contribution to the uncertainty shown on the effective emittance. The uncertainty on the β-function is not taken into account.

In the top row of Fig. 4.2 the red points indicate again the data shown already in Fig. 4.1, measured directly after injection of the corresponding train. It is clearly visible

that between the injection of each train and arriving at top energy some percentage of the intensity is lost in all bunches and that the leading trains are more affected. Considering, as an example, only the last bunches of each train, one observes about the same intensity directly after injection, while at top energy the intensity decreases towards the first train (i.e. towards bunches injected earlier in time). Doing the same for the emittance leads to a decrease towards the last train. This is the result of the intensity losses and emittance growth on the LHC injection plateau. At injection energy of the LHC, IBS is the dominant effect, space charge is negligible and RF noise plays only a minor role [100].

The bunch length is artificially blown-up during the ramp and therefore differs from the other parameters. The so-called *adiabatic damping* introduces a linear variation of the geometric beam emittances, ϵ, with energy. The normalised (energy-invariant) transverse emittances are defined as

$$\epsilon_n = \epsilon\sqrt{\gamma^2 - 1} \tag{4.2}$$

and the longitudinal one can be written as

$$\epsilon_s = 4\pi\sigma_p\sigma_s E_b/(Zc). \tag{4.3}$$

With $\sigma_{x,y} = \sqrt{\epsilon_n\beta_{x,y}/\gamma}$ and $\sigma_p \propto \sigma_s$, the transverse beam sizes ($\sigma_{x,y}$), divergences, bunch length (σ_s) and momentum spread (σ_p) are proportional to $1/\sqrt{\gamma}$, and thus shrink during acceleration. In the transverse plane this is an advantage, since it linearly increases the luminosity. In the longitudinal plane this is problematic, since the IBS increases strongly and the beam might become unstable, if bunches become too short. Therefore, RF phase-noise is applied to the beam to artificially blow-up the bunch length during acceleration [101]. As can be seen from the top right plot of Fig. 4.2, this procedure reduces the random spread observed at injection and leads to longer bunches at top energy. The bunch-by-bunch differences within trains, imprinted during the injection plateau of the SPS, are not flattened entirely. At top energy, a well shaped pattern is now also observable for the bunch length.

The huge differences from bunch to bunch shown in Fig. 4.2 result in the luminosity spread displayed in Fig. 4.3. The data presented was measured in Fill 2342 by the ATLAS experiment, directly after going into collisions. The visible pattern is dominated by the differences in N_b, since $\mathcal{L}$ is proportional to the product of the intensities of the two colliding bunches. Note that the filling pattern of the LHC is such that the leading bunches of trains in the two rings collide with each other in ATLAS and CMS. Since the bunch-by-bunch differences in ϵ_n are inversely correlated to N_b, the variations seen in Fig. 4.2 are amplified in Fig. 4.3. The luminosity of a train's last bunch can be up to six times higher than the first. The overlying slope connecting the last bunches of each train can now clearly be seen, which indicates the variations established during the time the trains sit at injection energy in the LHC.

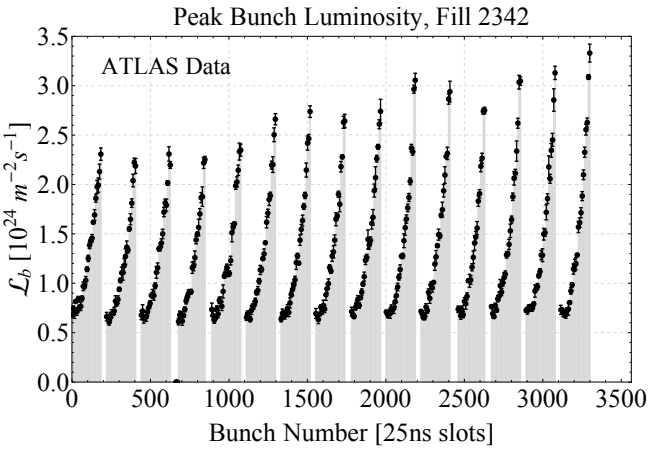

Figure 4.3.: Pb-Pb bunch-by-bunch peak luminosity.

	Design	**2011**		**2013**	
	Collision	**Injection**	**Collision**	**Injection**	**Collision**
E_b [Z GeV]	7000	450	3500	450	4000
N_b [10^8]	0.7	1.24 ± 0.30	1.20 ± 0.25	1.67 ± 0.29	1.40 ± 0.27
ϵ_n [μm.rad]	1.5	-	1.7 ± 0.2	1.3 ± 0.2	-
σ_s [cm]	7.94	8.1 ± 1.4	9.8 ± 0.7	8.9 ± 0.2	9.8 ± 0.1
$\mathcal{L}_{\text{peak}}$[$10^{27}$cm^{-2}s^{-1}]	1	-	0.4 ± 0.1	-	p-Pb

Table 4.1.: Average Pb beam parameters achieved in 2011 and 2013.

4.1.3. Statistics

After investigating the bunch-by-bunch differences on the example of selected fills, it is interesting to look at the distribution of parameters over the whole run and compare the performance between runs. Figure 4.4 shows an overview of the average (green) $\mathcal{L}_b$ (top, left), N_b (top, right), ϵ_n (bottom, left) and σ_s (bottom, right) at the beginning of collisions for each fill evolving over the 2011 Pb-Pb run. The green errorbars indicate the standard deviation of the bunch-by-bunch difference, while the blue and red dots present the bunch with the minimum and maximum value, respectively. Table 4.1 summarises the 2011 and 2013 averages bunch parameters measured after injection and at the beginning of collisions. The design parameters [42] are listed as well for comparison.

Emittance

As mentioned before, the emittance data is limited and a direct, reliable, systematic measurement over time is not available for most fills. The effective emittance can

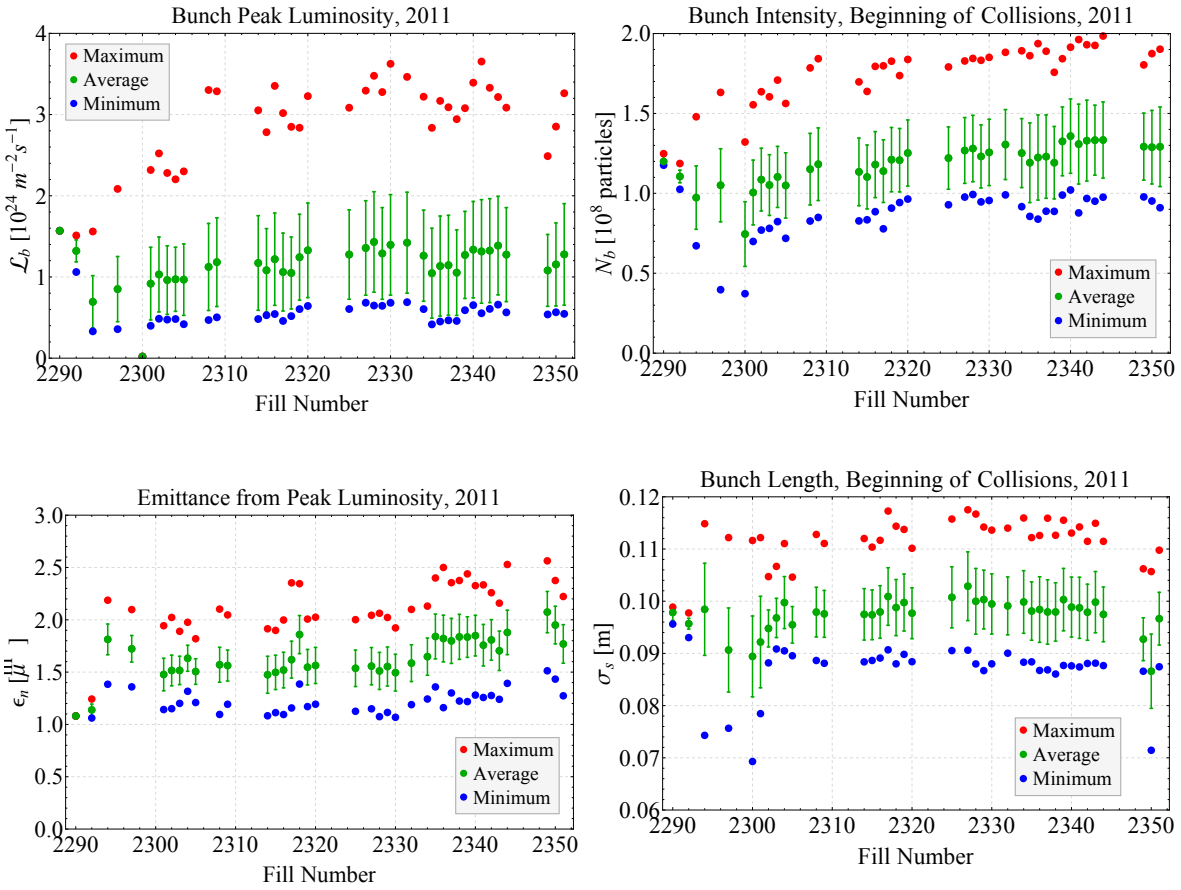

Figure 4.4.: 2011 run overview. Top: peak bunch luminosity (left) and bunch intensity (right), bottom: normalised emittance calculated from luminosity, intensity and bunch length data (left) and bunch length (right). Green shows the average over all bunches with its standard deviation, blue and red the bunch with the minimum and maximum value, respectively.

only be calculated through the combination of luminosity, intensity and bunch length data in collisions. From Eq. 4.1 it is clear that this analysis provides only a combined value of the two beams and both planes, which is even less directly related to the individual beam sizes in p-Pb collisions. Here the beam sizes of the proton and lead ion beams can be and evolve differently. Hence, useful information about the lead beam emittance can only be extracted from Pb-Pb luminosity in 2011. Figure 4.4 shows that the beam average of the effective emittance is rather stable between fills. The average emittance in 2011 determines to $\epsilon_n = 1.7 \pm 0.2\,\mu$m, close to the nominal value. The difference of the bunches with minimum and maximum emittances with respect to the average, suggests that the distribution of the single bunch values was relatively symmetric around the mean.

Bunch Length

The bunch length is artificially blown-up during acceleration and can therefore be controlled to a certain extent. For this reason the bunch length is very reproducible from fill to fill. The average bunch length was $\sigma_s = 9.8 \pm 0.7\,$cm at the beginning of collisions in 2011. The random spread could be significantly reduced to $\pm 0.1\,$cm by keeping the same average length in 2013. The luminosity only depends on σ_s via the crossing-angle reduction factor given in Eq. (2.24), and is thus not in first order relevant to the luminosity performance.

Intensity

The intensity is frequently and continuously measured, providing enough data to perform a statistical analysis of the absolute values and distributions at different moments of the cycle and the performance enhancement between fills and runs. Figure 4.4 shows that N_b, and with it $\mathcal{L}_b$, were steadily increased throughout the run and that the fill's mean is shifted towards lower values. This indicates that the intensity distribution within a train is not linear, but the population in the low intensity regime is enhanced, while only a few bunches have very high N_b. Figure 4.5 confirms this observation by comparing histograms of the intensity distributions in 2011 and 2013 directly after injection and at the beginning of collisions. All curves are asymmetric with the mean shifted to the lower side of the spectrum. In 2011 (top, left) the particles losses from injection (black) to flat top (red) were small and mainly observed in high intensity bunches. An average bunch intensity of $N_b = (1.20 \pm 0.25) \times 10^8$ ions per bunch was available at top energy. In 2013 (top right) the delivered intensities could be increased by about 30% to $N_b = (1.67 \pm 0.29) \times 10^8$ ions per bunch in the injectors. However, due to problems related to the new mode of operation (p-Pb), a big fraction of the initial intensity was lost on the way into collisions. The intensity, which survived until the start of collisions, was $N_b = (1.40 \pm 0.27) \times 10^8$ ions per bunch, still about 15% more than in 2011, see bottom plot. The top right plot shows that these losses affected all bunches, regardless of their initial intensity, in the same way. The overall shape of the

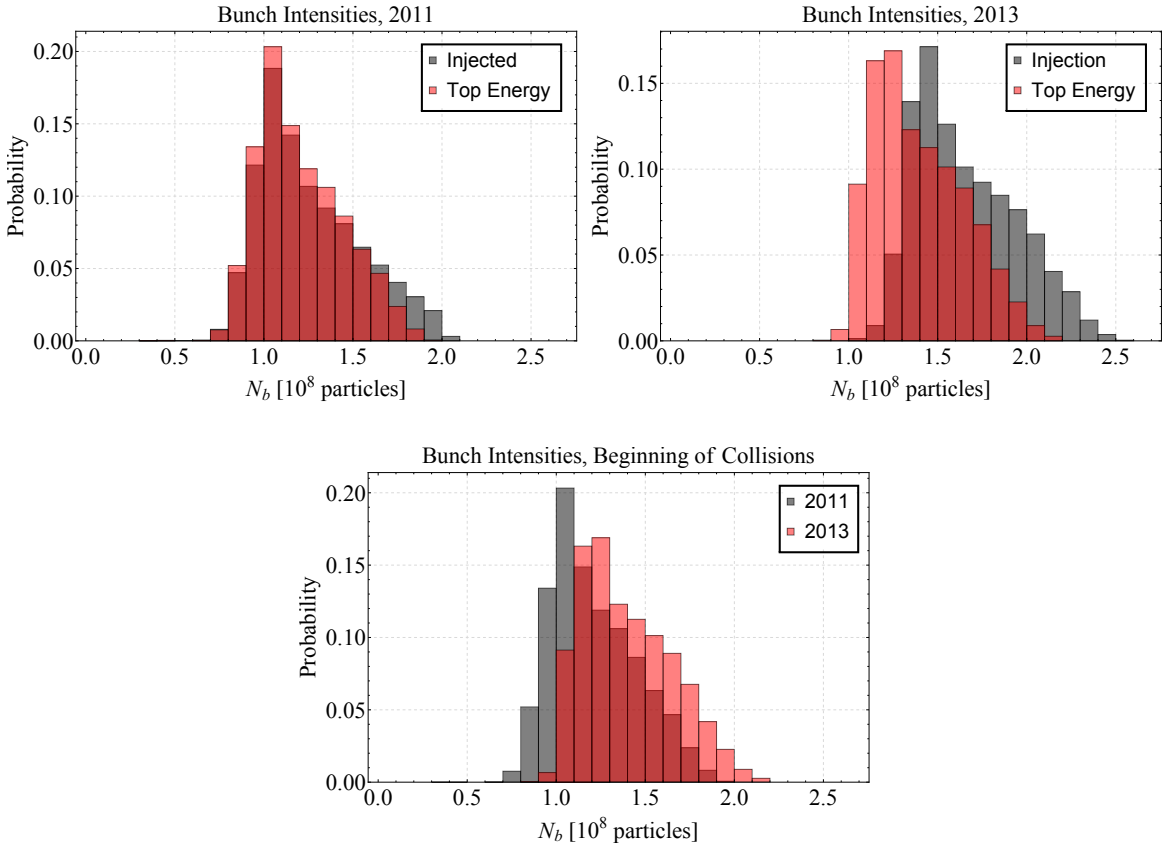

Figure 4.5.: Distribution of peak bunch intensities. Top: comparison between injected and colliding peak intensities in 2011 (left) and 2013 (right). Bottom: comparison between 2011 and 2013 intensities at the beginning of collisions.

distribution is similar, but shifted to lower intensities.

Table 4.2 shows the intensities produced in LEIR and their survival rates until injection and collisions in the LHC in 2011 and 2013. The performance enhancement in 2013 was mainly achieved by improving the extracted intensity from LEIR [102] and the new optics used in the SPS [95], which reduces IBS and space charge effects. Since the 2013 losses were clearly related to p-Pb operational issues, one can expect the improved performance of the injectors as established in 2013, combined with the transmission efficiency in the LHC from injection into collisions of 2011, in a future Pb-Pb run.

Luminosity

The distributions of the peak (top) and integrated (bottom) bunch luminosities from 2011 are shown in Fig. 4.6. The number of bunches with a certain luminosity are

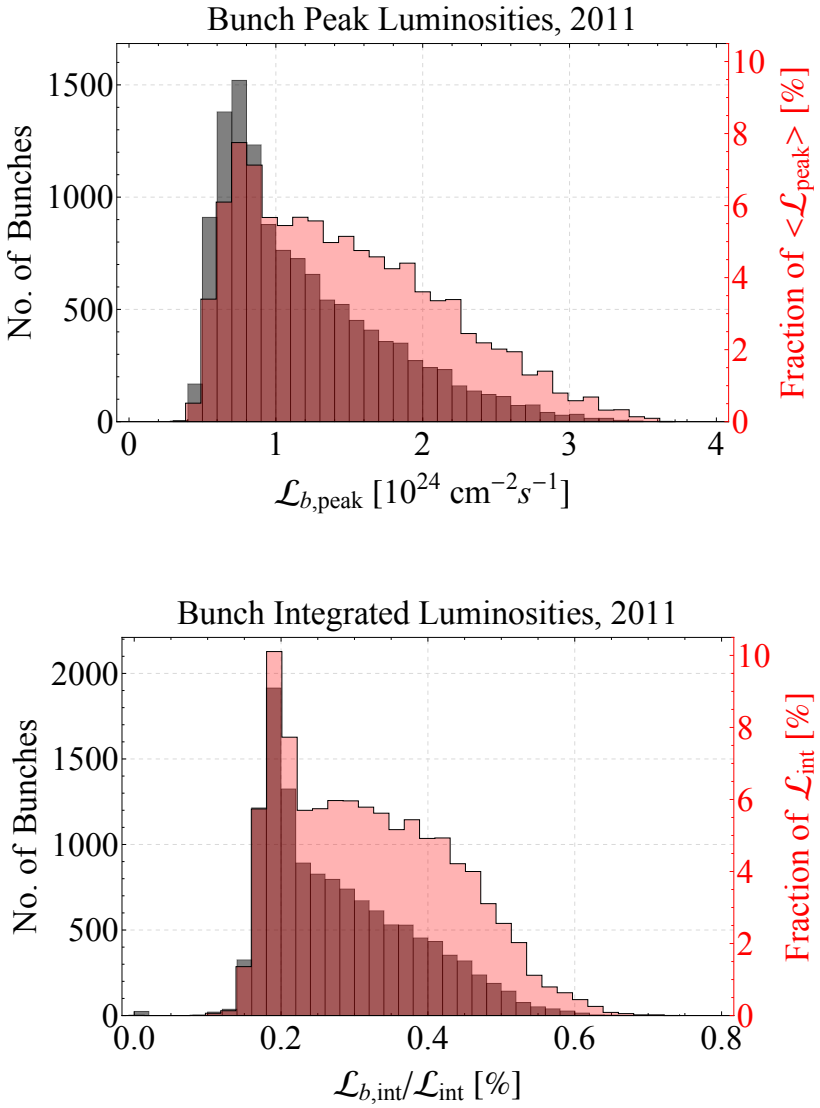

Figure 4.6.: Distribution of the peak (top) and integrated (bottom) bunch luminosities over all fills of the 2011 run.

	2011	**2013**
Beam out of LEIR		
LEIR pulse intensity	9×10^8	11×10^8
Intensity per future LHC bunch	4.5×10^8	5.5×10^8
Beam in the LHC		
Transmission LEIR $\rightarrow$ LHC Inj.	27%	30%
Injected intensity per bunch into LHC	1.24×10^8	1.67×10^8
Transmission LHC Inj. $\rightarrow$ Coll.	96%	86%
Intensity at the Beginning of Collision	1.20×10^8	1.44×10^8
Transmission LEIR $\rightarrow$ LHC Coll.	27%	26%

Table 4.2.: Measured bunch intensities and transmission rates from LEIR into LHC. Intensities are given in number of ions. Best transmission is define as 30% from LEIR to LHC injection and 96% from LHC injection into collision, leading to a full survival rate of 29% [48, 103].

shown in black, the red bars present the percentage these bunches contribute to the total luminosity ($\propto \mathcal{L}_b \times$ no. bunches per bin). All fills, which went into "stable beams" are taken into account. The amount of integrated luminosity clearly depends on the time spent in collisions, which is different for each fill. To compare between fills, the integrated luminosity per bunch, $\mathcal{L}_{b,\mathrm{int}}$, is normalised to the sum over all bunches, $\mathcal{L}_{\mathrm{int}}$.

The distributions in the top and bottom plot have a similar shape, which underlines the correlation between them. About 50% of the bunches have peak luminosities in the lower third of the spectrum, $\mathcal{L}_b \leq 1 \times 10^{24}\,\mathrm{cm}^{-2}\mathrm{s}^{-1}$. These are the low intensity bunch pairs, sitting in the head of the trains. But, the plots make clear that actually these bunches give the highest contribution to the total peak and integrated luminosity. The mean values of the red curves are shifted to the right compared to the black distribution, indicating that the bunches in the middle of the trains are equally important for the total luminosity production. On the other hand, bunches with very high values are rare, thus their contribution to the total sum is small.

4.2. Beam Evolution on the Injection Plateau

To investigate the degradation of the bunches during the injection process of all trains, the time evolution on the LHC injection plateau of four single bunches (dots, labelled B1–B4) was measured and compared to CTE simulations (lines, corresponding colours). Because of the limited time for such studies, the measurements were done in parallel to the setup of the machine and had to be performed on single "pilot bunches", featuring different properties compared to bunches in a train. Their emittances are about half, while their intensities are only slightly smaller than the average values of normal train bunches.

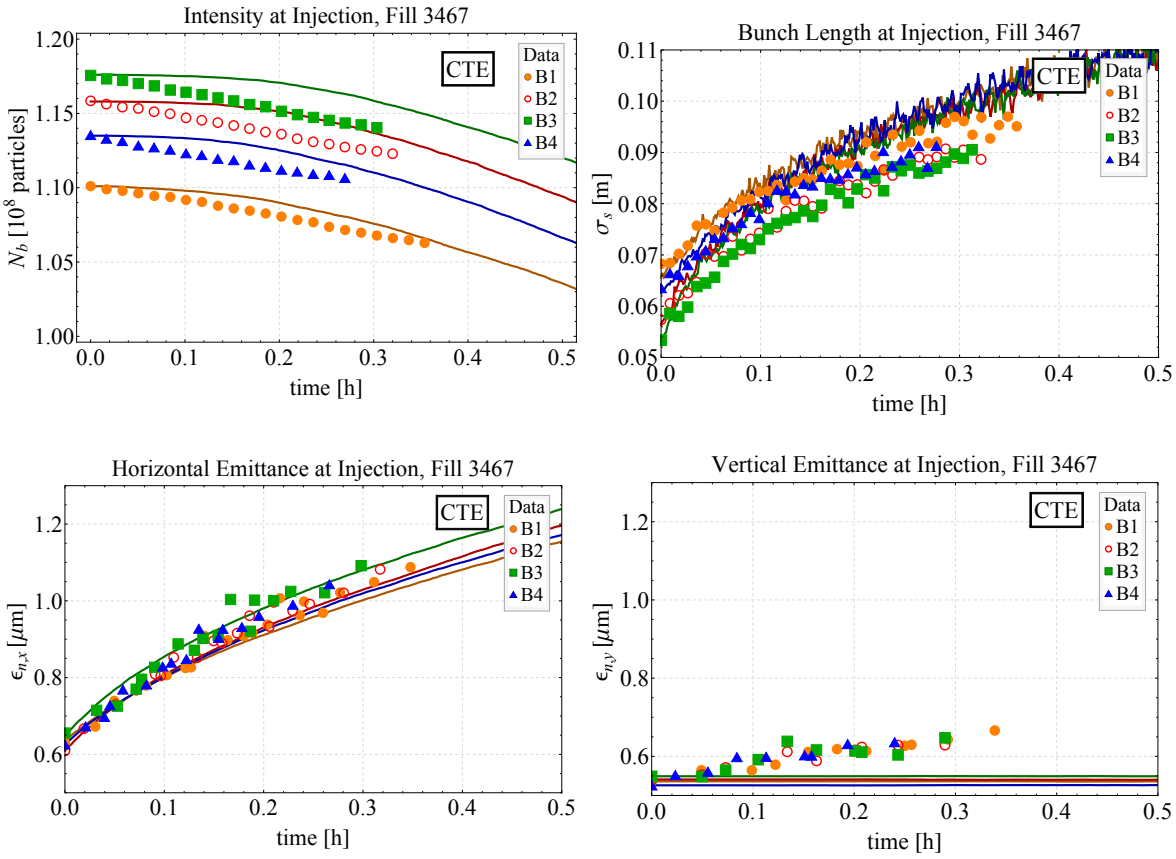

Figure 4.7.: Pb single bunch evolution at the injection plateau. Top: intensity (left) and bunch length (right), bottom: horizontal (left) and vertical (right) emittance evolution of four single bunches. Dots: measurement, lines: simulation. Note the suppressed zeros.

The simulation assumes uncoupled transverse motion. In this case, the vertical IBS growth rate is negative, but very small, and does not lead to emittance blow-up. The results are presented in Fig. 4.7. The initial horizontal IBS growth rate for the measured bunches was below 20 minutes, suggesting a fast growth in the horizontal plane, as observed. The horizontal growth is well predicted by the simulation, while in the vertical plane an additional growth is observed in the measurement. This could, for instance, be introduced by coupling of the transverse motions, leading to an exchange of a fraction of the horizontal growth to the vertical plane. An analysis solving a system of ordinary differential equations to obtain the beam evolution with time showed that for the coupling necessary to explain the observed vertical emittance growth, the horizontal emittance would grow too slowly to be compatible with the data. Hence, the observed vertical emittance growth cannot originate from coupling alone. An additional unknown source is present.

With relative differences below 2%, the predicted losses are only marginally smaller

than the observed. The only loss mechanism taken into account in the simulation is debunching, whereas, e.g., collimation losses are neglected, which could lead to a small underestimation of the total particles lost.

The RMS bunch length, σ_s, is measured by taking the full-width half-maximum (FWHM) of the longitudinal line density and deducing σ_s by assuming Gaussian shape: FWHM $= 2\sqrt{2\ln(2)}\sigma_s$. This is usually a valid approximation for hadron beams and assumed in the simulation by default. However, since the RMS is more sensitive to tails than the FWHM, an equivalent quantity is extracted from the simulated beam distribution and compared with the measurement. The measured σ_s grows slightly slower than the simulation. This presumably arises from the increased vertical emittance, reducing the longitudinal IBS. In general, one can conclude that, on the injection plateau, the measurements are well described by the simulation.

The particles lose about 7% of their intensity and double their horizontal emittance within 30 minutes, about the time required to fill both rings of the LHC with ions and therefore the time the first injected train has to wait before being ramped. Bunches injected later are accelerated earlier in their evolution curve to arrive at top energy with smaller ϵ_n and higher N_b. It should be noted that the bunches presented had similar initial properties. The evolution of bunches in the head and tail of the train will have a larger spread compared to the evolutions shown, due to the large bunch-to-bunch variations.

4.3. Evolution of Colliding Beams

Following the differences in the initial luminosity the bunches also suffer from different luminosity lifetimes: bunches with high initial values show a much faster luminosity decay than others, however their integrated luminosity is also higher.

Figure 4.8 shows the N_b (top left), σ_s (top right), horizontal (bottom left) and vertical (bottom right) ϵ_n evolution of two bunches in Beam 1 of Fill 2292. Beam 2 evolved similarly, but is not presented. In Fig. 4.9 the corresponding time evolution of $\mathcal{L}_b$ for the two bunches shown in Fig. 4.8 is presented. Fill 2292 was the second fill of the 2011 run, which went into "stable beams" and had only 9 bunches per beam. The solid lines present the simulation results. The dots display the measurement, averaged over 5 min including the standard deviation, in case of the luminosity, intensity and bunch length. The BSRT is gated to one bunch for a short period of time, before switching to the next. Therefore, the dots showing the emittance measurement are the averages over one BSRT measurement period for the given bunch. The BSRT measurement is more noisy compared to the measurement of the other beam parameters, but a clear trend is recognisable. Because of the uncertainties in the calibration of the BSRT's absolute emittance values, the effective emittances, calculated from the peak luminosity, are used as simulation input for both transverse emittances of both beams (round beams). The BSRT measurements shown were offset to agree with the initial emittances used in the simulation.

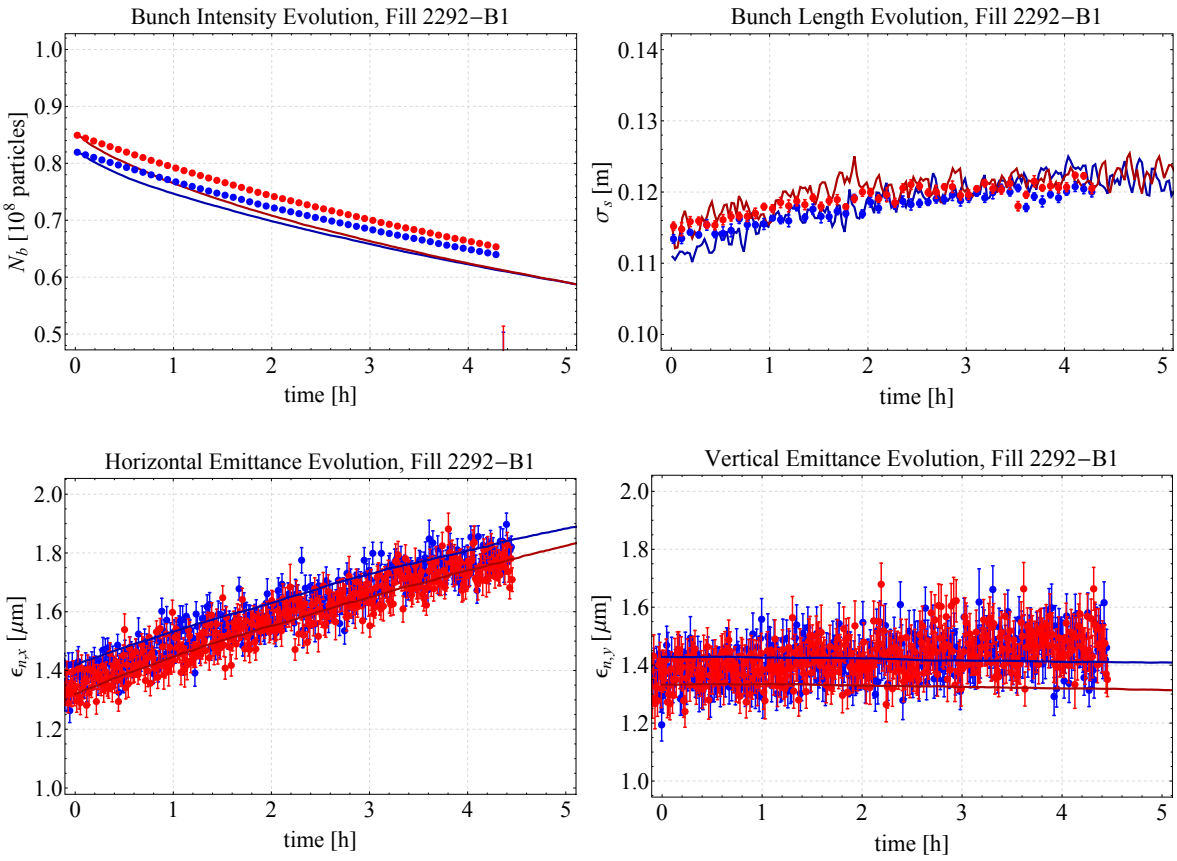

Figure 4.8.: Pb bunch evolution during collisions. Top: intensity (left) and bunch length (right), bottom: horizontal (left) and vertical (right) emittance evolution (measured by the BSRT) of two single bunches in Beam 1 during Fill 2292. The bunches shown collide with the corresponding bunches of Beam 2 and produce the luminosity displayed in Fig. 4.9. The dots (lines) present the measurement (simulation).

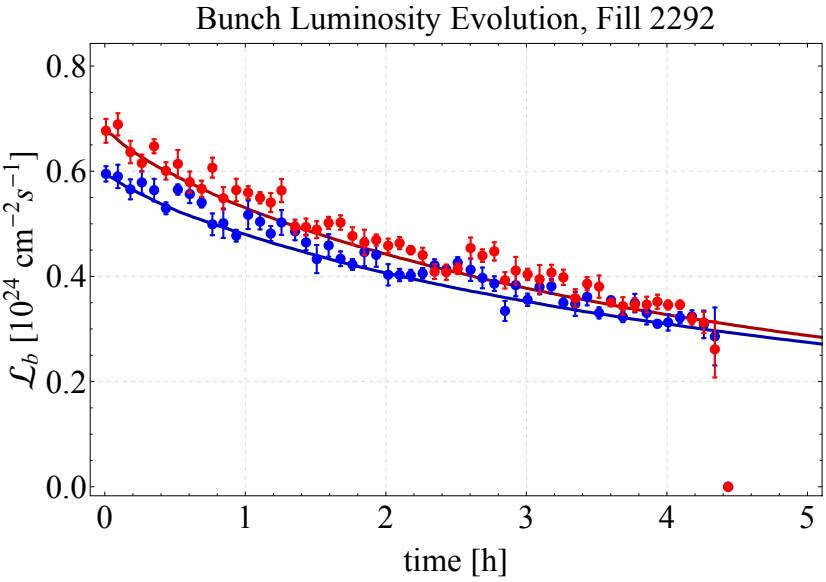

Figure 4.9.: Pb-Pb luminosity evolution of two single bunch pairs colliding during Fill 2292. The dots (lines) present the measurement (simulation).

Using the effective emittance in all planes introduces an uncertainty on the emittance, but also the luminosity and intensity evolution. The emittances are chosen such the initial luminosity fits the data. However, the beams might are not round. In this case, two scenarios are possible. The vertical emittance growth rate would always be very small and not lead to significant beam blow-up. The horizontal growth rate, however, could be drastically different. For a vertically larger (and thus horizontally smaller) beam, the horizontal IBS would be enhanced, resulting in a faster horizontal emittance growth and thus faster luminosity decay, followed by a reduced intensity decay, compared to equal beam sizes. If, on the other hand, the horizontal emittance is larger, one could expect weaker horizontal IBS and less emittance growth, slowing down the luminosity but increasing the intensity decay.

Comparing the measured and simulated beam and luminosity evolution shows that the bunch length, horizontal emittance and luminosity fit perfectly to the prediction. As already seen for the evolution on the injection plateau, a small additional vertical emittance growth is observed, which is not explained by IBS.

Measurements of the longitudinal beam profile of lead ions in the LHC [101] showed that the injected profile is close to a Gaussian. Nevertheless, this distribution gets distorted during the ramp by the artificial longitudinal blow-up, leading to a flatter profile with truncated tail, more similar to an elliptical or water-bag distribution. Thanks to the diffusion introduced by IBS, the profile returns to a Gaussian shape after a few hours into physics. The slight overestimation of the particle losses in the simulation most probably occurs because of this distorted initial beam profile compared to the

assumed Gaussian. Particles in the tails of the distribution are the first to get lost, due to the debunching effect of IBS. Thus, a Gaussian distribution with long tails, as used in the simulation, would show an enhanced decay rate compared to a distribution with truncated tails. Taking into account the truncated longitudinal profiles at the start of physics, the uncertainty on the initial emittances and the large scatter of the emittance and luminosity measurements, the small discrepancy in the intensity decay can be justified.

4.4. Benchmark CTE Tracking Simulations with Data

In order to have more statistics, the 39 fills of the 2011 Pb-Pb run, which went into "stable beams", are considered for a systematic analysis. To minimise uncertainties, fills in which "van der Meer Scans" were performed, to calibrate the luminosity measurements of the experiments, are not included. Some fills showed glitches in the acquired data, which could bias the result and these were also excluded. Moreover, to draw conclusions on the agreement of simulation and measurement under average operational conditions, only fills longer than 5 h and featuring the standard filling scheme with 358 bunches per beam were taken into account. In this scheme, 356 bunch pairs collide in IP1/5 and 336 in IP2. After applying these criteria, 21 fills are suitable for the analysis. The simulations are compared to the bunch and total luminosity measured by the ATLAS experiment and the FBCT intensity measurement of the LHC.

To quantify the goodness of the simulation in comparison to data, two benchmark parameters, ξ and ψ, are defined as the average instantaneous ratio and the ratio of the integrals between a simulated and measured quantity U over the fill duration $t_{\text{fill}} = 5\,\text{h}$:

$$\xi = \frac{1}{t_{\text{fill}}} \int_0^{t_{\text{fill}}} \frac{U_{\text{sim}}(t)}{U_{\text{meas}}(t)} \mathrm{d}t \tag{4.4}$$

$$\psi = \frac{\int_0^{t_{\text{fill}}} U_{\text{sim}}(t)\mathrm{d}t}{\int_0^{t_{\text{fill}}} U_{\text{meas}}(t)\mathrm{d}t}, \tag{4.5}$$

where U is either one of the the quantities $\mathcal{L}_b$, N_{b1}, N_{b2} for the single bunch, or $\mathcal{L}$, N_1, N_2 for the total beam analysis. The closer the values of ξ and ψ are to 1, the better the agreement between measurement and prediction. ψ is a direct measure of the goodness of the predicted integrated luminosity, while ξ focuses on the instantaneous values. Both quantities are expected to give similar results. In principle, ξ and ψ could also be determined for ϵ_n and σ_s, but since the luminosity and intensity are the key parameters with the best measurement coverage, the analysis will be focused on them.

4.4.1. Statistical Analysis

Single Bunch Evolution

From each fill, 312 bunch pairs were suitable for the bunch-by-bunch analysis. In order to distribute the available collisions as evenly as possible between the three experiments, the 4^{th} train of Beam 2 and the 12^{th} train of Beam 1 were made of 11 PS-batches, instead of the usual 12. Because of this, these trains were only colliding in IP1 and 5, while the corresponding train in the opposite beam had interactions in all three IPs. This asymmetric collision scheme leads to a stronger intensity decay of the bunches with the full number of head-on collisions compared to their collision partners in the other beam. In the simulation this effect cannot be taken into account, therefore these two trains were rejected from the analysis. All bunch pairs analysed had individual beam properties and luminosities, while all collided in three experiments with $\beta^* = 1\,\text{m}$ and a half crossing-angle of $\theta_c = 125\,\mu\text{m}$ in IP1/5 and $\theta_c = 60\,\mu\text{m}$ in IP2.

The top row of Fig. 4.10 presents histograms of ξ (black) and ψ (red) for $U = \mathcal{L}_b$ (left) and $U = N_b$ (right) calculated for the 312 bunches per fill of the 21 fills included in the study. The distributions for ξ and ψ have similar shape, mean and standard deviation for both quantities. A very good agreement is found for the intensity, where the average goodness is underestimated by about 4% with a standard deviation of 2%. The overestimation of the simulated debunching losses, as discussed in Chapter 4.3, explains the shift to lower values. The distribution for $\mathcal{L}_b$ is broader, but also shows an excellent agreement of on average 3% with an RMS of 4%. The direction of the discrepancy is correlated to the bunch population.

Total Beam Evolution

The bottom row of Fig. 4.10 investigates the agreement of the total luminosity (left) and intensity (right) evolution. Unfortunately, with only 21 points the statistics are rather small.

The black histograms show ψ for $U = \sum \mathcal{L}_b$ and $U = \sum N_b$, comparing the total beam quantities as the sum of the single bunch values at each t. In order to keep the uncertainties small, the two trains colliding under an asymmetric collision scheme in the two beams, are omitted in the summation.

From an operational and practical point of view, it is interesting to investigate the agreement of the beam evolution as a whole rather than of single bunches. For this purpose, the arithmetic means of the bunch intensity, length and transverse emittance (deduced from the bunch luminosity) over all bunches of each beam are calculated and used as input for a single simulation run per fill. Assuming all bunches are equal to the average, the results are then multiplied by $k_b = 356$ to obtain the total beam current and luminosity. For this analysis, bunches colliding in a different number of IPs, in one but not the other beam, cannot be separated. This introduces an intrinsic uncertainty

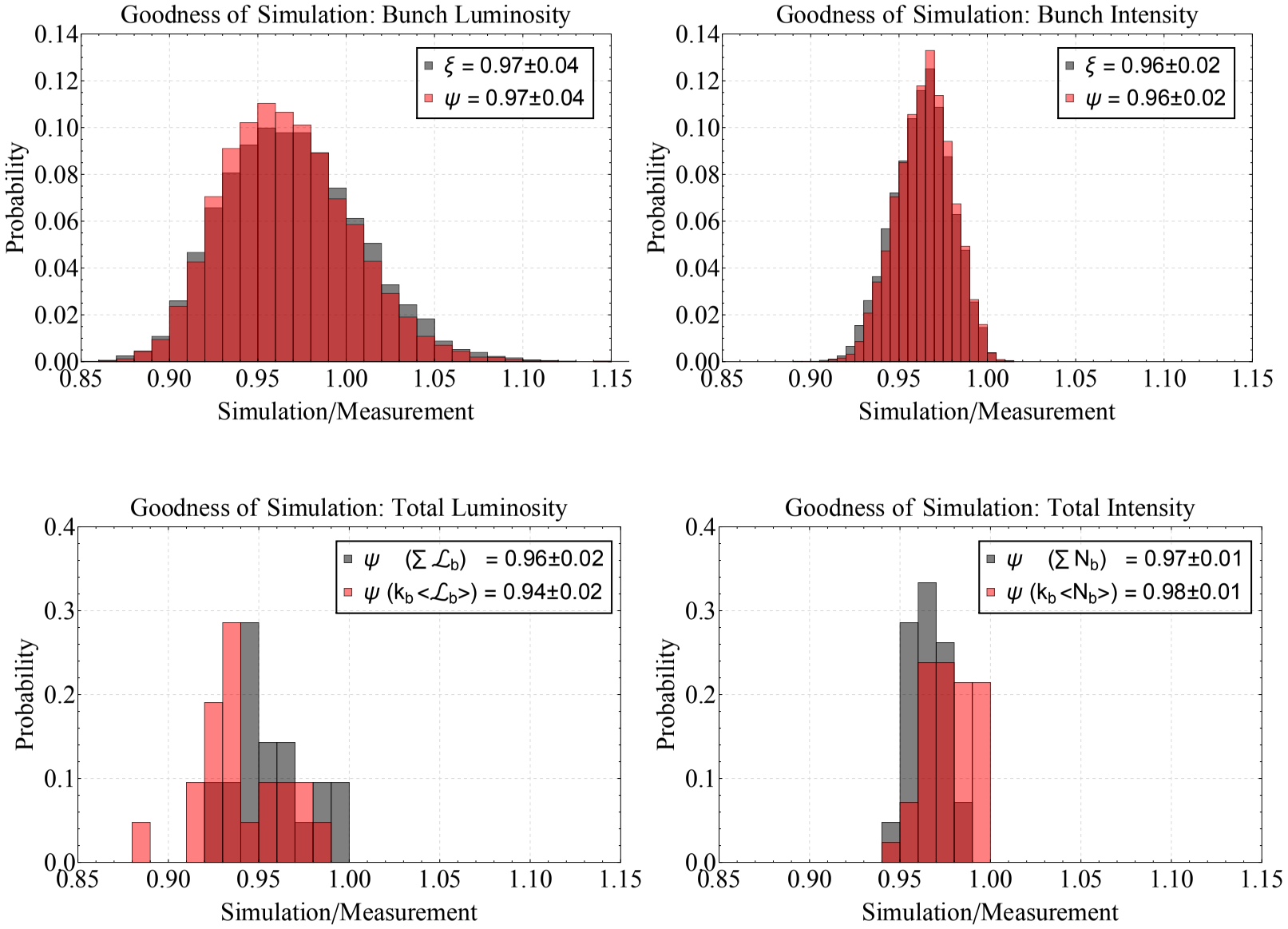

Figure 4.10.: Goodness of CTE simulation in Pb-Pb collisions for the prediction of bunch-by-bunch (top) and total (bottom) luminosity (left) and intensity (right) evolution.

to the agreement between simulation and measurement. If the effect is significant, the simulated total luminosity and beam population would decay faster compared to the measurement, where not all bunches of both beams collide in 3 IPs. The red histograms on the bottom of Fig. 4.10 present ψ, comparing the total beam evolution measured with the prediction based on average bunch parameters.

A tendency to faster decaying $\mathcal{L}$ is visible for the average bunch approach, while for N the trend is reversed. This indicates that the effect of different collisions schemes of the two trains might not be the source of the shift. Comparison of the measured and simulated evolution curves shows that the peak luminosity value is too small in the simulation, while the initial beam intensity fits perfectly ($k_b\langle N_b\rangle = \sum_{i=1}^{k_b} N_{b,i}$). Considering that the single bunch peak luminosities were well reproduced, confirms that the correct values for β^*, θ_c and $\tilde{\varepsilon}_n$ were used. An explanation could be that the average value of the single bunch effective emittances is not a good approximation of the emittance representing the total beam. A value of the emittance giving the correct total peak luminosity, and thus a better agreement in the evolution, could be obtained by calculating $\tilde{\varepsilon}_n$ from the total peak luminosity itself, while using the number of colliding bunches and the bunch averages $\langle N_b\rangle$ and $\langle\sigma_s\rangle$.

In general, the agreement between simulation and data is very good for all the approaches presented, regardless of the focus on single bunches or the total beam.

The quality of CTE tracking simulations was previously investigated by studying the parameters ξ and ψ for the intensity and luminosity evolution of Au-Au collisions in the BNL Relativistic Heavy Ion Collider (RHIC) [77]. The results also showed an excellent agreement for the bunch population, while the integrated luminosity was on average overestimated by 13%.

4.4.2. Sources of Uncertainty

- Figure 4.11 shows ψ for $t_{\text{fill}} = 5\,\text{h}$ as a function of the bunch number for the example of Fill 2342. Trains 4 and 12 are rejected, leaving the two empty spaces around slot 750 and 2500. The intensity (black) evolution of the trains' leading bunches is very well predicted with $\psi \approx 1$. However, a bunch-by-bunch structure, related to the variations imprinted on the SPS flat bottom, is visible for N_b with decreasing agreement between simulation and data towards the tails of the trains. The luminosity (red) looks more randomly distributed. The calculation of ξ shows similar results.
- By comparing the evolution of N_b for head and tail bunches, it is observed that the overestimated intensity decay, which was already seen in Fig. 4.8, is enhanced for tail bunches. Tail bunches do not only have a higher N_b, but they are also longer, compared to bunches in the front. Naturally, the debunching losses increase with increasing σ_s, since particles are closer to the bucket boundaries and get lost more easily. Keeping in mind that the longitudinal bunch profiles in the real machine have rarely populated tails, but the simulated distributions are assumed to be

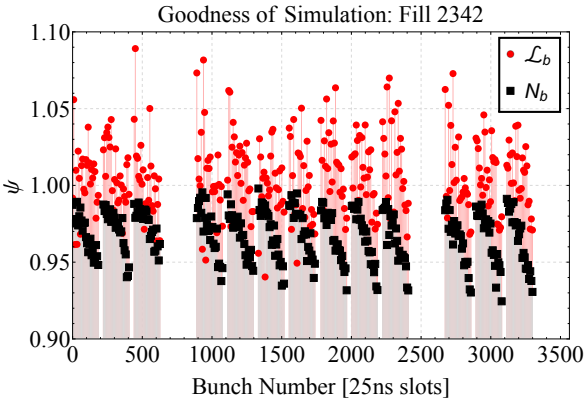

Figure 4.11.: Goodness of CTE simulation in the prediction of Fill 2342. Black: Intensity, red: luminosity

Gaussian, enhances the simulated debunching rate further with respect to the measured one, especially for the long bunches from the train's end.

- The measured and predicted curves veer away from each other with time, leading to a decreasing ψ and ξ with increasing t_{fill}. Because of this, the benchmark parameters for fills that were aborted after a short time ($t_{\text{fill}} < 1\,\text{h}$) are close to 1, imitating a better average goodness of the simulation. In order to obtain a consistent picture, the integration boundary, t_{fill}, should be equal for all considered cases. To investigate the simulation quality under average operational conditions, $t_{\text{fill}} = 5\,\text{h}$ was chosen.
- The quantities ξ and ψ are suitable for investigating the agreement between simulation and measurement in case of perfect agreement or a systematic offset between the curves[2]. However, for instance, an oscillation of one curve around the other could be invisible, or is at least alleviated, in the calculation of these parameters. This is the reason why $\psi(\mathcal{L}_b)$ in Fig. 4.11 looks more random compared to $\psi(N_b)$. As explained above, the predicted intensity shows a systematically stronger decay than the measurement, while this is not the case for the luminosity evolution. Here, it happens that the two curves cross each other, leading to a mitigation of the discrepancies in the sum over all data points. Nevertheless, ψ is the ratio of the simulated and observed integrated luminosity after t_{fill} hours in collisions, which is in any case an important parameter.
- One of the biggest issues is the determination of the absolute values of the initial transverse emittances. These were not measured directly, but an effective value was deduced from the peak luminosity and other measured parameters. This value was then assumed in both planes and beams, neglecting the possibility of flat beams.
- As discussed in Chapter 2.5.4, the total cross-section was determined at

[2] as, e.g., observed for the intensity

$E_b = 3.5Z\,\mathrm{TeV}$[3] by a combination of recent measurements and calculations with a uncertainty of several percent.

[3]as used in 2011

5. Semi-Empirical Luminosity Model

The main goal is to optimise the integrated luminosity for the experiments. It naturally scales with the amount of time the beams are in collisions, i.e. the fill length, but also with the available peak luminosity, which is the sum of the single bunch luminosities at the start of collisions. In general the (peak) luminosity increases with the number of bunches per beam and the brightness (ratio of the intensity w.r.t. the emittance) per bunch.

In the previous chapter the bunch intensities and emittances were shown as a function of the bunch number along the beam (Fig. 4.1). It was explained how the bunch-by-bunch variations build up due to the strong dynamic effect at low energy through the injector chain and at the injection plateau of the LHC. Figure 5.1 shows again the influence of this spread in beam properties on the peak luminosity of Fill 2351. Not only because the luminosity is proportional to the square of the bunch intensity, but also because N_b is the beam parameter suffering from the strongest degradation, makes the intensity distribution in the LHC the most important contribution to the spread of the bunch luminosities.

The actual shape of the slope imprinted on the intensity, and with it on the luminosity, in the SPS (red line in Fig. 5.1) depends on the beam properties injected from the PS and how strong the bunches will suffer from the dynamic effects at low energy. Nevertheless, for a given PS performance, the distribution of the intensities and peak luminosities would change when the filling scheme is changed.

Adding more bunches to a train, means that the bunches which are injected first have to wait even longer at low energy in the SPS, because more cycles of the PS are required to construct the full train. This leads to larger losses and emittance blow-up, reflecting in a smaller luminosity production for these bunches. Of course, lengthening the train yields a higher luminosity per train, however, the gain is added to the head of the train, in the regime where the least luminosity is produced. Due to the given length of the LHC, a lengthening of the trains also leads to a reduction of the maximum number of trains to be fit into one LHC beam. From this it can be understood that, in contrast to the proton-proton operation, it is not necessarily the best solution to make the trains in lead-lead operation as long as possible and maximise the number of bunches per beam up to technical limits. Considering the huge bunch degradation in the SPS, one has to find a compromise between the number of bunches per train, which is proportional to the time spent in the SPS, and the total number of bunches

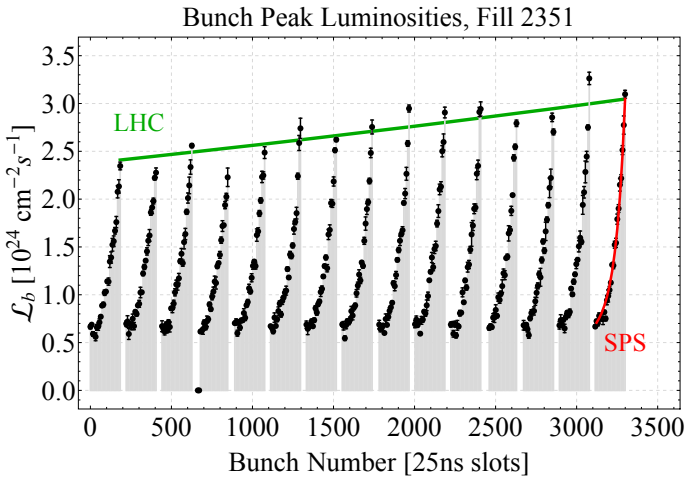

Figure 5.1.: Degradation of the peak bunch luminosities in the SPS and LHC.

in the beam, to optimise the luminosity in the LHC.

As was pointed out already, the bunch degradation in the SPS is influenced by several effects of different strength (mainly IBS, space charge and RF noise). It is non trivial to distinguish between them and extremely difficult to predict the amount of particle losses and beam blow-up during the SPS cycle. Nevertheless, for the luminosity production in the LHC it is not directly important which effects in the SPS influence the beam by what amount, but how the beams arrive in the LHC and how large the actual luminosity outcome is. Therefore, it is desirable to find a description of what is observed in the LHC without relying on the detailed knowledge of the processes happening in the SPS.

In the following, the 2011 bunch-by-bunch intensity and luminosity data, as measured by FBCTs in the LHC and the ATLAS experiment, respectively, is used to derive an empirical, but analytic, model to describe the intensity and peak luminosity as a function of the bunch position within the beam. This model will then be used in Chapter 6 to estimate the potential peak and integrated luminosity for different filling schemes to find the optimal train length and achieve the highest possible integrated luminosity. A summary of this model and its capabilities were presented at the International Particle Accelerator Conference 2014 in Dresden [20].

5.1. The Peak Luminosity Model

5.1.1. Degradation in the SPS

Investigating again the bunch-by-bunch luminosity of one train from Fig. 5.1, where the last train is highlighted in red. The bunches which show the highest luminosity

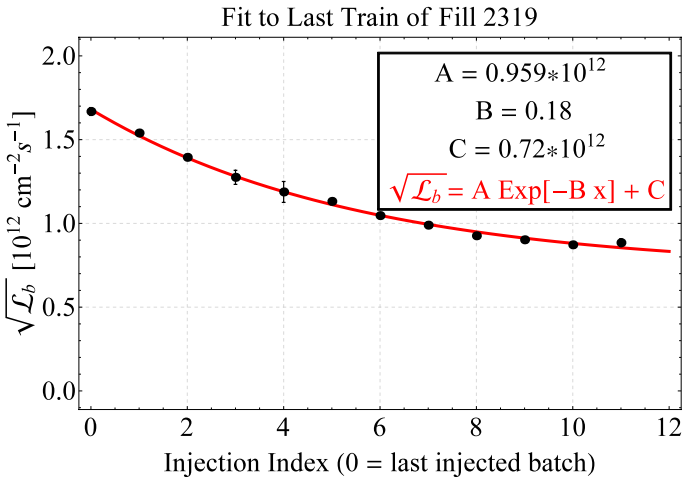

Figure 5.2.: Exponential fit to the square root of the initial bunch luminosities of the last injected train at the beginning of collisions. Starting with the last batch of the train at position zero.

value were injected last to the SPS. After their injection, the ramp was started almost immediately, hence they had no time to loose particles and blow-up in emittance. The two bunches just before had to wait only for one PS cycle (3.6 seconds) and so on. Thus, the inverse order of the injections from the PS can be interpreted as the increasing amount of waiting *time* in the SPS. It is a valid approximation to assume that all bunches arriving from the PS are (within statistics) equal. Therefore, the (red) curve, the bunches of one train describe in Fig. 5.1, can be interpreted as the inverse time evolution of the single bunch peak luminosity reduction caused by the length of the injection procedure in the SPS.

The exact functional description of the decay curve is unknown. It was found that an *exponential decay* with increasing waiting time

$$\sqrt{\mathcal{L}_b} = \lambda_\infty + (\lambda_0 - \lambda_\infty)\exp[-\alpha\, n] \tag{5.1}$$

is suitable to describe the observation. Here the constants λ_0 and λ_∞ are the initial and asymptotic values of $\sqrt{\mathcal{L}_b}$ at $n = 0$ and $n = \infty$, respectively. α can be interpreted as a decay rate.

The general aim is to find a filling scheme, which provides the bunches with the highest possible brightness in the LHC. The brightness of a particle bunch is defined as the ratio of its intensity and its emittance. The luminosity is a quantity with its origin in the interplay of two particle bunches and its square root shows the proportionality

$$\sqrt{\mathcal{L}_b} \propto N_b/\sqrt{\epsilon}, \tag{5.2}$$

in a collision of two equal bunches ($N_b = N_{b1} = N_{b2}$, $\epsilon = \epsilon_1 = \epsilon_2$). $\sqrt{\mathcal{L}_b}$ is therefore a good indication of the brightness of the colliding bunches and convenient to use for

the fit. The proportionality relation (5.2) holds, since only equivalent bunches of the two beams collide in ATLAS and CMS, i.e. the first bunch of Beam 1 collides with the first bunch of Beam 2 etc., which had spent the same time in the SPS.

The bunches not only lose brightness in the SPS, but also at the injection plateau of the LHC. An overlying slope, indicated as the green line in Fig. 5.1, connecting the trains becomes visible. After the last train is injected, the energy ramp is started immediately, giving the last injected train no time to decay. Because of this reason, the last train is assumed to show the cleanest picture of the peak luminosity reduction caused in the injectors, without disturbances from the LHC injection plateau.

Figure 5.2 shows an exponential fit of form (5.1) to $\sqrt{\mathcal{L}_b}$ of the bunches in the last injected train of fill 2319. The data points in the plot are the average over the two bunches in one PS-batch, which are produced simultaneously and are assumed to have similar beam conditions. The errorbars indicate the standard deviation over these bunches, showing how small the differences are. To describe the time evolution, the batch positions were inverted to start at *injection index* $= 0$ with the batch injected last to the SPS. The agreement between fit function and data is excellent.

This kind of fit was performed for all well behaved fills of the 2011 lead-lead run. The averages of the fit parameters over all fills were taken to build a general function, describing the behaviour of the last train over the whole run:

$$\sqrt{\mathcal{L}_b}(\mathrm{SPS}) = \bar{\lambda}_\infty + (\bar{\lambda}_0 - \bar{\lambda}_\infty)\exp[-\bar{\alpha}_{\mathrm{SPS}}\, n] \tag{5.3}$$

$$\bar{\lambda}_0 = 1.75 \times 10^{12}\,\mathrm{cm}^{-1}\mathrm{s}^{-1/2} \tag{5.4}$$

$$\bar{\lambda}_\infty = 0.71 \times 10^{12}\,\mathrm{cm}^{-1}\mathrm{s}^{-1/2} \tag{5.5}$$

$$\bar{\alpha}_{\mathrm{SPS}} = 0.187, \tag{5.6}$$

where $n \in \mathbb{Z}^+$ represents the injection index. $\bar{\lambda}_0^2 = 3 \times 10^{24}\,\mathrm{cm}^{-2}\mathrm{s}^{-1}$ determines the maximum single bunch peak luminosity of 2011, equal to the average peak luminosity of the last train's last bunch. α is given in units of "number of injections". The decay rate per second is obtained when α is divided by the time between two injections. Since the expression asymptotically approaches λ_∞ (and not zero), this decay rate describes the time after which $\sqrt{\mathcal{L}_b}(\mathrm{SPS})$ has decreased to $(\bar{\lambda}_0 - \bar{\lambda}_\infty)/e + \bar{\lambda}_\infty$.

5.1.2. Degradation in the LHC

The decay in the LHC is much less significant and only leads to a modulation from one train to the next of the already imprinted bunch-by-bunch differences from the SPS. It is sufficient to fit an exponential of the form (5.1) with $\lambda_\infty = 0$. The fit has to be performed on a data set of equivalent bunches, which experienced the same length of the SPS injection plateau and thus are at equal indices inside their trains. Grouping equivalent PS-batches together means that 12 fits (one per PS-batch) are possible per fill. Tail bunches show a faster decay compared to head bunches, mainly due to different intensities, and thus individual decay curves are required to describe

the effect in full detail. However, it is desired to find a single equation describing all bunches to be able to modify the filling scheme freely. There are two ways to obtain an average representation of the decay in the LHC: averaging the fit parameters over all bunches, or using the fit of a bunch with average beam parameters from the core of the train. Both options are comparable and give similar results. The calculation of the mean fit parameters over all fills from 2011 gives:

$$\sqrt{\mathcal{L}_b}(\mathrm{LHC}) = \bar{\Lambda}_0 \exp[-\bar{\alpha}_{\mathrm{LHC}}\, n] \tag{5.7}$$

$$\bar{\Lambda}_0 = 1.19 \times 10^{12}\,\mathrm{cm}^{-1}\mathrm{s}^{-1/2} \tag{5.8}$$

$$\bar{\alpha}_{\mathrm{LHC}} = 0.0084, \tag{5.9}$$

where $\bar{\Lambda}_0^2 = \bar{\mathcal{L}}_{b,\mathrm{peak}} = 1.4\times10^{24}\,\mathrm{cm}^{-2}\mathrm{s}^{-1}$ states the average single bunch peak luminosity achieved in 2011.

5.1.3. Full Position-depended Model

To describe the full effect, the degradation in the LHC (Eq. (5.7)) has to be normalised, to only act as a modulation, and be multiplied by the fit result of the more pronounced degradation in the SPS (Eq. (5.3)). This yields the desired analytical equation to describe the peak values of the (square root of the) luminosity at the start of collisions:

$$\sqrt{\mathcal{L}_\mathrm{b}} = F_E F_{Nb}\, \bar{\lambda}_0 (\bar{\lambda} + (1-\bar{\lambda}) \exp[-\bar{\alpha}_{\mathrm{SPS}}\, (l_{\mathrm{PS}}\, n_{\mathrm{bu}})]) \exp[-\bar{\alpha}_{\mathrm{LHC}}\, (l_{\mathrm{LHC}}\, n_{\mathrm{tr}})], \tag{5.10}$$

with $\bar{\lambda} = \bar{\lambda}_\infty/\bar{\lambda}_0$. The simplified form of Eq. (5.7), yields a normalisation constant of $1/\bar{\Lambda}_0$, leaving the exponential part $\exp[-\bar{\alpha}_{\mathrm{LHC}}\, n]$. The factor $F_E = (\beta^*_{2011}/\beta^* \times E_b/E_{b,2011}) = (1\,\mathrm{m}/3.5Z\,\mathrm{TeV} \times E_b/\beta^*)$ scales β^* and the energy from the 2011 to the desired values. n_{bu} is the index of the PS-batch inside its train and n_{tr} is the index of its train inside the beam. The factors l_{PS} and $l_{\mathrm{LHC}} \in \mathbb{R}^+$ were introduced as an option to adjust the time intervals between PS injections into the SPS and SPS injections into the LHC.

The reference PS cycle from 2011, for which $l_{\mathrm{PS}} = 1$, had a length of $t_{\mathrm{PS}} = 3.6\,\mathrm{s}$. The SPS cycle length, t_{SPS}, depends on the number of PS-batches, n_{batch}, to be accumulated and a constant, t_r, accounting for the remaining parts of the cycle, for instance, pre-cycle and ramp:

$$t_{\mathrm{SPS}} = t_{\mathrm{PS}} \times (n_{\mathrm{batch}} - 1) + t_\mathrm{r}. \tag{5.11}$$

For the 2011 SPS cycle this calculates to $t_{\mathrm{SPS}} = 3.6\,\mathrm{s} \times (12-1) + 8.4\,\mathrm{s} = 48\,\mathrm{s}$. To mitigate the IBS effect on the LHC injection plateau and distribute it evenly over both beams, SPS trains are injected alternately into Beam 1 and 2, doubling the time between two injections for each beam compared to the SPS cycle length. In case one PS beam is lost during the accumulation in the SPS, the whole SPS fill is dumped at the end of the cycle. This ensures a constant time spacing of batches in SPS, but leads to large uncertainties of the time spacing in the LHC. The model is built on an average over many fills, automatically folding in the time variation due to lost SPS cycles.

The average time spacing between LHC injections, as was in 2011 (approximately 110 seconds), is assumed by setting $l_{\mathrm{LHC}} = 1$. l_{PS} and l_{LHC} should be set to the ratio of the desired to the reference time spacing, as quoted above, to obtain the appropriated scaling. With $t_{\mathrm{PS}} = 3.6\,\mathrm{s}$ and $t_{\mathrm{LHC}} = 110\,\mathrm{s}$ the fitted decay constants can be converted to $1/\bar{\alpha}_{\mathrm{SPS}} = 19\,\mathrm{s}$ and $1/\bar{\alpha}_{\mathrm{LHC}} \approx 3.4\,\mathrm{h}$.

Equation (5.10) is based on the beam parameters as they were achieved in 2011. Nevertheless, in the 2013 p-Pb run the Pb bunch intensities injected into the LHC were increased by about 30%. The bunch intensities are expected to be pushed still higher in future. To account for the better performance, it is desirable to include a scaling with N_b. Certainly, scaling with the bunch intensity is difficult. The dynamic effects in the SPS and LHC scale with N_b, thus the exponential curves will change their shape. To account, at least in a very primitive way, for the gain in $\mathcal{L}$ due to an increase in intensity, the scaling factor F_{Nb} was introduced in Eq. (5.10), following the law of Eq. (5.2). F_{Nb} scales all bunches by the same factor which, however, is a pessimistic approach.

The total peak luminosity is given by the sum over all single bunch values. It is sufficient to calculate $\mathcal{L}_b$ for each PS-batch of each train with Eq. (5.10) and multiply by the number of bunches per batch. This leaves the number of bunches per PS-batch as a free parameter of the model.

Equation (5.10) provides a formalism to estimate the peak luminosity of each bunch depending on its exact position inside the beam for any filling scheme. The number of bunches per PS-batch, the number of batches per train and the number of trains per beam can be chosen freely, obeying the usual constraints related to technical limitations.

5.1.4. Verification with Data

The left plot of Fig. 5.3 shows $\mathcal{L}_b$ calculated with Eq. (5.10) (red squares) compared to the data of the last fill from 2011 (black dots). In case of the calculation two red squares are always overlapping. The space between them is too small to be resolved in the plot. The calculation reproduces the measured data well, as can also be seen in the left plot of this figure. A linear fit (red line) shows that the points nicely lie on a line through the origin with only small deviations from the zero intercept and a slope equal to unity.

The evolution of the total peak luminosity over the whole 2011 run is displayed in Fig. 5.4. The errorbars indicate the statistical fluctuations between consecutive measurements of $\mathcal{L}_b$ for all colliding bunches. The red line shows the sum over the single bunch values calculated with the model. The modelled peak luminosity lies in the upper third of the 2011 performance. It has to be noted, that the blue points were excluded in the construction of the model. These fills were either part of the commissioning program and had filling schemes with less bunches or showed bad data not usable for the analysis. This confirms that the model can represent the average

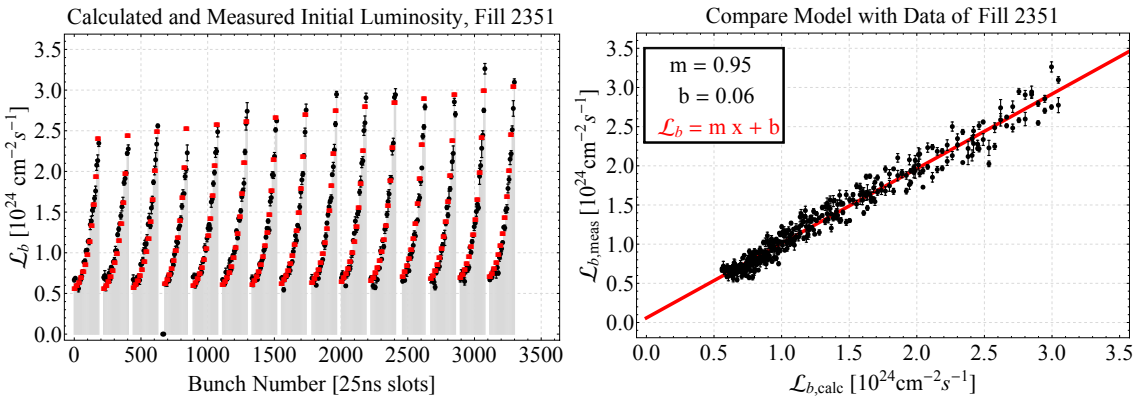

Figure 5.3.: Comparison between model (5.10) (red) and the data (black dots) of Fill 2351. Left: bunch-by-bunch $\mathcal{L}_b$ along the beam, right: fit of measured $\mathcal{L}_b$ as a function of the calculated $\mathcal{L}_b$.

bunch peak luminosity distribution of a 2011 lead fill.

5.2. The Intensity Model

5.2.1. Importance of the total Beam Intensity for Luminosity

The peak luminosity is an important parameter to estimate the performance of a collider, nevertheless, the overall goal is to collect as much physics data as possible, which is measured in integrated luminosity.

Two filling schemes (1 and 2) with different numbers of bunches ($k_{b1} > k_{b2}$) can provide the same total peak luminosity $\mathcal{L} = \mathcal{L}_1 = \mathcal{L}_2$, if the one with the smaller number of bunches per beam features bunches with higher bunch intensities, $N_{b1} < N_{b2}$, compensating the missing bunches. In the case of lead ions, it was discussed in Chapter 4.3 that bunches with a higher peak luminosity (and thus higher bunch intensity, as for scheme 2) decay with a shorter lifetime compared to bunches starting at a lower peak value. In the sum over all bunches, scheme 1 would therefore integrate more luminosity, because the single bunches decay slower.

It will be shown in the following that scheme 1, with many bunches but small single bunch intensities, which delivers more integrated luminosity, has the higher total beam intensity. Hence, it is very important to not only optimise the peak luminosity, but also the total beam intensity to maximise the integrated luminosity.

Considering the general luminosity equation (2.21) for equal and round beams, it holds that

$$\mathcal{L} \propto k_b N_b^2. \tag{5.12}$$

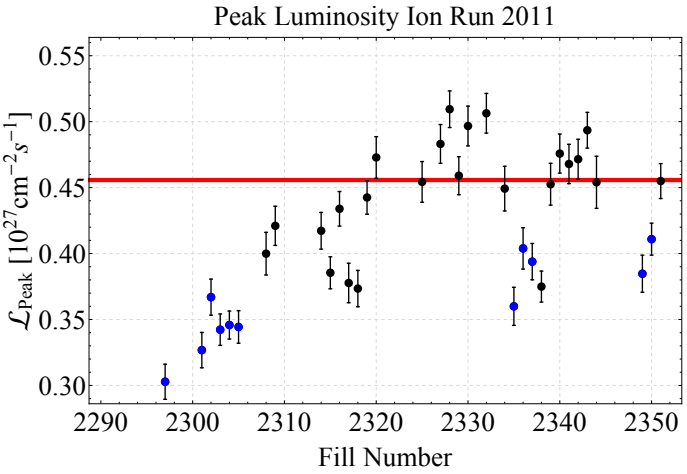

Figure 5.4.: Peak luminosity per fill of the 2011 Pb-Pb run (black dots) compared to the model calculation (5.10) (red line). Fills marked in blue were not considered in development of model. Note suppressed zero.

Without loss of generality

$$\mathcal{L}_1 = \mathcal{L}_2 \quad \text{with} \quad k_{b1} > k_{b2} \quad \text{and} \quad N_{b1} < N_{b2} \tag{5.13}$$

is assumed.

$$\Rightarrow k_{b1} N_{b1}^2 = k_{b2} N_{b2}^2 \tag{5.14}$$

$$\Rightarrow \frac{k_{b1}}{k_{b2}} = \frac{N_{b2}^2}{N_{b1}^2} \tag{5.15}$$

The total beam intensity, N, for both schemes are given by

$$N_2 = k_{b2} N_{b2} \tag{5.16}$$

$$\text{and} \quad N_1 = k_{b1} N_{b1} \tag{5.17}$$

$$= \frac{N_{b2}^2}{N_{b1}^2} k_{b2} N_{b1} \tag{5.18}$$

$$= \underbrace{\frac{N_{b2}}{N_{b1}}}_{>1} k_{b2} N_{b2} \tag{5.19}$$

$$> k_{b2} N_{b2} = N_2. \tag{5.20}$$

To estimate the initial bunch-by-bunch peak intensities for a given filling scheme, a similar model as for the initial peak luminosities is built from the 2011 Pb-Pb data. The LHC has two FBCTs, which are capable of measuring the beam intensity bunch-by-bunch for both beams independently. The bunch intensities just after the injection of each train are shown as the red dots in Fig. 4.2 (top, left). If the data of each

train is taken right after its injection, all trains describe equivalently well the effect imprinted by the SPS without any disturbance from the LHC injection plateau or ramp. When treating the luminosities it was only possible to use the last train of each fill at collision energy. Certainly, this train was already influenced by the LHC ramp and squeeze, as can be seen by comparing the red and black dots in Fig. 4.2. The high intensity bunches lose most particles during the ramp, influencing the slope of the fitted curve. It is important to obtain a clean knowledge of the intensities injected into the LHC, to optimise the filling scheme for the highest beam intensity from the injectors. Maximising the transition to top energy in the LHC is a separate problem, to be dealt with in the LHC.

5.2.2. Full Position-dependent Model

At injection energy in the LHC, N_b gives a very clean picture of the degradation from the SPS with high statistics, since all trains of both beams can be used for the analysis. Similar to Eq. (5.1) a fit of the form

$$N_b = \lambda_\infty + (\lambda_0 - \lambda_\infty)\exp[-\alpha\, n] \tag{5.21}$$

was performed for each train of all fills right after its injection. Equivalent to the luminosity model, the average over the two bunches from the same PS-batch was taken and the data points were inverted before fitting. Averaging the fit parameters for all trains of the whole 2011 run yields:

$$\begin{aligned} N_b(\mathrm{SPS}) &= \bar{\lambda}_{N\infty} + (\bar{\lambda}_{N0} - \bar{\lambda}_{N\infty})\exp[-\bar{\alpha}_{N,\mathrm{SPS}}\, n] && (5.22)\\ \bar{\lambda}_{N0} &= 1.83 \times 10^8\,\mathrm{ions} && (5.23)\\ \bar{\lambda}_{N\infty} &= 0.95 \times 10^8\,\mathrm{ions} && (5.24)\\ \bar{\alpha}_{N,\mathrm{SPS}} &= 0.196, && (5.25) \end{aligned}$$

where $\bar{\lambda}_{N0}$ represents the maximum bunch intensity injected into the LHC, which is equal to the average of the last bunches' intensities of 2011.

As done for the luminosity model, the effect arising at the LHC injection plateau is evaluated via an exponential fit, of the form (5.21) with $\lambda_\infty = 0$, to bunches from equivalent PS-batches at the start of collisions. The average of the fit parameters over both beams and all fills give:

$$\begin{aligned} N_b(\mathrm{LHC}) &= \bar{\Lambda}_{N0}\exp[-\bar{\alpha}_{N,\mathrm{LHC}}\, n] && (5.26)\\ \bar{\Lambda}_{N0} &= 1.24 \times 10^8\,\mathrm{ions} && (5.27)\\ \bar{\alpha}_{N,\mathrm{LHC}} &= 0.0043. && (5.28) \end{aligned}$$

The normalisation factor of Eq. (5.26) is given by $1/\bar{\Lambda}_{N0}$, which is equal to the inverse of the run average of N_b injected. The final analytical equation to describe the peak

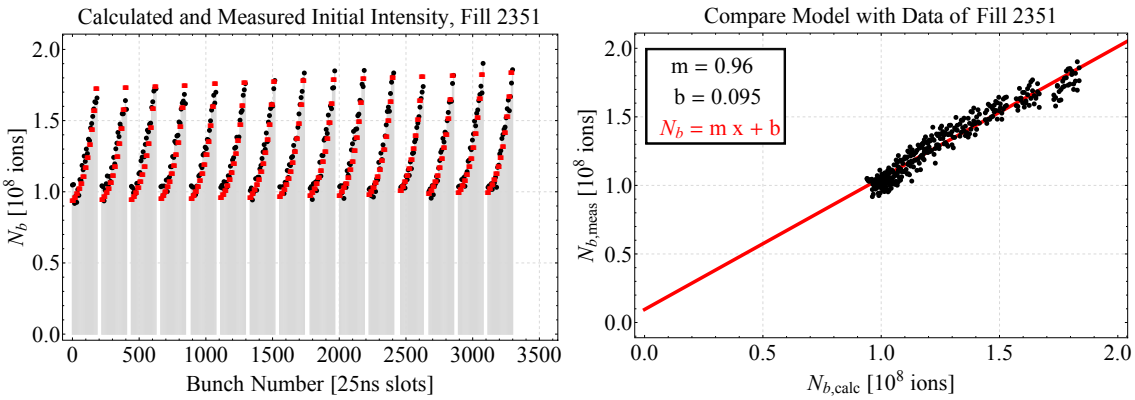

Figure 5.5.: Comparison between model (5.10) (red squares) and the data (black dots) of lead Fill 2351.

values of the initial bunch intensities at top energy is given by

$$N_b = F_{Nb}\,\bar{\lambda}_{N0}(\bar{\lambda}_N + (1-\bar{\lambda}_N)\exp[-\bar{\alpha}_{N,\mathrm{SPS}}\,(l_{\mathrm{PS}}\,n_{bu})])\exp[-\bar{\alpha}_{N,\mathrm{LHC}}\,(l_{\mathrm{LHC}}\,n_{\mathrm{tr}})], \quad (5.29)$$

where $\bar{\lambda}_N = \bar{\lambda}_{N\infty}/\bar{\lambda}_{N0}$. F_{Nb} is again introduced to provide a simplified linear intensity scaling to account for a better performance of LEIR. $F_{Nb}\,\bar{\lambda}_{N0} = N_{b,\mathrm{max}}$ can be interpreted as the absolute value of the expected maximum bunch intensity.

5.2.3. Verification with Data

The left plot of Fig. 5.5 shows the calculations obtained by Eq. (5.29) (red squares) for the 2011 filling scheme compared to the data of fill 2351 (black dots) at $E_b = 3.5Z$ TeV as function of the bunch position within the beam. The right plot displays the measured values as a function of the calculation. A fit (red line) to this data set shows that the measurement is well reproduced by the model. For perfect agreement the fit should pass the origin with a slope of 1.

Figure 5.6 shows an overview of the total beam intensities of the 2011 run. The model calculation in shown as the red line. The fills marked in blue, were excluded in the development of the model. The plot confirms that the model reproduces the average beam intensity of a fill from 2011.

5.2.4. SPS Degradation Improvements in 2013

It is worth noting again that the degradation curve obtained by this procedure is highly dependent on the performance of the SPS and downstream machines. Which means, if there are performance improvements in these machines, as was very well seen in the 2013 p-Pb run, the resulting decay curve might look significantly different. Table 5.1 summarises the fit parameters for the intensity and luminosity model obtained with

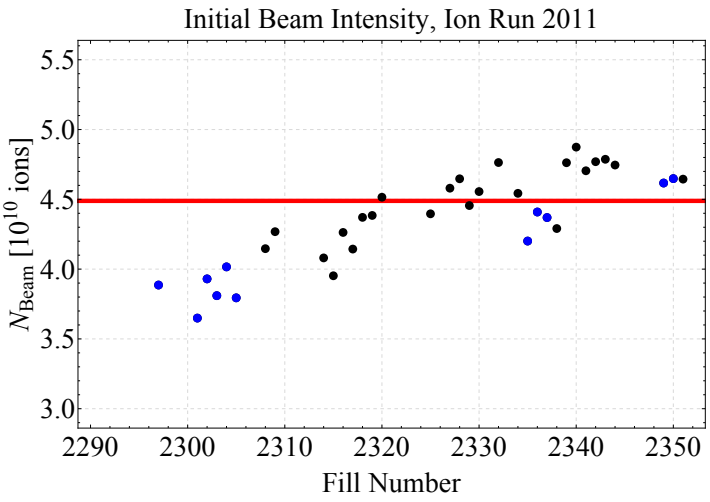

Figure 5.6.: Peak beam intensity per fill of the 2011 Pb-Pb run (black dots) compared to the model calculation (5.29) (red line). Fills marked in blue are excluded from the development of the model. The propagated error on consecutive measurements of N_b is too small to be resolved. Note the suppressed zero.

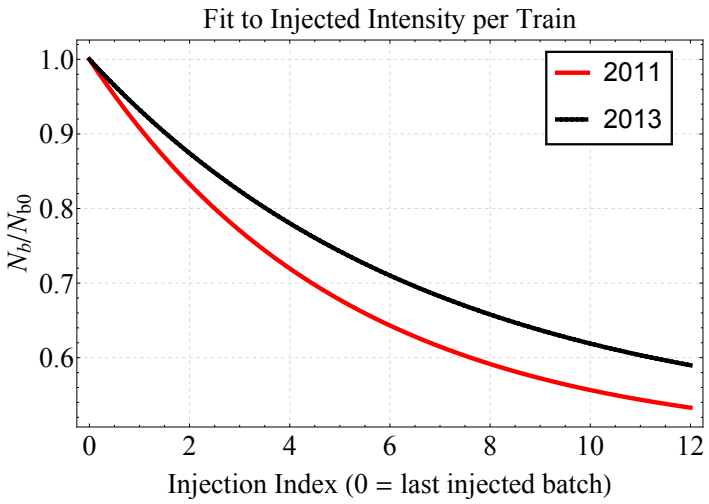

Figure 5.7.: Fits to SPS intensity degradation for 2011 and 2013.

	SPS			LHC	
Model	$\bar{\lambda}_0$	$\bar{\lambda}_\infty$	$\bar{\alpha}_{\mathrm{SPS}}$	$\bar{\Lambda}_0$	$\bar{\alpha}_{\mathrm{LHC}}$
	2011				
N_b(injection) [10^8 ions]	1.83	0.89	0.196	-	
N_b(start of coll.) [10^8 ions]	1.79	0.90	0.193	1.24	0.0043
$\sqrt{\mathcal{L}_b}$ [$10^{12}\,\mathrm{cm}^{-2}\mathrm{s}^{-1}$]	1.75	0.71	0.187	1.19	0.0084
	2013				
N_b(injection) [10^8 ions]	2.06	1.04	0.147	-	
N_b(start of coll.) [10^8 ions]	1.87	0.80	0.121	1.44	0.0028

Table 5.1.: Fit parameters of the luminosity and intensity model obtained in 2011 and 2013. The units given in the first column are valid for the λs, the αs are given in "number of injections".

the data of 2011 and 2013. Figure 5.7 compares the fits of the intensity at injection for both years. The curves are normalised to the peak values, $\bar{\lambda}_0$, of the corresponding year. Even with higher single bunch intensities in 2013, the degradation is slower, owing mainly to the reduced IBS achieved by the new Q20 optics in the SPS implemented in 2012 [95].

The results in the last line of Table 5.1 are quoted for completeness, but should not be used for further analysis. They are biased by strong losses related to special p-Pb operational issues in 2013 and are not representative.

5.2.5. Extracting Emittance Degradation

Comparing the fit results in Table 5.1 for the LHC effect, shows that the square root of the luminosity decays almost twice as fast as the intensity. This arises from the fact that in the luminosity, the intensity decay and emittance growth are combined. Normalising Eq. (5.2) to the initial luminosity $\sqrt{\mathcal{L}_{b0}}$ gives

$$\frac{\sqrt{\mathcal{L}_b}}{\sqrt{\mathcal{L}_{b0}}} = \frac{N_b/N_{b0}}{\sqrt{\epsilon_n/\epsilon_{n0}}} \quad \Rightarrow \quad \sqrt{\frac{\epsilon_n}{\epsilon_{n0}}} = \frac{N_b/N_{b0}}{\sqrt{\mathcal{L}_b/\mathcal{L}_{b0}}}, \tag{5.30}$$

from which a relation for the emittance evolution can be extracted. Since the constants $\Lambda_0 = \sqrt{\mathcal{L}_{b0}}$ and $\Lambda_{N0} = N_{b0}$ are equal to the initial values of the luminosity and intensity, Eq. (5.7) and (5.26) imply an equation for the emittance:

$$\sqrt{\frac{\epsilon_n}{\epsilon_{n0}}} = \exp[(\bar{\alpha}_{\sqrt{\mathcal{L}},\mathrm{LHC}} - \bar{\alpha}_{N,\mathrm{LHC}})x] = \exp[\bar{\alpha}_{\sqrt{\epsilon},\mathrm{LHC}}x], \tag{5.31}$$

resulting in an growth rate of $\bar{\alpha}_{\sqrt{\epsilon},\mathrm{LHC}} = \bar{\alpha}_{\sqrt{\mathcal{L}},\mathrm{LHC}} - \bar{\alpha}_{N,\mathrm{LHC}} = 0.0041$ for $\sqrt{\epsilon_n} \propto \sigma_{x,y}$ (beam size), which translates to $1/\bar{\alpha}_{\epsilon,\mathrm{LHC}} = 1/(2\bar{\alpha}_{\sqrt{\epsilon},\mathrm{LHC}}) = 3.7\,\mathrm{h}$. This growth rate is in excellent agreement with the calculated IBS growth rate for a bunch with 2011

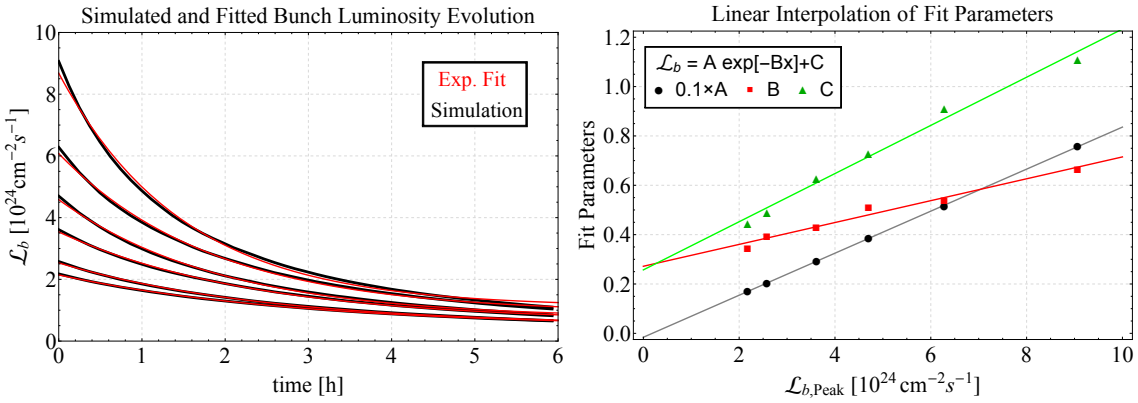

Figure 5.8.: Left: Exponential fits (red) to the simulated (black) bunch-by-bunch luminosity evolution (here at $7Z$ TeV). Right: Linear fits (lines) to the parameters obtained (dots) by the fits done in the left plot. The values of parameter A are divided by 10 to fit to scale.

average parameters at injection energy. The initial value of the emittance determined by this formalism is $\epsilon_{n0} = f_{\mathrm{rev}}\gamma/(4\pi\beta^*)\Lambda_{N0}^2/\Lambda_0^2 = 1.44\,\mu$m, which is smaller than the value obtained from the bunch-by-bunch analysis quoted in Table 4.1.

Because of the non-zero λ_∞ in Eq. (5.3) and (5.22), the extraction of the emittance growth time and initial emittance from the SPS effect is not obvious. Moreover, this growth is the combination of several effects and neither a prediction nor a measured value are available for comparison.

5.3. Modelling the Total Luminosity Evolution

The beam and luminosity evolution of a single bunch pair during collisions can be predicted with the Collider Time Evolution (CTE) program [77], introduced in Chapter 3.1.1. Because of large bunch-by-bunch differences, bunches at the head of a train will evolve differently from bunches sitting in the middle or tail. In principle, a simulation should be done for all individual bunches separately depending on their beam parameters. The sum over all bunches would then give the total beam and luminosity evolution.

To maximise the luminosity by adjusting the filling scheme, the $\mathcal{L}_b$ evolution of all bunches for the different options have to be simulated and summed up to identify the potentially best scheme. The simulation of hundreds of bunches is, however, very time consuming. To save resources and time, an interpolation method based on a few representative simulation runs is employed. This adequately estimate the potential instantaneous and integrated luminosity evolution of the complete ensemble of bunches.

The evolution of six typical bunches covering the expected spectrum of bunch properties at the desired collision energy is simulated with CTE, see black curves in left plot

of Fig. 5.8. The simulated luminosity decay for each of these bunches is parametrised by an exponential fit of the form

$$\mathcal{L}_b = A \exp[-B\,x] + C, \tag{5.32}$$

see red curves in left plot. The fits do not perfectly match the simulations, but they are good enough for the purpose. Plotting the fit parameters A, B and C against the bunches' peak luminosity, as displayed in the right plot of Fig. 5.8, shows that each group lies approximately on a line. Hence, it is convenient to interpolate between them by performing a linear fit to each of the original fit parameter groups. From these interpolations the luminosity decay curves can be extracted for individual bunches with a given peak luminosity.

The model described by Eq. (5.10) can be used to calculate the bunch peak luminosities for a given filling scheme, which then build the base to determine the single bunch decay curves from the linear interpolations above. The single bunch exponential functions are summed up to obtain the total instantaneous luminosity. To determine the total integrated luminosity, the equation for the total instantaneous luminosity is integrated. In Fig. 5.9 the measured luminosity evolution of fill 2342 is compared to the results obtained by the procedure described. Eq. (5.10) is constructed to give the average bunch peak luminosities achieved in 2011. To verify the interpolation technique and the agreement with the measured luminosity evolution, the calculations in Fig. 5.9 are based on the measured peak values instead of the results from Eq. (5.10). The luminosity decay is slightly faster for the model, this arises from the systematic overestimation of the single bunch intensity losses in the simulation, as described in Chapter 4.3. Nevertheless, the agreement is still excellent.

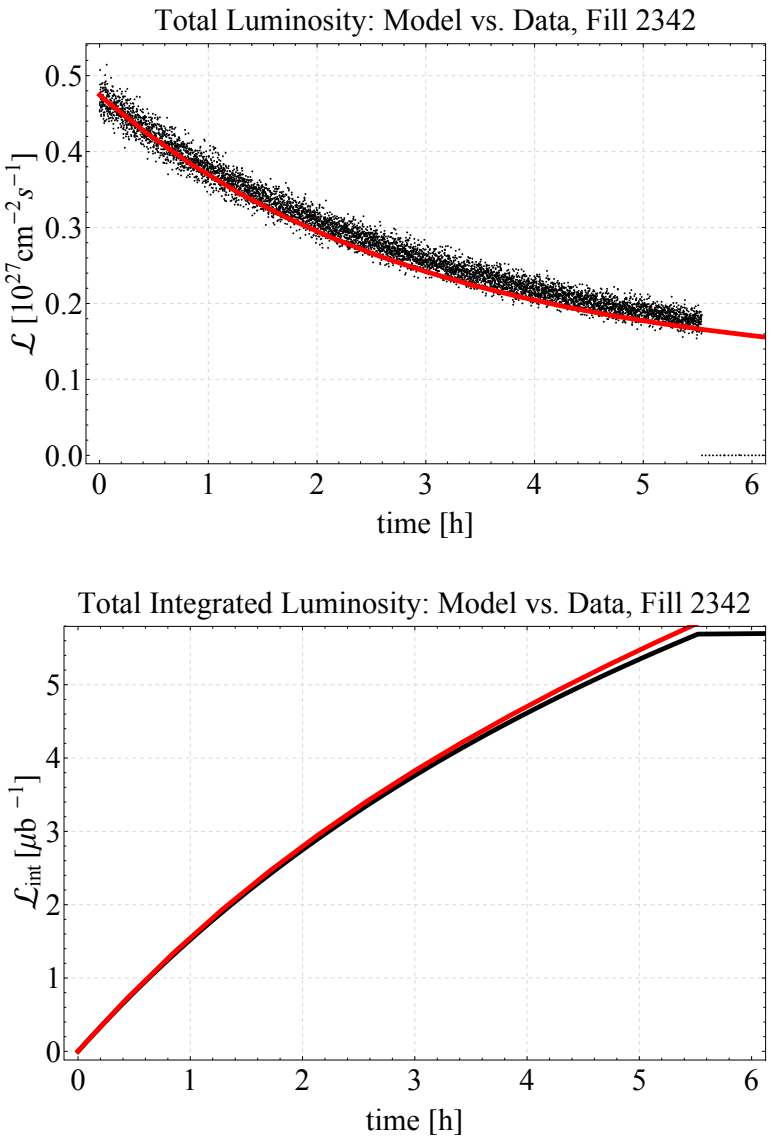

Figure 5.9.: Instantaneous (left, black) and integrated (right, black) luminosity evolution of Fill 2342 compared to the prediction of the full luminosity model (red).

6. Predictions for Future Runs

This chapter addresses the luminosity performance in Pb-Pb collisions of the LHC after the current long shut-down LS1 in Run 2 and for the HL-LHC era (Run 3 and beyond). Injector and detector upgrades are planned during LS2, leading to different considerations for the two periods. Without these upgrades luminosity levelling will be required in Run 2. The potential performance with full peak luminosity is presented, followed by the derivation of analytic equations to estimate the luminosity outcome with levelling. Calculations for several operation scenarios are discussed. The semi-emperical luminosity model from Chapter 5 is then used to make predictions for Run 3. Many of the results obtained in this chapter were already presented at several occasions and referred in papers, see for example Refs. [20, 21, 104, 105].

6.1. Potential Upgrades and Filling Schemes

The LIU (LHC Injector Upgrade) project [19] considers several options for the upgrade of the heavy-ion injector complex [17]. The upgrades focus on the increase of the total lead beam intensity, which can be achieved by increasing the single bunch intensity (limited by the dynamic effects at low energy) and by decreasing the spacing between bunches to fit more bunches into one LHC ring. The impact on the Pb-Pb luminosity should be addressed in this chapter for the most crucial upgrades: the intensity increase in LEIR, the batch compression and bunch splitting in the PS, the slip stacking in the SPS and the choice of the SPS kicker rise-time.

Trains injected into the LHC have a bunch spacing defined in the PS, with gaps between PS batches set by the SPS. The construction of filling schemes is discussed in detail in Chapter 2.3.3. Table 6.1 gives an overview over potential upgrade stages and the related final bunch spacings in the LHC in terms of PS and SPS spacings and number of bunches per PS batch. In the following, filling schemes will be defined over the bunch spacing within and between batches, in the notation: PS/SPS ns. For instance, features the 100/225 ns scheme, labelled as *present (2015)* in Table 6.1, a bunch spacing of 100 ns within a PS-batch and 225 ns between batches. In the 2011 run a 200/200 ns scheme was used.

6.1.1. Reduction of Bunch Spacing

While the distance between trains injected into the LHC and batches injected into the SPS is limited by the rise-times of the respective injection kickers, the spacing within

PS spacing [ns]	SPS spacing [ns]	Bunches/PS batch	Scenario
100	225	2	Present (2015)
100	100	2	SPS kicker
100	225	4	Bunch splitting
50	**50**	**4**	**Full upgrade**

Table 6.1.: LS2 upgrade scenarios: SPS injection kicker, LEIR intensity increase and bunch splitting in the PS; the full upgrade combines all with slip stacking in the SPS.

a batch can be adjusted by *RF gymnastics* in the PS [46, 47]. By a sufficiently slow increase of the harmonic number at constant magnetic field, it is possible to compress the spacing between the bunches present in the PS without intensity losses or blow-up. As already demonstrated during machine development sessions in the PS in 2013 (see [17] and Appendix B), the present conditions of the PS would allow a batch compression to a spacing of 100 ns after LS1. A batch compression to 50 ns would allow even more bunches to be squeezed into one LHC ring, but cannot be performed with the current PS RF hardware and would require a major upgrade.

The current minimum rise-time of the full SPS injection system is 225 ns. A new, faster ramping, kicker is foreseen in the LIU project. In the *LIU-SPS* 50 ns *Injection System for Pb Ions Review* on Friday 4th October 2013 [106] it was decided to build a kicker with 100 ns rise-time. This seems to be the most feasible and cost effective option. By now, it is unlikely that the originally considered 50 ns SPS kicker [107] will be built.

Under these considerations and the assumption of the current injector performance, a 100/100 ns scheme with 2-bunch-PS-batches could be one stage of the upgrade. This scenario, labelled as *SPS kicker* in Table 6.1, requires little operational development, but the installation of a new SPS injection system during LS2.

6.1.2. Increasing LEIR Performance and Bunch Splitting

Increasing the extracted intensity from LEIR, which is discussed in more detail in the following section, is completely independent of the decision about the SPS kicker. Bunches with higher intensity suffer more from dynamic effect at low energy in the injectors. In case the LEIR intensity could be increased by (at least) 40%, the two bunches have to be split into 4 in the PS to mitigate these effects, especially on the SPS injection plateau. Without SPS kicker upgrade, a 100/225 ns scheme with 4-bunch-PS-batches could be created. Table 6.1 calls this scheme *bunch splitting* scenario.

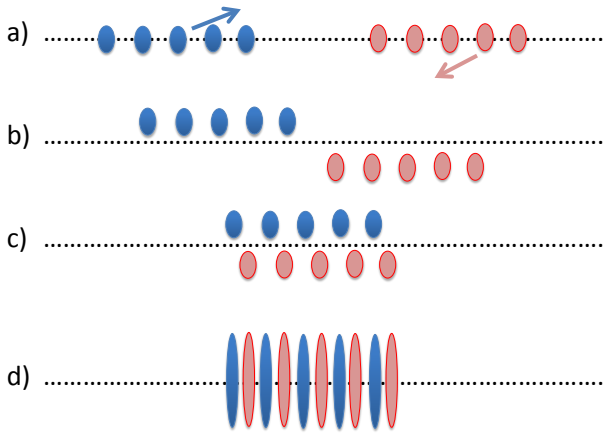

Figure 6.1.: Principle of slip stacking [108].

6.1.3. Slip Stacking

The *full upgrade* scenario includes a LEIR intensity upgrade, bunch splitting followed by batch compression to 100 ns in the PS, the installation of a new SPS kicker with 100 ns rise-time and, as a final stage, *slip stacking* in the SPS.

In the full upgrade scenario, slip stacking in the SPS could provide a 50/50 ns-like scheme. The SPS is filled with two "super-batches" of 24 bunches each, constructed out of 6 × 4-bunch-PS-batches. The bunches are separated by 100 ns everywhere in this SPS beam. The principle of the then performed slip stacking is illustrated in Fig. 6.1 [108]: *a*) The two super-batches are captured by two independently controlled pairs of 200 MHz Travelling Wave Cavities. The RF frequencies of the two systems are varied to decelerate the first and accelerate the second batch. *b*) The batches are allowed to slip until they interleave, *c*) brought back to the same energy and *d*) are recaptured at an average RF frequency. This technique introduces a large longitudinal emittance blow-up, but is the most promising option to achieve a 50/50 ns spacing.

6.2. Intensity Scaling for Model Calculations

One of the major upgrades to be implemented is to increase the intensity extracted from LEIR. At the moment the most important limitation comes from strong intensity losses during the RF capture and energy ramp. Great progress has been made in understanding these losses, and possible sources have been identified [50, 102]. This already led to the big intensity improvement between the 2011 and 2013 runs. Table 6.2 lists the LEIR performance and transmission efficiencies until injection in the LHC and into collisions in the past years. The third column gives an estimate of the performance, if the intensity extracted out of LEIR could be increased by 40% compared to 2013. In this case, the 2 bunches have to be split into 4, to mitigate IBS and space charge

	2011	**2013**	**LEIR +40%**
Beam out of LEIR			
LEIR pulse intensity	9×10^8	11×10^8	15.4×10^8
Number of bunches per batch	2	2	4
Intensity per future LHC bunch	4.5×10^8	5.5×10^8	3.9×10^8
Beam in the LHC			
Transmission LEIR $\rightarrow$ LHC Inj.	27%	30%	30%
Injected intensity per bunch into LHC	1.24×10^8	1.67×10^8	1.2×10^8
Transmission LHC Inj. $\rightarrow$ SB	96%	86%	96%
Intensity in Stable Beams (SB)	1.20×10^8	1.44×10^8	1.1×10^8
Transmission LEIR $\rightarrow$ LHC SB	27%	26%	29%
Intensity Scaling Factors			
F_{Nb} for best transmission	1	1.33	0.92

Table 6.2.: Measured bunch intensities and scaling. Intensities are given in number of ions. Best transmission is define as 30% from LEIR to LHC injection [103] and 96% from LHC injection into collisions, leading to a full survival rate of 29%. The decrease in bunch intensity in the last column is due to the applied bunch splitting, the total beam intensity is in fact increased.

effects. The result is a smaller current per bunch, but more bunches per beam.

In 2013 not only higher bunch intensities were delivered by LEIR, but also a higher fraction survived until the LHC. However, during the LHC ramp and adjust a great fraction was lost, due to issues especially related to the new p-Pb mode of operation. These losses are not expected in a Pb-Pb run and likely to be reduced in the next p-Pb run. Therefore, the estimates presented in this chapter use the derived peak luminosity model of Eq. (5.10), assuming an intensity scaling, F_{Nb}, combining the best performances of both years. In this way, the highest intensity per bunch, which can reasonably be expected from experience, is obtained.

In the following, the factor $F_{\mathrm{Nb}} = 1.33$ is assumed in all filling schemes working with 2 bunches per PS-batch, as they were used in the past runs. If 4-bunch-PS-batches are considered, $F_{\mathrm{Nb}} = 0.92$ is used, including the assumption of a 40% performance increase in LEIR.

6.3. LHC Run 2

6.3.1. Potential Performance

Performance with the 2011 Filling Scheme

To restart the LHC after the long shutdown in 2015, the first obvious option to consider would be to run with the same filling scheme as in 2011, providing 358 bunches per beam with a bunch spacing of 200 ns within trains of 24 bunches. A beam energy of $E_b = 6.5Z$ TeV and $\beta^* = 0.5$ m are foreseen. The luminosity scales inversely with β^*. Since the beam size is adiabatically damped during acceleration, the luminosity increases linearly with energy. Compared to 2011 parameters ($E_b = 3.5Z$ TeV and $\beta^* = 1$ m), luminosities higher by a factor $F_E = 6.5/3.5 \times 1/0.5 = 3.7$ are within reach.

Bunch intensities as high as in 2013 are expected from the injectors, on average $N_b = 1.67 \times 10^8$ ions per bunch. With the reduced transition rate of only 86%, compared to 96% in 2011, survived $N_b = 1.4 \times 10^8$ ions per bunch the transition into collisions. Nevertheless, it is expected that the transition rate of 2011 can be recovered. With the aid of Table 6.2, an increase in the single bunch lead intensity of 33%, giving an intensity scaling factor of $F_{Nb} = 1.33$, is estimated. With these assumptions a peak luminosity of

$$\mathcal{L} = 3 \times 10^{27}\,\mathrm{cm}^{-2}\mathrm{s}^{-1} \tag{6.1}$$

could easily be reached.

Filling Scheme Optimisation

A new optics, the so-called *Q20-optics* [109], was implemented in the SPS in 2012, to improve the space charge and IBS issues by working with larger beam sizes. Compared to the previous *Q26-optics*, the new version has a reduced number of total betatron oscillations per turn, namely 20 instead of 26 (as the name suggests), leading to a higher average β-function.

Four kicker modules are available to guide the beam from the transfer line into the SPS. With the Q26-optics it was enough to use three out of four modules for the injection of lead bunches, providing a minimum batch spacing of 200 ns. However, with the new optics the kick enhancement of the quadrupoles near injection is weaker and all modules have to be used for the injection. Whereas, the fourth one, which was not used with Q26, is the strongest and needs a longer rise-time, limiting the batch spacing to a minimum of 225 ns for the new optics.

For the next run, a filling scheme with an alternating bunch spacing of 100 (PS) and 225 ns (SPS) within trains could be used. Constructing a filling scheme, which can be used for operation in the LHC, is complicated and many constraints have to be taken into account. The luminosity potential of a certain bunch structure can be estimated in first order with a simplified filling scheme, considering the following points only:

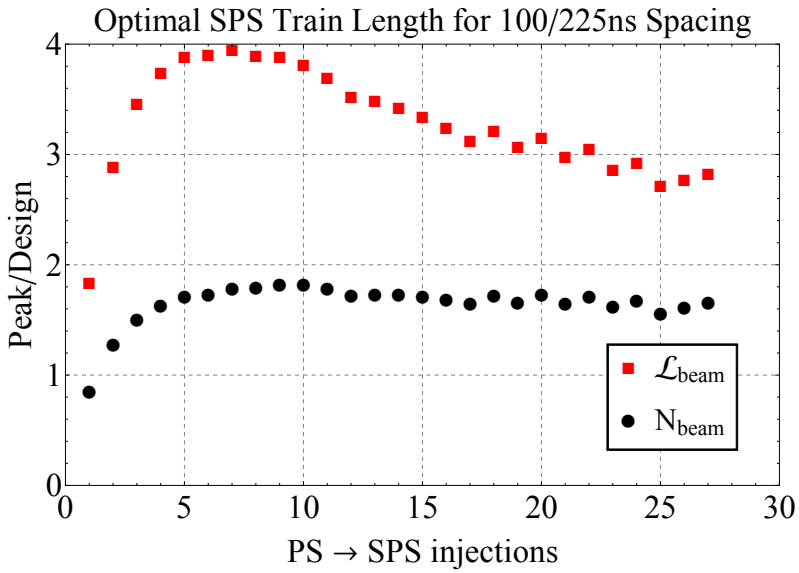

Figure 6.2.: Identification of the optimal SPS train length, calculated with Eq. (5.10) and (5.29).

- The RF system settings used for Pb bunches in the SPS limit the train's length to 40% of the SPS circumference.
- The LHC injection kicker rise-time is 900 ns.
- An abort gap of 3.3 μs has to be left unpopulated for the dump kickers to rise.
- All bunches in the beam collide with an equal partner (good approximation for collisions in IP1 and 5. Since the ring is filled by quadrant, the first bunches of trains collide in also IP2, however the equality of collision partners is disturbed by train to train differences).

As was discussed in detail in Chapter 5, the longer the bunches spent at the SPS injection plateau the more brightness they lose. Thus, there is an optimum number of PS-batches per train, which provides the highest peak luminosity. Taking the potential bunch spacing and constraints from the list above, Eq. (5.10) and (5.29) can be used to calculate the total $\mathcal{L}_{\text{peak}}$ and N for a varying number of PS-batches per train, by filling as many trains of one kind as possible into the LHC.

Figure. 6.2 shows such an optimisation, where the total peak luminosity (red) and intensity (black) with respect to the design value [42] is plotted as a function of PS-batches per train. After a steep slope for very short trains, a small plateau between 5 and 10 PS-batches per train predicts the highest $\mathcal{L}_{\text{peak}}$. The fact that the $\mathcal{L}_{\text{peak}}$ decay curve of one train sitting in the SPS asymptotically approaches a constant value, and that the total number of bunches per beam is about constant for very long trains, decreases the achievable luminosity after the plateau. The maximum luminosity of

$$\mathcal{L} = 4 \times 10^{27}\,\text{cm}^{-2}\text{s}^{-1} \tag{6.2}$$

is reached for 7 PS-batches per train and 29 trains per beam. The maximum total beam intensity, which gives an indication of the expected $\mathcal{L}_{\text{int}}$, tends to longer trains. The maximum N is reached with 9 PS-batches and 24 trains per beam, adding up to a higher total number of bunches per beam. In operation it is more practical to work with not too short trains and since the 9-batch/24-train scheme delivers only marginally less $\mathcal{L}_{\text{peak}}$, it is suggested as the optimal solution. With this optimised filling scheme, it could thus be possible to improve the peak luminosity by about 30%.

6.3.2. Analytical Considerations for Luminosity Levelling

The expected luminosities, estimated in the previous section, exceed the design by a factor four. In its current state, the ALICE detector is restricted to peaks of $\mathcal{L}_{\text{peak}} = 1 \times 10^{27}\,\text{cm}^{-2}\text{s}^{-1}$, the design value for which the detector was built. This value corresponds to a rate of about 8000 events/s or 0.7 events/turn, based on an hadronic cross-section of $\sigma_{c,\text{hadron}} = 8\,\text{b}$. The limit is imposed by the Time Projection Chamber (TPC) that acts as the tracker for ALICE. The TPC is capable of a detailed reconstruction of events with thousands of secondary particle tracks, as it is the case in high energy heavy-ion collisions. The maximum usable luminosity is limited by the event pile-up due to the long drift times ($90\,\mu\text{s} \approx 1\,\text{turn}$) in the TPC [110].

The foreseen upgrade to 6-7 times this value will only be implemented in LS2 [16]. ATLAS and CMS do not have such a restriction, since they were built to process much higher rates in p-p operation, and can easily handle the predicted Pb-Pb luminosities.

A peak luminosity below the given limit can be obtained by

- reducing the number of colliding bunches in IP2,
- adjusting the value of β^* (either to a constant high value or β^*-levelling), or
- levelling with separation.

The first option would be realized by changing the filling scheme, so that fewer bunches are colliding in ALICE. The advantage of levelling is that it keeps $\mathcal{L}_{\text{peak}}$ more or less constant at the maximum value. Levelling is either performed by slowly decreasing a transverse separation of the two beams, or by adjusting the value of β^* from large to small values, while the beams are colliding head-on. When the beams are fully overlapping, or the target value can no longer be reached, because the beam conditions degraded, the luminosity decays in the usual way. Compared to the first option, additional data could be integrated during the period of levelling at the highest possible rates.

The integrated luminosity of a fill starting levelled, does not depend directly on the levelling technique used. To get an estimate, the luminosity can be set to a constant value during the levelling period and be calculated with the equations derived below after levelling stops.

The luminosity is calculated via Eq. (2.21). In the approximation of equal beams ($N_b = N_{b1} = N_{b2}$, $\sigma = \sigma_1 = \sigma_2$) and zero crossing-angle ($F = 1$), Eq. (2.21) simplifies

to

$$\mathcal{L} = \frac{N_b^2 f_{\mathrm{rev}} k_b}{4\pi\sigma_x\sigma_y} = \frac{N_b^2 f_{\mathrm{rev}} k_b \gamma}{4\pi\beta^* \sqrt{\epsilon_{n,x}\epsilon_{n,y}}} = A\frac{N_b^2}{\sqrt{\epsilon_{n,x}\epsilon_{n,y}}}, \tag{6.3}$$

where the factor $A = f_{\mathrm{rev}} k_b \gamma/(4\pi\beta^*)$ is constant at a given energy, γ, $\epsilon_{n,x}$ and $\epsilon_{n,y}$ are the horizontal and vertical normalised emittances. The luminosity evolution is hence given by the decay of N_b and the blow-up of ϵ_n.

The particle loss rate due to collisions in one IP is given by

$$\frac{dN}{dt} = -\sigma_c \mathcal{L}(t), \tag{6.4}$$

which decreases with decaying $\mathcal{L}$(t). σ_c is the total event cross-section of interactions removing particles from the beam. Inserting Eq. (6.3) into (6.4) leads to a differential equation describing the intensity evolution

$$\frac{dN}{dt} = -A\sigma_c \frac{N_b^2(t)}{\sqrt{\epsilon_{n,x}(t)\epsilon_{n,y}(t)}}, \tag{6.5}$$

where $N = k_b N_b$. N_b(t), $\epsilon_{n,x}$(t) and $\epsilon_{n,y}$(t) are time dependent. The time evolution of the emittance is affected by several effects, which can have different strengths in the two transverse planes. IBS and radiation damping have the largest influence. RF and other noise sources or beam-gas scattering can also play a role, however, they are considered to be small in the LHC. In general, ϵ_n will evolve following

$$\frac{d\epsilon_n}{dt} = (\alpha_{\mathrm{IBS}}(t) - \alpha_{\mathrm{rad}} \pm \alpha_{\mathrm{other\,effects}})\epsilon_n(t), \tag{6.6}$$

where the IBS growth rate α_{IBS}(t) depends on time, because of its dependence on N_b and ϵ_n itself. Equation (6.5) and (6.6) form a system of coupled differential equations. It is impossible to find an exact analytical solution for this system, considering the full dependence on the emittance.

Approximations will be made to derive analytical equations, which can describe the intensity and luminosity evolution as a function of time, with levelling in some or all IPs.

1st Approximation: ϵ_n = const.

At $E_b = 6.5Z$ TeV, the planed beam energy for Run 2, the radiation emittance damping time (see Chapter 2.5.2) calculates to $1/\alpha_{\mathrm{rad},x,y} = 16$ h in the transverse and $1/\alpha_{\mathrm{rad},s} = 8$ h in the longitudinal plane. Compared to the initial IBS growth times (see Chapter 2.5.1), $1/\alpha_{\mathrm{IBS},x} \approx 8$ h and $1/\alpha_{\mathrm{IBS},s} \approx 10$ h, radiation damping is strong enough to partly counteract the horizontal IBS growth, while even slow bunch length

shrinkage can be expected. With total initial emittance growth rates of

$$\alpha_{\epsilon x} = \alpha_{\mathrm{IBS},x} - \alpha_{\mathrm{rad},x} \approx 1/16\,\mathrm{h} \tag{6.7}$$
$$\alpha_{\epsilon y} \approx -1/16\,\mathrm{h} \tag{6.8}$$
$$\alpha_{\epsilon s} \approx -1/40\,\mathrm{h}, \tag{6.9}$$

the emittance variations with time are small and in first approximation it can be considered as constant. For only one colliding bunch pair, $k_b = 1$, and initially round beams ($\epsilon_{n,x}(0) = \epsilon_{n,y}(0) = \epsilon_{n0}$), the ordinary differential equation (ODE) system

$$\frac{dN_b}{dt} = -A_1\sigma_c\frac{N_b^2(t)}{\epsilon_{n0}} \tag{6.10}$$
$$\frac{d\epsilon_{n,x}}{dt} = 0 \tag{6.11}$$
$$\frac{d\epsilon_{n,y}}{dt} = 0 \tag{6.12}$$
$$\frac{d\sigma_s}{dt} = 0 \tag{6.13}$$

has to be solved. Where $A_1 = A(k_b = 1) = f_{\mathrm{rev}}\gamma/(4\pi\beta^*)$. The system is decoupled and the equations for the emittances and bunch length are trivial:

$$\epsilon_n(t) = \epsilon_{n,x}(t) = \epsilon_{n,y}(t) = \epsilon_{n0}, \tag{6.14}$$
$$\sigma_s(t) = \sigma_{s0}. \tag{6.15}$$

The equation for the intensity can be solved by the separation of variables and integration of both sides:

$$\frac{dN_b}{N_b^2} = -A_1\sigma_c\frac{dt}{\epsilon_{n0}} \tag{6.16}$$
$$\Longrightarrow -\frac{1}{N_b} = -\frac{A_1\sigma_c}{\epsilon_{n0}}t - C_1 \tag{6.17}$$
$$\Longrightarrow N_b(t) = \frac{1}{A_1\sigma_c t/\epsilon_{n0} + C_1}. \tag{6.18}$$

C_1 is a constant of integration, which is determined from the starting condition

$$N_b(t=0) = N_{b0} \tag{6.19}$$
$$\Longrightarrow C_1 = \frac{1}{N_{b0}}, \tag{6.20}$$

thus

$$N_b(t) = \frac{N_{b0}}{A_1 N_{b0}\sigma_c t/\epsilon_{n0} + 1}. \tag{6.21}$$

Inserting Eq. (6.21) into (6.3) for $k_b = 1$, leads to the bunch luminosity evolution

$$\mathcal{L}_b(t) = \frac{A_1}{\epsilon_{n0}} \left(\frac{N_{b0}}{A_1 N_{b0} \sigma_c t / \epsilon_{n0} + 1} \right)^2 \tag{6.22}$$

$$= \mathcal{L}_{b0} \left(\frac{1}{A_1 N_{b0} \sigma_c t / \epsilon_{n0} + 1} \right)^2 . \tag{6.23}$$

This formalism can be expanded for collisions in several IPs with different properties by replacing

$$\mathcal{L}_b(t) \to \sum_{j=1}^{n_{\mathrm{IP}}} \mathcal{L}_{bj}(t) = \frac{N_b^2(t)}{\epsilon_{n0}} \sum_{j=1}^{n_{\mathrm{IP}}} A_{1j} = \frac{N_b^2(t)}{\epsilon_{n0}} \frac{f_{\mathrm{rev}}\gamma}{4\pi} \sum_{j=1}^{n_{\mathrm{IP}}} \frac{1}{\beta_j^*} = \frac{N_b^2(t)}{\epsilon_{n0}} B \tag{6.24}$$

in Equation (6.4). Only the local β-function can be set independently for different IPs, thus the sum in Eq. (6.24) would only change its value during a given fill if β^*-levelling is used. It does not change dynamically with time and will be considered as constant in the following. Therefore, Eq. (6.21) and (6.23) are valid to calculate the intensity and luminosity evolution for several IPs with different properties by replacing $A_1 \to B = \frac{f_{\mathrm{rev}}\gamma}{4\pi} \sum_{j=1}^{n_{\mathrm{IP}}} \frac{1}{\beta_j^*}$. If all IPs are equivalent, B simplifies to $B \to A_1 \times n_{\mathrm{IP}}$, where n_{IP} is the number of IPs.

The collision pattern can change from bunch to bunch. The total beam intensity and luminosity evolution is given by the sum over all single bunches:

$$N(t) = \sum_{i=1}^{n_b} N_{bi}(t) \tag{6.25}$$

$$\mathcal{L}(t) = \sum_{i=1}^{k_b} \mathcal{L}_{bi}(t). \tag{6.26}$$

Here n_b is the number of bunches per beam, which can be different from the number of colliding bunch pairs, k_b, in the given IP.

Include Levelling

The goal is to keep the levelled IP at a constant maximum luminosity, $\mathcal{L}_{\mathrm{max}}$, as long as the peak luminosity for total beam overlap or minimal β^* is larger than the limit. During levelling the burn-off losses are less than described by Eq. (6.5), since the $\mathcal{L}$ is kept at a lower value. The total rate of lost particles for $n_{\mathrm{IP,lev}}$ levelled and n_{IP}

non-levelled IPs in collisions is given by

$$\frac{dN_b}{dt} = \underbrace{-\sigma_c \sum_{i=1}^{n_{\mathrm{IP,lev}}} \mathcal{L}_{b,\max,i}}_{\mathrm{C=const.}} \underbrace{-\sigma_c \sum_{j=1}^{n_{\mathrm{IP}}} \mathcal{L}_{bj}(t)}_{\frac{N_b^2(t)}{\epsilon_{n0}}B} . \tag{6.27}$$

The first term, summing over the levelled IPs, is a constant and only the second term varies with time. This differential equation can still be solved by the separation of variables and integration of both sides:

$$\Longrightarrow dt = \frac{dN_b}{-C - \sigma_c B N_b^2/\epsilon_{n0}} = -\frac{\epsilon_{n0}}{\sigma_c B}\frac{dN_b}{(C' + N_b^2)} \tag{6.28}$$

$$\Longrightarrow t = -\frac{\epsilon_{n0}}{\sigma_c B}\left(\frac{1}{\sqrt{C'}}\arctan(\frac{N_b}{\sqrt{C'}}) - D_1\right) \tag{6.29}$$

$$\Longrightarrow N_b(t) = \sqrt{\frac{C\epsilon_{n0}}{\sigma_c B}}\tan\left[\left(D_1 - t\frac{\sigma_c B}{\epsilon_{n0}}\right)\sqrt{\frac{C\epsilon_{n0}}{\sigma_c B}}\right] . \tag{6.30}$$

The integral

$$\int \frac{dx}{a^2 + x^2} = \frac{1}{a}\arctan\left[\frac{x}{a}\right] \quad \text{for} \quad a > 0 \tag{6.31}$$

is only defined for $a > 0$, which implies that Eq. (6.30) is only defined for $C > 0$. Using again the starting condition $N_b(t = 0) = N_{b0}$ to evaluate the constant of integration D_1, leads to

$$D_1 = \sqrt{\frac{\sigma_c B}{C\epsilon_{n0}}}\arctan\left(N_{b0}\sqrt{\frac{\sigma_c B}{C\epsilon_{n0}}}\right) \tag{6.32}$$

and hence

$$N_b(t) = \sqrt{\frac{C\epsilon_{n0}}{\sigma_c B}}\tan\left[\sqrt{\frac{\sigma_c BC}{\epsilon_{n0}}}(\sqrt{\frac{\epsilon_{n0}}{C\sigma_c B}}\arctan\left(N_{b0}\sqrt{\frac{\sigma_c B}{C\epsilon_{n0}}}\right) - t)\right] . \tag{6.33}$$

Note that, because of Eq. (6.31), Eq. (6.33) is only valid in the case of at least one levelled IP and only as long as the peak luminosity, which would be achievable without levelling, is higher than the desired levelled luminosity: $\mathcal{L}_{b,\max} \leq \mathcal{L}_b = A_1 N_b^2/\epsilon_{n0}$.

To calculate the luminosity evolution from Eq. (6.33) the two cases of the levelled and non-levelled IPs have to be distinguished. As desired, in the valid regime of Eq. (6.33), the levelled IPs will be provided with a constant luminosity $\mathcal{L}_{b,\max,i}$. For

the non-levelled IPs the luminosity can be calculated as a function of time via

$$\mathcal{L}_b(t) = \frac{C}{\sigma_c}\tan^2\left[\sqrt{\frac{\sigma_c BC}{\epsilon_{n0}}}\left(\sqrt{\frac{\epsilon_{n0}}{C\sigma_c B}}\arctan\left(N_{b0}\sqrt{\frac{\sigma_c B}{C\epsilon_{n0}}}\right) - t\right)\right]. \quad (6.34)$$

According to Eq. (6.31), $\mathcal{L}_{\max} = 0$ is forbidden, however, in the limit where $\mathcal{L}_{\max}$ is decreased to the order of background, Eq. (6.34) gives the same numerical result as Eq. 6.23 for n_{IP} non-levelled IPs. In the limit of only levelled IPs ($n_{\mathrm{IP}} \to 0$),

$$\Longrightarrow N_b(t) \to N_{b0} - Ct = N_{b0} - \sigma_c t \sum_{i=1}^{n_{\mathrm{IP,lev}}} \mathcal{L}_{b,\max,i}, \quad (6.35)$$

reduces $N_b(t)$ linearly with time, because of the constant burn-off rate.

In general, levelling can only be applied to the beam as a whole, rather than to single bunches, thus

$$\mathcal{L}_{\max} = \sum_{i=1}^{k_b} \mathcal{L}_{b,\max,i} = \frac{f_{\mathrm{rev}}\gamma}{4\pi\beta^*_{\max}} \sum_{i=1}^{k_b} \frac{N_{bi}^2}{\epsilon_{ni}} \quad (6.36)$$

is the parameter that can be adjusted from the control room. If all bunches are equal and collide under equivalent conditions, the equations derived above, can simply be multiplied by k_b to obtain the total beam evolution. Nevertheless, if bunches have varying initial parameters, they will evolve differently. To get a correct prediction, the $\mathcal{L}_{b,\max,i}$ have to be determined at every time step from the constant $\mathcal{L}_{\max}$ as described by Eq. (6.36).

Levelling is stopped when $\mathcal{L}_{\max}$ can no longer be reached. Depending on the levelling method, either when beams fully overlap or the minimal value of β^* is reached. In the case of several IPs levelled to different $\mathcal{L}_{\max,i}$, each levelled IP has to be monitored separately, if the potential peak luminosity is still above the levelling limit. As soon as one IP no longer satisfies this condition, levelling is stopped in that IP and it becomes a non-levelled IP in Eq. (6.27). To calculate the luminosity for the subsequent period, until the next levelled IP falls below the limit, the number of IPs have to be updated in Eq. (6.27) as $n_{\mathrm{IP,lev}} \to (n_{\mathrm{IP,lev}} - 1)$ and $n_{\mathrm{IP}} \to (n_{\mathrm{IP}} + 1)$.

When the potential luminosity of the last levelled IP has degraded below $\mathcal{L}_{\max}$, the intensity and luminosity will again evolve as described by Eq. (6.21) and (6.23), respectively.

2nd Approximation: $\alpha_\epsilon = \mathrm{const.}$

In a second approximation the total emittance growth rates, α_ϵ, are assumed to be constant and equal to the initial values quoted above. In this case, the ODE system

to be solved is:

$$\frac{dN_b}{dt} = -A_1\sigma_c\frac{N_b^2(t)}{\sqrt{\epsilon_{nx}(t)\epsilon_{ny}(t)}} \tag{6.37}$$

$$\frac{d\epsilon_{nx}}{dt} = \alpha_{\epsilon x}\ \epsilon_{nx}(t) \tag{6.38}$$

$$\frac{d\epsilon_{ny}}{dt} = \alpha_{\epsilon y}\ \epsilon_{ny}(t) \tag{6.39}$$

$$\frac{d\sigma_s}{dt} = \frac{1}{2}\ \alpha_{\epsilon s}\ \sigma_s(t). \tag{6.40}$$

The values of the α_ϵ can be positive or negative, leading to growth or damping, respectively. Setting α_ϵ to a constant, implicitly assumes that IBS is independent of the beam parameters, which decouples some of the equations. Even though the initial emittance variations are small, N_b will decrease drastically due to burn-off, reducing IBS, and $\alpha_{\epsilon x}$ could switch sign during the store. Equation (6.38) to (6.40) describe an exponential behaviour for the transverse emittances and bunch length:

$$\epsilon_{n,x}(t) = \epsilon_{n0}\ \exp[\alpha_{\epsilon x}t] \tag{6.41}$$

$$\epsilon_{n,y}(t) = \epsilon_{n0}\ \exp[\alpha_{\epsilon y}t] \tag{6.42}$$

$$\sigma_s(t) = \sigma_{s0}\ \exp[\alpha_{\epsilon s}t/2], \tag{6.43}$$

where the same initial conditions as in the 1$^{\text{st}}$ approximation are applied. Note that $\alpha_{\epsilon x}$ and $\alpha_{\epsilon y}$ are in general different and that thus the transverse emittances evolve differently. Inserting Eq. (6.41) and (6.42) into (6.37) leads to

$$\frac{dN_b}{dt} = -A_1\sigma_c\frac{N_b^2(t)}{\epsilon_{n0}\ \exp[(\alpha_{\epsilon x}+\alpha_{\epsilon y})t/2]}. \tag{6.44}$$

Separating the variables and integrating both sides gives the time evolution of N_b:

$$N_b(t) = \frac{\epsilon_{n0}N_{b0}}{\epsilon_{n0} - 2A_1\sigma_c N_{b0}(\exp[-(\alpha_{\epsilon x}+\alpha_{\epsilon y})t/2]-1)/(\alpha_{\epsilon x}+\alpha_{\epsilon y})}. \tag{6.45}$$

Finally, by combining Eq. (6.3), (6.41), (6.42) and (6.45) one obtains the time evolution of the luminosity:

$$\mathcal{L}_b(t) = \mathcal{L}_{b0}\frac{\epsilon_{n0}^2\exp[-(\alpha_{\epsilon x}+\alpha_{\epsilon y})t/2]}{(\epsilon_{n0} - 2A_1\sigma_c N_{b0}(\exp[-(\alpha_{\epsilon x}+\alpha_{\epsilon y})t/2]-1)/(\alpha_{\epsilon x}+\alpha_{\epsilon y}))^2}. \tag{6.46}$$

Levelling can be included by replacing $\epsilon_{n0} \to \epsilon_{n0}\exp[(\alpha_{\epsilon x}+\alpha_{\epsilon y})t/2)]$ in Eq. (6.27), leading to an inhomogeneous differential equation of the form

$$\frac{dN_b}{dt} = -B\sigma_c\frac{N_b^2(t)}{\epsilon_{n0}\ \exp[(\alpha_{\epsilon x}+\alpha_{\epsilon y})t/2]} - D. \tag{6.47}$$

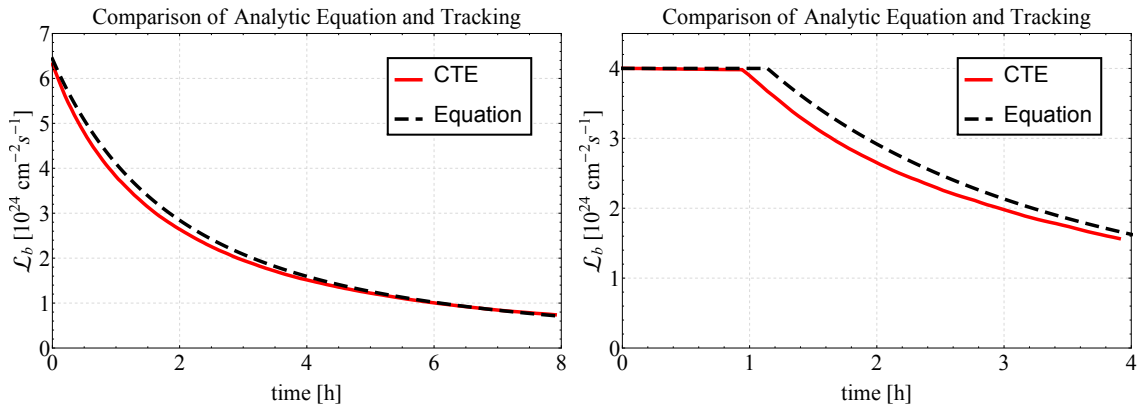

Figure 6.3.: Comparison of the analytic calculation (dashed red line) and CTE simulation (black solid line) with (right) and without (left) luminosity levelling in one IP.

The homogeneous solution of this equation ($D = 0$) represents the case without levelling, which is given by Eq. (6.45), when replacing $A_1 \to B$.

6.3.3. Agreement of the Analytical Approach with Simulations

It was shown that the initial emittance variations due to IBS and radiation damping are slow. To verify that this behaviour is a good approximation over the duration of the entire fill, CTE simulation were performed, based on the expected average bunch parameters for Run 2. The left plot of Fig. 6.3 compares the luminosity evolution of one colliding bunch pair in 3 IPs, each at $\beta^* = 0.5\,\mathrm{m}$ and with zero crossing-angle, obtained by the simulation (red) and Eq. (6.23) (black). Because of the varying emittances, the luminosity decay is slightly enhanced in the tracking simulation compared to the analytical curve, assuming the same emittances at all times. Nevertheless, the differences are small and both curves are in good agreement. This result confirms that the assumption of constant emittances is a good approximation, at least for the beam conditions expected for Run 2.

In the course of this study, the CTE program was extended to treat β^*-levelling. A general switch to activate luminosity levelling for the given simulation run was introduced. The settings for each IP are specified in the input file. It can be chosen, if the given IP is levelled and its $\mathcal{L}_{\mathrm{max}}$ (sum over all bunches pairs simulated) can be set in units of $\mathrm{cm}^{-2}\mathrm{s}^{-1}$. The β^* input value given, is taken as the lower limit for the levelling process. The program checks at each simulation turn, if the potential luminosity at minimal β^* is still above $\mathcal{L}_{\mathrm{max}}$. The β^* value used for the determination of the delivered luminosity is then recalculated separately for each IP to satisfy $\mathcal{L} = \mathcal{L}_{\mathrm{max}}$. According to the actually delivered luminosity, the corresponding number of particles are removed from the beam.

The right plot of Figure 6.3 shows a comparison of the bunch luminosity evolution from simulation and analytical calculation under the same conditions as in the left plot, but with levelling in one IP to $\mathcal{L}_{b,\max} = 4 \times 10^{24}\,\mathrm{cm}^{-2}\mathrm{s}^{-1}$. The luminosity decay is in good agreement, as already confirmed by the plot on the left. However, the simulated potential luminosity falls below $\mathcal{L}_{\max}$ about 15 min earlier, because the emittance has increased by about 10% within the first hour of store, while ϵ_n is assumed to be constant in the analytic calculation. The constant ϵ_n leads to a higher instantaneous value of the potential luminosity, delaying the moment when levelling has to be stopped. This discrepancy can be mitigated, if the analytic calculation is done with the emittance expected at the end of the levelling period, rather than at the beginning of collisions. With this correction, the agreement between tracking and the analytic approach is very good.

6.3.4. Luminosity Estimates with Levelling

Finding the moment when levelling stops in a bunch-by-bunch manner for each experiment, is rather complicated. As described by Eq. (6.36), the single bunch properties of all bunches have to be checked at each time step to provide, as an ensemble, a potential luminosity of $\mathcal{L} > \mathcal{L}_{\max}$. Nevertheless, as could be shown in Chapter 4.4 and 6.3.3 that the total beam evolution is well predicted by the CTE results for a bunch with average beam parameters. In the following, the analytic equations derived above are used to estimate the total beam luminosity evolution, starting collisions with a levelling period, for k_b bunches with average beam parameters.

Figure 6.4 shows the instantaneous (left) and integrated (right) luminosity in ALICE (top) and in ATLAS/CMS (bottom) for 3 different levelling scenarios, based on the parameters given in Table 6.3.

ALICE is the only experiment with a constraint on the maximum luminosity, therefore the most obvious scenario would be to level ALICE to $\mathcal{L}_{\max} = 1 \times 10^{27}\,\mathrm{cm}^{-2}\mathrm{s}^{-1}$ and give the maximum available rate to ATLAS and CMS, which is shown in red. However, in this case, the burn-off introduced by the high collision rate in ATLAS and CMS would "eat up" the particles very fast, leading to a short levelling time for ALICE. Depending on the average fill length, the integrated luminosity of ALICE would thus be reduced compared to its available maximum, for constant luminosity over the whole fill duration.

In general, it is desired to obtain similar amounts of integrated luminosity for all experiments by the end of the run. Reducing the burn-off rate in IP1 and 5 by levelling

$\mathcal{L}_{\max}$ (IP2)	E_b	N_b	ϵ_n	β^*	$\sigma_{c,\mathrm{tot}}$	k_b
$1 \times 10^{27}\,\mathrm{cm}^{-2}\mathrm{s}^{-1}$	$6.5Z$ TeV	1.6×10^8 ions/bunch	$1.5\,\mu$m	0.5 m	508 b	432

Table 6.3.: Parameters used for Pb-Pb luminosity estimates with levelling in Run 2.

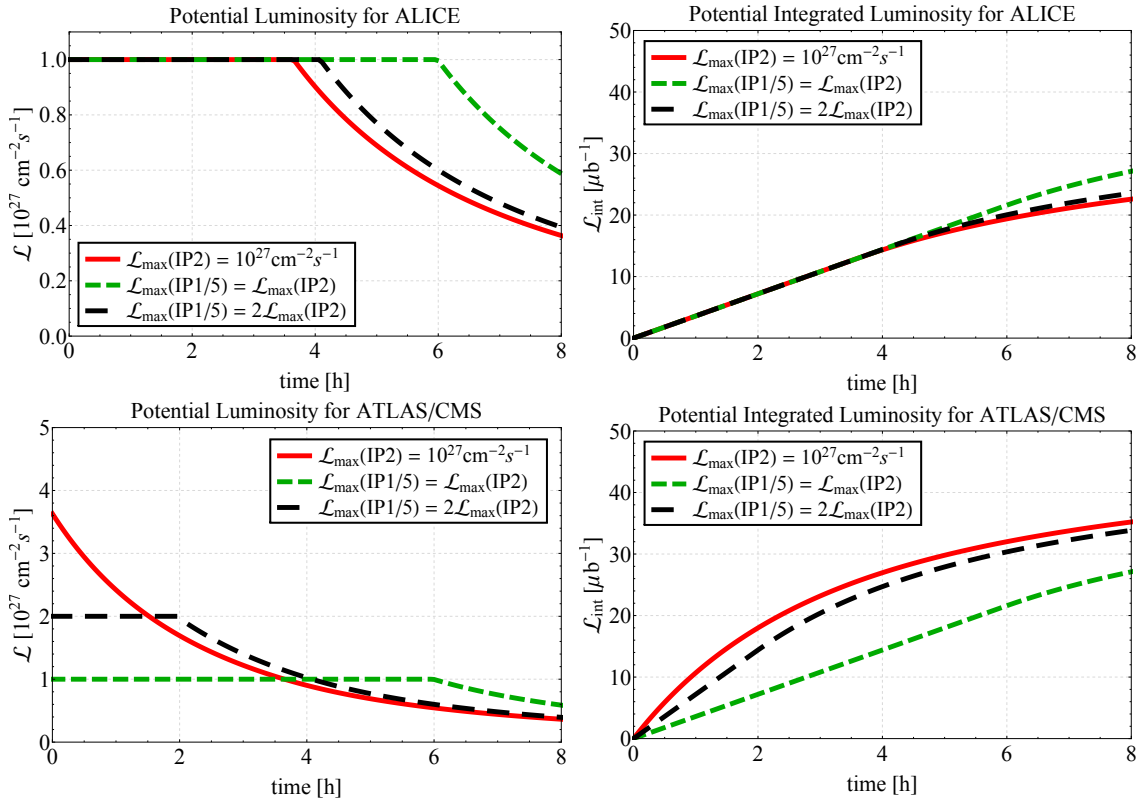

Figure 6.4.: Instantaneous (left) and integrated (right) luminosity evolution in ALICE (top) and ATLAS/CMS (bottom) for different number of experiments levelled. Initial parameters are listed in Table 6.3.

should be considered to mitigate the intrinsic disadvantage of ALICE. Restricting all experiments to the same $\mathcal{L}_{max}$, as shown in green, would provide a fair-share solution, but reduce the integrated luminosity for ATLAS and CMS by about 1/3 in 6 h, while the gain for ALICE in same time is small. Only for longer fills, it becomes more important. Note that, as seen in the previous section, the analytic equations predict a slightly too long levelling duration, therefore it becomes even more important for ALICE to reduce the peak rates for the other experiments.

Another approach could be to level IP1/5 to a intermediate value, e.g. twice the limit of IP2 (black), to prolong the levelling period, but without too strong restrictions for the two multi-purpose detectors. Alternatively, β^* could be set to a higher value in IP1/5 compared to IP2.

If ALICE has significantly fallen behind the other experiments in terms of collected data, a private fill, where the beams only collide in IP2, could be considered.

6.4. HL-LHC Era: Run 3 and beyond

6.4.1. Single Bunch Evolution at $7Z$ TeV

Bunches with different beam parameters will evolve differently, due to the dependence of IBS on the beam parameters themselves and because of the different event production rates in collisions. The spread of the initial beam parameters originates at the SPS and LHC flat bottom. This leads to a variety of single bunch evolution curves within the beam. Figure 6.5 shows the simulated evolution of three typical bunches from the head, middle and tail of a train in Pb-Pb collisions at $7Z$ TeV with 3 experiments taking data. In each simulation run, two initially equal bunches are tracked with CTE, assuming no transverse coupling.

At this energy the radiation damping is already strong enough to partly counteract the IBS, which leads to only a slow emittances growth in the horizontal plane, while the bunch length and vertical emittance are even slowly damped. The very rapid intensity burn-off, due to the high collision rates, halves the intensity of the most intense bunches after only 2 h, leading to a luminosity half-life of less than 1 h for these bunches. However, bunches featuring such high N_b are rare and the major contribution to the overall luminosity outcome is provided by the bunches of average and lower intensity, as discussed in Chapter 4.1.3.

6.4.2. Estimates using the Full Luminosity Model

The luminosity upgrade of the ALICE detector is going to be installed in LS2, removing the constraints on the peak luminosity, so that levelling will no longer be necessary. As introduced at the beginning of this chapter, several potential upgrades in the injector chain are foreseen, resulting in several potential injection schemes providing different numbers of bunches with varying properties. The estimates shown in this section are calculated with the luminosity and intensity model derived in Eq. (5.10) and (5.29), respectively, for a beam energy of 7 TeV. Using these models implies that the bunch properties as observed in the 2011 Pb-Pb run are assumed. Potential differences in the beam shape and conditions, arising from the new techniques to produce the beam in the injectors, most importantly bunch splitting and slip stacking, are *not* taken into account. Only the bunch intensity can be scaled linearly as described in Chapter 5.1. The intensity scaling factors are taken from Table 6.2; for the scenarios with unsplit bunches (2 bunches per batch) $F_{\mathrm{Nb}} = 1.33$ and for split bunches (4 bunches per batch) $F_{\mathrm{Nb}} = 0.92$ is used.

Figure 6.6 compares the 100/100 ns scenario (Table 6.1, SPS kicker) with the full upgrade, providing a 50/50 ns spacing. On the left, a scan of the total peak luminosity and intensity is shown as a function of the number of PS-batches per SPS train. The maximum peak luminosity for the 100/100 ns scenario evaluates to

$$\mathcal{L} = 5.4 \times 10^{27}\,\mathrm{cm}^{-2}\mathrm{s}^{-1}. \tag{6.48}$$

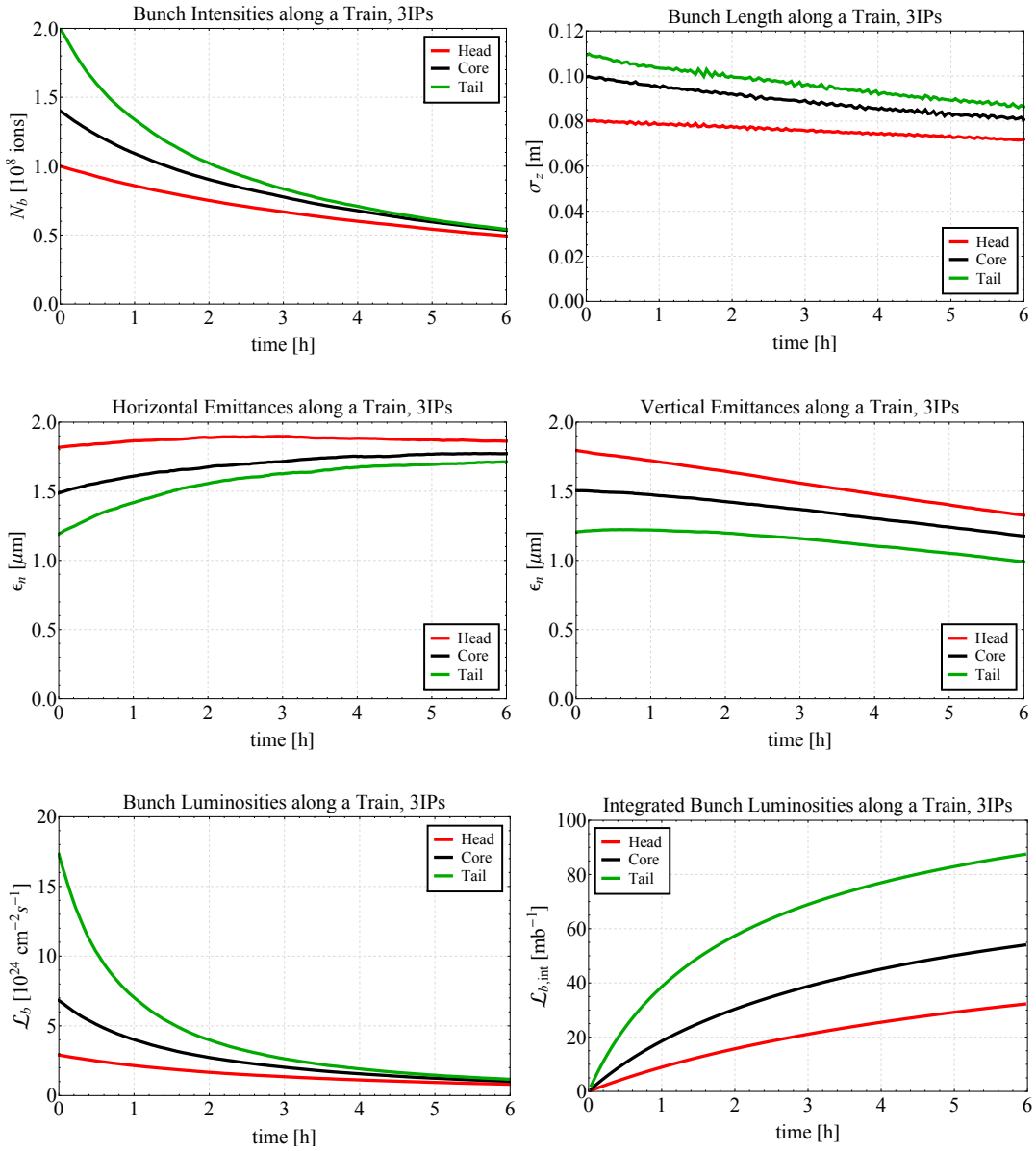

Figure 6.5.: Beam and luminosity evolution for 3 typical bunches at $7Z$ TeV with 3 IPs in collision. Top: Intensity (left), bunch length (right), middle: horizontal (left) and vertical (right) emittance, bottom: instantaneous (left) and integrated (right) bunch luminosity.

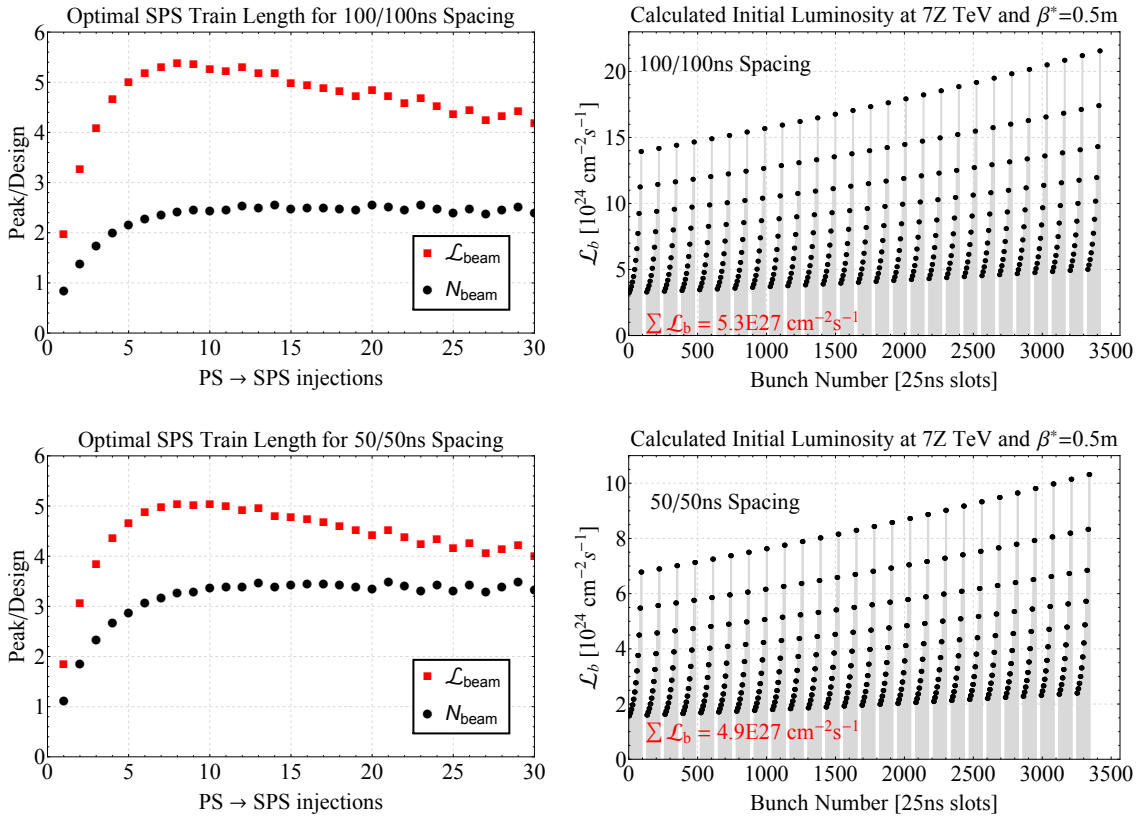

Figure 6.6.: Left: Optimisation of the SPS train length calculated with Eq. (5.10) for the 100/100 ns (top) and 50/50 ns (bottom) spacing options. Right: Bunch-by-bunch peak luminosities for the corresponding schemes using 12 PS-batches per SPS train.

If the 2011 intensity performance ($F_{\mathrm{Nb}} = 1$) is assumed the peak would be at $\mathcal{L} = 4 \times 10^{27}\,\mathrm{cm}^{-2}\mathrm{s}^{-1}$. The filling scheme calculated to deliver the highest peak luminosity uses 8 PS-batches per train and 36 trains per beam. The maximum peak luminosity for the full upgrade, obtained with 8 PS-batches and 35 trains per beam, is $\mathcal{L} = 5.1 \times 10^{27}\,\mathrm{cm}^{-2}\mathrm{s}^{-1}$, slightly below the 100/100 ns scheme. However, the total beam intensity is enhanced by almost 40%. This is possible, because the 50/50 ns scheme provides about twice as many bunches, with an average single bunch intensity of more than half of the unsplit case. Remember that an increased LEIR performance is assumed for split bunch scenarios with 4-bunch-PS-batches, but for unsplit 2-bunch-PS-batches the current injector performance is used.

Since the integrated luminosity is defined by the total beam intensity rather than the peak luminosity, the filling scheme delivering the maximum beam intensity is believed to be the optimal choice for operation. In case of the 100/100 ns scheme, 12 PS-batches and 27 trains give numerically the maximum $N = 1.05 \times 10^{11}$ ions/beam, while the full upgrade requires 13 PS-batches and 25 trains per beam to achieve $N = 1.44 \times 10^{11}$ ions/beam. Note that the 2011 trains consisted of 12 PS-batches, which seems to

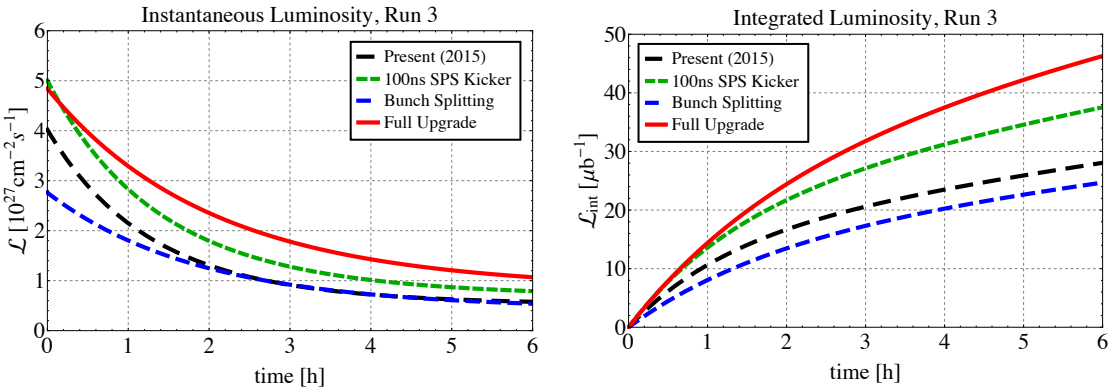

Figure 6.7.: Expected instantaneous (left) and integrated (right) luminosity evolution for the upgrade options listed in Table 6.1.

be close to the optimal length for maximising the total beam intensity. Comparing the left plots of Fig. 6.6 and Fig. 6.2 shows that independent of the filling scheme, the beam intensity arrives at a rather constant plateau for trains built of ∼8 or more PS-Batches. For longer trains, the increase in N is small, but less time is needed to accumulate the whole LHC filling, however the risk to lose a train due to a missing PS-batch increases. Therefore, the compromise of 12 PS-batches seems to be a good choice.

The right plots of Fig. 6.6 show the bunch-by-bunch luminosities for the 100/100 ns (top) and 50/50 ns (bottom) schemes for 12 PS-batches per train and the corresponding maximum number of trains per beam. The two plots look very similar at first sight but, because of the smaller single bunch intensities, the single bunch peaks on the bottom are about half of the ones in the top plot. Each black dot indicates a full PS-batch, which in the bottom plot consists of 4 instead of only 2 bunches. The 4-bunch-PS-batch trains are 50 ns longer (from the bucket of the first to the bucket of the last bunch) compared to the 2-bunch-PS-batch trains, moreover these filling schemes are not optimised for operation, therefore the 50/50 ns scheme features one train less.

The above indicates that a higher integrated luminosity can be expected from the 50/50 ns scenario, as can also be verified from the luminosity evolution plotted in Fig. 6.7. The 100/100 ns case (green dashed line) starts with a little higher peak luminosity, but decays faster due to its higher single bunch intensities compared to the 50/50 ns case (red solid line), which gives more integrated luminosity already after approximately 1 h in collision. Additionally, Figure 6.7 shows the luminosity evolution for the present filling scheme with 100/225 ns spacing and 2013 beam performance in black. The blue curve assumes the same spacings as the black, but because of the smaller single bunch intensities after the splitting, the peak and integrated luminosity are reduced.

Figures 6.8 shows the maximum beam intensity (top left) achievable with the different upgrade stages of Table 6.1 as a function of the SPS kicker rise time. The peak (bottom

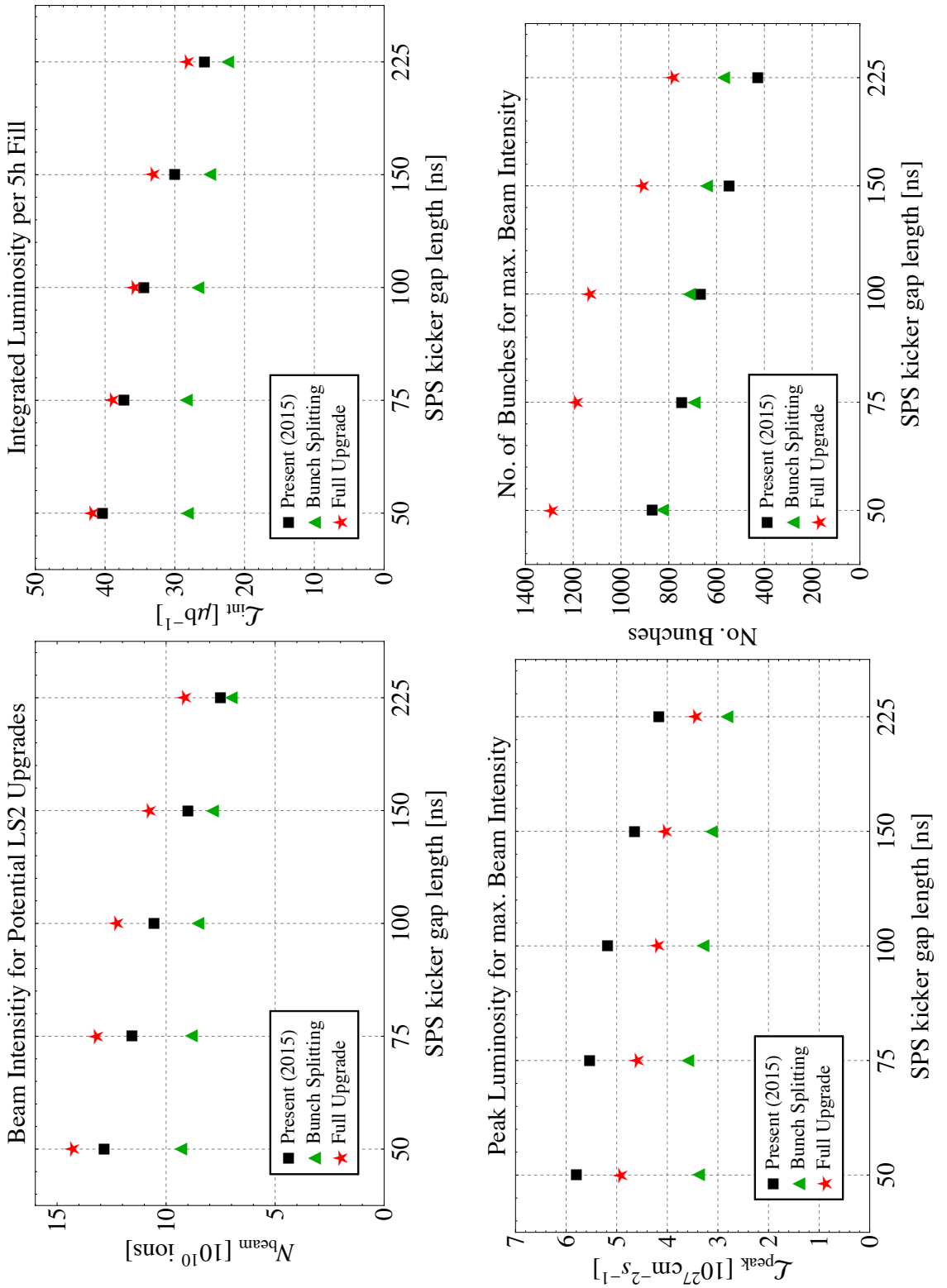

Figure 6.8.: Expected maximum beam intensity (top left) and corresponding peak (bottom left) and integrated (top right) luminosity, and number of bunches (bottom right) for several potential upgrade scenarios for after LS2. The values for the optimal combination of number of bunches per PS-batch and batches per train, delivering the highest beam intensity are shown.

left) and integrated (after 5 h, top right) luminosity and the number of bunches per beam (bottom right) are calculated corresponding to the peak intensity. The scenarios assuming 40% more intensity from LEIR and bunch splitting are displayed as the red stars and green triangles. The difference between the two is the bunch spacing within former PS-batches; the red stars use 50 ns and the green triangles 100 ns. For smaller bunch spacings, the total number of bunches and thus the total beam intensity is significantly enhanced. The full upgrade scenario of Table 6.1 provides the highest beam intensity and integrated luminosity with the largest number of bunches per beam (red star in the upper left corners of the plots). In this case, a bunch spacing of 50 ns is obtained by a batch compression to 100 ns spacing after the splitting in the PS, a 100 ns SPS kicker and slip stacking in the SPS. The difference between the green triangles and the black squares, which use the same spacings (the filling scheme are slightly different because of the different optimisation), arises because of the higher single bunch intensities without splitting.

These predictions were made based on the particle losses in the SPS as observed in 2011. The bunch intensities of 2011 and 2013 were at the limit in terms of space charge and IBS, leading to a fast decay. For smaller bunch intensities, as would be the case for split bunches, these curves would be flatter and more of the original intensity could be conserved until the LHC. This could lead to an improvement of bunch intensities, and thus the luminosity, in scenarios applying bunch splitting compared to the presented results. This would further increase the advantages of the full upgrade with respect to the present scheme.

Integrated Luminosity per Run

The expected amount of integrated luminosity per run can be estimated in two ways. First, by taking the product of the integrated luminosity of an average fill times the expected number of fills per run. And secondly, by the fraction of the average integrated luminosity per fill in the previous run over the maximum achieved peak luminosity over all fills:

$$H = \frac{\mathcal{L}_{\text{int run, average}}}{\mathcal{L}_{\text{peak, max}}} = \frac{\mathcal{L}_{\text{int total, run}}/t_{\text{run}}}{\mathcal{L}_{\text{peak, max}}}. \tag{6.49}$$

The average integrated luminosity can be estimated as the fraction of the total integrated luminosity in the whole run over the length of the run. Empirically it was found that $H = \text{const.}$, leading to the total integrated luminosity for a run with a given peak luminosity and length. The factor achieved in the 2011 Pb-Pb run was about $H \approx 160\,\mu\text{b}^{-1}/(29\,\text{d}\ 0.5\,\text{Hz.mb}^{-1}) \approx 0.13\,\text{s}^{-1}$.

Summary

Table 6.4 summarizes the results for the different upgrade options. Values for the peak and integrated luminosity per fill are given. The expected integrated run luminosity is calculated with Eq. (6.49) and under the assumption of 30 fills of 5 hours. Also

Scenario	$\mathcal{L}_{\mathbf{peak}}$ [Hz/mb]	$\mathcal{L}_{\mathbf{int}}$ **after 3h** [μb^{-1}]	$\mathcal{L}_{\mathbf{int}}$ **after 5h** [μb^{-1}]	$\mathcal{L}_{\mathbf{int,run}}$ **run with 30×5h** [nb^{-1}]	$\mathcal{L}_{\mathbf{int,run}}$ **from Eq.**(6.49) [nb^{-1}]	**Years to integrate 10 nb^{-1}**
2011	3.2	16	20	0.6	1.0	17
Present (2015)	4.2	21	26	0.8	1.3	13
SPS kicker	5.2	27	35	1.0	1.7	10
Bunch Splitting	2.8	17	23	0.7	0.9	15
Full Upgrade	5.0	32	42	1.3	1.6	8

Table 6.4.: Summary of luminosity estimates for Run 3 and beyond.

the number of years needed to integrate the requested 10 nb^{-1} [16] for the complete upgrade period after LS2, based on the assumption of 30 fills per run, is listed. The numbers for the 200/200 ns filling scheme, as was used in 2011, are given for reference as well.

6.4.3. Dependence on SPS Degradation

The estimates just presented were calculated with the decay curves fitted to the performance of the SPS in 2011. However, as could be seen from Fig. 5.7, the intensity decay was reduced in 2013, leading to a higher N_b conserved until injection in the LHC and thus a higher potential $\mathcal{L}$. Neither Pb-Pb collisions, nor bunch-by-bunch emittance measurements in the SPS were collected in 2013, hence a luminosity degradation curve under the improved conditions is not available. Nevertheless, a rough estimate of the potential luminosity improvement for the better SPS performance can be based on the measured N_b degradation. The N_b and $\mathcal{L}_b$ are calculated for the 2011 filling scheme with Eq. (5.29) and (5.10), using the fit parameters given in Table 5.1, for both the 2011 and 2013 performance. The intensity scaling factors, F_{Nb}, are adjusted such that the maximum bunch intensities of both years are equal to the 2013 value. Like this, the decay in the SPS can be studied separately from N_b extracted from LEIR.

There is an uncertainty introduced by the dependence of the degradation curve on the actual beam parameters, which is a known issue of the model. However, increasing the slope of 2011, to take account for the higher N_b, would lead to worse estimates since, after the improvements of 2013, higher bunch brightnesses can be achieved in combination with a slower degradation.

The relative difference

$$\frac{\Delta U}{U} = \frac{U_{2013} - U_{2011}}{U_{2011}} \tag{6.50}$$

with U being either N_b or $\mathcal{L}_b$, between the years is determined for each bunch with respect to 2011. The maximum and mean values with the corresponding standard

	$\frac{N_{2013}-N_{2011}}{N_{2011}}$	$\frac{N_{2013}^2-N_{2011}^2}{N_{2011}^2}$	$\frac{AN_{2013}^2-\mathcal{L}_{2011}}{\mathcal{L}_{2011}}$	$\frac{AN_{2011}^2-\mathcal{L}_{2011}}{\mathcal{L}_{2011}}$
Mean	0.08	0.14	0.29	0.13
RMS	0.03	0.08	0.18	0.09
Maximum	0.11	0.24	0.57	0.27

Table 6.5.: Potential improvement of luminosity estimates with 2013 SPS performance. $A = f_{\mathrm{rev}}\gamma/(4\pi\beta^*\epsilon_n)$, where ϵ_n was chosen such $\mathcal{L}_b$of the bunch with maximum $N_b$determined with the 2011 intensity and luminosity model are equal.

deviation can be found in Table 6.5. The best agreement (zero relative difference) is by construction found for the bunch with the maximum N_b, while the discrepancy increases towards the head of the train. Table 6.5 shows that the relative differences of N_b had improved on average by around 8%, while N_b^2 increased by 14% between the years. N_b^2 is an important parameter, since in the approximation of constant emittances it is a measure of the luminosity.

Investigating $(AN_{2011}^2 - \mathcal{L}_{2011})/\mathcal{L}_{2011}$, with $A = f_{\mathrm{rev}}\gamma/(4\pi\beta^*\epsilon_n)$, approximates the contribution of the emittance blow-up in the SPS to the peak luminosity. The contribution of the emittance growth at the LHC injection plateau was discussed in Chapter 5.2.5 and is taken into account by introducing a factor $\exp[-\alpha_{\mathrm{IBS,LHC}}\ (l_{\mathrm{LHC}}\ n_{\mathrm{tr}})]$ in Eq. (5.29) before calculating N_b. The IBS emittance growth rate, $\alpha_{\mathrm{IBS,LHC}}$, is assumed for average N_b at $E_b = 450Z\,\mathrm{GeV}$ in the LHC. If the emittance blow-up in the SPS was small, $AN_{2011}^2 \approx \mathcal{L}_{2011}$, however a relative error of around 13% is found by assuming constant emittance. This error has to be subtracted when the luminosity performance is approximated by computing $(AN_{2013}^2 - \mathcal{L}_{2011})/\mathcal{L}_{2011}$. The result is in agreement with the one obtained for N_b^2 and approximates that the luminosity could be increased by potentially about 15%, using the improved SPS degradation curve of 2013 for the model calculations. The same study using the filling scheme for the full upgrade scenario gives compatible results.

6.4.4. Increasing Luminosity by Running Off-Momentum

The Robinson criterion of Eq. (2.49) states that the sum of the damping partition numbers is a constant. However, the distribution between them can be changed by displacing the particle orbit transversely, which is done in operation by varying the RF frequency, f_{RF}. The corresponding momentum change is $\delta \equiv \frac{\Delta p}{p} = -\frac{1}{\eta}\frac{\Delta f_{\mathrm{RF}}}{f_{\mathrm{RF}}}$, where $\eta = \frac{1}{\gamma_T^2} - \frac{1}{\gamma^2}$ is the slip factor. In case of an off-momentum orbit, the quadrupoles also act as dipoles. This dipole component from the quadrupoles has to be added to $\mathcal{I}_{4,xy}$ given by Eqs. (2.51) and (2.52), using $\kappa_x = (kD_x + \underline{k}D_y)\delta$ and $\kappa_y = (-\underline{k}D_x + kD_y)\delta$ [38], where k and $\underline{k}$ are normal and skew quadrupole strengths, respectively, and D_{xy}

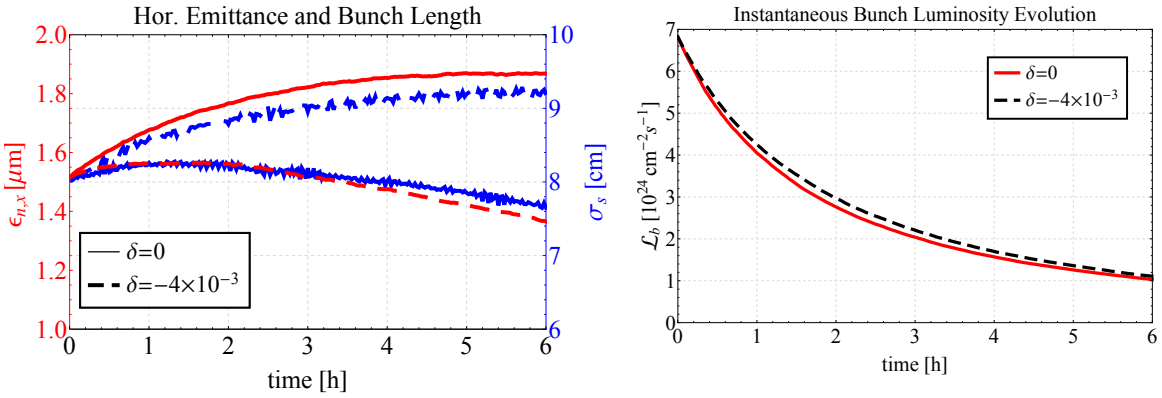

Figure 6.9.: CTE simulated effect on longitudinal and transverse damping by running off-momentum. Left: horizontal emittance (red) and bunch length (blue), right: bunch luminosity evolution for a beam circulating on the central orbit, $\delta = 0$ (solid lines), and off-momentum orbit, $\delta = -4 \times 10^{-3}$ (dashed lines).

the dispersion. The change in $\mathcal{I}_{4u}$ is with $u = x, y$

$$\Delta\mathcal{I}_{4u} = 2\mathcal{I}_{6u}\delta, \tag{6.51}$$

where $\mathcal{I}_{6u}$ is given by Eqs. (2.53) and (2.54).

According to the definition of the damping partition numbers, J_i, in Eq. (2.48) and the radiation damping rates in Eqs. (2.45) to (2.47), the change in $\mathcal{I}_{4u}$ leads to a variation of the radiation damping rates for the three planes. For a well chosen direction and amount of the momentum shift, the longitudinal damping can thus partly be transferred to the transverse planes, resulting in reduction of the emittances and potentially a higher luminosity.

Running on an off-momentum orbit in the LHC is necessary in p-Pb operation to equalise the revolution frequencies of the two species and collide in the experiments. Therefore, this procedure is already established and could be used in Pb-Pb operation to enhance the luminosity.

To estimate the maximum benefit on the transverse emittance a CTE simulation with a very large $\delta = -4 \times 10^{-3}$ is compared to $\delta = 0$. For comparison, during the 2013 p-Pb run the relative momentum deviation was $\delta = \pm 2.3 \times 10^{-4}$ at $4Z$ TeV for p and Pb respectively, generating a maximum horizontal offset of the central trajectory of 0.5 mm. Figure 6.9 shows the results of the two simulation runs. The assumed δ almost exchanges the horizontal and longitudinal damping times, decreasing the horizontal and vertical emittance, but increasing the bunch length, as desired. However, the effect on the luminosity (right) is marginal.

Since implementing off-momentum orbits in the LHC takes additional commissioning

time from the already short total run time, it is believed that the small potential gain in luminosity is not worth the effort.

7. Secondary Beams Emerging from the Collisions

An introduction and the background to the secondary beams emerging the collisions is given in Chapter 2.5.4. This chapter covers an analysis of the secondary beam losses during Pb-Pb operation in 2011, as well as the analysis of an end-of-fill experiment testing the bump mitigation technique in IR5. Moreover, potential collimator locations, the integration in the LHC lattice and a formalism to track a secondary beam distribution from the IP to the impact in the beam screen are discussed.

As shown, the BFPP1 beam is the most dangerous, therefore all countermeasures presented here focus on this beam, but most of the considerations are applicable for the other beams mentioned.

7.1. Impact Distributions

To evaluate the quench potential of the secondary beam ions, their impact distribution has to be calculated. Their fragmentation and energy deposition in the magnet coil and cold mass should then be studied with FLUKA [70]. FLUKA simulations are performed by a team of specialists [111] and will not be discussed here. This section only describes how to calculates the beam distribution impacting in the aperture, which is required as FLUKA simulation input, but is also interesting for general considerations (see Section 7.3).

7.1.1. Particle Distribution at the IP

Because the BFPP particles are generated in the collision, their distribution is given by the luminosity density in phase space, which differs from the phase space distribution of the $^{208}Pb^{82+}$ ions in the colliding bunches. Assuming zero periodic dispersion and head-on collision between identical Gaussian bunches at an IP, the transverse BFPP ion distribution is given by [66]

$$\rho(u,u') = \frac{\beta^*}{\sqrt{2}\pi\sigma^{*2}} e^{\frac{-2u^2-(\alpha^* u+\beta^* u')^2}{2\sigma^{*2}}}, \tag{7.1}$$

where u is the position and u' the angle coordinate, with $u = x, y$. The beam size of the colliding main bunches at the IP is given by $\sigma^* = \sqrt{\beta^*\epsilon}$. β^* and α^* are the lattice

functions at the IP and ϵ is the geometric emittance.

The integration $\rho(u, u')$ over u' in the full range gives the projection to the u-axis

$$\rho(u) = \frac{1}{\sqrt{\pi}\sigma^*} e^{\frac{-u^2}{\sigma^{*2}}}. \tag{7.2}$$

This equation describes a Gaussian distribution with a standard deviation of

$$\sigma_u = \frac{\sigma^*}{\sqrt{2}}, \tag{7.3}$$

implying that the BFPP beam is a factor $1/\sqrt{2}$ narrower than the original main beam distribution. Accordingly, it follows for the projection on the u' axis

$$\rho(u') = \frac{\beta^*}{\sqrt{\pi(2+\alpha^{*2})}\sigma^*} e^{\frac{-u'^2\beta^{*2}}{\sigma^{*2}(2+\alpha^{*2})}} \tag{7.4}$$

with a standard deviation of

$$\sigma_{u'} = \sqrt{\frac{(2+\alpha^{*2})}{2\beta^{*2}}}\sigma^*. \tag{7.5}$$

As can be seen from Eq. (7.1), the u and u' coordinates of single particles, i, are correlated. To take account for this correlation, u_i values should be generated randomly according to Eq. (7.2) and inserted into Eq. (7.1). This produces $\rho_i(u_i, u')$ distributions, describing values of u' for a given u_i. Random generation of one u'_i, using the $\rho_i(u_i, u')$ for each u_i, obtains the desired correlated coordinate pairs (u_i, u'_i).

The momentum and longitudinal position distribution of the BFPP beam has the same shape and standard deviation as the main beam and will be approximated as Gaussian in the following.

7.1.2. Optical Tracking

Transfer Matrices

The change of horizontal particle coordinates inside certain lattice elements can be calculated via

$$\begin{pmatrix} x_1 \\ x'_1 \\ \delta \end{pmatrix} = \mathbf{M} \cdot \begin{pmatrix} x_0 \\ x'_0 \\ \delta \end{pmatrix}, \tag{7.6}$$

where (x_0, x'_0, δ) are the position, angle and relative momentum deviation (given by Eq. 2.66) of the particle at the entrance of the element, whose effect on the particle's coordinates is described by the transfer matrix $\mathbf{M}$. The new coordinates at the exit

of this element are (x_1, x_1', δ). The transformation of the vertical coordinates follows accordingly. The transfer matrices describing the evolution of the trajectory vector from the start of a dipole, a quadrupole and a drift space to a point s within the element are given by [37]

$$\mathbf{M}_{\text{dipole}} = \begin{pmatrix} \cos(\frac{s}{R}) & R\sin(\frac{s}{R}) & R(1-\cos(\frac{s}{R})) \\ -\frac{1}{R}\sin(\frac{s}{R}) & \cos(\frac{s}{R}) & \sin(\frac{s}{R}) \\ 0 & 0 & 1 \end{pmatrix} \tag{7.7}$$

$$\mathbf{M}_{\text{QF}} = \begin{pmatrix} \cos(\sqrt{|k|}s) & \frac{1}{\sqrt{|k|}}\sin(\sqrt{|k|}s) & 0 \\ -\sqrt{k}\sin(\sqrt{|k|}s) & \cos(\sqrt{|k|}s) & 0 \\ 0 & 0 & 1 \end{pmatrix} \tag{7.8}$$

$$\mathbf{M}_{\text{QD}} = \begin{pmatrix} \cosh(\sqrt{k}s) & \frac{1}{\sqrt{k}}\sinh(\sqrt{k}s) & 0 \\ \sqrt{k}\sinh(\sqrt{k}s) & \cosh(\sqrt{k}s) & 0 \\ 0 & 0 & 1 \end{pmatrix} \tag{7.9}$$

$$\mathbf{M}_{\text{drift}} = \begin{pmatrix} 1 & s & 0 \\ 0 & 1 & 0 \\ 0 & 0 & 1 \end{pmatrix}. \tag{7.10}$$

the bending radius of the dipole is R and k is the strength of the quadrupole. Every quadrupole focuses (QF, $k < 0$) in one, but defocuses (QD, $k > 0$) in the other plane. A horizontally bending dipole acts as a drift space in the vertical plane. In case the transfer through an element of length L should be calculated: $s = L$. A detailed description can for example be found in Ref. [35].

A transfer through a sequence of n elements (including drifts) is described by the matrix product of the single element matrices:

$$\mathbf{M}_{\text{seq}} = \mathbf{M}_n \cdot \mathbf{M}_{n-1} \cdot \ldots \cdot \mathbf{M}_2 \cdot \mathbf{M}_1, \tag{7.11}$$

where M_1 describes the transfer through the first element at whose entrance the particle coordinates (x_0, x_0', δ) are known.

Because of the high number of elements in the LHC, it is convenient to extract $\mathbf{M}_{\text{seq}}$ from MADX. To correctly treat the dispersive trajectories of the BFPP ions, a MADX *TWISS* calculation [41], starting from the initial conditions at the IP and using a *DELTAP* = δ_0, obtained by Eq. (2.66) with $\delta_p = 0$, should be performed. The single particle coordinates generated according to Eq. (7.1) in the IP, can now be tracked to the entrance of the element in which they will impact, using Eq. (7.6) and $\mathbf{M}_{\text{seq}}$ obtained by MADX.

Beam Matrix Tracking

In order to obtain single particle coordinates at a certain element, it is convenient to make use of the statistical properties of a particle ensemble and only track the

beam envelope created at the IP. In this way, single particle coordinates are generated according to the expected distribution at the last element.

The evolution of the phase ellipse along a beam transport line is given by [35]

$$\boldsymbol{\sigma}_1 = \mathbf{M} \cdot \boldsymbol{\sigma}_0 \cdot \mathbf{M}^T \tag{7.12}$$

with $\mathbf{M}^T$ as the transpose of the transfer matrix $\mathbf{M}$. $\boldsymbol{\sigma}$ is the so-called beam or $\boldsymbol{\sigma}$-matrix at the starting (0) and end (1) point of the sequence. In a two-dimensional phase space and assuming a Gaussian beam distribution the $\boldsymbol{\sigma}$-matrix is given by [35]

$$\boldsymbol{\sigma}_u = \begin{pmatrix} \langle u^2 \rangle & \langle uu' \rangle \\ \langle uu' \rangle & \langle u'^2 \rangle \end{pmatrix} = \epsilon \begin{pmatrix} \beta & -\alpha \\ -\alpha & \gamma \end{pmatrix}, \tag{7.13}$$

where the $\langle\rangle$ indicate the expectation value of the bracketed quantity. ϵ is the geometric emittance and β, $\alpha = -\beta'/2$ and $\gamma = (1+\alpha^2)/\beta$ are the lattice functions. Equation (7.13) is valid for each transverse plane. For the considerations made in this chapter, the longitudinal positions inside the bunch are not important. Nevertheless, the single particle momentum deviation has to be taken into account, because it leads to a divergent path. The $\boldsymbol{\sigma}$-matrix of the longitudinal plane simplifies to

$$\boldsymbol{\sigma}_l = \begin{pmatrix} 0 & 0 \\ 0 & \sigma_p^2 \end{pmatrix}, \tag{7.14}$$

where here $\sigma_p = \sqrt{\langle (\Delta p/p)^2 \rangle}$ describes the relative momentum spread of the main beam.

The 6D $\boldsymbol{\sigma}$-matrix describing the secondary beams at the IP is given by

$$\boldsymbol{\sigma}_{\mathrm{BFPP}} = \begin{pmatrix} \frac{\epsilon\beta_x^*}{2} & -\frac{\alpha_x^*\epsilon}{2} & 0 & 0 & 0 & 0 \\ -\frac{\alpha_x^*\epsilon}{2} & \frac{(2+\alpha_x^{*2})\epsilon}{2\beta_x^*} & 0 & 0 & 0 & 0 \\ 0 & 0 & \frac{\epsilon\beta_y^*}{2} & -\frac{\alpha_y^*\epsilon}{2} & 0 & 0 \\ 0 & 0 & -\frac{\alpha_y^*\epsilon}{2} & \frac{(2+\alpha_y^{*2})\epsilon}{2\beta_y^*} & 0 & 0 \\ 0 & 0 & 0 & 0 & 0 & 0 \\ 0 & 0 & 0 & 0 & 0 & \sigma_p^2 \end{pmatrix}. \tag{7.15}$$

The expectation values of Eq. (7.13) were determined via [112]

$$\langle g(v) \rangle = \int_{-\infty}^{\infty} g(v)\rho(u,u')dudu' \tag{7.16}$$

with $v = u, u'$ and $\rho(u,u')$ given by Eq. (7.1). The $\boldsymbol{\sigma}_{\mathrm{BFPP}}$-matrix at the IP is tracked as

$$\boldsymbol{\sigma} = \mathbf{M}_{\mathrm{seq}} \cdot \boldsymbol{\sigma}_{\mathrm{BFPP}} \cdot \mathbf{M}_{\mathrm{seq}}^T \tag{7.17}$$

to the front plane of the magnet of impact. Normal distributed random numbers for x, x', y, y' and δ are generated with the standard deviations given by the square roots of the matrix elements σ_{11}, σ_{22}, σ_{33}, σ_{44} and σ_{66} of the transferred matrix in Eq. (7.17). To obtain the impact distribution on the beam screen, all particles are tracked individually with Eq. 7.6, starting from the front plane of the element of impact.

Tracking inside the Element of Impact

For the distance travelled inside the last element, a corresponding matrix with $s < L$ has to be used. Depending on the initial conditions, the exact impact position s will be different for each particle. A scan over s in the last element could be performed to find the last value before $x_1 > A_x$. This technique is slow, since for one particle many matrix operations, proportional to the step size Δs, have to be calculated.

An analytic determination of the impact position s_{impact} is more practical and accurate. The shape of the beam screen is the intersection of an ellipse by a rectangle (see Fig. 12.1 in [40]). In a dipole, the ellipse's axes are equal, thus it is a circle with the radius $r_{\text{bs}} = 22\,\text{mm}$, while the interception by the rectangle is orthogonal to the y-axis of the particle's coordinate system. The round shape of the beam screen leads to $x_{\text{max}} = A_x < r_{\text{bs}}$ for $y_0 \neq 0$. In general, the orbit should fulfil $x = y = 0$ at the IP and since y is not affected by dipoles, the y_0 coordinates of the BFPP ions are distributed around $y = 0$. The rectangular interception at $A_y = 17.15\,\text{mm} < r_{\text{bs}}$ will be neglected in this calculation, because the beam size is small compared to the beam pipe radius.

The particle's trajectory, depending on its initial conditions, is given by Eq. (7.6). To find s_{impact}, the interception point of the particle's trajectory with the cylinder describing the beam screen, $r_{\text{bs}}^2 = A_x^2 + y_0^2$, is to be determined by using the condition $x_1 = A_x$. Thus, for each particle the equation

$$\sqrt{r_{\text{bs}}^2 - y_0^2} = M_{11}(s)x_0 + M_{12}(s)x_0' + M_{13}(s)\delta \tag{7.18}$$

has to be solved for s. The y_0' coordinate does not influence s_{impact}, but only the y-width of the distribution on beam screen. The obtained $s_{\text{impact},i}$ are then inserted in Eq. (7.6) to calculated the 6D coordinates. The techniques developed will be applied in Section 7.3 and 7.4.

7.2. Secondary Beams during Operation

7.2.1. Loss Patterns around the Ring

Three snap-shots of the beam losses measured in 2011 with the Beam Loss Monitors (BLM) installed on both beams around the whole circumference of the LHC are visualised in Fig. 7.1a. All signals are shown on a logarithmic scale and are normalised to the highest peak observed with all experiments in collision, which is the one to the

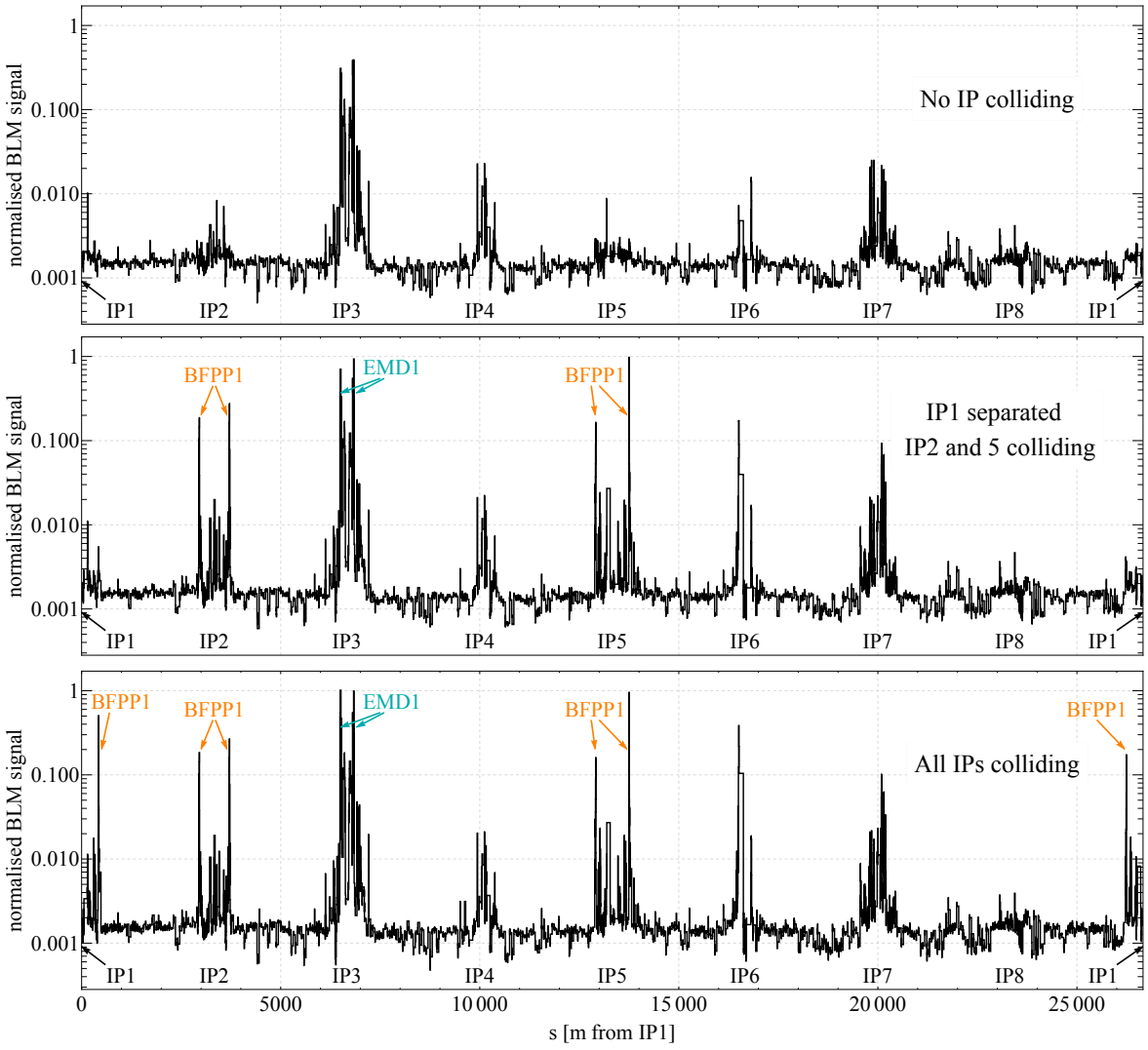

(a) BLM signals for different number of IPs in collision.

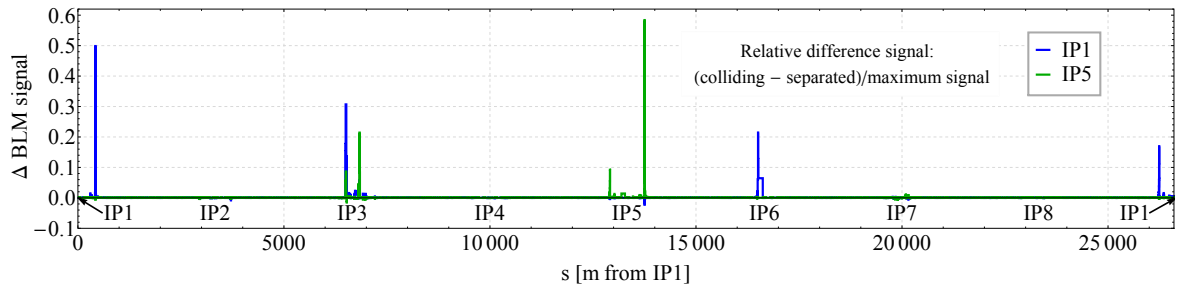

(b) Difference of BLM signals between IP1 or IP5 colliding and separated.

Figure 7.1.: BLM signals as a function of s position around the ring. (a) Top: All IPs separated, no collisions. Middle: IP2, and 5 are colliding, IP1 is separated. Bottom: all three IPs are in collisions. (b) Relative difference in BLM signal due to collisions in IP1 (blue) and IP5 (green).

right of IP5 in the bottom plot.

The data shown in the top plot was measured shortly before the beams were brought into collisions in Fill 2337, the beams were separated in all IPs. Loss peaks appear as foreseen in IR3 and 7, where the momentum and betatron collimation are operating. As was shown in Ref. [113], the small peaks in IR1, 2, 5 and 6 are most probably fragmentation products produced in IR7, which survived the collimation. The origin of the losses in IR4 is still under study. It is probable that these are fragmentation products surviving IR3. A relatively constant but low background signal is present everywhere around the machine.

The middle picture of Fig. 7.1a shows the situation with IP2 and 5 colliding, but IP1 separated. High losses around the two colliding IPs are now observed, featuring a symmetric pattern with two very high peaks to both sides of each IP. These correspond to the BFPP1 beams getting lost in the dispersion suppressor of the outgoing beam. It should be underlined here that these BFPP1 losses are among the highest observed in the whole ring. The height of the peaks is influenced by the position of the BLMs with respect to the secondary beam's impact point. Since the BLMs are not at exactly the same positions to the left and right side of the IPs, different fractions of the total losses are seen. The peaks between the ones identified as BFPP1 arise from other collision debris, which is lost mainly in the dedicated absorbers. The losses in IR3, 7 and 6 increased as well. As will be shown below, the additional losses in IR3 are luminosity correlated and identified as the EMD1 beam. Figure 2.11 shows that the EMD1 beam emerging IP2 does not impact in the DS, but stays on a dispersive orbit parallel to the main beam. The situation for IP1 and 5 is similar. The EMD1 beam lies outside the allowed momentum deviation and is therefore absorbed in the momentum collimation section in IR3.

The bottom plot in Fig. 7.1a shows the situation after IP1 was also brought in collision. This is the standard situation in heavy-ion operation with beams colliding in three experiments. The BFPP1 beam losses around ATLAS become visible at the left and right edges of the plot, while the losses in IR3 and 6 are increased further. Only small differences are observed in IR7.

The locations of collision related losses become more evident if the middle curve (with IP1 separated) is subtracted from the bottom one (all IPs colliding), as shown in the blue line of Figure 7.1b. The green line indicates the relative difference between the standard situation of three colliding IPs and with IP5 separated. Note the linear scale. The the blue curve shows remaining signals only around IR1, 3 and 6, meaning that only here particles produced in collisions in IP1 (or fragments of them) got lost. In case of the green curve, remaining signals are observed in IR5 and 3. The monitors giving the collision related signals in IR6 are all mounted on Beam 2, which travels from the right to the left side of this plot. It is difficult to exactly identify the source or type of the losses observed. Probably those in IR6 are generated by an EMD beam emerging from IP1 together with Beam 2 or fragmentation products of these particles generated in IR7.

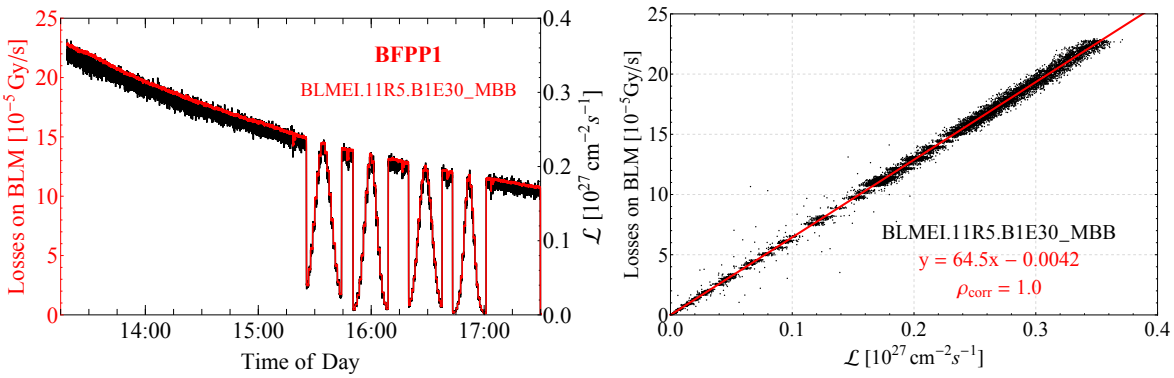

Figure 7.2.: BFPP1 losses in IR5. The data was taken in Fill 2337, VdM scans were performed. Left: CMS online luminosity (black) and BLM signal (red) time evolution, right: BLM data as a function of luminosity (black) and linear fit (red).

7.2.2. Bound-Free Pair-Production Losses

Van der Meer (VdM) scans, are used by the experiments to calibrate the luminosity measurements. In such a scan the beams are separated completely in a given IP, before they are moved slowly through each other, crossing the total overlap, until they are completely separated again with the beams in the opposite positions. During a VdM scan the luminosity, and with it the collision related losses, show rates between zero and maximum, leaving a clear signature that can easily be identified, if plotted as a function of time (see Fig. 7.2). The correlation between luminosity and secondary beam losses is as well present in standard operation, but the BLM measurement is influenced also by losses from other sources, making it more difficult to clearly identify its relation to the luminosity.

The total luminosity evolution measured by CMS (black) during four VdM scans in IP5 in the second half of Fill 2337 is shown in the left plot of Fig. 7.2. The superimposed red line corresponds to the measurement of the BLM called[1] BLMEI.11R5.B1E30_MBB, which showed the highest signal in the DS (cell 11, Beam 1) to the right of IP5. It is installed just behind the expected impact point of the BFPP1 beam. A strong correlation is obvious. The BLM signal plotted as a function of luminosity is a straight line (see right plot of Fig. 7.2, fit shown in red), verifying the correlation.

All BLM signals between IP5 and the end of the outgoing Beam 1 DS are visualised in Fig. 7.3. Time goes along the vertical, the BLM position is displayed on the horizontal axis. The considered signals are rescaled between 0 (no signal) and 1 (highest signal in the considered data set) to fit on the colour scale shown on the right. BLMs are not evenly spaced and only cover fractions of the circumference, leaving large gaps without

[1]for the LHC naming convention see Chapter 2.2.3

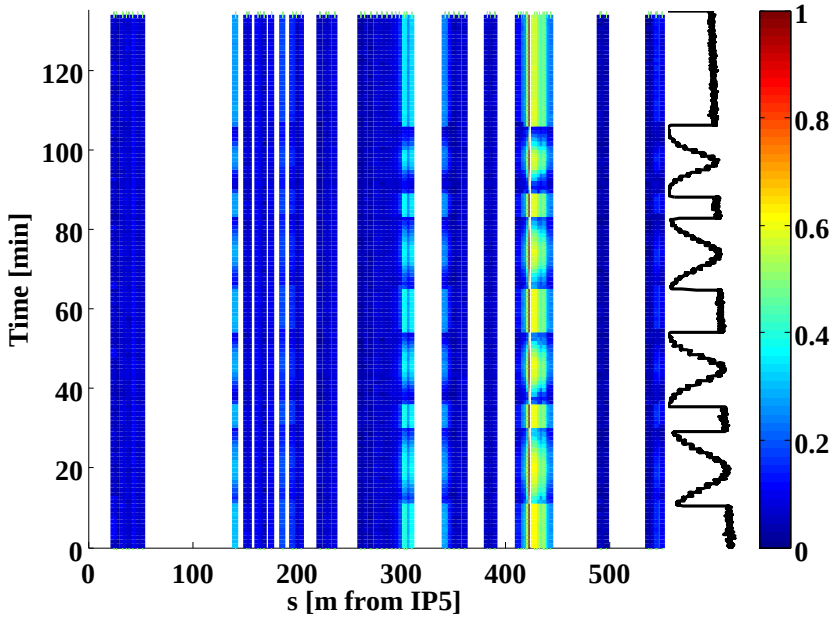

Figure 7.3.: Rescaled BLM signals ([0, 1] = [no, high] measurement, colour weighted) to the right of IP5 during VdM scans in Fill 2337. The total luminosity evolution is indicated along the right vertical axis.

measurement (white). The total luminosity evolution is indicated as the black trace along the vertical axis on the right. Where the BLM signals are high (mainly around $s = 300$ and 420 m), an oscillation according to the change in luminosity can clearly be observed at many BLMs.

To quantify the correlation and to obtain a parameter, which can be used to individually investigate the BLM signal, $\mathcal{D}$, of all monitors with respect to the luminosity, $\mathcal{L}$, the so-called correlation coefficient, ρ_{corr}, is introduced [112]

$$\rho_{\text{corr}} = \frac{\overline{\mathcal{D}\mathcal{L}} - \bar{\mathcal{D}}\bar{\mathcal{L}}}{\sigma_{\mathcal{D}}\sigma_{\mathcal{L}}}, \tag{7.19}$$

where

$$\bar{\mathcal{R}} = \frac{1}{N}\sum_{i=1}^{N}\mathcal{R}_i \qquad \text{and} \qquad \sigma_{\mathcal{R}} = \sqrt{\overline{\mathcal{R}^2} - (\bar{\mathcal{R}})^2} \tag{7.20}$$

with $\mathcal{R} = \mathcal{L}, \mathcal{D}$ or $\mathcal{D}\mathcal{L}$ and i running over consecutive measurements. The range of ρ_{corr} is defined between [0, 1]. Independent data sets are indicated by $\rho_{\text{corr}} = 0$, while $\rho_{\text{corr}} = 1$ suggests full correlation. The correlation between the BLM shown in Fig. 7.2 and the luminosity is visibly very high and ρ_{corr} evaluates to about 1.

The evaluation of ρ_{corr} for all BLMs right of IP5 until the end of the DS is shown

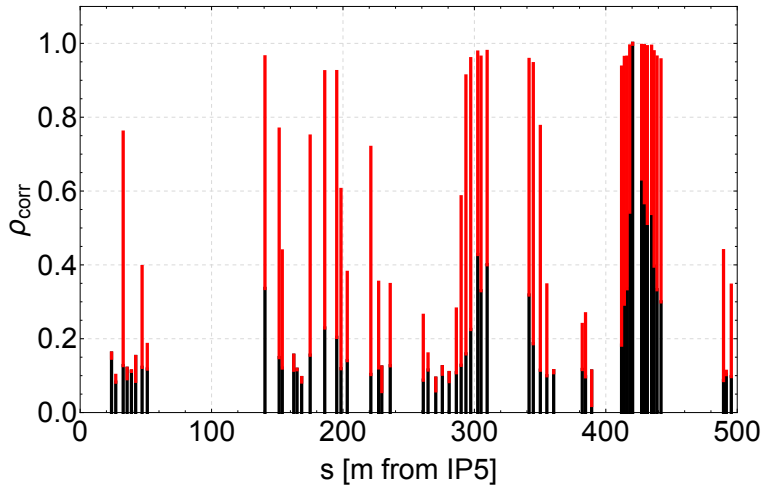

Figure 7.4.: Correlation coefficient, ρ_{corr} (red), between CMS luminosity and BLM signals right of IP5. The black bars show the logarithm of the BLM signals scaled to a range [0, 1] (0 = lowest, 1 = highest BLM signal in the considered data set) shortly before the VdM scans in IP5 were started.

in red in Fig. 7.4. The black bars show the logarithm of $\mathcal{D}$ scaled to a range [0, 1] (0 = lowest, 1 = highest BLM signal in the considered data set) shortly before the VdM scans were started. The locations where high losses are observed, show highly luminosity correlated signals ($\rho_{\text{corr}} \approx 1$), as already seen in Fig. 7.3. The cluster of the peaks around 420 m corresponds to the BFPP1 impact. The second group close to 300 m arises most probably from other collision debris and is observable behind all experiments at approximately the same position. Determining the same quantities for other fills, shows equivalent results.

The BFPP2 beam is not visible in the BLM data. Because of its low cross-section, $\sigma_{\text{BFPP2}} = 6\,\text{mb}$, an event rate of only $dR/dt = \sigma_{\text{BFPP2}}\mathcal{L} \approx 1.5\,\text{Hz}$ is expected at an instantaneous luminosity of $\mathcal{L} = 0.25 \times 10^{27}\,\text{cm}^{-2}\text{s}^{-1}$, as measured shortly before the start of the VdM scans. Compared to the event rate of the BFPP1 beam, $dR/dt \approx 70\,\text{kHz}$, the BFPP2 signal would be more than four orders of magnitude lower and hence hidden in the background (see Fig. 7.1).

7.2.3. Electromagnetic Dissociation Losses

As mentioned in the discussion of Fig. 7.1, the EMD1 beam does not impact closely behind the IPs, but survives until the momentum collimation in IR3. By looking again at the VdM scans done in Fill 2337, first in IP1 and later in IP5, in combination with BLM signals to the left and right of IP3, the EMD losses in IR3 can directly be observed.

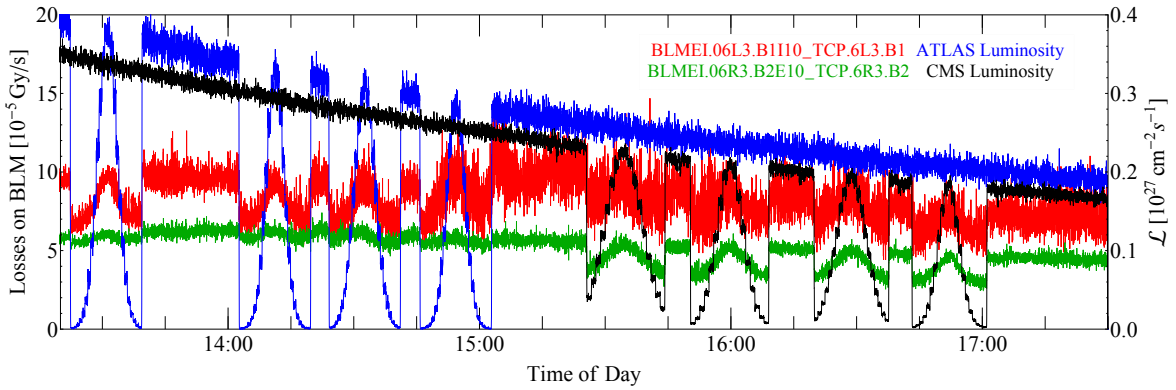

(a) Time evolution of luminosity and BLM signals in IR3.

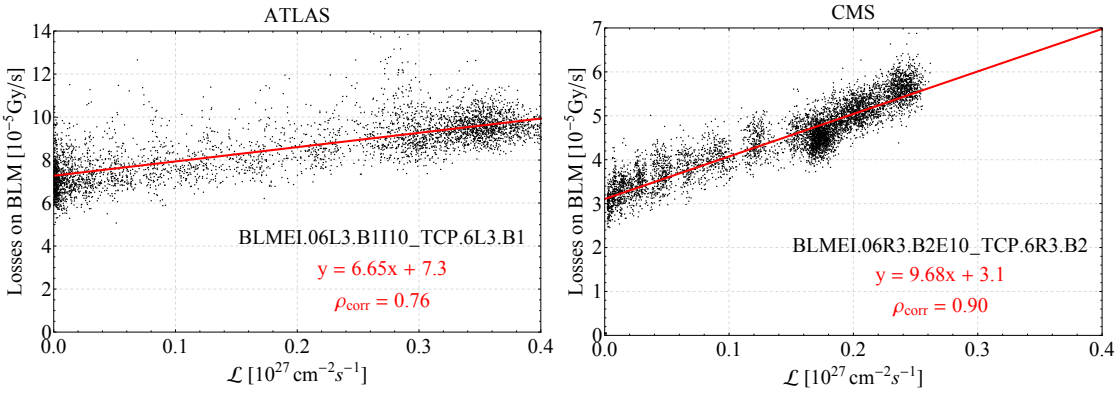

(b) Linear correlation between luminosity and BLM signals in IR3.

Figure 7.5.: EMD1 losses in IR3. (a) Time evolution of luminosity in IP1/5 and the signal at the BLM closest to the primary collimators (TPC) of both beams in IR3. The data was taken in Fill 2337, VdM scans were performed first in IP1 and later in IP5. (b) Correlation between luminosity and the signal of the indicated BLM during the period of the VdM scans in the corresponding experiment.

The evolutions of the ATLAS (blue) and CMS (black) online luminosity is shown in Fig. 7.5a. The VdM scans are clearly visible as the luminosity periodically takes values from zero to its maximum. Also shown are the loss signals measured with two detectors close to the primary collimator (TCP) in IR3. According to the travel direction of the two beams, a Beam 1 monitor was chosen on the left (red) and a Beam 2 monitor on the right (green) of IP3.

The losses measured around IR3 are the sum of the EMD beam and the normal momentum collimation of the main beam. Nevertheless, a clear correlation between the ATLAS luminosity and the BLM installed on the left of IP3 (red) is observable during the VdM scans in IP1. The luminosity signature in the signal of the BLM shown in green is small. A similar structure is present in the second half of the fill during the VdM scans in IP5. Here a strong correlation to the CMS luminosity is observed in the green trace, while the signature is perturbed by other losses in red signal.

The EMD1 beam, emerging from IP1 in direction of Beam 1, has to pass via IR2 through about one quarter of the total circumference before it arrives on the left side of IR3 (compare Fig. 2.4). On the other hand, the EMD1 beam emerging from IP1 in direction of Beam 2 has to pass via IR8 and 5 though about three quarters of the ring before it arrives on the right side of IR3. For the beams emerging from IP5 the path length is shorter for Beam 2. It is easy to understand that the longer the EMD beam travels on an orbit close to the aperture, the more of its intensity is getting lost on the way to IR3. Consequently, the losses measured in IR3 that can be correlated to the luminosity become less evident compared to other losses.

By plotting the measured losses in IR3 as a function of the luminosity, as shown in black in Fig. 7.5b, their dependence can be quantified. The data of the two BLMs discussed above are shown over the period of the VdM scans in the corresponding experiment. Only the monitor closest to the scanned IP is shown. Unlike Fig. 7.2, the linear fits (red) give y-axis intercepts at about half of the maximum signal, which confirms the presences of losses from other sources. The correlation coefficients of $\rho_{\text{corr}} = 0.76$ and 0.9 are reduced compared to the BFPP1 analysis, pointing as well to the disturbances by other losses.

7.3. Bump Mitigation Technique

In 2011, the secondary beams carried not enough energy to cause quenches. After the first long shutdown (LS1) the beam energy will be increased to $E_b = 6.5Z\,\text{TeV}$, a filling pattern with 100/225 ns (see Chapter 6), instead of 200/200 ns as in 2011, is foreseen to fit more bunches into one LHC ring, and as usual it is desired to further raise the single bunch intensity. These improvements are meant to increase the luminosity, but naturally the intensity of the secondary beams emerging from the IPs will increase accordingly. Peak luminosities above the nominal value [42] are expected (see Chapter 6.3). At these luminosities the energy deposited by the BFPP1 beam into the superconducting dipole could lead to quenches and might make it difficult to smoothly

operate the machine. Other than ATLAS and CMS, ALICE is limited to a peak of $\mathcal{L} = 10^{27}\,\mathrm{cm}^{-2}\mathrm{s}^{-1}$ and will be levelled to not exceed this limit. Therefore, the risk of quenches will be higher in IR1 and 5 and mitigation of secondary beam losses is even more important.

Reference [66] proposes to introduce an orbit bump in the dispersion suppressor to pull the BFPP1 beam away from the aperture. Depending on the shape and size of the bump, different scenarios are possible (ordered by bump amplitude and complexity):

- The impact angle between the beam and the aperture would be reduced, distributing the losses over a larger area and reducing the density of the loss spot.
- The beam could be steered out of the dipole and into the empty cryostat, where the deposited particles have less damage potential.
- The impact point could be spread out over two cells. The bump has to be large enough that the beam only scratches the aperture close to the original impact location, but a certain fraction survives until the next crest of the betatron oscillation and impacts fully two cells further downstream.

The described technique was first tested in the scope of this thesis in an end-of-fill experiment in 2011. A bump was introduced at the right side of IP5, where the highest losses in the entire ring were observed (see Fig. 7.1). The analysis of this experiment is presented in the next section. Following that, the influence of the optics on the impact distribution for 2015 is discussed.

7.3.1. Analysis of the 2011 Bump Experiment in IR5

Initial Conditions

The experiment took place during the second half of Fill 2319. The initial situation in terms of losses to the right side of IP5 is shown in Fig. 7.6. The black bars indicate the BLM signals, where the highest peak at around $s = 420\,\mathrm{m}$ is cut at $10\,\mu\mathrm{Gy/s}$, but actually reaches about $80\,\mu\mathrm{Gy/s}$. The other signals are shown to their full strength on a linear scale. At the time of the experiment, the beams had been in collision for more than 7 h. The horizontal beam size had blown up from its initial value by about 20%, while the vertical emittance was about constant through the fill. The absolute values of the emittances are uncertain. From the luminosity and intensity measurements at the beginning of collisions an initial average value of $\tilde{\varepsilon}_n = 1.5\,\mu\mathrm{m}$ was approximated for both beams and planes. With this, the emittance during the experiment were estimated to $\epsilon_{n,x} \approx 2.1\,\mu\mathrm{m}$ and $\epsilon_{n,y} \approx 1.5\,\mu\mathrm{m}$. Based on this values, the 10σ horizontal envelope of the main beam (blue) and the 1σ horizontal envelope of the BFPP1 beam (red) are indicated in Fig. 7.6. The main beam line elements are presented as boxes on the central orbit, while the gray area on the top corresponds to the aperture. CMS measured the luminosity during the experiment to be on average $\mathcal{L} \approx 0.11 \times 10^{27}\,\mathrm{cm}^{-2}\mathrm{s}^{-1}$.

The predicted impact point of the BFPP1 beam lies in the superconducting dipole

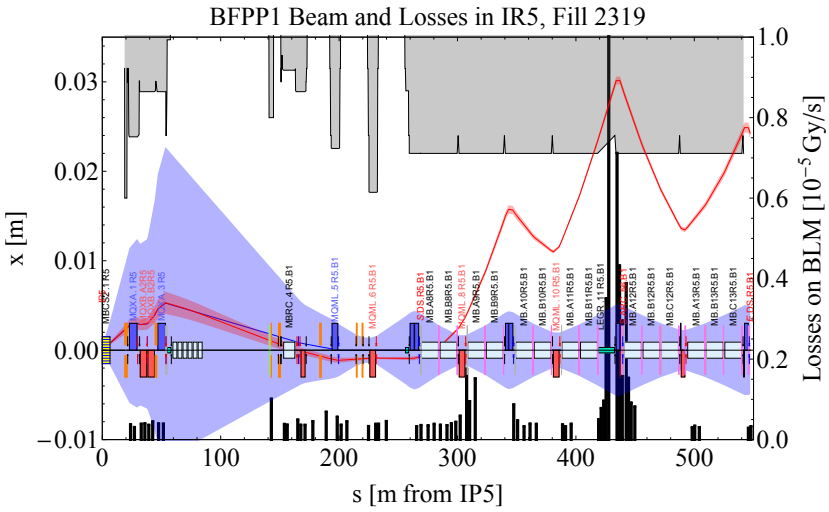

Figure 7.6.: BFPP1 1σ beam envelope (red line) and main beam 10σ envelop (blue) in IR5. Black bars show BLM signals just before introducing the bump. The hight of the peak at $s = 420\,\mathrm{m}$ is cut off, it reaches $80\,\mu\mathrm{Gy/s}$. The gray blocks at the top indicate the aperture.

called MB.B11R5 and is a few metres upstream of the BLM with the highest signal. After the impact of an ion in the beam screen, it will break up into fragments and generate a forward directed particle shower, which deposits its peak power up to several metres behind the initial impact location. In general, the power deposition upstream of the impact point is very small [114].

Experimental Setup

Starting from this situation, a three magnet orbit bump, with a maximum deflection of $x_{\mathrm{bump}} = -2.6\,\mathrm{mm}$ in the horizontal plane at the quadrupole in cell 11 (Q11, at $s = 437\,\mathrm{m}$), was gradually introduced in steps of 0.2 mm. The maximum bump amplitude was limited for reasons of machine protection under physics conditions. The behaviour of the beam and the influence of the bump was monitored at each step.

Figure 7.7 compares the simulated beam trajectories without bump (main beam gray, BFPP1 red) with a bump of full amplitude (main beam blue, BFPP1 green). Since a horizontal bump is required, the corrector magnets used to build it are installed next to the horizontally focussing quadrupoles in cell 9, 11 and 13 (Q9, Q11 and Q13). These correctors are called

1. MCBCH.9R5.B1
2. MCBH.11R5.B1
3. MCBH.13R5.B1,

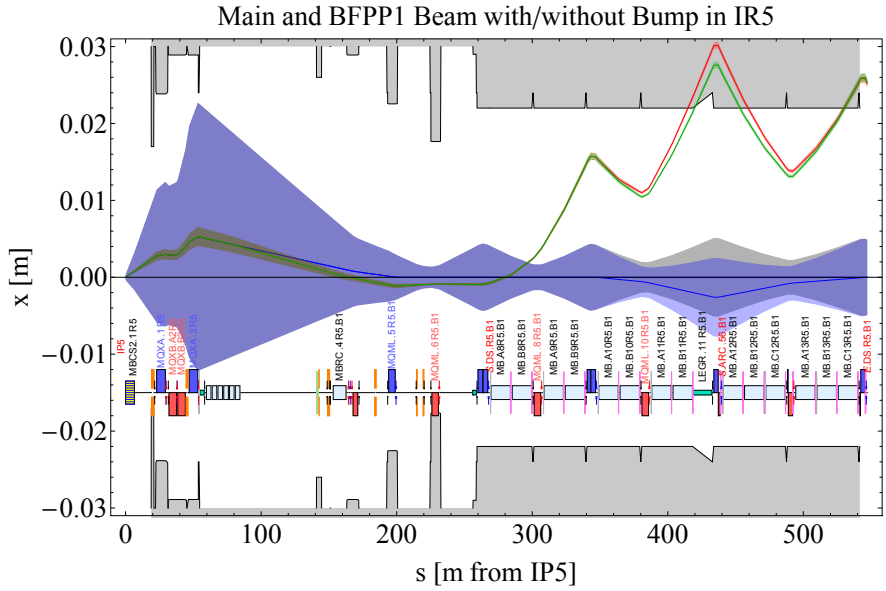

Figure 7.7.: BFPP1 1σ (red/green) and main beam 10σ (gray/blue) envelopes in IR5 with (green/blue) and without (red/gray) orbit bump. The beam is shifted $x = -2.6\,\mathrm{mm}$ around the quadrupole MQ.11R5.B1 located 437 m to the right of IP5. The gray bars on the top and bottom indicate the beam pipe aperture.

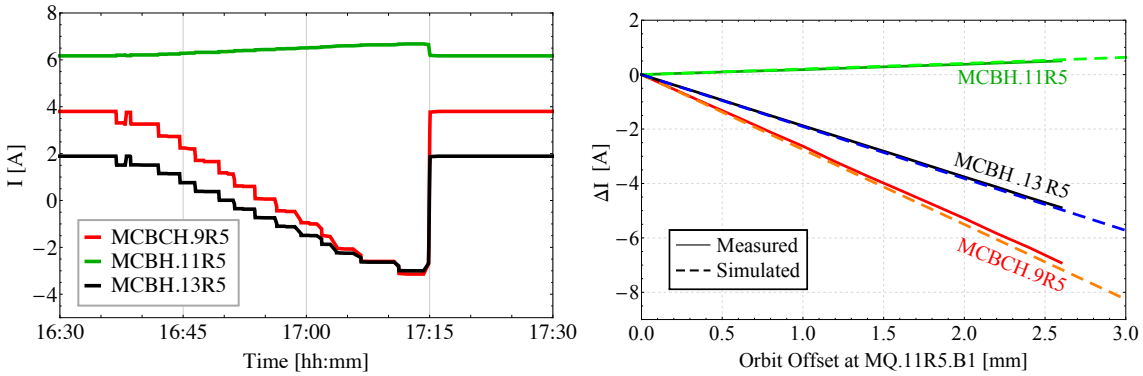

Figure 7.8.: Current evolution of the three orbit correctors used to create the bump during the experiment. Left as a function of time, right as a function of bump amplitude compared to simulated values.

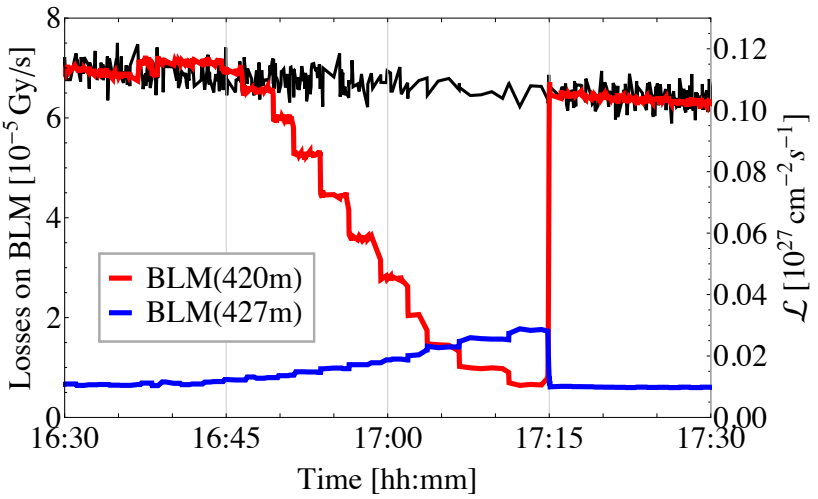

Figure 7.9.: Loss evolution at the two BLMs with the highest signal (red, blue) and luminosity (black) during the bump experiment. The BLMs are referred to by their s positions.

in the LHC MADX sequence. As desired, the main beam orbit in Fig. 7.7 gets offset by $-2.6\,\mathrm{mm}$ at Q11, shifting the impact point of the BFPP1 beam slightly to the right and reducing its impact angle by a few percent. Figure 7.8 shows the measured current driving the three orbit correctors creating the bump as a function of time through the experiment (left) and as a function of the expected bump amplitude (right, solid lines). The linear correlation between the bump amplitude and the corrector strength is evident. The MADX simulation (dashed lines) of the bump and the corresponding corrector strengths is in good agreement with the measurement.

Interpretation of the Results

The loss evolution at the BLM measuring the highest dose closest to the impact before introducing the bump (BLMEI.11R5.B1E30_MBB, at $s = 420\,\mathrm{m}$, labelled BLM(420m), red), the dose of the consecutive BLM (BLMEI.11R5.B1E21_LEGR, at $s = 427\,\mathrm{m}$, labelled BLM(427m), blue) and the luminosity (black) is shown in Figure 7.9. As the bump is increased, the losses at BLM(420m) gradually reduce, while the measurement of BLM(427m) increases. The luminosity is not affected. At full bump amplitude, the dose at BLM(420m) has decreased by about one order of magnitude, while the amount on the subsequent monitor is increased by about a factor of two. This confirms the success of the experiment. The losses could be moved out of the superconducting magnet and into the connecting empty cryostat. In the following, the observations will be analysed in detail by investigating the BLM signals close to the impact region in comparison with dedicated FLUKA simulations.

The results of this analysis are shown in Figs. 7.10 to 7.13. These figures follow

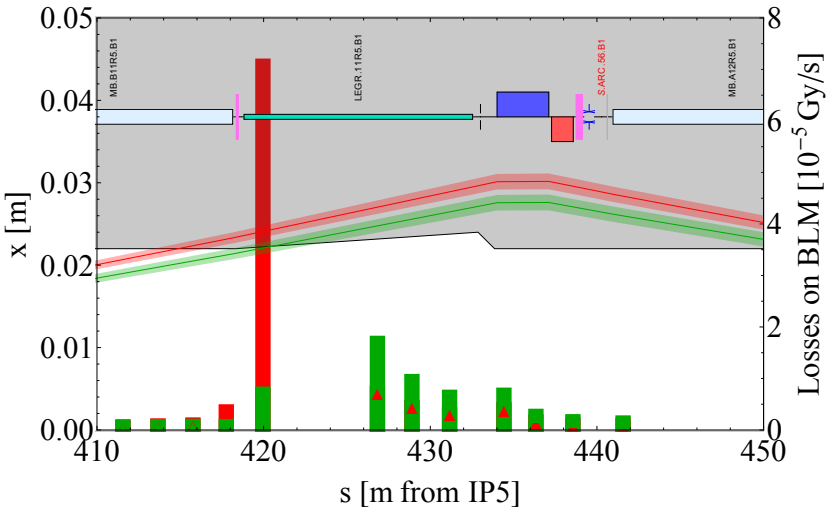

Figure 7.10.: Zoom to the BFPP1 impact region right of IP5. BFPP1 3σ beam envelope and BLM losses around the impact point are shown before the experiment (red) and with a $-2.6\,\mathrm{mm}$ orbit bump (green). The red triangles indicate the hidden red bars. The gray area at the top indicates the aperture.

a general color scheme, displaying the situation without orbit bump in red and with full bump amplitude ($x_{\mathrm{bump}} = -2.6\,\mathrm{mm}$) in green. A zoom to the impact region is displayed in Fig. 7.10: the simulated BFPP1 3σ envelopes and the BLM losses before the experiment and with the full bump amplitude are shown. The red triangles indicate the size of the hidden red bars. The gray area in the top half of the plot indicates the aperture. Figure 7.11 presents the corresponding 6D impact coordinates of 50000 $^{208}\mathrm{Pb}^{81+}$ ions hitting the beam screen, generated following the procedure described in Section 7.1.

Since the impact angle (Fig. 7.11 middle right) becomes smaller by increasing the bump, the s distribution widens (top left). The majority of the particles impact close to the x-axis, where $A_x = 22\,\mathrm{mm}$. The particles in the tails of the distributions have $|y| > 0$ and thus a slightly reduced maximum x position (middle left), originating from the curvature of the beam pipe. The x, y, y' and energy distributions are not affected by the horizontal orbit bump.

The impact distributions were used as input for FLUKA simulations of the particle showers, kindly performed by the CERN FLUKA team (EN/STI) [115]. The results of these simulations are shown in Figs. 7.12 and 7.13. Only the region of interest between the MB.B11R5.B1 and the MQ.11R5.B1 was taken into account. The FLUKA setup for the LHC includes the BLMs mounted on the outside of the magnets. A comparison of the simulated (blue) and measured BLM signals before the start of the of the experiment (left) and with full bump amplitude (right) is shown in Fig. 7.12, on

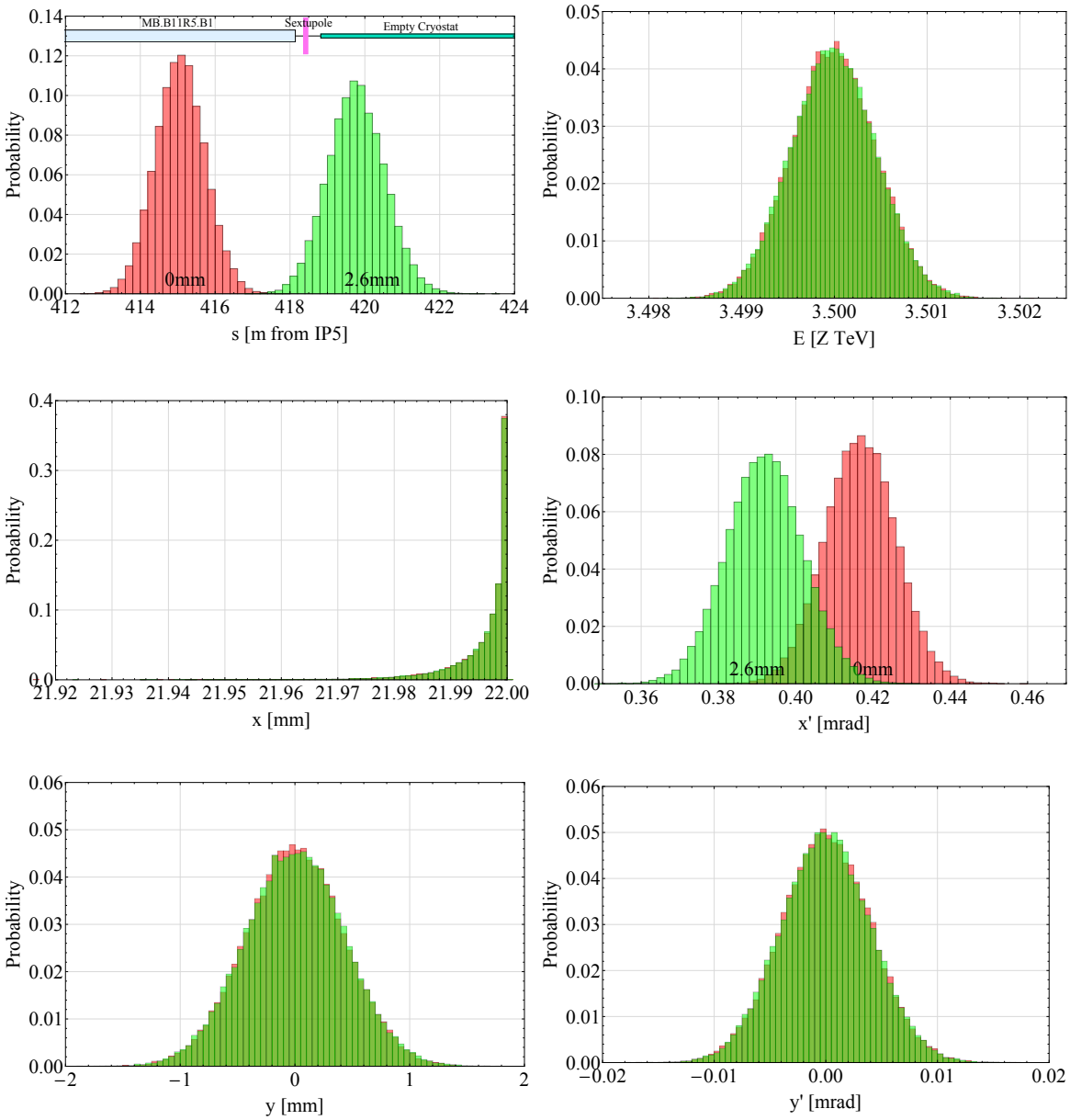

Figure 7.11.: Generated BFPP1 impact coordinates for 50000 $^{208}\mathrm{Pb}^{81+}$ ions without (red) and with maximum bump (green) for the experiment in IR5. $\epsilon_{n,x} = 2.1\,\mu\mathrm{m}$ and $\epsilon_{n,y} = 1.5\,\mu\mathrm{m}$ were assumed. From left to right: top s, energy E; middle x, x'; bottom y, y'.

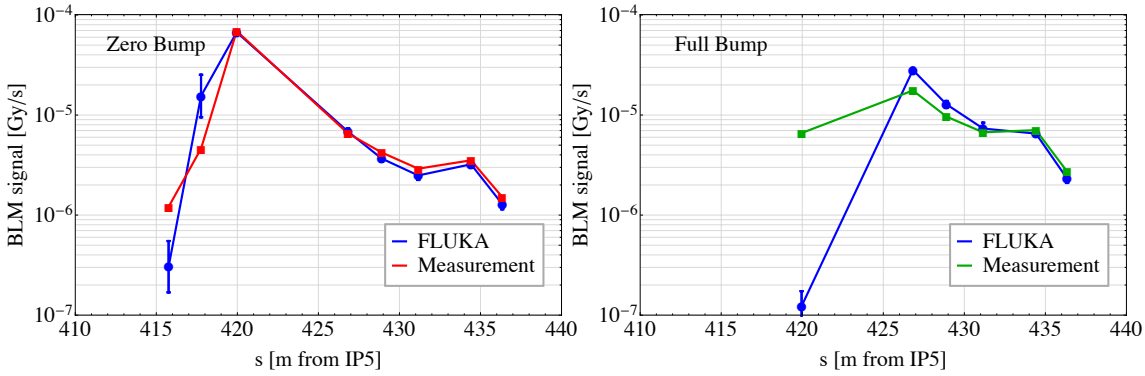

Figure 7.12.: Comparison of FLUKA simulated BLM signals (blue) with the measurements with zero (red) and full (green) bump amplitude. Courtesy of A. Lechner and the CERN FLUKA team [115].

a logarithmic scale. The peak power density in the magnet coils is shown in Fig. 7.13, with zero and full bump amplitude. The cryostat after the MB.B11R5 is empty and does not have a magnet coil, thus no data was calculated here.

It is impossible to determine the energy deposition of every impinging particle, hence only a small (compared to the total number of particles in the beam) number of single particles is treated with FLUKA and the results are normalised to a given luminosity. This introduces statistical uncertainties on the simulation, which are also indicated in the plots. The simulation results are scaled to $\mathcal{L} = 0.11 \times 10^{27}\,\mathrm{cm}^{-2}\mathrm{s}^{-1}$, which is the average CMS online luminosity during the experiment (see Fig. 7.9).

In case of BFPP ions, the particular s position of the losses depends on the beam screen dimension, which is assumed to be $r_{\mathrm{bs}} = 22\,\mathrm{mm}$ in the tracking simulation. However, in reality the beam screen is slightly larger to account for mechanical tolerances, alignment in the vacuum chamber etc. In FLUKA, the actual beam screen dimension, i.e. 23.25 mm, is used. The initial particles for the simulation are generated with $r_{\mathrm{bs}} = x_{\mathrm{max}} = 22\,\mathrm{mm}$ and the drift until the aperture of the FLUKA geometry is calculated inside FLUKA. The influence of the magnetic dipole is taken into account in FLUKA. The impact s positions on a 1.25 mm larger beam pipe are shifted 2 to 3 m further downstream. The mean impact position with zero bump amplitude is moved from $s = 415.1\,\mathrm{m}$ (as shown in Fig. 7.11, top left) to about 417.7 m, which implies that the initial distribution now lies partially outside of the magnet, since the dipole ends at $s = 418.14\,\mathrm{m}$. At $x_{\mathrm{bump}} = -2.6\,\mathrm{mm}$, the mean impact position moved from $s = 419.8\,\mathrm{m}$ to about 422.8 m. Only a small tail of the particle distribution impacts in the dipole. The core of the particle shower now misses the monitor at $s = 420\,\mathrm{m}$ and its signal is strongly reduced, while the signal of the monitor at 427 m is increased, see Fig. 7.10. This second monitor is installed 7 m downstream of the first. In this gap, the particle shower widens and reduces its density and intensity, such the signal measured at the second monitor is smaller than the reduction of the first. A large fraction of the losses becomes invisible for the system.

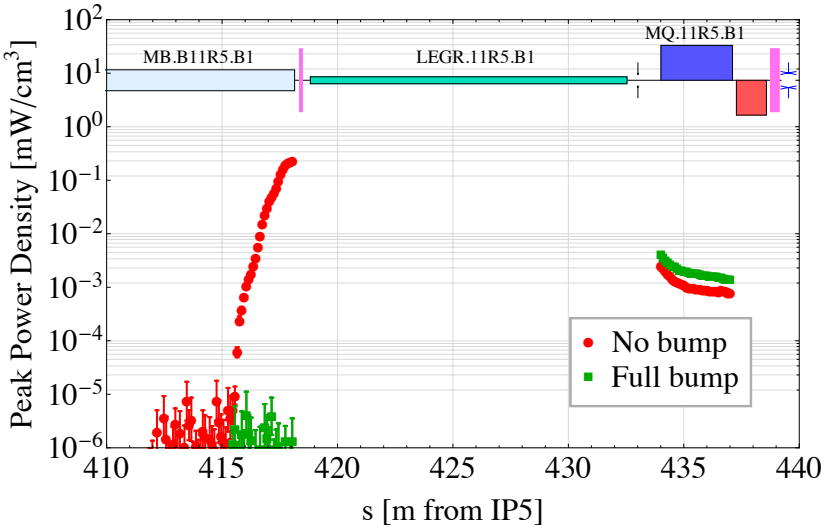

Figure 7.13.: FLUKA simulated peak power density in the magnet coils during bump experiment with (green) and without (red) bump. Normalised to $\mathcal{L} = 0.11 \times 10^{27}\,\mathrm{cm}^{-2}\mathrm{s}^{-1}$. Courtesy of A. Lechner and the CERN FLUKA team [115].

In general, a good absolute agreement of simulated BLM signals with the measured ones is found (see Fig. 7.12), however some discrepancy is present. In particular for the case with orbit bump (right), where it looks as if the beam impacts a bit more upstream than what was assumed (probably between the original and the new s position). Unfortunately, FLUKA can only track fully stripped nuclei, which is not correct in case of the investigated $^{208}\mathrm{Pb}^{81+}$ ions of the BFPP1 beam, resulting in an uncertainty on the new s positions. Moreover, the actual emittance of the impacting beam has a significant influence on the simulation results. Since the BFPP1 beam emittance is related to the main beam emittance according to Eq. 7.3, the uncertainty on the measured emittance discussed in Section 7.3.1 propagates to the FLUKA results. The agreement between simulation and measurement in Fig. 7.12 is better behind the peak loss.

The simulated peak power density in the magnet coils shown in Fig. 7.13 is an indicator for potential quenching of the magnet and can be compared to current estimates of the quench limits [90–93]. The particle shower produced by the impacting particles is strongly forward directed and deposits its peak power a few metres downstream, resulting in higher statistics and a better accuracy of the simulation downstream from the peak.

Without the bump, the peak power density in the coil of MB.B11R5.B1 increases until the end of the magnet (see Fig. 7.13), hence the actual peak probably lies outside. With the bump, the power deposited in the MB is significantly reduced, without dangerously increasing the peak power in the Q11. In any case, the peak power in the Q11

Bump amplitude	**zero**	**full** (2.6 mm)
MB.B11R5 [W]	0.28	< 0.001
LEGR.11R5 [W]	0.64	0.81
MQ.11R5 [W]	0.06	0.10

Table 7.1.: Total power lost in the different magnets during bump test, simulated with FLUKA. Normalised to $\mathcal{L} = 0.11 \times 10^{27}\,\mathrm{cm}^{-2}\mathrm{s}^{-1}$, as measured. LEGR.11R5 labels the empty cryostat behind MB.B11R5. Courtesy of A. Lechner and the CERN FLUKA team [115].

is low and likely no problem even for higher luminosities and energies. The systematic uncertainty is of the order of a factor two, and is mainly driven by the uncertainty of the exact impact location [116]. If losses would occur half a metre more upstream, the peak would probably be higher (with the presently assumed loss location, a fraction is lost in the interconnect). However, the values are still a reasonable estimate of the power load to the magnet [116]. Table 7.1 summarises the total power on the different magnets with and without bump, again normalized to $\mathcal{L} = 0.11 \times 10^{27}\,\mathrm{cm}^{-2}\mathrm{s}^{-1}$. The particle showers were calculated only until the end of the MQ.11R5.B1, however some particles will deposit energy further downstream. The amount of energy leaving the FLUKA geometry is increased in the full bump case, since the peak of the energy deposition is shifted downstream. The MQ.11R5.B1 is the magnet absorbing the highest power in the full bump scenario.

Because of the low luminosity, there was no risk of quenches. Nevertheless, it was shown that the bump mitigation technique is a powerful tool to reduce the heat load to magnets.

7.3.2. Considerations for Operation

In general, a detailed FLUKA study would be necessary to find the optimal bump amplitude for given beam and machine conditions in terms of heat load in the magnet coils of the MB.B11 and Q11. The optimal setting would ideally feature an energy deposition in both magnets below the quench limit [90–93]. The FLUKA results strongly depend on the impacting beam distribution, which on the other hand depend on the optics, bump amplitude and energy.

The 2011 experiment was performed at $E_b = 3.5Z\,\mathrm{TeV}$, $\beta^* = 1\,\mathrm{m}$ and a half crossing angle of $\theta_c = 120\,\mu\mathrm{rad}$ in IP1 and 5 and $\theta_c = 60\,\mu\mathrm{rad}$ in IP2. The foreseen optics for after LS1 are still under discussion and may change before the start of the run. At the time of writing, $E_b = 6.5Z\,\mathrm{TeV}$, $\beta^* = 0.5\,\mathrm{m}$, $\theta_c = 135\,\mu\mathrm{rad}$ in IP1/5 and $\theta_c = 60\,\mu\mathrm{rad}$ in IP2 are considered as the baseline, which is assumed in the following calculations. However, the β^*-value for the start up in 2015 would more likely be $\beta^* = 0.6\,\mathrm{m}$.

Nevertheless, a simulation using the baseline optics will give a good indication of what can be expected. The results are presented in the next subsection. Preceding

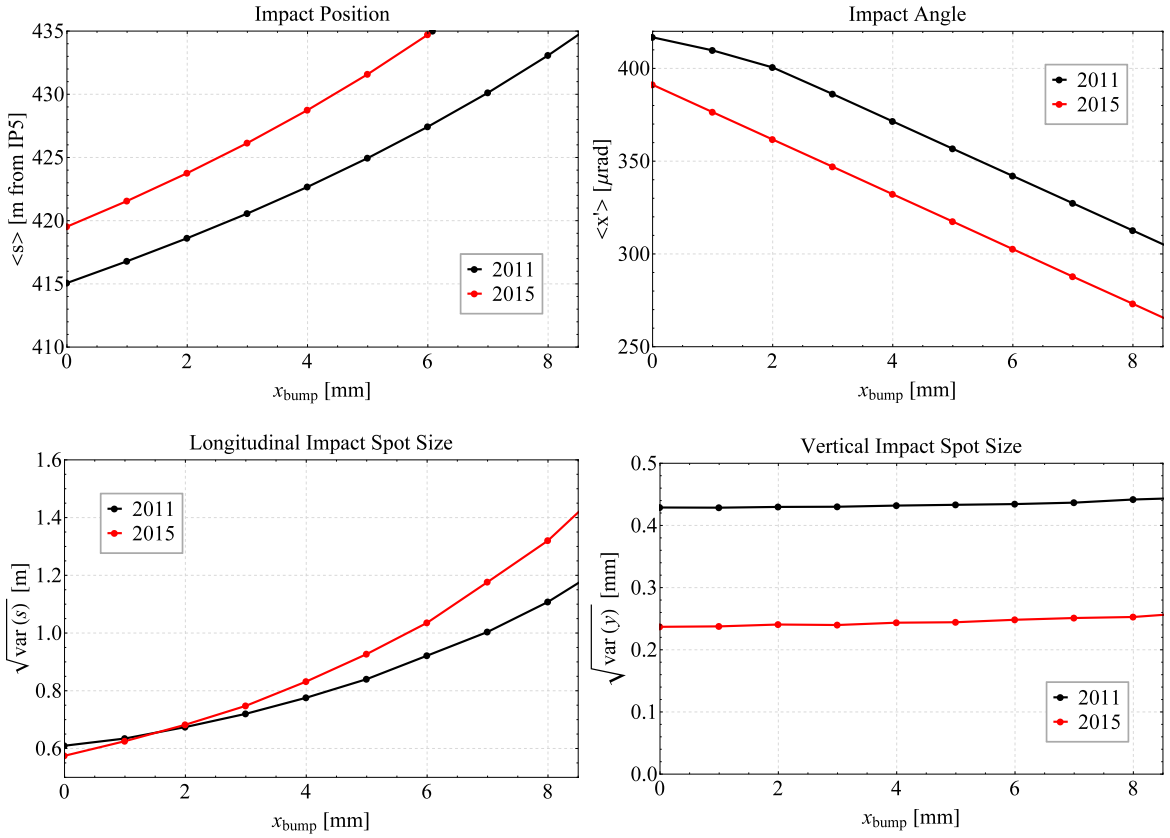

Figure 7.14.: BFPP1 impact position (top left), angle (top right), longitudinal (bottom left) and vertical 1σ spot size (bottom right) as a function of the absolute bump amplitude.

this, the influence of different optics configurations are discussed by investigating the statistical properties of the impacting particle distributions.

Influence of Optics on Impact Distribution

The average impact position (top left), angle (top right), longitudinal (bottom left) and vertical 1σ spot width (bottom right) are shown in Fig. 7.14 as a function of the absolute bump amplitude, x_{bump}, in Q11 for the 2011 (black) and the baseline 2015 (red, $\beta^* = 0.5\,\text{m}$) optics settings listed above. The dots indicate the simulated bump steps. Initial emittances of $\epsilon_{n,xy} = 1.5\,\mu\text{m}$ are assumed for both cases.

Under normal operational conditions (without bump) in 2011, the BFPP1 beam hits the beam pipe inside the superconducting dipole MB.B11R5.B1, at about 415 m behind IP5. The larger the bump, the further downstream the impact positions and the smaller the impact angle. A reduced impact angle increases the area of the loss spot and thus reduces the density of the deposited energy. At $x_{\text{bump}} \approx 1.75\,\text{mm}$ the beam is able to pass the magnet and enters the connecting drift space. Equation (7.6)

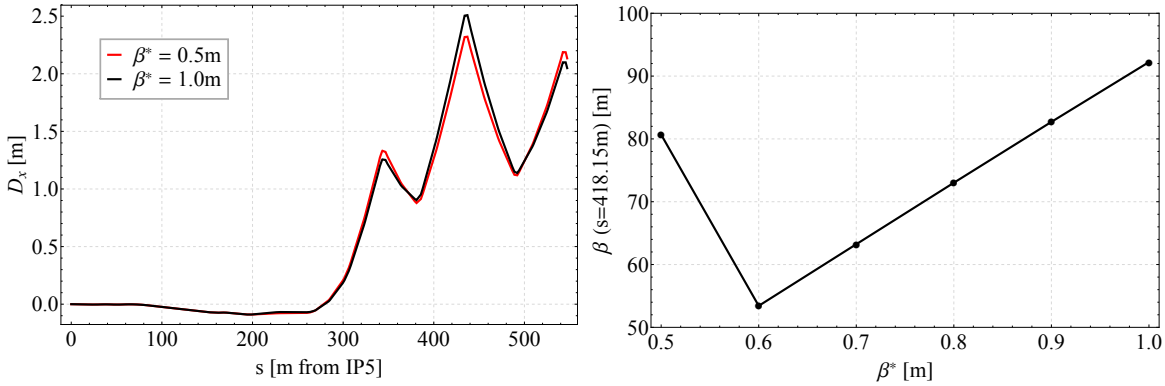

Figure 7.15.: Change of the local, single-pass dispersion in the DS (left) and the β-function at MB.B11R5.B1 (right) from $\beta^* = 1\,\mathrm{m}$ to $0.5\,\mathrm{m}$.

shows in combination with Eq. (7.7) that both the position and angle coordinates are changed during the passage of a bending magnet, however the angle is constant in drift spaces (Eq. (7.10)). This is the reason for the little kink in the black line just before $x_{\mathrm{bump}} = 2\,\mathrm{mm}$ in the right top plot of Fig. 7.14. From this point on, the average beam impact position lies outside the dipole and in the empty connection cryostat (drift space). The impact angle is now equal to the x' at the exit of the dipole, until the beam enters the next magnetic element, which is the quadrupole Q11 starting at $s = 434\,\mathrm{m}$.

For $x_{\mathrm{bump}} > 8\,\mathrm{mm}$, the beam has entered the quadrupole and gets a focusing kick, changing the sign of x', its orbit moves away from the aperture and does not impact anymore. However, due to the particle distribution around the orbit, a certain fraction of the $^{208}\mathrm{Pb}^{81+}$ ions will still impact close to the entrance of Q11. By further increasing x_{bump} it could be possible to avoid the impact in Q11 but the full energy would then be deposited in Q13. Moreover, for these large bump amplitudes one has to take care that enough margin is kept between the main beam and the opposite side of the aperture. The drawback of a large orbit bump is that the beam moves closer to the quadrupole, increasing the risk of quenching it.

For the considered 2015 optics (shown in red in Fig. 7.14), the mean impact position without bump lies already outside of the dipole. The impact angle is reduced accordingly. Nevertheless, the spot size is expected to be smaller due to the higher energy. The difference between the two curves mainly arises from the change of the local single-pass dispersion introduced by the reduction of β^* from 1 m to 0.5 m, see Fig 7.15 (left). The crossing angle change has little influence.

Figure 7.16 shows the influence of varying β^* on the impact position (top left), angle (top right) and longitudinal (bottom left) and vertical 1σ spot size (bottom right). The impact position is similar to 2011 from $\beta^* = 1.0\,\mathrm{m}$ to $0.6\,\mathrm{m}$, while the angle and spot size decrease slowly. The step from $\beta^* = 0.6\,\mathrm{m}$ to $0.5\,\mathrm{m}$ is dominated by the movement of the trajectory due to the change in the local dispersion. The spot size decreases

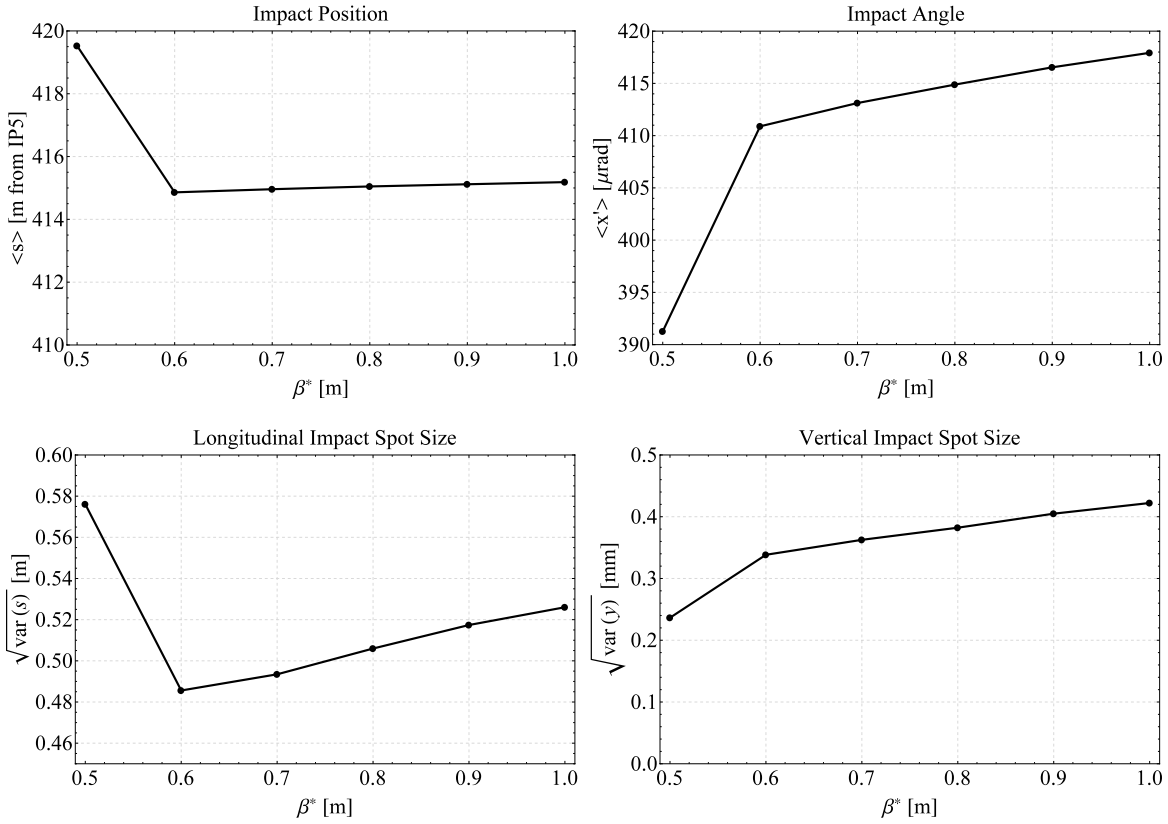

Figure 7.16.: BFPP1 average impact position (top left), angle (top right), longitudinal (bottom left) and vertical 1σ spot size (bottom right) as a function of β^*.

mainly because the local β-function at the dipole decreases with β^*, see Fig. 7.15 (right). Only for $\beta^* \leq 0.5\,\text{m}$ the initial BFPP1 impact position lies outside the dipole.

In the real machine the orbit feedback controls the main beam orbit to a precision of about $\Delta x = 0.1\,\text{mm}$. As was shown, the BFPP impact properties are sensitive to small optics changes, thus a slightly off-centred orbit could have a large effect on the impact distribution. Assuming an orbit offset of $\Delta x = 0.1\,\text{mm}$ at the entrance of the MB.B11 for the BFPP1 beam and solving Eq. (7.18) with $x_0 \to (x_0 + \Delta x)$, leads to a change of the mean impact position in the order of $\Delta s = \pm 0.25\,\text{m}$. The impact angle changes by about $\Delta x' = \pm 1\,\mu\text{rad}$. This and other uncertainties on the optics, could bring the beam very close to the exit of the dipole, for both $\beta^* = 0.5\,\text{m}$ and $0.6\,\text{m}$. It has to be seen during the run and under operational conditions which bump amplitude is actually needed.

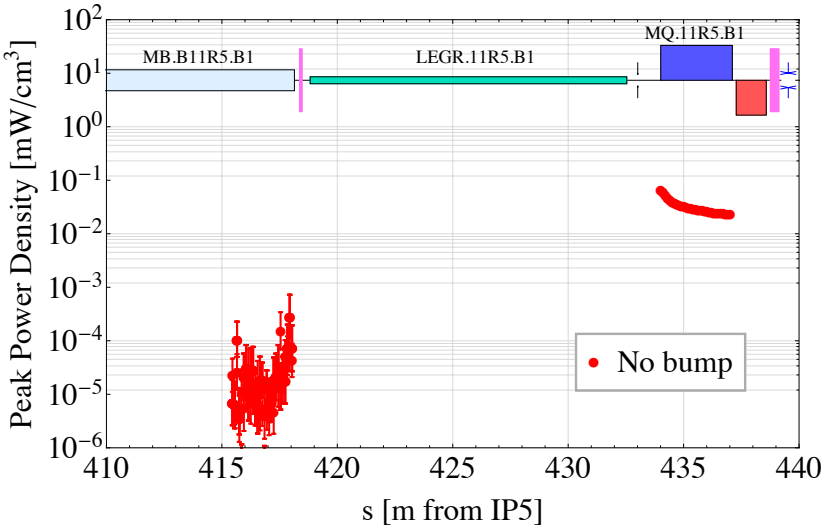

Figure 7.17.: FLUKA simulated peak power density in the magnet coils for an impact distribution generated assuming the 2015 baseline optics at $E_b = 6.5Z$ TeV. The Values are normalised to $\mathcal{L} = 1 \times 10^{27}\,\mathrm{cm}^{-2}\mathrm{s}^{-1}$. Courtesy of A. Lechner and the CERN FLUKA team [115].

FLUKA Simulations for 2015 Baseline Optics

As was shown in Fig. 7.14, the average impact position of the BFPP1 beam, assuming the 2015 baseline optics with $\beta^* = 0.5\,\mathrm{m}$, lies outside of the MB already without orbit bump. In fact, the average impact position under these conditions is similar to the one obtained with the full orbit bump of $x_{\mathrm{bump}} = -2.6\,\mathrm{mm}$ during the 2011 experiment at $\beta^* = 1\,\mathrm{m}$. The FLUKA-simulated peak power density in the magnet coils for an impact distribution generated using the 2015 baseline optics with $\beta^* = 0.5\,\mathrm{m}$ at $E_b = 6.5Z$ TeV, assuming zero external orbit bump and a luminosity of $\mathcal{L} = 1 \times 10^{27}\,\mathrm{cm}^{-2}\mathrm{s}^{-1}$, is shown in Fig. 7.17.

As already expected from the 2011 results, the power density in magnet coils does not represent any risk of quench also in the 2015 case, if the secondary ions are lost in the connection cryostat. The power density in the MB is low, because the magnet lies upstream of the impact. In the MQ, which is the most loaded magnet, the exposure to the coils stays below $0.1\,\mathrm{mW/cm}^3$, hence no risk of quench is expected, even for several $10^{27}\,\mathrm{cm}^{-2}\mathrm{s}^{-1}$ in luminosity [116]. In case the optics are such that the BFPP1 impact position lies inside the MB, an orbit bump can still be introduced to move the losses into the empty cryostat.

These results bring confidence that for the luminosities and energies expected after LS1 the bump mitigation technique can be applied to avoid quenches due to secondary beam losses by moving the BFPP1 beams into the empty cryostats. Simulations were only performed for IR5 so far, but similar results are expected for IR1. Since the BFPP1 beam gets lost in IR2 closer to the IP, a more complicated four magnet orbit

bump is necessary to move the impact point downstream into the empty cryostat. Once the beam impacts in the empty cryostat, similar power distributions as in IR5 are expected.

7.4. Collimators in the Dispersion Suppressor

As shown in Fig. 2.11a, the secondary beams overlay with the main beam close to the IP, but start to separate as soon as they enter dispersive regions with strong dipole fields. To absorb these beams before they can impact in the beam screen, dedicated collimators could be installed permanently in suitable locations. A collimator consists of two parallel jaws, made of a material qualified to constantly absorb high fluxes of particles over short distances (e.g. carbon). The opening gap between the two jaws can be adjusted to, ideally, only absorb these particles, which would otherwise impact elsewhere in the beam pipe, but not those, which are well on track. Naturally, the closer the jaws come the main beam, the more particles will be absorbed and the faster the beam intensity will decay. For this reason, a location should be chosen, where the secondary beams are well separated from the main beam, but remain far enough away from the aperture. In all IPs the beams completely overlap until Q8. As can be seen by comparing Fig. 2.11a and 7.7 the impact positions of, e.g., the BFPP1 beam in IR2 and IR5 differ due to the different optics. The situation in IR1 is similar to IR5. Figure 7.18 shows the beamline elements to the right of (a) IP2 and (b) IP5, labelled with the MADX element names. The beamlines shown already include the DS collimators at the favoured positions (at about 350 m (IP2) and 330 m (IP5)), which will be derived in the following. The DS collimators are displayed as orange bars between two shorter dipoles (light blue boxes).

In IR2 the beam is lost before the first crest of the betatron oscillation in the second dipole of cell 10 (MB.B10), while in IR1 and 5 the beam survives until the second betatron peak and hits the second dipole of cell 11 (MB.B11). Therefore, only the range between Q8 and MB.B10/11 is suitable to install the collimators. This region is fully equipped with magnets. The only possibility to fit in a collimator is to replace one of the 14.3 m long dipoles with an arrangement of two shorter ($L \approx 5.3\,\mathrm{m}$), but stronger ($B_{\max} = 11\,\mathrm{T}$), dipoles enclosing a $\sim 0.8 - 1\,\mathrm{m}$ long collimator.

The considered range in IR2 contains four dipole magnets (MB.A9, MB.B9, MB.A10, MB.B10, see Fig. 7.18), out of which only two are suitable as potential collimator locations: MB.B9 and MB.A10, which are the second and first dipole of cell 9 or 10, respectively. In MB.B10 they are already too close to the aperture, while at MB.A9 (the first dipole after Q8) the beams move too close to the main beam. Even in MB.B9 the collimator gap would have to be very narrow. Therefore, **MB.A10** is the preferred collimator position in IR2. Note that here the BFPP2 beam can most probably not be caught, because it impacts the beam screen at the beginning of MB.A10, nevertheless, due to its very low intensity (see Table (2.3)) this is not thought to be a problem. Depending on the opening gap, the EMD1 beam misses the jaw and will circulate until

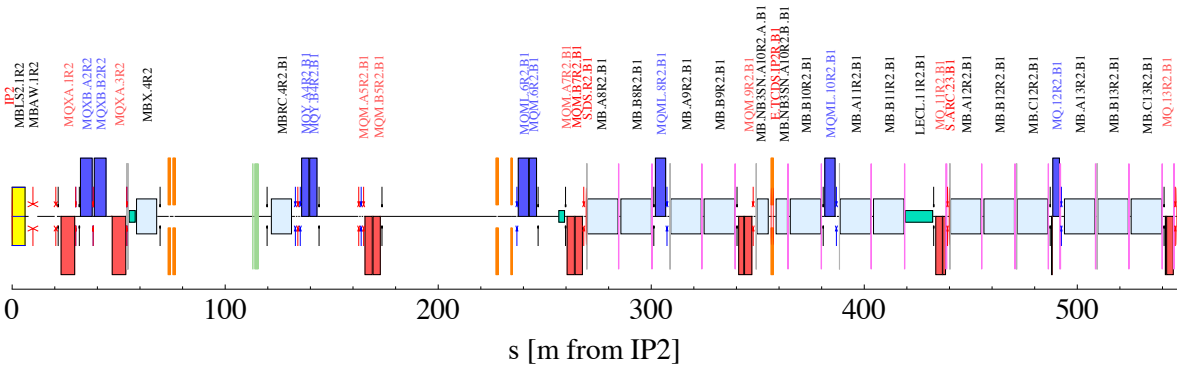

(a) IP2.

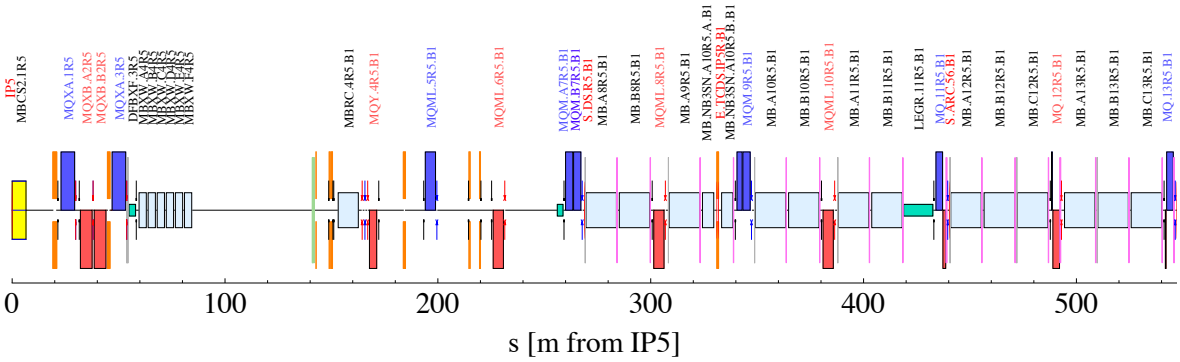

(b) IP5.

Figure 7.18.: Modified beamline including the DS collimators to the right of (a) IP2 and (b) IP5. IP1 is equivalent to IP5. The DS collimators are located at about 350 m (IP2) and 330 m (IP5), shown as orange bars between two shorter (5.5 m long) dipole magnets (light blue boxes).

IR3.

The fact that the BFPP1 beam travels further in IR1 and 5, leaves two more potential collimator locations in MB.A11 and MB.B11. However, MB.A9 and MB.B11 are not useful, due the same reasons as in IR2. Three of the four remaining magnets lie behind the first oscillation peak and are therefore not favoured. The preferred position in IR1 and 5 thus determines to **MB.B9**. Plots of the secondary beams emerging to the right of the IP1, 2 and 5 in the horizontal plane, similar to Fig. 2.11a, are shown in Appendix C. The mentioned potential collimator positions are marked with black bars and the preferred locations are highlighted in green.

Impact particle distributions were generated according to the procedure described in Section 7.1 for two cases in all IPs:

- Under normal operational conditions, with the impact position on the beam screen in the mentioned dipole.
- On the front plane of the collimator, after the arrangement was installed in the

sequence.

Both cases assume nominal optics. These distributions were provided to the CERN FLUKA team [111] to study the best collimator length, material and the heat load introduced by the shower particles. The results for IP2 can be found in Ref. [114]. The study for IP1/5 is still ongoing.

8. Potential for Stochastic Cooling

8.1. Motivation

As was shown in the previous chapters the luminosity burn-off rate at high energy and especially with three experiments in collisions will become very strong and thus lead to short fills (in the order of a few hours). The IBS will be reduced, but still lead to a non-negligible fraction of particle losses due to debunching. The radiation damping is enhanced, but not yet able to completely dominate the IBS emittance growth and reduce the beam dimensions during store.

To increase the integrated luminosity, particle losses from other sources than burn-off and emittance growth have to be minimised. The initial emittance and bunch intensity is imprinted by the injectors. The emittance is an invariant of motion and only changes due to dynamic effects that exert non-conservative forces, like space-charge, IBS or synchrotron radiation. However, an external beam cooling system could be used to reduce the emittance during a store.

At the Relativistic Heavy Ion Collider (RHIC) [5], 3D stochastic cooling of bunched gold (Au) and uranium (U) beams has been very successful [22–26,117]. The emittance growth and the debunching component of the losses during collisions were substantially reduced, improving the luminosity lifetime and lengthening fills. In uranium operation, it was even possible to increase the instantaneous luminosity by more than a factor of three over its initial value, because of the highly efficient emittance cooling. The potential of stochastic cooling could also be exploited for LHC heavy-ion beams with a similar approach [27, 78].

This chapter begins with an introduction to the principle of stochastic cooling, followed by a proposal of a proof-of-principle experiment in the LHC based on a minimised setup, using the existing Schottky pickups and a single cooling cavity at the same frequency. The benefits of a 3D cooling system for both beams in heavy-ion operation are investigated with CTE simulations and possible issues are discussed. Moreover, the potential of a first stage 1D cooling system is considered.

This chapter is partly based on the experience I gained during a visit to the Brookhaven National Laboratory (BNL), where I participated in the commissioning of the stochastic cooling system of RHIC, preceding its 2014 high energy Au-Au run. Several results in this chapter were presented at the COOL'13 workshop in Mürren, Switzerland [27] and the International Particle Accelerator Conference 2014 in Dresden, Germany [28].

8.2. Beam Cooling and the LHC

The "temperature" of a particle beam is an analogy describing the phase-space density (emittance) of the beam. A high temperature corresponds to strong statistical fluctuations in the particles' properties. Small beams with small emittances, hence "cold" beams, are generally desired. Beam cooling aims to increase the phase-space density of circulating beams in a storage ring. Up to date, four main methods are used: radiation cooling [118], electron cooling [45, 119], stochastic cooling [120] and laser cooling [121]. Three other methods are under development: ionisation cooling of muons [122, 123], optical stochastic cooling [124] and coherent electron cooling[1] [127]. A résumé of the existing beam cooling methods is given in Ref. [128]. From these methods, only radiation, electron and stochastic cooling are theoretically applicable for heavy-ions in the LHC. Coherent electron cooling might be applicable but the principle has not yet been demonstrated.

Radiation cooling is equivalent to the effect of radiation damping introduced in Chapter 2.5.2. As can be seen from Eqs. 2.45 to 2.47, the cooling rates strongly depend on the energy, γ, the particle's mass, m_{ion}, and charge number, Z, [38]: $\alpha_{\text{rad}} \propto \gamma^3 Z^2/m_{\text{ion}}$. Thus, radiation damping is most efficient for light particles, like electrons and positrons. Only at the energies reachable in the LHC, radiation damping starts to become visible for lead ions (see Chapter 6.4.1) and even for protons. The radiation cooling rates for Pb at top energy in the LHC are $\alpha_{\text{rad},s} = 1/(6.3\,\text{h})$ in the longitudinal and $\alpha_{\text{rad},x,y} = 1/(12.6\,\text{h})$ in the transverse planes. With fill durations in the order of 6 h, the radiation damping is not yet sufficient to obtain the desired cooling effect. Chapter 9 shows that if the energy is increased further, radiation damping becomes one of the effects dominating the beam and luminosity evolution in hadron collisions.

Electron cooling works with a cold (small transverse momentum spread) co-moving electron beam, which is injected in a straight section on top of the circulating ion beam. If the electrons move at exactly the same speed as the ions ($\gamma_e = \gamma_{\text{ion}}$), scattering processes between the particles transfer transverse momentum from the ions to the electrons[2] and cooling of the ion beam emittance is obtained. Heavy ions with $E_b = 7Z$ TeV have a relativistic gamma of $\gamma = 2963.5$. To achieve the same γ with electrons, an electron beam energy of about 1.5 GeV is required. Section 2.7.2 of Ref. [38] quotes a transverse electron cooling rate that is proportional to the electron beam current and inversely proportional to the fifth power of γ. Assuming the same beam size and angular spread for ion and electron beams, and that the cooling section occupies about 20 m of the total circumference, an electron beam current of over 1000 A would be required to obtain a cooling rate in the order of 1 h. Even though this estimate is very rough, it makes clear that electron cooling in the LHC is ruled out.

This leaves stochastic cooling as the only potential option to improve the luminosity performance with cooling in the LHC. Stochastic cooling uses a broadband feedback system to increase the phase-space density by measuring the statistical fluctuations

[1] A proof of principle test [125, 126] is planned in RHIC for 2015.
[2] Analogue to the interactions between particles in a combined hot and cold gas.

(Schottky noise) of small sections (samples) of the particle beam and correcting for the sample averages. Thereby, the spread in the corresponding beam properties is gradually reduced. A more detailed introduction of the principle is given in the next section as basis for the calculations presented in this chapter. Stochastic cooling can be used at all energies. The cooling rate strongly depends on the number of particles (per bunch), the bunching ratio (bunch length/circumference) and the bandwidth of the system. In general, stochastic cooling is most efficient to cool very hot beams to a moderate "temperature".

8.3. Basic Principle of Stochastic Cooling

In the following, the principles of stochastic cooling are explained in a simplified picture. Since stochastic cooling is a very complex and complicated technique, this is only meant as an introduction to understand the background of the calculations which will follow, it does not aim to explain all technical details. This section is predicated on the explicit description given by D. Möhl in his lecture notes [120]. The Reader familiar with the theoretical background might continue in Section 8.4.

Transverse stochastic cooling acts on the single particle betatron oscillations, while longitudinally the momentum spread should be reduced. The basic idea is similar for both planes, however the technical realisation and importance of certain effects is somewhat different.

8.3.1. Transverse Cooling

Test Particle Picture

To start with, only one circulating particle is assumed in the storage ring. This particle will have position and angle deviations form the closed orbit, which the focusing system (quadrupoles and higher order magnets) tries to restore and bring the particle back to the central orbit. This results in betatron oscillations of the particle around the central orbit. The cooling system is designed to damp these oscillations, a basic setup is shown in Fig. 8.1. The particle's transverse position is measured by a pickup at each turn, while the measured signal is proportional to the position offset from the central trajectory. In a simplified manner of speaking, this signal is amplified and a sent to a kicker further downstream. The kicker then applies an angle correction proportional to the position error measured at the pickup.

Certainly, cooling can only work, if the correction signal is synchronised with the particle's arrival at the kicker. Moreover, Figure 8.2 illustrates the importance of the distance between pickup and kicker in terms of betatron phase advance. A particle measured at the pickup in the crest of its oscillation has a pure offset error, but zero angle (top picture). If the correction is applied a quarter of a wavelength later, it is possible to completely cancel the oscillation, since then the pure offset error has

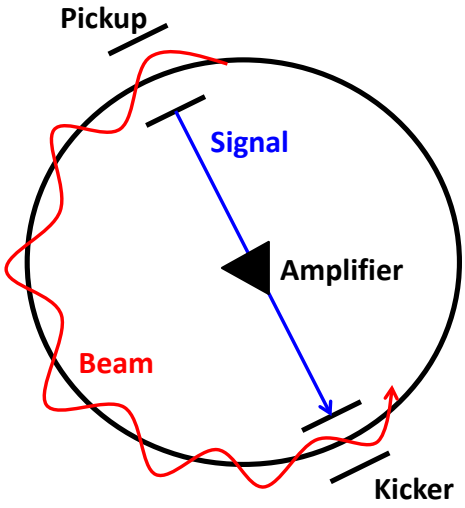

Figure 8.1.: Basic arrangement of a transverse stochastic cooling system. The beam position is measured at the pickup, the signal is amplified and sent across the ring to correct the angle by a kick proportional to the measured offset. Sketch based on Fig. 2.1 of [120].

transformed into a pure angle error. Only the angle is directly affected by a kick. For optimal transverse cooling efficiency, the pickup should be installed in a position with maximum amplitude error (crest of betatron oscillation) and the betatron phase advance between pickup and kicker should be about $(n + 1/2)\pi$, where n is an integer counting full oscillation periods. Since the signal is delayed in the cables and the particles' velocity is usually close to the speed of light, it is for the signal to take a "shortcut"[3]. The n additional oscillation periods allow more time for the signal to arrive at the kicker in time with the beam. For a particle passing the pickup in another phase (middle picture), the oscillation can only partly be cancelled and it takes several iterations to eliminate the oscillation. In the worst case, if the pickup measures zero amplitude at the zero-crossing of the oscillation (bottom picture), no correction is applied.

Sample Picture

Because of the finite bandwidth, W, of the cooling system, the short pulse induced by an off-axis particle passing the pickup is broadened into a pulse of length

$$T_s = \frac{1}{2W} \tag{8.1}$$

[3]either through the centre of the ring or by running backwards through the tunnel (see also Section 8.3.2)

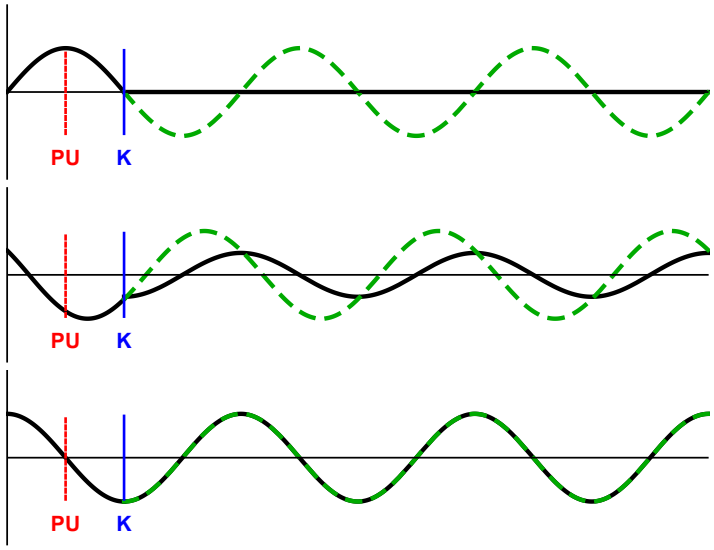

Figure 8.2.: Betatron oscillation of a single particle and the importance of the positions of pickup (PU) and kicker (K) for transverse cooling. The black solid line describes the corrected trajectory of the particle, while the green dashed line shows what would have been its path without correction, for PU and K spaced by $\pi/2$ but positioned at different phases of the oscillation. Sketch based on Fig. 2.2 of [120].

(Nyquist theorem) [129], as illustrated in Fig. 8.3. For simplification a rectangular approximation of the pulse is assumed. A test particle passing the system at t_0 will be affected by kicks of all particles passing during the time interval $t_0 \pm T_s/2$. These particles define the *sample of the test particle*. A uniform beam with N particles and of length T_{rev} (revolution time) consists of $n_s = T_{\mathrm{rev}}/T_s$ samples of length T_s, while each sample contains

$$N_s = \frac{N}{n_s} = \frac{N}{2WT_{\mathrm{rev}}} \tag{8.2}$$

particles.

In this picture, the beam is subdivided into n_s samples and the samples' center of mass are treated independently by the cooling system. By reducing the average sample error, the errors of the individual particles will slowly decrease. The test particle picture is still valid, in case W can be made large enough such $N_s = 1$.

Coherent and Incoherent Effects

In the test particle picture the cooling can be seen as two competing effects (see Fig. 8.4):

1. the *coherent effect* of the test particle upon itself via the cooling loop;

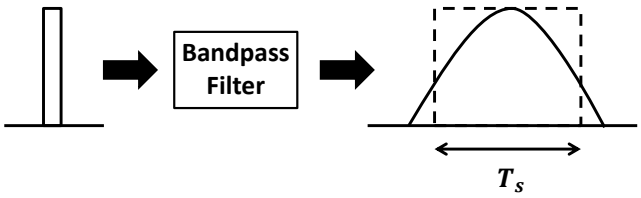

Figure 8.3.: Input and output signals of a low-pass system and rectangular approximation to the output pulse. Sketch based on Fig. 2.5 of [120].

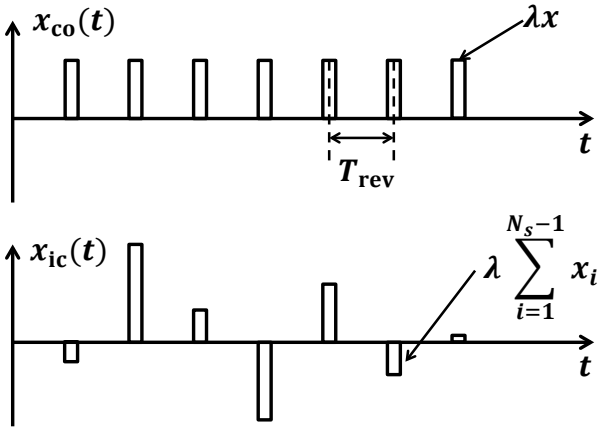

Figure 8.4.: Coherent and incoherent signals competing for cooling in the test particle picture. Sketch based on Fig. 2.7 of [120].

2. the *incoherent effect*, describing the perturbation of the test particle by the other sample members.

While the first effect is responsible for the desired cooling effect, the second introduces a heating term, counteracting the cooling.

Calling x the position error of the test particle at the pickup and the corresponding kick at the kicker Δx, the corrected error after the kicker would be

$$x_c = x + \Delta x.$$

Without any other particles present, the kick is proportional to the measured test particle's offset: $\Delta x = -\lambda x$, with λ as proportionality constant. However, with $N_s \gg 1$, the kicks of the other sample members have to be added:

$$x_c = x - \lambda x - \sum_{i=1}^{N_s-1} \lambda_i x_i$$

with

$$\Delta x = \underbrace{-\lambda x}_{\text{coherent}} \underbrace{- \sum_{i=1}^{N_s-1} \lambda_i x_i}_{\text{incoherent}} . \tag{8.3}$$

For a simplified rectangular signal, all sample particles see the same response and $\lambda_i = \lambda$. Hence,

$$\Delta x = -\lambda x - \lambda \sum_{i=1}^{N_s-1} x_i = -\lambda \sum_{i=1}^{N_s} x_i = -\lambda N_s \langle x \rangle_s,$$

where in the last equality the sum over the x_i of the whole sample was rewritten in terms of the average sample error

$$\langle x \rangle_s = \frac{1}{N_s} \sum_{i=1}^{N_s} x_i. \tag{8.4}$$

The corrected error becomes

$$x_c = x - \lambda N_s \langle x \rangle_s = x - g \langle x \rangle_s. \tag{8.5}$$

The factor $g \equiv \lambda N_s$ is called gain and can be interpreted as the *fraction of observed sample error corrected per turn.* g is proportional to the amplification λ, representing the electric gain of the system, and the number of sample particles N_s.

We made the transition from the test particle to the sample picture, showing the operational principle of the cooling system. The average sample error is measured and a correcting kick, proportional to $\langle x \rangle_s$, is applied to the test particle (and the other sample members). In this way the correction is independent of the single test particle itself, but relies on the statistical properties of the ensemble. In the rectangular response model, all particles in the sample receive the same correction $-g\langle x \rangle_s$, thus the sample average is reduced to $\langle x_c \rangle_s = (1 - g)\langle x \rangle_s$.

Approximating the Cooling Rate

To estimate the potential efficiency of the cooling system, quantified by the cooling rate, the amount of heating arising from the incoherent term must be evaluated. Finding an analytic description of the incoherent term is lengthy and will only be sketched here, however the reader should be directed to the well documented derivation in [120].

As a first crude approximation, it is assumed the incoherent term averages to zero, providing an estimate of the upper limit of the achievable performance. With cooling, an exponential decay of the test particle's error is expected with the number of turns

n: $x(t) = x_0 e^{-\alpha_{\mathrm{cool},n} n}$. The cooling rate per turn is then given by

$$\alpha_{\mathrm{cool},n} = -\frac{1}{x}\frac{dx}{dn} \approx -\frac{1}{x}\frac{\Delta x}{\Delta n} \overset{\Delta n=1}{\approx} = -\frac{\Delta x}{x} = \frac{g}{N_s} = \frac{g}{N} 2WT_{\mathrm{rev}}, \tag{8.6}$$

where Eq. (8.3) neglecting the incoherent term ($\Longrightarrow \Delta x = -\lambda x$) was inserted, using $g = \lambda N_s$. Recalling the interpretation of g as the fractional correction per turn, it is natural to assume $g \leq 1$. Correcting more than the measured sample error would lead to heating. $g = 1$ is set, to obtain an upper limit. By inserting Eq. (8.2) into Eq. (8.6), and dividing by the time required for one turn, T_{rev}, a first approximation of the cooling rate per second as a function of the total number of particles, N, and the system bandwidth, W, is obtained:

$$\alpha_{\mathrm{cool}} = \frac{2W}{N}. \tag{8.7}$$

To derive a more accurate equation of the cooling rate, the incoherent term should be treated as a random fluctuation, rather than assuming it averages to zero. In the sample picture, a random beam sample of N_s particles is considered and a correction $-g\langle x\rangle_s$ is applied, corresponding to its average error $\langle x\rangle_s$. Owing to the finite number of sample particles, $\langle x\rangle_s$ fluctuates around the beam average with a variance of $(\langle x\rangle_s)^2 \rightarrow x_{\mathrm{RMS}}^2/N_s$ (error to the mean), where x_{RMS} is the RMS beam error. By investigating the square of the change for a test particle over one turn, $\Delta(x^2) = x_c^2 - x^2$, it can be shown (see Chapter 2.7 in [120]) that by correcting $\langle x\rangle_s \rightarrow (1-g)\langle x\rangle_s$, the sample variance is reduced on average by $(2g - g^2)/N_s$. This leads to a cooling rate of

$$\alpha_{\mathrm{cool}} = \frac{W}{N}(2g - g^2). \tag{8.8}$$

The fact that the measured signal has to be amplified, makes it necessary to include a noise term, taking care of electronic noise in the pickup and preamplifier. This effect manifests itself the same way as noise by the other particles, thus it increases the incoherent term. To take this into account, Eq. (8.8) can be modified by replacing $g^2 \rightarrow g^2(1+U)$, where U is the ratio of the expected noise to the expected signal power, called *noise-to-signal ratio*. Note that the electric noise tends to be constant, whereas the signal decreases as the beam shrinks, therefore U might increase during cooling. To obtain the best cooling efficiency at all times, g has to be adjusted to compensate for the changing U, such that α_{cool} is always maximized at $g = g_0 = 1/(1+U)$.

For full correction and in case the sample population is constant, the sample error will be zero after the kicker and cooling stops, as no error signal is observed. However, due to the momentum spread, particles perform a synchrotron oscillation around the design particle ($\Delta p/p = 0$) and will move to other samples. This *mixing* of the sample populations re-randomises the distribution such that the sample error reappears, until ideally all particles have zero error. If the mixing is fast and a complete re-randomisation happens between kicker and pickup, the previous assumption of ran-

dom samples still holds. Nevertheless, incomplete mixing slows down the cooling. If it takes M turns for a particle of typical momentum error to move by one sample length, T_s, with respect to the design particle, then the cooling rate can expected to be M times slower. $M \geq 1$ is called the *mixing factor* and by definition

$$M = \frac{T_s f_{\mathrm{rev}}}{\eta \frac{\Delta p}{p}}, \tag{8.9}$$

where η is the phase-slip-factor of Eq. (2.15) and f_{rev} is the revolution frequency. In case of the rectangular response model, T_s is given by Eq. (8.1), however in general T_s depends on the kick frequency and thus is proportional to the the center frequency of the system. Because the test particle is affected by the kicks of the other particles as long as they are in the same sample (for M rather than for 1 turn), the incoherent heating is increased by a factor M. Equation (8.8) can account for that by the substitution $g^2(1+U) \rightarrow g^2(M+U)$. It is important to take care that there is good mixing ($M \rightarrow 1$), since the slower the mixing the slower the cooling.

Unfortunately, the mixing is also present on the way between pickup and kicker. The signal path is synchronised to the travel time of the design particle. If the test particle has $\Delta p/p \neq 0$, it arrives too early or late at the kicker with respect to its correction signal. In a regular lattice, the travel time from pickup to kicker is a fixed fraction of the time required from kicker to pickup. A pickup-to-kicker mixing factor, $\tilde{M}$, can then be defined proportionally to $M = \alpha_M \tilde{M}$, with $\alpha_M \approx \alpha_c$ and α_c as the momentum compaction factor given by Eq. (2.13). Without proof, the coherent factor in Eq. (8.8) can be modified as $g \rightarrow g(1-\tilde{M}^{-2})$ to account for the bad mixing between observation and correction.

Gathering the considerations just made leads to a final equation for the cooling rate:

$$\alpha_{\mathrm{cool}} = \frac{W}{N}\left[2g(1-\tilde{M}^{-2}) - g^2(M+U)\right]. \tag{8.10}$$

This equation has a maximum

$$\alpha_{\mathrm{cool},0} = \frac{W}{N}\left[\frac{(1-\tilde{M}^{-2})^2}{M+U}\right] \tag{8.11}$$

at

$$g = g_0 = \frac{1-\tilde{M}^{-2}}{M+U}.$$

It is desired to keep the unwanted mixing between observation and correction small, $\tilde{M}^{-2} \rightarrow 0$, and observe a freshly randomised beam in the next turn at the pickup, $M \rightarrow 1$. This situation can be obtained by a clever choice of bending and focusing properties of the storage ring, however, this is no option in the LHC, where there is little freedom to change the existing lattice. In the best of all cases ($M = 1$, $U = 0$

and $\tilde{M}^{-2} = 0$), Eq. (8.11) yields

$$\alpha_{\text{cool, max}} = W/N.$$

Comparing this result to the first crude estimate in Eq. 8.7, it is found that neglecting the incoherent term leads to an equation overestimating the optimal cooling rate only by a factor 2.

The considerations made so far are based on a coasting beam. Bunched beam stochastic cooling, as needed in the LHC, is more difficult. From the time-domain point of view, it is clear that with decreasing bunch length the sample population increases, which reduces the cooling rate accordingly. An upper limit for the cooling rate in the bunch beam case can be estimated from the coasting beam formalism, by considering the bunch as a part of the coasting beam and replacing $N \rightarrow N_b/B_f$ in Eq. (8.11):

$$\alpha_{\text{cool}} \leq \frac{W}{N_b/B_f}\left[\frac{(1-\tilde{M}^{-2})^2}{M+U}\right] < \frac{W}{N_b/B_f}, \tag{8.12}$$

where N_b is the number of particles per bunch and B_f =[total length of the bunch/ circumference] the bunching factor.

8.3.2. Longitudinal Cooling

The momentum spread leads to a spread in the revolution frequency, thus particles will arrive at the pickup at slightly different times relative to design particle ($\Delta p/p = 0$). The difference of the average arrival times of a sample in two consecutive turns, t_0 and t_1, gives indication of the average momentum error of the sample. For $\Delta p/p \gtrless 0$, a correction proportional to the momentum deviation, but with opposite sign (kick $\propto -\Delta p/p \lessgtr 0$), is required to obtain the optimum $\Delta p/p = 0$. Above transition, the path length of a particle with, for instance, larger momentum is increased and it will arrive later compared to the reference particle. Thus, $\Delta t = t_0 - t_1 < 0$ indicates the direction and strength of the desired correction. If the average momentum spread of the sample is already $\Delta p/p = 0$, the difference in the arrival times between two consecutive turns is $\Delta t = 0$ and no correction is required. Figure 8.5 sketches the measurement of Δt for a set of samples, separated by the black boxes. The dots show the particles positions within the beam and the dashed lines indicate the sample averages. In the third row, the two upper pictures are overlaid to show the differences between the two turns more clearly. The black arrows on the bottom indicate the applied kicks to each sample.

To combine the information of the previous and current turn, a so-called Notch-filter is used. This filter splits the signal in two parts, delays the first part by exactly on revolution, and takes the difference of the second part from current turn and the delayed part from the previous turn. It is essential for the performance of the cooling that the delay line is exactly one turn long, to filter out the revolution line, so that for

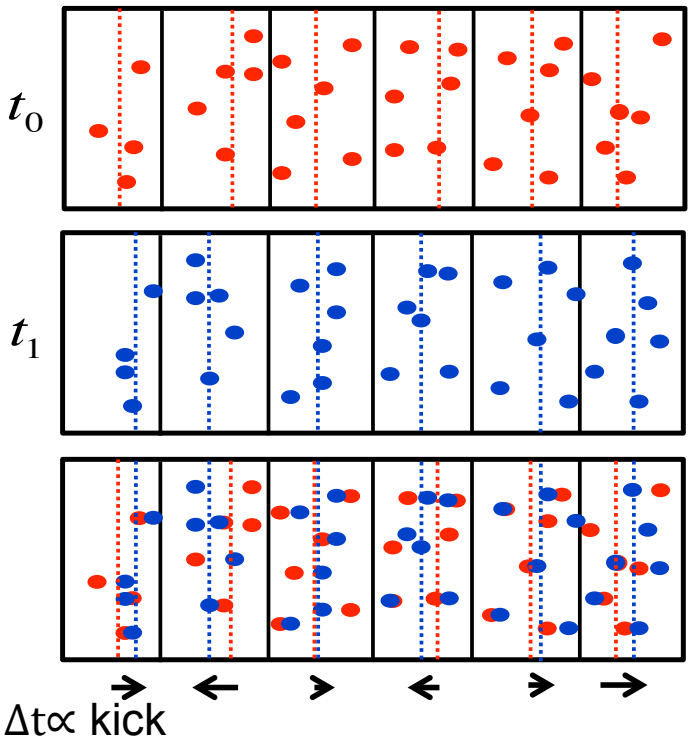

Figure 8.5.: Sketch measuring Δt per sample for longitudinal stochastic cooling. The black boxes separate the samples, the dots show the single particles and the dashed lines indicate the sample average. In the bottom row, the two pictures above are overlaid and the length of the arrows indicate the difference between the turns, which is proportional to the strength and direction of the correction.

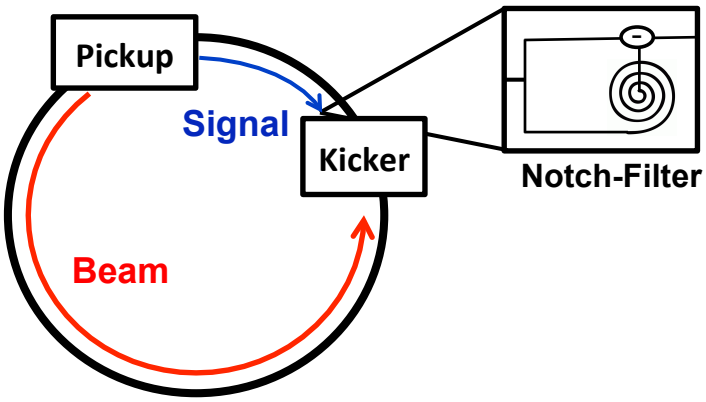

Figure 8.6.: Tunnel arrangement for longitudinal stochastic cooling in a large ring.

$\Delta p/p = 0 \Rightarrow \Delta t = 0$.

For longitudinal cooling, the kicker is an RF cavity with a longitudinal field, exerting a longitudinal kick, which changes the particles momentum proportional to the detected error.

A sketch of a possible installation for longitudinal stochastic cooling in a large ring, e.g. the LHC, is shown in Fig. 8.6. To achieve a synchronisation between particle and signal, the signal path has to be shorter than the beam travel distance between pickup and kicker. Arranging a signal shortcut by pulling a cable across the ring, as done in small machines, would require digging a new tunnel with a length of several kilometres in case of the LHC, which is not affordable. Therefore, the pickup signal is led through the tunnel in opposite direction to the beam. A transverse cooling system in the LHC, would be confronted with the same problem and requires the same technique to transmit the signals.

8.4. Experimental Setup for Proof of Principle Test

To demonstrate that stochastic cooling can work for heavy ions in the LHC, a test with a minimal cooling system is considered. The existing Schottky pickups centred on 4.8 GHz would be used to measure the beam signal. A single longitudinal or transverse cavity at the same frequency would be installed in IR4 to apply the correction to Beam 1. To enhance the cooling efficiency, a low intensity test bunch would be cooled and, depending on the cooled plane, either its length or transverse emittance reduction would be observed over time.

As the work presented here was performed during the first long shutdown of the LHC, which had not ended by the time of writing, no experimental results are available yet. In general, long time-scales have to be expected to plan and conduct experiments in the LHC. The earliest date to perform new measurements on heavy ions would be November 2015.

In this section the experimental setup of this proof of principle test is discussed, taking into account the required hardware (Schottky pickups, cooling cavity, signal processing), potential tunnel locations to install the equipment, commissioning and operation of the system, as well as required beam parameters. Estimates of the expected performance are given.

8.4.1. LHC Schottky Signals

Each particle of charge Ze in a bunched beam follows synchrotron oscillations of the frequency f_s ($\ll f_{\mathrm{rev}}$), having a random amplitude and phase. This results in a time difference with respect to the synchronous particle, circulating with f_{rev}, thus causes a phase modulation of each particle of the bunched beam. The longitudinal Schottky spectrum appears as a set of synchrotron satellite lines spaced by f_s around each

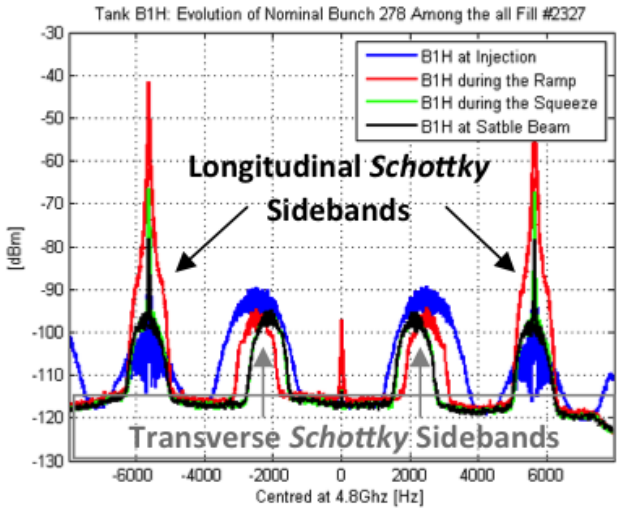

Figure 8.7.: Longitudinal and transverse sidebands of the detected LHC Schottky signal with 1.1×10^8 Pb^{82+} ions. Courtesy of M. Wendt [28].

revolution harmonic hf_{rev}.

Similarly to the longitudinal synchrotron oscillation, the transverse betatron oscillation around the central orbit ($f_\beta > f_{\mathrm{rev}}$) introduces a frequency modulation in the Schottky spectrum. Betatron sidebands appear at a distance of $\pm q f_{\mathrm{rev}}$ around the revolution harmonics, where q is the non-integer part of the tune.

Figure 8.7 shows longitudinal and transverse Schottky signals of two harmonics around $hf_{\mathrm{rev}} \approx 4.8$ GHz of a Pb beam detected by a broadband transverse Schottky pickup in the LHC in different operating conditions. The narrow peaks of the longitudinal harmonics at around ± 5600 Hz express the coherent signal contents, i.e., the amplitude is $\propto N$. The "hump" below the peak displays the incoherent longitudinal Schottky signal. Because of the random phase, the amplitude is reduced to $\propto \sqrt{N}$. The individual synchrotron frequency satellite lines become only visible if zoomed in closely.

As can be seen from Fig. 8.7, the detection of the transverse Schottky signals for Pb ions in the LHC works well. With a few minor modifications the detection of the longitudinal Schottky signals can be improved to provide signals for the feasibility test. For instance, one could improve the longitudinal Schottky signal level by summing the signal from the two adjacent slotted-waveguide couplers and operating the pickup at a different harmonic in the range $4.6\,\mathrm{GHz} < hf_{\mathrm{rev}} < 5.0\,\mathrm{GHz}$.

8.4.2. Cavity Design

A preliminary design for a longitudinal test cavity was developed by S. Verdú-Andrés and is shown in Fig. 8.8. Its characteristics are listed in Table 8.1. The design was scaled from the longitudinal kicker in RHIC to suit the 4.8 GHz centre frequency of the

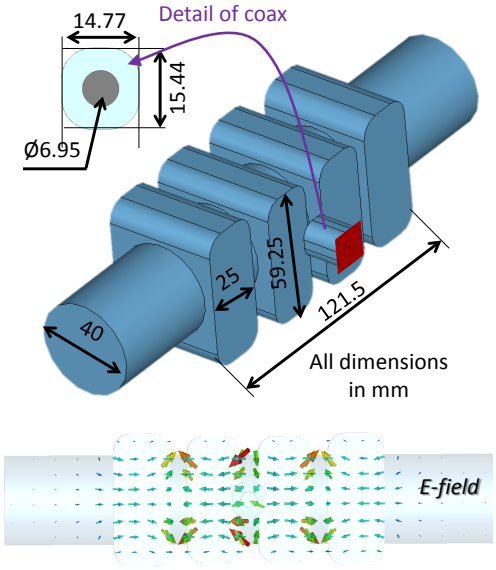

Figure 8.8.: Preliminary design of a longitudinal stochastic cooling test cavity centred on 4.8 GHz. Courtesy of S. Verdú-Andrés [130].

f	R/Q	Q_{load}	V_{RMS}	t_{fill}
4.8 GHz	142 Ω	2150	6 kV	143 ns

Table 8.1.: Preliminary test cavity parameters.

existing LHC Schottky pickups [130].

Test Cavity Characteristics

The voltage of $V_{\text{RMS}} = 6\,\text{kV}$ corresponds to the longitudinal voltage excited along the beam axis of the kicker for a maximum input power of 40 W provided by the amplifier. The test kicker is designed to increase the geometric shunt impedance[4], R/Q. The higher the R/Q, the lower the power requirements, such that higher voltages can be attained with the available power, which increases the cooling effect. Finding an optimum loaded[5] Q is important, as it directly affects the power requirement and the filling time, t_{fill}, (time to reach peak field) of the structure. The larger the Q, the lower the power needed to reach a given voltage, but also the longer t_{fill} becomes. The

[4] $R/Q = |V|^2/(2\omega W)$, where the shunt impedance, R, is given by $R = |V|^2/(2P_{\text{loss}})$ with V as the acceleration voltage of the cavity and P_{loss} the power lost in the cavity walls due to ohmic heating. The quality factor, Q, is defined as $Q = \omega W/P_{\text{loss}}$, where $\omega = 2\pi f$ and W is the stored energy. The Q factor is 2π times the number of RF cycles it takes to dissipate the energy stored in the cavity. It also determines the maximum energy the cavity can fill to with a given input power [131].

[5] Ohmic losses are not the only loss mechanism in a cavity. The *loaded* Q factor includes also losses from other sources, e.g., from the couplers, and is defined as $Q_{\text{load}} = \omega W/P_{\text{tot}}$, where P_{tot} is the total power loss.

available power is limited by the amplifier. The filling time will be limited by the time structure (bunch spacing) of the beam. With an expected bunch spacing of alternating 100 ns and 225 ns in 2015 (see Chapter 6), a filling time of $t_{\text{fill}} = 143\,\text{ns}$ means that the previous and/or subsequent bunch will receive an unwanted partial kick. Since the cavity signal is devoted to correct noise signals measured on the test bunch, the impact on the neighbouring bunches acts as a noise-like (heating) source, which could lead to additional emittance growth and particle losses. However, these bunches would only feel a reduced signal, thus the disturbances are expected to be small.

Unlike the RHIC transverse cavity design, or a future system for LHC operation, the cavity for this test would have a fixed aperture, constraining the inner radius to be compatible with the beam size at injection. Moreover, the cavity's pipe radius, r, must be small enough, such that its cut-off frequency, f_c, is higher than the operation frequency, $f = 4.8\,\text{GHz}$. In combination with a sufficiently long pipe, this ensures the frequencies excited in the cavity are attenuated exponentially and do not enter the connected beam pipe (with a larger radius), where they could travel over long distances and interfere with the pickup signal.

Cut-off Frequency

The cut-off frequency of an electromagnetic waveguide is the lowest frequency for which a particular mode will propagate in it. For transverse magnetic (TM) modes of a circular waveguide, f_c is determined by the following equation [132]:

$$f_c = \frac{c}{2\pi r} p_{nm}, \tag{8.13}$$

where p_{nm} is the mth root of the Bessel function, $J_n(x)$, of the first kind, which satisfies $J_n(p_{nm}) = 0$. In case of transverse electric (TE) modes p_{nm} is replaced by p'_{nm} in Eq. (8.13), where p'_{nm} are the roots of $J'_n(x)$, which is the derivative of J_n with respect to its argument. Values of p_{nm} and p'_{nm} are given in mathematical tables [132]; the lowest $p_{nm} = p_{01} = 2.405$, thus the first TM mode to propagate is TM_{01}. Since this is greater than $p'_{11} = 1.841$ for the lowest order TE mode, the TE_{11} mode is the dominant mode of a circular waveguide.

As visible in Fig. 8.8, the kickers are not simple rectangular or circular cavities and will operate on modes with both longitudinal and transverse field components. However, the TM_{01} mode is the first mode that may propagate along the beam pipe for a longitudinal kicker and the TE_{11} mode is the first mode that may propagate for a transverse kicker. Looking at the field distribution in the beam pipe of the longitudinal kicker on the bottom of Fig. 8.8, the RF field pattern is such that only monopole, longitudinal modes can be excited. This will be similar for transverse modes in a transverse kicker. To obtain $f_c > 4.8\,\text{GHz}$ a pipe radius of $r < 2.4\,\text{cm}$ and $r < 1.8\,\text{cm}$ is required to attenuate the TM_{01} and TE_{11} mode, respectively.

Mode Propagation

If the radius, r, of the beam-pipe surrounding the cavity is such that the modes excited are above the cut-off frequency ($f > f_c$), they will propagate, but their power is attenuated exponentially as $P(z) = P_0 \exp[-2\beta_c z]$, with an attenuation constant of [64]

$$\beta_c(f) = \sqrt{\frac{\varepsilon}{\mu}} \frac{1}{\sigma \delta_c} \left(\frac{C_{\text{pipe}}}{2A_{\text{cross}}} \right) \frac{\left(\frac{f}{f_c}\right)^{1/2}}{\left(1 - \frac{f_c^2}{f^2}\right)^{1/2}} \left[\xi_c + \eta_c \left(\frac{f_c}{f} \right)^2 \right]. \tag{8.14}$$

Here $\varepsilon = \varepsilon_0$ is the permittivity and $\mu = \mu_0$ the permeability of vacuum, since the LHC beam pipe is under high vacuum. The conductivity of the pipe wall is given by σ, while C_{pipe} is the circumference and A_{cross} is the area of the pipe cross-section[6]. The skin depth at the cut-off frequency is $\delta_c = (1/(\pi \mu_{\text{cu}} f_c \sigma)^{1/2})$, with $\mu_{\text{cu}} = 1.2566\,\mu\text{H/m}$ being the permeability of copper. ξ_c and η_c are dimensionless numbers of the order of unity. In a circular waveguide, $\eta_c = 0$ and $\xi_c = 1$ for TM modes and $\eta_c = 1$ and $\xi_c = 1/(p'^2_{nm} - n^2)$ for TE modes [133].

After a distance $z_e = 1/(2\beta_c)$ the power of the mode has decayed to $1/e$ of its initial value. Figure 8.9 shows the propagation distance $1/(2\beta_c)$ of the TE_{01}, TE_{11} and TM_{01} modes as a function of the pipe radius at $f = 4.8\,\text{GHz}$. The system will be installed in a warm area and thus the conductivity of copper at room temperature, $\sigma = 1/17\,\text{n}\Omega\text{m}$ [134], was used. The curves start at the radius corresponding to the cut-off frequency of the given mode. Already for slightly larger radii, the modes can propagate hundreds of metres. This implies that, as soon as $f_c < 4.8\,\text{GHz}$, the modes cannot be confined in the cavity, but propagate into the ring. In the long straight section (LSS) the beam pipe radius is 40 mm. For $f < f_c$, β_c becomes imaginary and the mode is attenuated very rapidly in the first section directly after the resonant cavity and does not propagate.

In the current planning for the layout (Fig. 8.10), the locations of the cavity and Schottky monitors are separated by only about 300 m, which could become critical in case of propagation, since the kicker signal could interact with the pickup. It is strongly recommended to choose a pipe radius small enough such that $f_c > 4.8\,\text{GHz}$ in order to avoid that the modes leave the cavity.

A design for a transverse test cavity could be as well obtained by modifying an existing RHIC design. The RHIC transverse cooling system uses frequencies in the range of 4.8 to 7.8 GHz, thus a transverse cavity, centred at the desired 4.8 GHz would be already available. However, its pipe diameter of 2 cm in the closed position, has to be scaled up to the required $\sim 3.6\,\text{cm}$, as discussed in the next section.

[6] For a circular waveguide, $(C_{\text{pipe}}/2A_{\text{cross}}) = 1/r$, thus the attenuation rate is inversely proportional to the beam pipe radius, meaning that the larger the pipe, the longer it takes to attenuate the mode.

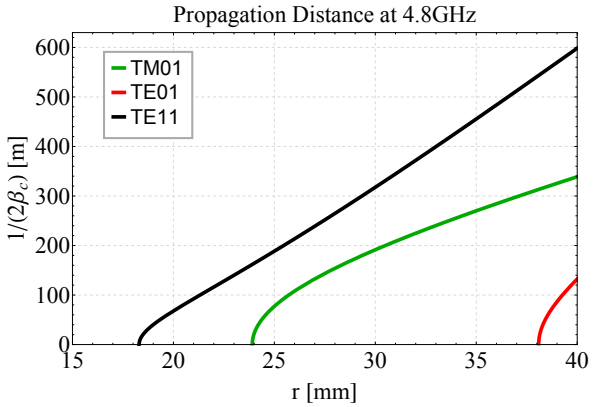

Figure 8.9.: Propagation distance of the TE_{01} TE_{11} and TM_{01} modes as a function of the beam pipe radius at 4.8 GHz. A conductivity of $\sigma = 1/17\,\mathrm{n\Omega m}$ for copper at room temperature was used.

8.4.3. Experiment Layout and Locations

The schematic machine layout in IR4 (boxes on the central orbit) is displayed in Fig. 8.10 together with the horizontal (blue) and vertical (red) 10σ beam envelopes at injection energy. A cavity with a fixed aperture of about 4 cm diameter would not meet the impedance requirements[7] for p-p operation. Therefore, the cavity should be installed in a technical stop preceding the Pb-Pb operation and removed afterwards. Short term installations in the beam pipe are possible in certain prepared locations, highlighted in green in Fig. 8.10. The Schottky pickup positions are highlighted in orange. The choice of the Schottky pickup depends on the plane to be cooled, since the left (right) pickup measures in the vertical (horizontal) plane. Concerning the cavity location, the right-hand side position provides a greater margin in terms of beam size. Here, a cavity radius of about 2 cm is required to be compatible with the beam size at injection. For the final design, exact aperture calculations have to be performed to validate the pipe radius and to ensure the collimation hierarchy is not perturbed.

The preferred cavity location is about 253 m or 311 m upstream of either of the two Schottky pickups, which means the beam has to travel almost a full turn before being corrected. This is not an optimal arrangement, since the unwanted mixing between observation and correction will be maximised, while the wanted mixing between kicker and pickup can only happen over a short distance. It should be considered to measure and correct only every second turn, so that the beam has time to mix. Moreover, this implies that the pickup signal has to be delayed by almost a full turn before being sent to the kicker to arrive in time with the beam.

A block diagram, sketching the possible signal processing and transport for a reduced cooling system is displayed in Fig. 8.11, featuring only one kicker cavity in one plane. Given the length of the LHC, it is the easiest to use optical cables for signal

[7] For reasons of beam stability, each machine has an impedance budget which should not be exceeded.

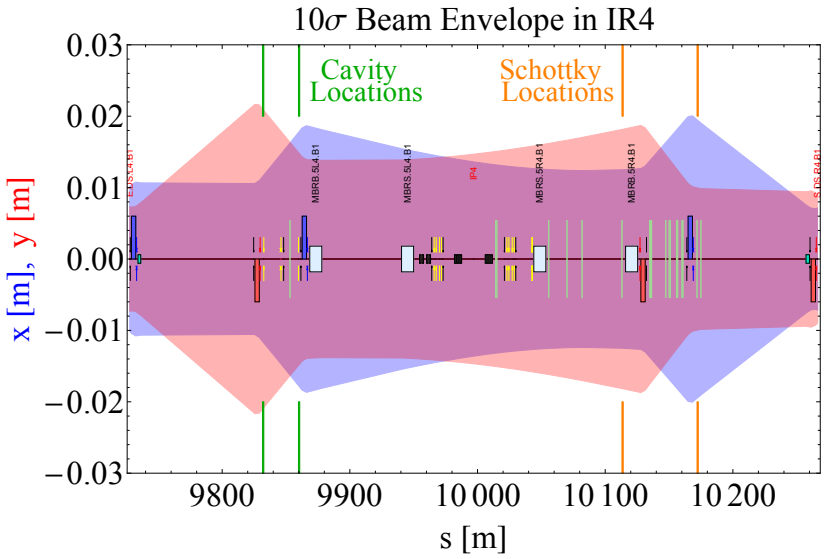

Figure 8.10.: IR4 layout and 10σ horizontal (blue) and vertical (red) beam envelopes at injection energy. s marks the position around the LHC ring, $s = 0$ in IP1. Potential positions for the test cavity are marked in green, the Schottky pickups of Beam 1 are highlighted in orange. The beam line elements are indicated as boxes on the central orbit.

transportation. The measured pickup signal is processed and converted into an optical signal (E/O) before being amplified (Amp.) and delayed by the pickup-to-kicker distance the beam has to travel. This requires a thermal isolation box to cool the delay line of more than 26 km and guarantee a constant length. The precise length is set at the pico metre scale with a piezo optical delay. After a second amplification, the installations differ for a longitudinal or transverse system. In case of longitudinal cooling, the signal is split and processed in a notch-filter; half of it is delayed by exactly a full turn, while the difference of the other half and the 1-turn-delay signal from the previous turn is taken, followed by a conversion back into an electrical signal. This filtering is not necessary for transverse cooling and only a conversion from optical back to electrical signals is performed. The output signal is monitored on a spectrum analyser to ensure the quality. The signal is amplified, and potentially sent through a bandpass filter, before the final signal is obtained by comparing with reference Beam Transfer Functions (BTF) and sent via a coaxial cable to the kicker.

8.4.4. Cooling System Commissioning and Operation

After the system has been installed in the tunnel, it needs to be commissioned before it is ready for operation.

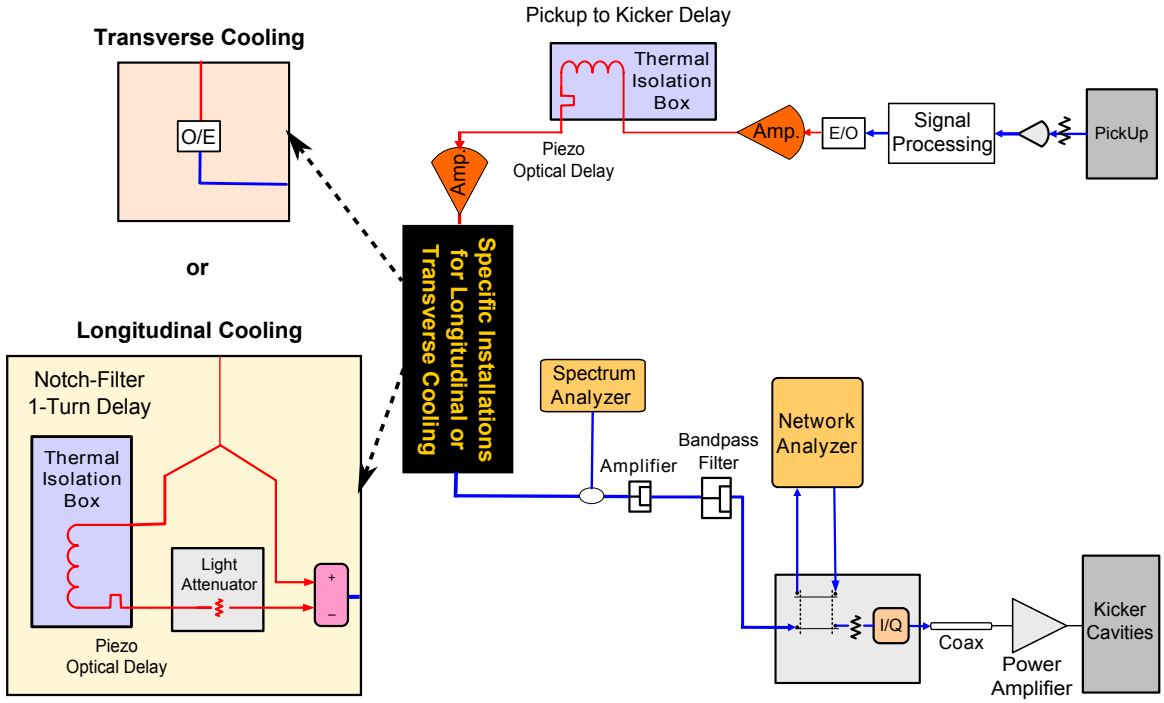

Figure 8.11.: Low level block diagram for minimised stochastic cooling system dedicated to proof of principle test. The black box contains either the installations for transverse or longitudinal cooling, shown in the extracted boxes on the left. Inspired by the RHIC signal processing chain [135].

Fine-Tuning the Cavity Resonant Frequency

To achieve the best efficiency of the cooling system with a small error on the applied kick, it has to be confirmed that the cavity is operating at the correct frequency. During the manufacturing, the cavity's resonance frequency is measured in the lab and adjusted to the desired value with tuning screws, which extend into the resonance volume of the cavity. One has to take care that the resonant frequency, measured in air and at room temperature, is extrapolated and corrected to fit tunnel conditions. It is possible that the cavity gets slightly detuned during transport and installation. Unfortunately, in the tunnel the cavity is sealed inside a vacuum tank and the tuning screws are not accessible. Once installed, the only possibility to adjust the resonant frequency is by changing the temperature with heaters mounted inside the vacuum tank. Heating up the cavity leads to a small expansion of the material, which slightly changes the cavity's resonant frequency. This procedure can only be used for the final fine-tuning and frequency stabilisation, since the possible frequency change is in the order of only a few parts in a thousand.

To measure the resonant frequency of the cavity, the transmission coefficient S_{21}

[132] of the cavity is measured with a network analyser. Power is injected on port 2 at a certain frequency and the power output at port 1 is measured. A frequency scan will show a dip at the resonant frequency, where most of the power is absorbed.

This measurement is independent of the beam in the machine and could be performed at any time in the cycle. The cavity temperature has to be controlled and kept constant to maintain the desired resonance frequency.

Optimising Delays and Signals

To avoid unwanted beam losses and to achieve a good signal and kick quality, the beam should go through the center of the pickup and cavity. Since the cavity cannot be moved, an orbit scan, using external orbit bumps, should be used to move the beam inside the cavity. The beam loss rate as function of the beam position is monitored to find the optimal trajectory.

The Schottky signal quality will improve the closer the pickup plates are placed to the beam and the better the beam is centred between the plates. The two pickup plates can be moved independently to easily centre the beam. While moving the pickup plates the Schottky signals will change. For a transverse Schottky signal, the difference of the measurements at the two pickup plates is taken. Since the revolution and coherent signals are equal for both plates, the better the beam is centred, the higher is the power in the betatron side-bands and the lower is the power in the revolution line, which is the desired shape. It is also possible to move the pickup plates in the longitudinal direction by a few millimetres to ensure the beam signal arrives at the same time at both plates. To obtain a high transverse cooling efficiency, the ratio of the power integral in the betatron sidebands over the revolution line (filtering the coherent signal) must be as large as possible for all kicker frequencies at a given pickup plate distance. This ensures a good signal at all cooling frequencies of the system. The discussed test, however, cools at one frequency only.

The notch-filter is only needed for longitudinal cooling and calculates the difference of the just measured signal and the signal of the previous turn. The delay must exactly be one revolution, such that the dominant revolution line and the coherent signal are suppressed and the different particle arrival times with respect to the synchronous particle become visible. Note that the filtering has to be applied before amplification, otherwise unusable parts of the signal are amplified, taking power from the amplifier, that is consequently not available for cooling. The spectrum analyser should be used to confirm that deep notches show the absence of the revolution line. To improve the signal, the delay length could be varied by either adjusting the temperature in the thermal isolation box or by the piezo optical delay. Figure 8.12 shows notch-filtered longitudinal Schottky signals, measured on the Blue beam at RHIC during the setup of the stochastic cooling system at the beginning of the 2014 high energy Au-Au run, after a first optimisation of the signal. The red trace shows the signal without cooling, the yellow trace was measured with one operating longitudinal cooling cavity. The *signal suppression* (reduction of the "shoulders" of the signal), visible on the yellow

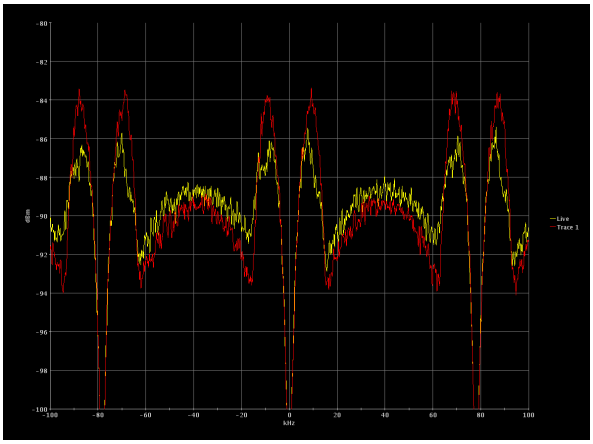

Figure 8.12.: Longitudinal Schottky signals of the Blue beam at RHIC after the notch filter. The red trace shows the signal with cooling switched off, the yellow line was measured with one longitudinal cooling cavity operating. The reduction of the "shoulders" of the signal shows that cooling is working. Courtesy of K. Mernick.

line compared to the red, shows that the cooling is working.

Measuring Reference Beam Transfer Functions

By driving a beam with a periodic signal and measuring the resulting beam response the Beam Transfer Function (BTF) is obtained. With circulating beam in the machine, a network analyser sweeps over a set of frequencies, which excite the cavity under investigation. The beam response is then measured at the pickup and brought back to the network analyser, where the S_{21} measurement gives the BTF as a function of frequency. An example of a transverse BTF plotted in polar coordinates and measured on the Yellow beam in RHIC during the stochastic cooling commissioning at the beginning of the 2014 Au-Au run is shown in Figure 8.13.

The orientation and shape of the function in the complex plane is influenced by the phase and total gain of the signal. The gain has two contribution: the electrical gain from the I/Q modulator, which is the last element before the signal is sent to the cavity, and the loop gain, which is introduced in the cavity and pickup by the beam itself. While the beam is cooled, the loop gain changes and the I/Q modulator gain should be adjusted for compensation to keep the total gain, and with it the BTF, constant. One has to make sure that no phase shift occurs.

The gain and phase settings for good cooling produce a BTF that is symmetric and well centred around the horizontal axis, as the one in Fig. 8.13. Once the correct settings are found by varying the phase and gain of the I/Q, a reference BTF is saved. During cooling, the feedback loop corrects the I/Q gain according to the reference. During a BTF measurement the cavity is not available for cooling, thus the feedback correction should only be done from time to time. For the feasibility experiment,

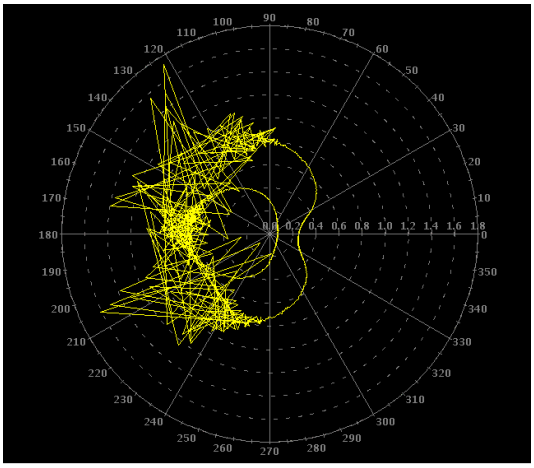

Figure 8.13.: Horizontal BTF, displayed in polar coordinates, used as reference for feedback loop, measured on the Yellow beam at RHIC. The spikes on the left hand side arise from the modulation of the betratron sidebands caused by the synchrotron motion. Courtesy of K. Mernick.

with only one operating cavity, the feedback correction could be performed by hand when required ($\simeq 15\,\mathrm{min}$). To prove that the cooling is working, a suppression on the Schottky signal can be measured.

8.4.5. Beam Setup

The aim of the experiment is to observe the cooling effect in terms of bunch length or emittance reduction on a test bunch. According to Eq. (8.12), the cooling time is given by $1/\alpha_{\mathrm{cool}} \propto N_b/(W\sigma_s)$. Hence, the cooling is fast for low intensity, long bunches cooled with a broad bandwidth system. The presented test setup has a very narrow bandwidth and the cooling will be slow, thus the expected effect is small. Moreover, at 6.5 or $7Z\,\mathrm{TeV}$ the radiation damping is strong enough to lead to a natural shrinkage of the bunch length and vertical emittance, which has to be distinguished from the cooling effect. Therefore, the reduction should be measured on an initially long, low intensity test bunch with respect to a non-cooled witness bunch featuring the same beam properties. Furthermore, the observed bunches should be non-colliding to obtain a clean signal with the least disturbances from other sources as possible.

In general, it is desired to perform the experiment as parasitically as possible, in order to keep the perturbation of the physics run to a minimum. The experiment could be run in several setups:

1. Using the pilot or first bunch of the first train, these feature the lowest intensity in the normal filling scheme.
2. Changing the filling scheme and placing two additional non-colliding, low intensity test bunches with the same properties between the usual trains used for physics operation.

3. Performing a dedicated experiment with only the two test bunches in the machine.

The first option would be the least perturbing, since the filling scheme would not have to be changed and measurements would be taken parallel to normal operation. However, the bunch spacing is small and neighbouring bunches might be disturbed. This also means that the direct neighbours, which would have similar beam parameters, since they originate from the same LEIR batch, cannot be used as the witness bunch. The leading bunch of the next train could be used instead. Moreover, the experiment could be carried out either at injection or collision energy. Cooling at injection would be possible, because the test cavity will have a fixed aperture. A future full cooling system would need a mechanism to open at injection and close at top energy, due to the high frequencies and the small apertures required. The bunches under consideration provide the longest observation time, when conducting the experiment at the injection plateau, while the remaining beam is injected. Nevertheless, the time available for cooling would be limited to only about 30 min[8]. Cooling during physics would only be limited by the fill length, but these bunches are colliding.

Changing the filling scheme potentially leads to a reduction of the total number bunches, which reduces the luminosity. On the other hand, the intensity of the test bunches could be freely chosen (to a certain extent) to enhance the cooling. Single bunches can be injected into the LHC with a minimal spacing of 900 ns[9], which is definitely enough time for the cavity field to rise and decay without affecting other bunches. If a single bunch is injected just in front the abort gap before filling for physics, the cooling of this bunch could be observed during the filling process and be over-injected (kicked out) by the last train[10]. A modification of filling scheme would not be necessary.

In case an observation time at injection of 30 min is not sufficient to clearly observe an effect or a parasitic measurement during physics is not possible, a dedicated experiment would have to be conducted. This would have the advantage that all parameters could be freely chosen. However, since the commissioning is expected to be lengthy, the time available might be too short for optimisations. The first two scenarios could be done during all fills of the entire run, leaving room for variations and tests.

Possible beam parameters of dedicated bunches with optimised properties are listed in Table 8.2. The intensity is chosen to be the lowest deliverable to the LHC, which is limited by the SPS instrumentation [48]. Due to the lower intensity, the emittances will be reduced as well. Since the cooling rate increases with σ_s, bunch lengths limited by the size of the bucket are assumed, which could be obtained by applying longitudinal blow-up before starting the cooling.

[8] average time required to fill the LHC with beam

[9] time the LHC injection kicker needs to rise

[10] When filling the LHC, the first bunch is always injected into the first bucket, subsequent buckets are filled (according to the injection scheme) until the abort gap, which must have a minimum particle-free length of 3 μs [40] to give the dump kickers sufficient time to rise.

N_b	ϵ_n	σ_s
4×10^7 ions/bunch	$1\,\mu$m	12.5 cm

Table 8.2.: Bunch parameters for testing stochastic cooling.

8.4.6. Expected Performance

The cooling efficiency depends not only on the beam parameters, but also on cooling system settings and available kick strength. CTE simulations of a non-colliding bunch, with the parameters given in Table 8.2, were performed for various system settings at injection and top energy. The configuration accomplishing the best cooling result is shown in Fig. 8.14. Each row of plots represents the effect of cooling in a different plane. For each simulation run, a narrow bandwidth system, corresponding to only one cavity centred at 4.8 GHz, was cooling in the longitudinal (top), horizontal (middle) or vertical (bottom) plane. Only the beam size evolution in the cooled plane (bunch length, horizontal or vertical emittance, respectively) is shown. Since the cooling rate is small, the effect on the other planes or the intensity is marginal. The evolution of the cooled bunch (black) is compared to a non-cooled bunch (red), for cooling at injection energy (left) and $6.5Z$ TeV (right).

At $6.5Z$ TeV the radiation damping is strong enough to lead to a shrinkage of the bunch length and vertical emittance without cooling. An uncoupled machine is assumed, thus the IBS dominates the radiation damping in the horizontal plane and a small growth is observed. Applying cooling in the given plane, reduces the beam longitudinal and vertical dimensions faster and can revert the horizontal growth into damping. However, the overall difference between a cooled and non-cooled bunch is small in all planes and probably difficult to clearly measure.

The simulations indicate that performing the experiment at injection energy could increase the efficiency of the cooling due to the physically larger beam sizes at low energy. At this energy, the radiation damping is negligible and no shrinkage is expected without cooling. For the given setup, the cooling is most efficient in the horizontal plane. Already after 1 h of cooling about $0.2\,\mu$m difference in horizontal emittance compared to the free beam evolution is predicted. In the vertical plane only half of this value is reached. The effect on the bunch length is small. From this, an experiment of horizontal cooling at injection energy looks most promising.

As explained in the introduction of this chapter, the phase advance between pickup and kicker is essential for transverse cooling. In all three cases, the cavity is installed in the right hand side position marked in green in Fig. 8.10. The left Schottky is a vertical, while the right is an horizontal pickup. The one corresponding to the plane of cooling is used. Moreover, the horizontal and vertical tunes are different, which leads to a different phase advance between pickup and kicker for the horizontal and vertical cooling experiment, explaining the different efficiencies in the transverse planes.

The technique of longitudinal cooling does not depend on the phase advance between pickup and kicker, thus the efficiency cannot be compared with the transverse planes.

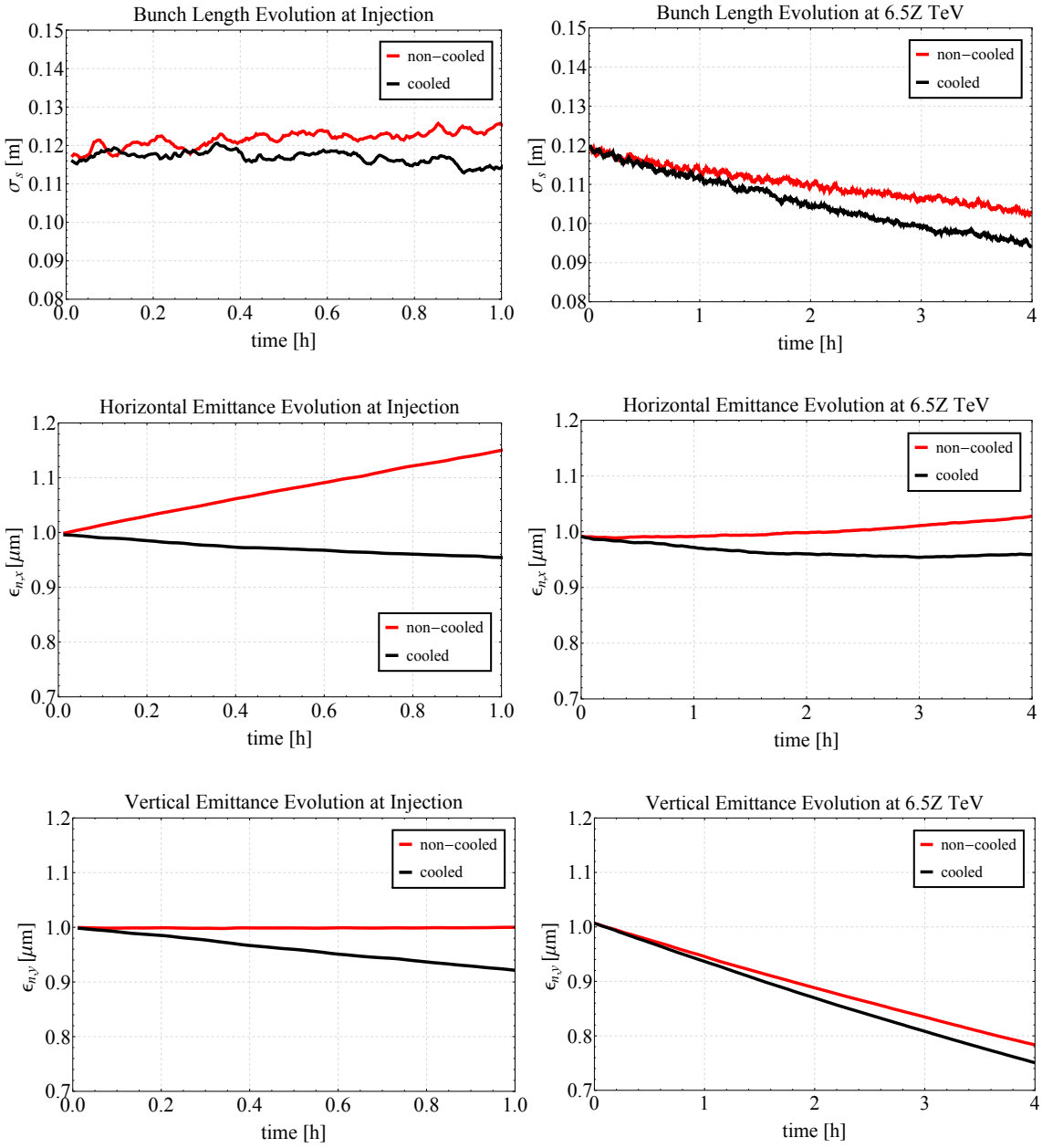

Figure 8.14.: Simulated beam evolution for cooling feasibility test in one plane. Black: cooled bunch, red: free beam evolution, no cooling applied. Top - bottom: bunch length, horizontal and vertical emittance for cooling only in the corresponding plane. Left: at injection, right: at 6.5Z TeV.

8.4.7. Measurements during the Experiment

In the LHC the bunch length is continuously measured for each bunch with the Beam Quality Monitor (BQM), while for transverse emittance measurements the BSRT and the wire scanners are available. A measurement of a single bunch's length is therefore easily accessible. As discussed before, the BSRT provides bunch-by-bunch measurements, but the absolute calibration of the emittance is difficult. This would not be a big issue for the given experiments, since we are interested in the relative difference between bunches, which is believed to be accurate. Nevertheless, at injection energy the lead ions do not emit enough light for single bunch measurements and only integrated values over the whole beam are available (for a sufficient number of circulating bunches). This does not suit the requirements for the experiment at the injection plateau. Therefore, to monitor the single bunch emittances at injection energy only the wire scanners are usable. Their disadvantage is that they can only be used for a limited number of bunches in the machine, which would eliminate the possibility of conducting the test parasitically during the injection process of physics beam.

Considering this information, a setup of horizontal cooling is proposed to be tested during dedicated machine time at injection energy. Since the test cavity would have a fixed aperture and be present over the whole run, a major part of the cooling commissioning could be performed in parallel to normal operation and additional time would be limited to the actual measurements. On top of this, staying at injection energy, keeps the required time short, since no magnet ramp is needed. Once the system is operational, one could think of performing tests during periods when the physics beam is delayed in the injectors, but single low intensity bunches are available.

8.5. 3D Heavy-Ion Cooling in LHC

8.5.1. System Properties

Cooling Rate and System Bandwidth

Assuming average Pb bunch parameters of 2013, shown in Table 8.3, a cooling system with a bandwidth of $W = 5 - 20\,\mathrm{GHz}$ is necessary to achieve reasonably fast cooling rate α_{cool} (see Eq. 8.12):

$$\frac{1}{\alpha_{\mathrm{cool}}} = \frac{N_b C_{\mathrm{LHC}}}{4\sigma_s W}\left[\frac{M+U}{(1-\tilde{M}^{-2})^2}\right] \approx 1.8\,\mathrm{h}, \tag{8.15}$$

where C_{LHC} is the circumference of the LHC, σ_s the RMS bunch length (to get the total length of the bunch the factor 4 is introduced). The mixing factor M is the number of turns it takes for a particle of RMS momentum error to move by one sample length, T_s, with respect to the nominal particle with $\Delta p/p = 0$. Using Eq. (8.9), $\gamma_T = 55.7$, $f_{\mathrm{rev}} = 11245\,\mathrm{Hz}$ and $\Delta p/p = 1.1 \times 10^{-4}$ of the nominal LHC and $W = 15\,\mathrm{GHz}$, the

Parameter	Unit	Head	Core	Tail
N_b	[10^8 ions]	1	1.4	2
$\epsilon_n = \epsilon\gamma$	[μm rad]	1.8	1.5	1.2
σ_s	[m]	0.075	0.9	0.10

Table 8.3.: Typical bunch parameters within one train in 2013, expected to be feasible in Run 3.

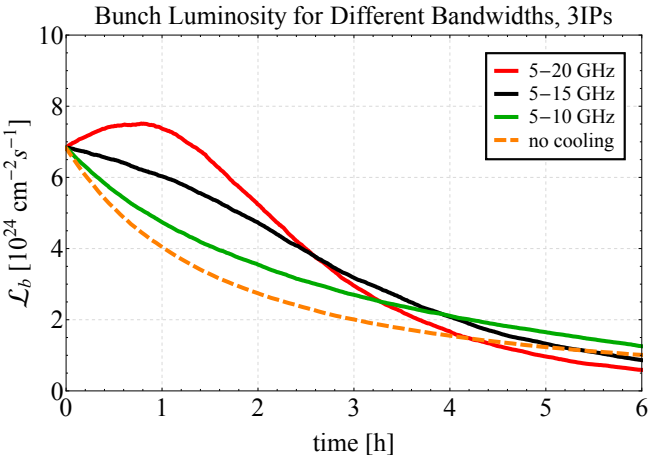

Figure 8.15.: Effect of cooling system bandwidth on luminosity.

mixing can be estimated to $M \approx 10$. $\tilde{M}^{-2} \to 0$ was assumed in the calculation, referring to the perfect situation of no (undesired) mixing between the pickup and kicker. The noise to signal ratio was set to $U = 0.01$, since compared to M this factor is usually small and has only little influence on the result. The computed cooling rate of Eq. (8.15) is an optimistic approximation, since the undesired mixing between pickup and kicker is neglected and the estimated M is usually too good. Moreover, the global slip factor η was used instead of the precise $\eta_{\mathrm{PU}\to\mathrm{K}}$ between pickup and kicker. But since the final tunnel locations of the system are unknown at the time of writing, $\eta_{\mathrm{PU}\to\mathrm{K}}$ is not available.

To obtain a broad bandwidth, the kicker system should consist of several cavity modules operating at a variety of frequencies. The frequency spacing of the cavity modules should approximately fulfil $\Delta f \approx c/(4\sigma_s)$. For an average RMS bunch length of $\sigma_s = 0.1\,\mathrm{m}$, $\Delta f \simeq 750\,\mathrm{MHz}$. So, for a system with a bandwidth of $W = (20 - 5)\,\mathrm{GHz} = 15\,\mathrm{GHz}$ about 20 cavity modules are required. Clearly, as described by Eq. (8.15), the smaller the bandwidth, the smaller the frequency coverage of the system and the less efficient the cooling. Figure 8.15 shows the effect of cooling on the instantaneous luminosity as a function of time for different values of the upper frequency and thus the bandwidth. For comparison, the situation without cooling (dashed orange line) is also shown.

The required RMS longitudinal voltages are 2 to 3 kV per cavity, the voltages required

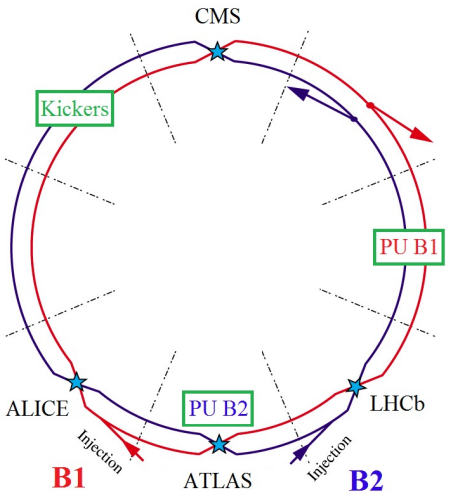

Figure 8.16.: Sketch of potential locations for stochastic cooling pickups (PU) and kickers in the LHC tunnel.

for the transverse planes are of the order of a few tens of Volts.

Tunnel Locations

The space required for the full 3D system is proportional to the number of cavity modules. Following the RHIC system, one has to expect a requirement of 12 to 15 m per plane and beam. The only place in the LHC tunnel where some 40 m of empty beam line could be available is in IR4, where the RF, feedback and many beam instrumentation systems are located.

For optimal mixing, the kicker-to-pickup distance should be large, while the pickup-to-kicker distance should be small, to preserve the relation between measured signal and beam condition. As a compromise, and also to match the signal and beam travel times, the pickups (length $L_{\mathrm{PU}} \simeq 1\,\mathrm{m}$) could be placed $\simeq 3/8$ of a turn downstream of the kickers, i.e., in IR7 for Beam 1 and in IR1 for Beam 2, see Fig 8.16. The pickup should be installed in the crest of the betatron oscillation and the betatron phase advance between pickup and kicker should be about $(n + 1/2)\pi$ for optimal transverse cooling efficiency.

Studies based on the currently expected optics after LS2, have shown that a cavity aperture of 1 cm could be possible, if the cavities are located just behind the IR4 dispersion suppressors, where the β-functions in both planes are sufficiently small. However, the separation of beam pipes may be marginal and further studies of the detailed mechanical design of the structures are required.

Mode Propagation

The discussed potential system location in IR4 would be in a warm section of the LHC, but adjacent to the dispersion suppressor, which is in the cold region. The beam pipe in this long straight section (LSS) is circular with a radius of 40 mm. From the results of Section 8.4.2 it can be seen that the TE_{11} mode has the lowest cut-off frequency, which is $f_c = 2.1\,\mathrm{GHz}$, in the given beam pipe.

The frequency dependence of the $1/e$ propagation distance of the TE_{01}, TE_{11} and TM_{01} modes, in an ideal circular waveguide with 40 mm radius and the wall conductivity of copper at room temperature, $\sigma = 1/(17\,\mathrm{n\Omega m})$ [134], is shown in the left plot of Fig. 8.17. The frequencies of a cooling system with $W = 5 - 20\,\mathrm{GHz}$ are above the cut-off frequencies for these modes, hence, they will propagate and live over many hundreds of metres in the ring, if they are not attenuated in the cavities themselves. The LSS is approximately 500 m long, corresponding to the maximum distance the modes travel in the warm beam pipe before they enter the cryogenic areas. Along this path, many instruments are installed, introducing perturbations to the perfectly smooth circular beam pipe, which reduces the calculated propagation distances. However, in general one should expect 10 to 15 $1/e$ distances before the modes can be consider as fully attenuated [136]. In particular the TE_{01} mode could lead to problems, since its propagation distance becomes very large for high frequencies, unlike the TE_{11} and TM_{01} modes, which have a maximum $1/(2\beta_c)$ between 5 and 10 GHz. Note that mode conversion is possible. Therefore, it is likely that at least a certain fraction of the power will survive until the dispersion suppressor. Nevertheless, the system might directly border the cryogenic region on one side, such modes travelling in this direction enter the cold area, carrying about their initial power.

The beam screen in the arcs is coated with a very high conductivity copper layer, with a $RRR = 100$ at screen temperatures of a few Kelvin [137], leading to a wall conductivity about a factor 100 higher compared to warm copper. The screen has a "racetrack" shape with slots on the flat sides. Because of these slots, the surface roughness, the magnetic resistance and the many interconnects between magnets, it can be expected that the actual conductivity is worse by about a factor 3. These arguments approximate the wall conductivity at cryogenic temperatures to $\sigma = 1/(0.6\,\mathrm{n\Omega m})$ [136].

To get an idea of the order of magnitude, it is fair to approximate the cross-section of the beam screen to be either circular or rectangular, as done in the right plot of Fig. 8.17. Here the $1/e$ propagation distance of the lowest mode in a rectangular (blue dashed) and the TE_{01} (red), TE_{11} (black) and TM_{01} (green) modes in circular waveguide are plotted as a function of frequency, assuming $\sigma = 1/(0.6\,\mathrm{n\Omega m})$. It is evident that with the low resistivity, power losses in the walls are small, leading to propagation over kilometres. From experience [136] it could be expected that, in reality, the calculated propagation distances are reduced by about a factor 10. Together with the required 15 $1/e$ distances for full attenuation, the calculated values should be multiplied by a factor $\sim$1.5 to obtain a "safe" distance.

Note that modes generated in one beam pipe can be reflected to the other in IPs

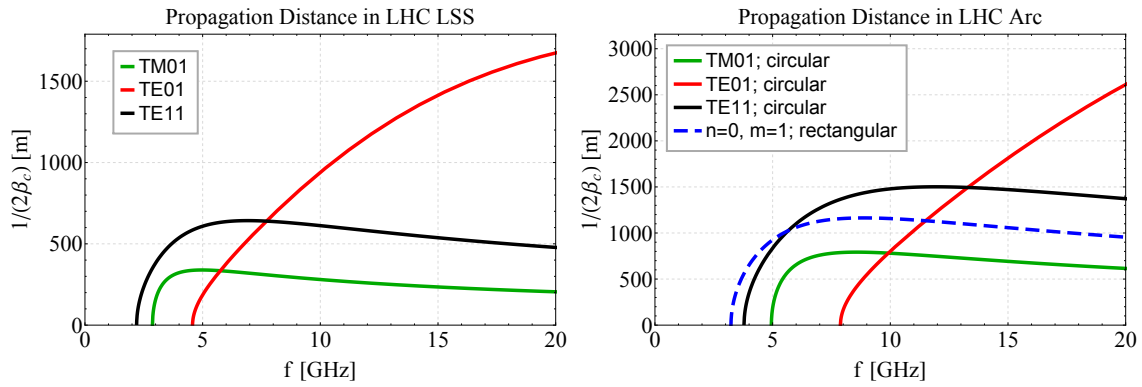

Figure 8.17.: Propagation Distance of the lowest TE and TM modes in warm (LSS, left) and cold (Arc, right) sections of the LHC.

where the beams are crossing in a common beam pipe. However, the loss coefficient in this situation is large. One octant of the LHC is about 3 km long and placing the pickups 3 IRs further downstream of the kicker should be sufficient to avoid significant cross talk. Nevertheless, due to the complexity of the machine, measurements are required to confirm these rough estimates.

To avoid propagation at any frequency of the system (up to 20 GHz), a cavity pipe radius of 4.4 mm would be necessary. This radius is at the limit of compatibility with the beam sizes in the considered region and the collimation hierarchy.

Impedance

For frequencies up to 20 GHz, the cavity apertures have to be as small as 1 to 2 cm in diameter; as in RHIC, this requires a special design allowing the devices to open at injection, when the beams are large, and close at top energy for cooling operation. Special care has to be taken that the system designed to cool heavy ions is compatible with the high intensity proton operation of the LHC.

Significant effort was invested into keeping the beam impedance of LHC to a minimum [138]. The small aperture of the series of cavities means that the impedances of (a) the cavities themselves, (b) the transition to these small apertures, and (c) the longitudinal and transverse resonant modes in the surrounding tank, need to be carefully minimized with the cavities both open and closed. Preliminary simulations performed by B. Salvant, optimized to obtain the effective impedance of the current RHIC kicker (one tank with 5 cavity modules at different frequencies), indicate that the low frequency impedance is dominated by (a) and can be modelled as bellow corrugations [139] (Fig. 8.18). The kicker impedance in open position is $\sim$2 mΩ in the longitudinal plane and $\sim$20 kΩ/m in the plane of plate separation[11]. A large number of these cavities would then represent a non-negligible fraction of the total longitudinal LHC impedance (currently $\sim$0.1 Ω) and transverse LHC impedance (currently

[11]This is a transverse impedance, hence has different units.

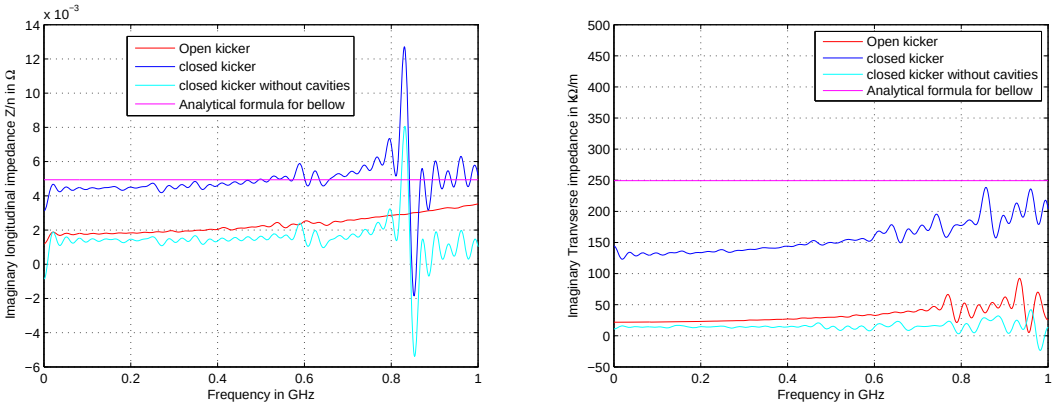

Figure 8.18.: Longitudinal and transverse simulated impedances of RHIC kicker open (red), closed (blue), closed with cavities filled by metal (cyan) and the formula in [139] (magenta). Courtesy of B. Salvant [28].

$\sim$2 MΩ/m at injection) [140]. Further studies should be performed in order to assess the resonant modes trapped in the large tank, as well as to optimise the RHIC design for use in the LHC.

8.5.2. Beam and Luminosity Evolution with Cooling at 7Z TeV

To estimate the potential benefit of a full 3D stochastic cooling system for Pb ions in the LHC, the luminosity and beam evolution are simulated with the CTE program. As usual, tracking with CTE takes IBS, radiation damping and beam population burn-off by collisions into account. In the scope of this study, CTE was extended to treating stochastic cooling as in [78]. Additionally to the specification of the initial beam parameters (N_b, ϵ_n, σ_s, V_{RF}), system properties, like bandwidths, gains and the delay between pickup and kicker, are required to simulate the beam evolution with stochastic cooling.

The following estimates are based on the initial parameters of three typical Pb bunches in an SPS train, as in 2013, see Table 8.3. The benefit of a cooling system with a bandwidth $W = 5$ to 20 GHz is shown in Fig. 8.19 and 8.20, where the single bunch-pair luminosity (bottom), intensity (top, left), bunch length (top, right) and emittance (middle) evolution through a 6 h fill is plotted. The dashed lines show the evolution without, the solid lines with cooling. The difference between the two figures is that in Fig. 8.19 an uncoupled machine is assumed, while Fig. 8.20 assumed full IBS coupling between the transverse planes.

Cooling shrinks the emittance and the beams collide more efficiently, thereby the fraction of the original stored beam that has to be dumped at the end of a fill is reduced. The variation of the bunch length is small, while the transverse emittances are reduced significantly. The horizontal emittance tends to an about constant value, where

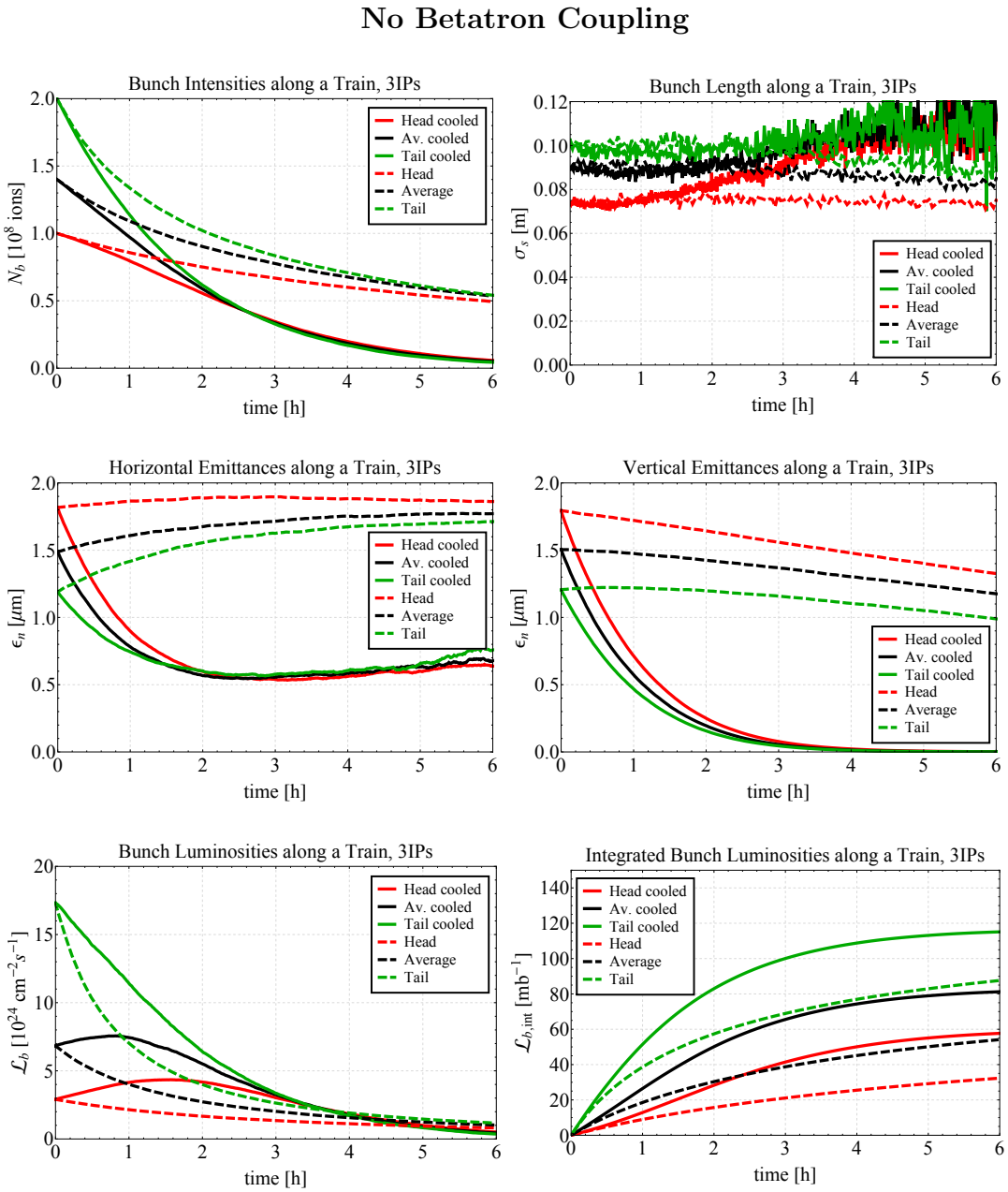

Figure 8.19.: Beam and luminosity evolution for three typical bunches at $7Z$ TeV with 3 IPs in collision, assuming no transverse coupling. Initial beam parameters are listed in Table 8.3. Top: intensity (left), bunch length (right), middle: horizontal (left) and vertical (right) emittance, bottom: instantaneous (left) and integrated (right) bunch luminosity.

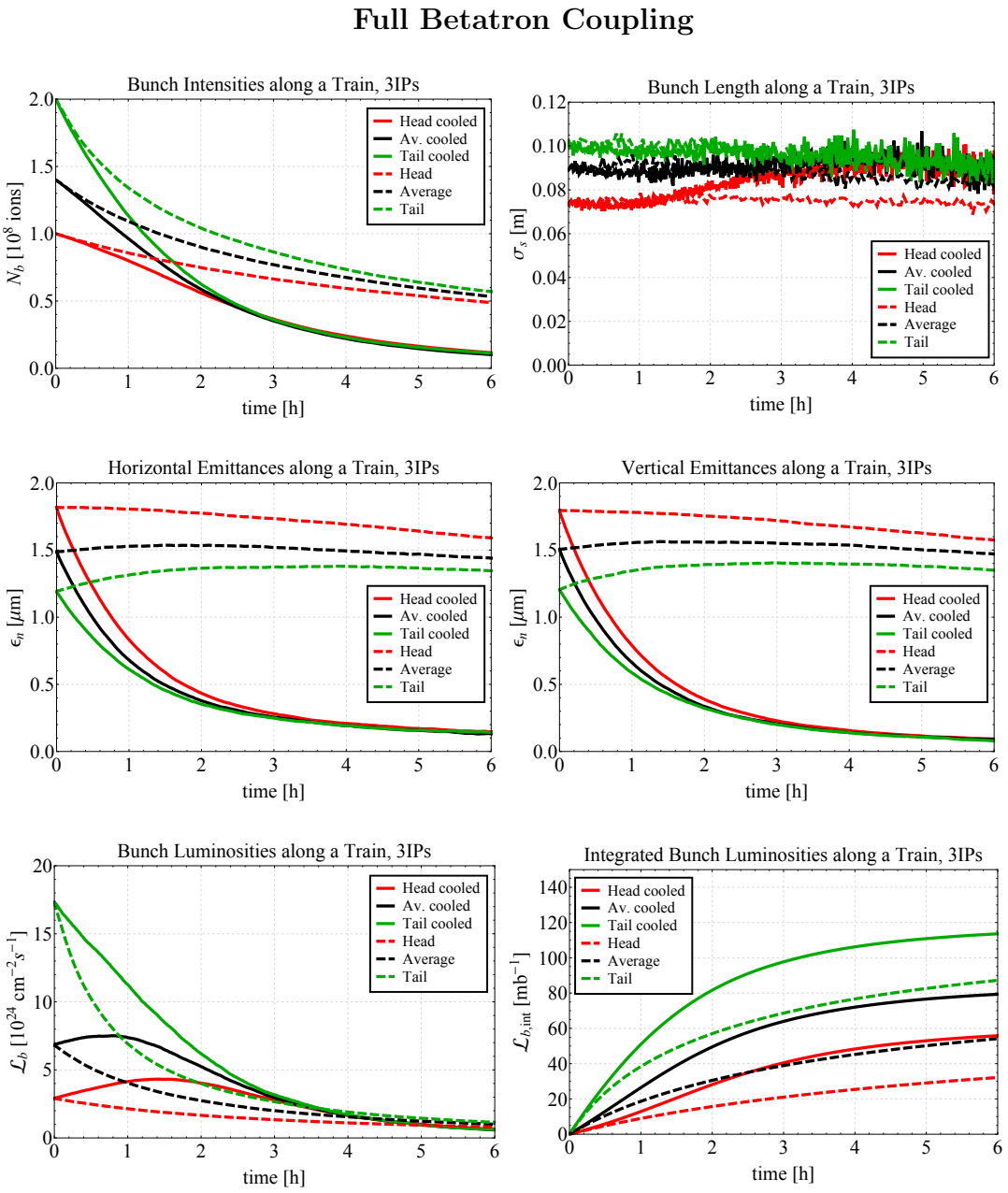

Figure 8.20.: Beam and luminosity evolution for three typical bunches at $7Z$ TeV with 3 IPs in collision, assuming fully coupled transverse motion. Initial beam parameters are listed in Table 8.3. Top: intensity (left), bunch length (right), middle: horizontal (left) and vertical (right) emittance, bottom: instantaneous (left) and integrated (right) bunch luminosity.

the IBS has become strong enough to counteract the cooling. A balance is reached when $\alpha_{\mathrm{IBS}} = \alpha_{\mathrm{rad}} + \alpha_{\mathrm{cool}}$. A priori, this balance can only happen momentarily since $N_b$changes due to burn-off. Without coupling, the vertical IBS is weak, even for very small beam sizes, which leads to a non-physically small vertical emittances after a few hours of cooling. In case of full IBS coupling, half of the horizontal emittance growth is transferred to the vertical plane, resulting in about equal transverse emittances through the fill. Also here, a balanced regime is reached within a few hours. Since the IBS is halved, the balance emittance value is reduced in horizontal, but raised to a reasonable size in the vertical plane.

Transverse cooling is in general more efficient than longitudinal, but the shrinking emittances increase the IBS in all three planes, holding the bunch length around its initial value. The bunch length growth in Fig. 8.19 is mainly introduced by the tiny vertical emittances, which are not realistic, and thus the evolution of σ_s is also not representative in case of zero betatron coupling.

Operating a collider with large betatron coupling is usually avoided, since the optics of the two planes are no longer independent, which for example complicates the orbit correction. In the LHC the coupling is well corrected and usually small, but non-zero. Thus, the real beam evolution is expected to be in between the two presented extremes. Unfortunately, it is not possible to simulate fractional coupling with CTE so far. Nevertheless, the intensity and luminosity evolution seem to be only marginally affected by the discussed issue.

The luminosity efficiency, $\eta_{\mathcal{L}}$, can be defined as the ratio of the integrated luminosity achieved per fill, $\mathcal{L}_{\mathrm{int}}$, summed over all experiments, to its potential maximum, when all particles of the beam with the smaller total intensity, N, have been collided:

$$\eta_{\mathcal{L}} = \frac{\sum_{\mathrm{IP}} \mathcal{L}_{\mathrm{int}}}{\mathcal{L}_{\mathrm{int,max}}} = \frac{\sigma_{c,\mathrm{tot}} \sum_{\mathrm{IP}} \mathcal{L}_{\mathrm{int}}}{\min(N_1, N_2)}, \tag{8.16}$$

where $\sigma_{c,\mathrm{tot}}$ is the total cross-section, removing particles from the beam. Typical good fills of the 2011 Pb-Pb run at a beam energy of $E_b = 3.5Z\,\mathrm{TeV}$ (and the 2012 p-p runs at $E_b = 4\,\mathrm{TeV}$) had $\eta_{\mathcal{L}} \simeq 15$–$20\%$. Predicted performance at $E_b = 7Z\,\mathrm{TeV}$ without cooling in a standard 6 h Pb-Pb fill is $\eta_{\mathcal{L}} \simeq 60\%$. Stochastic cooling could increase it to 88%, an increase in integrated luminosity per experiment approaching 50%.

8.6. First Stage 1D Cooling System

Commissioning a full 3D cooling system for the two beams, is a time consuming procedure, which might not be feasible in one month heavy-ion run. As a preliminary option, a system providing cooling only in one plane (of both beams) could be installed. This would reduce the initial cost and shorten the commissioning time, but give the possibility to gain experience with a reduced system and profit from cooling reasonably early.

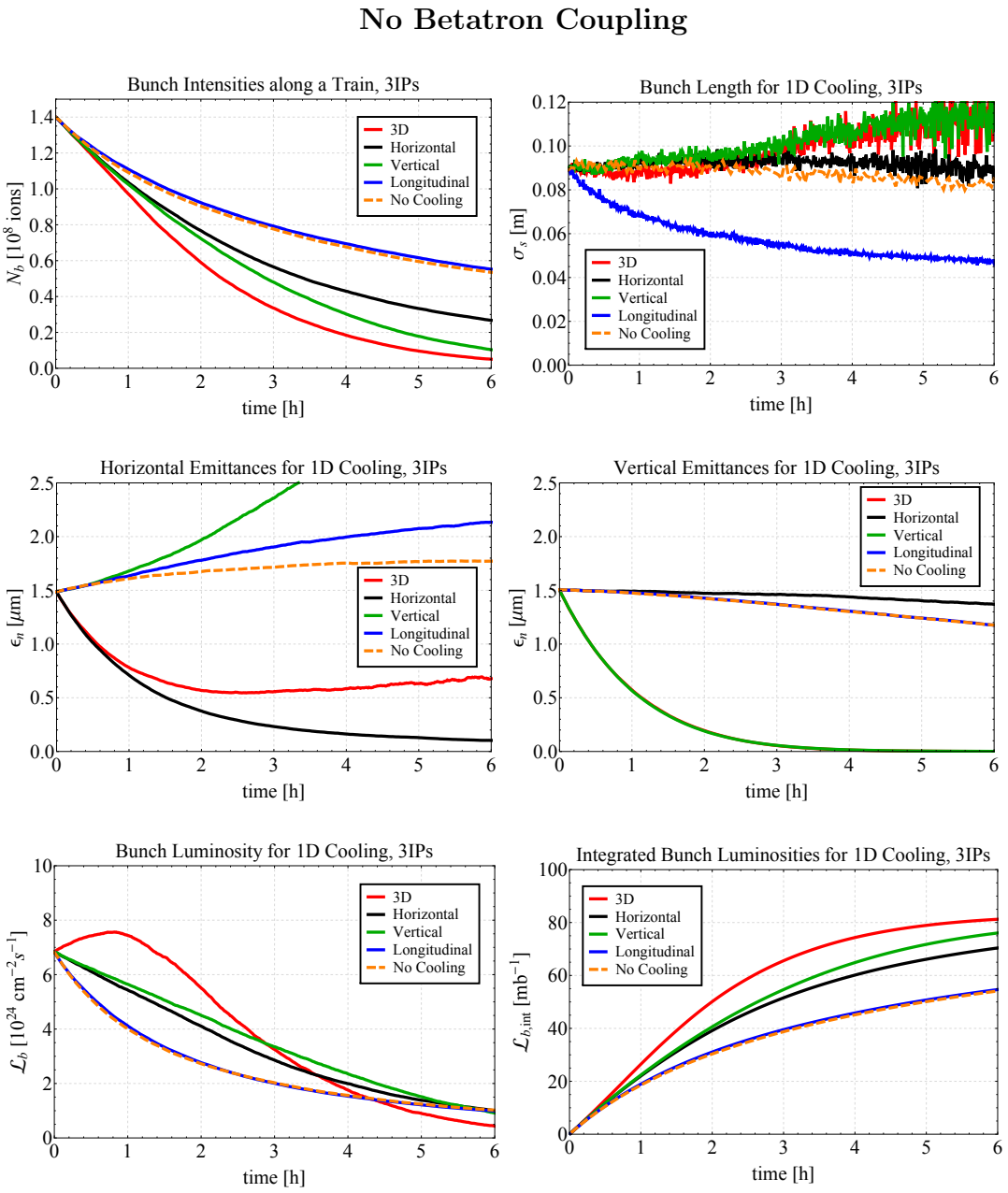

Figure 8.21.: Beam and luminosity evolution of a typical bunch at $7Z$ TeV for cooling both beams in one plane with 3 IPs in collision. Initial beam parameters are given in Table 8.3, column labelled with "core". Top: intensity (left), bunch length (right), middle: horizontal (left) and vertical (right) emittance, bottom: instantaneous (left) and integrated (right) bunch luminosity.

Figure 8.21 compares the beam and luminosity evolution for 3D cooling (red), as already shown in Fig. 8.19, with cooling both beams only in the horizontal (black), the vertical (green) or the longitudinal plane (blue). The evolution without cooling is displayed as the orange dashed line. The simulations shown assume uncoupled motion, leading to an unrealistically small vertical emittance and the corresponding bunch length growth for vertical cooling, as already seen in the 3D case. The $\epsilon_{n,y}$ evolution for only vertical and 3D cooling is very similar and the red line is hidden behind the green. Looking at $\epsilon_{n,x}$ shows that for the tiny $\epsilon_{n,y}$ the enhanced horizontal IBS leads to a fast horizontal blow-up. In the real machine, it could be expected that the small coupling mitigates this growth and keeps both planes at a reasonable size.

For only horizontal cooling, $\epsilon_{n,x}$ becomes small, but is kept well above zero by IBS. Also the vertical IBS is enhanced by the cooled horizontal plane, but the effect is much smaller compared to the previous situation of only vertical cooling. The radiation damped $\epsilon_{n,y}$ of the non-cooled case is only slightly smaller than the black line. The bunch length is similar to the non-cooled case.

Longitudinal cooling shrinks the bunch length, followed by increased horizontal IBS and thus emittance growth. The vertical IBS is only marginally affected and $\epsilon_{n,y}$ is similar to the non-cooled situation. The intensity burn-off in all cases corresponds to the smaller emittances and thus enhanced collision rate.

Comparing the luminosity evolution of cooling one or the other transverse plane gives a slightly larger benefit for vertical cooling, however, due to the unrealistically small vertical emittances, this might be overestimated. While the emittances of both planes are well behaved for horizontal cooling, also the luminosity evolution seems reasonable. The benefit in luminosity by cooling only in one plane is naturally smaller compared to a full 3D system, however the gain compared to no cooling is already significant.

8.7. Conclusions and Outlook

A stochastic cooling system in the LHC could dramatically shrink the emittance of heavy-ion beams as they collide and thereby approach the theoretical maximum integrated luminosity per fill without recourse to elaborate optics or crossing schemes.

The design of a proof-of-principle demonstration of stochastic cooling in the LHC was presented. Using the existing Schottky monitors centred at 4.8 GHz and one horizontal kicker cavity resonating at the same frequency, a minimised cooling experiment at injection energy was identified as the most promising setup.

First simulations with a full 3D cooling system have shown very promising results, peaking in an increase in integrated luminosity per experiment approaching 50%. Moreover, a first stage 1D cooling system, which could precede a full installation, could be considered to get experience and reduce initial commissioning time and cost. The luminosity gain of a reduced system is naturally lower, but already significant.

However, some key problems remain to be solved. It is challenging to build pickups

and cavities dealing with frequencies up to 20 GHz and a design does not exist yet. High frequency cavities require very small apertures in the order of a few centimetres, making it necessary to build devices, which can open at injection energy, when the beams are large, and close at top energy for operation. Thus, cooling during the injection plateau would not be possible. More importantly, these devices constitute a significant contribution to the overall impedance budget of the LHC, which is no problem in heavy-ion operation, but unacceptable for high intensity proton-proton operation. Not only would beam instabilities be expected, but the installation would also heat up and could be damaged. For these reasons, the system has to be designed to be effectively invisible in proton operation. As an alternative to a design which opens and closes, an innovative fixed aperture design could be envisaged at the expense of reduced upper frequencies [141]. This would limit the potential luminosity improvement but open the possibility to cool during injection and eliminate the mentioned issues for p-p operation.

9. The Future Circular Collider

9.1. Introduction

The Future Circular Collider (FCC) is a recently proposed collider study in a new 80–100 km tunnel at CERN in the Geneva area [142]. The design study includes three collider options: FCC-ee (formerly known as TLEP) a 90–400 GeV e^+e^- collider, seen as a potential intermediate step; FCC-hh, a hadron collider with a centre-of-mass energy of the order of 100 TeV in proton-proton collisions as a long-term goal; and FCC-he, combining both as a hadron-electron collider.

The beam energy of the hadron machine is expected to be $E_b = 50Z$ TeV. Its main purpose will be to search for new physics in energy regimes which have never been reached before. The FCC-hh will therefore spend most of its physics time providing proton-proton collisions to its experiments. Nevertheless, operating this machine with heavy ions is being considered. It would provide, for example, Pb-Pb and p-Pb collisions at $\sqrt{s_{\mathrm{NN}}} = 39$ and 63 TeV, respectively. From the heavy-ion physics point of view, using the FCC-hh as a heavy-ion collider would open a whole new regime of research opportunities [143].

This chapter discusses potential FCC-hh beam parameters for heavy-ion operation. The dominating beam dynamic effects and estimates for the time evolution of luminosity, intensity, emittances and bunch length by analytic equations and Collider Time Evolution (CTE) [77] simulations are presented. An approximated smooth lattice model is assumed. Lead-lead (Pb-Pb) and proton-lead (p-Pb) operation are considered. A short discussion of proton-proton (p-p) operation is based on the same techniques. The results of this study were submitted to Physical Review ST Accelerators and Beams [31].

9.2. General Assumptions

It is foreseen to operate the FCC-hh with different types of particles, e.g., protons (p) and lead-ions (Pb), but potentially also other ion species. The choice of certain parameters and hardware components has to ensure the compatibility with all potential beams. As mentioned, the production of p-p collisions will be the main task, restricting the heavy-ion run time to a few weeks per year, similar to the current LHC schedule. In order to optimise time and cost, the operation with different species should share mostly the same equipment, and machine settings should be kept as similar as possible.

For this reason, the parameters to be chosen for the heavy-ion operation are in line with those for p-p operation documented in [29], where possible.

This work focusses on the baseline option of a ring with $C_{\text{ring}} = 100\,\text{km}$ circumference requiring 16 T Nb_3Sn dipoles to provide a maximum beam energy of $E_b = 50Z\,\text{TeV}$.

9.2.1. Pre-Accelerator Chain

The study of this new hadron collider began only recently and the requirements for the pre-accelerator chain are still undefined. Assuming the same ratio of injection to full energy as for the LHC, the injection energy of the FCC-hh would be $E_{b,\text{inj}} = 3.3Z\,\text{TeV}$.

Taking the existing CERN infrastructure into account, reference [29] tentatively suggests three options for the last accelerator injecting into the FCC: a machine built either in the SPS, the LHC or the FCC tunnel. The magnet strength required for an injection energy of $3.3Z\,\text{TeV}$ would be 1 T, for an injector with normal conducting magnets in the 100 km FCC tunnel. 3.6 T, using superconducting LHC-type magnets (Nb-Ti) in the existing LHC tunnel. 13.5 T, using Nb_3Sn magnets replacing the SPS. A choice has not been made, but using the existing superconducting LHC magnets seems to be the most favoured and cost effective option today. Equipping the LHC magnets with new power converters and ramping to only about half their maximum field could reduce the ramp time to an acceptable value of a few minutes.

Based on this, it will be assumed here that the existing pre-accelerator complex, including the LHC, is used to accelerate the particles up to $3.3Z\,\text{TeV}$ before injection into the new ring. Both LHC rings are filled and the beams are injected in opposite direction into the FCC. This is a reliable but conservative assumption. Major upgrades are essential in the injector chain to satisfy the requirements of the FCC experiments and to obtain a realistic filling time. The heavy-ion programme will benefit from the efforts made. It can be expected that the performance and turnaround time will be significantly improved compared to the current situation, but the amount of improvement would be speculative today.

9.2.2. Smooth Lattice Approximation

At the time of this study, the lattice design is still preliminary [144]. However, for the calculation of many parameters and effects, the knowledge of certain lattice properties is required. In the design of a new machine, one has to respect some constraints, from which at least a first approximation of the range of these quantities can be derived.

As a baseline it is assumed that the lattice would be a similar FODO design as in the LHC (see Chapter 2.2.2). The maximum (and minimum) β-function in a FODO cell is directly proportional to the cell length, L_c [38]:

$$\beta^{\pm} = \frac{L_c(1 \pm \sin\frac{\mu}{2})}{\sin\mu} \propto L_c, \tag{9.1}$$

where μ is the phase advance per cell. To keep the beam size in the arcs at a reasonable value, L_c should not exceed twice the LHC value of $L_{c,\mathrm{LHC}} = 106.9\,\mathrm{m}$. It seems adequate to investigate cell lengths between one and two times the LHC value. A tendency to the upper range close, to $2\,L_{c,\mathrm{LHC}}$, seems to be favoured as a compromise between magnet aperture and strength.

The horizontal dispersion is produced in the bending magnets and is therefore proportional to the bending angle per cell, θ_c, times L_c. The average dispersion in a FODO cell, $\langle D_x \rangle$, is given by [38]:

$$\langle D_x \rangle = \frac{L_c \theta_c}{4} \left(\frac{1}{\sin^2 \frac{\mu}{2}} - \frac{1}{12} \right) \propto L_c \theta_c. \tag{9.2}$$

The total bending angle of the ring, the sum over $\theta_{c,i}$ of all cells, is 2π:

$$2\pi = \Sigma \theta_{c,i} = N_c \theta_c \tag{9.3}$$

$$\Rightarrow \theta_c = \frac{2\pi}{N_c}, \tag{9.4}$$

where N_c is the total number of FODO cells in the ring. The length of the circumference, filled by the arcs, is:

$$L_{\mathrm{arcs}} = N_c L_c = \frac{2\pi}{\theta_c} L_c. \tag{9.5}$$

Of this length, the dipoles themselves only occupy the fraction F_{arc}, giving:

$$L_{\mathrm{dipole}} = 2\pi\rho_0 = F_{\mathrm{arc}} L_{\mathrm{arcs}} = F_{\mathrm{arc}} \frac{2\pi}{\theta_c} L_c, \tag{9.6}$$

with ρ_0 as the dipole bending radius. It follows that the average horizontal dispersion is related to the cell length as:

$$\theta_c L_c = L_c^2 \frac{F_{\mathrm{arc}}}{\rho_0} \propto L_c^2 \tag{9.7}$$

$$\Leftrightarrow \langle D_x \rangle \propto L_c^2. \tag{9.8}$$

The vertical dispersion is in general very small and corrected for, therefore it is assumed to be zero:

$$\langle D_y \rangle = 0. \tag{9.9}$$

Assuming a phase advance of $\mu = \pi/2$ per cell and an arc filling factor of $F_{\mathrm{arc}} = 0.79$, as in the LHC, Eq. (9.1), (9.2) and (9.7) can be used to express the dispersion and β-functions in terms of the cell length L_c.

The momentum compaction factor, α_c, and the relativistic gamma factor at transi-

tion energy, γ_T, can be approximated via the average horizontal dispersion:

$$\alpha_c \equiv \frac{1}{\gamma_T^2} = \frac{1}{C_{\text{ring}}} \oint \frac{D_x}{\rho_0} \mathrm{d}s \approx \frac{2\pi \langle D_x \rangle}{C_{\text{ring}}}. \tag{9.10}$$

9.2.3. Beam Parameters

The potential beam parameter space is constrained by many different limitations, including the injector performance and dynamic effects in the whole operational cycle. The beam parameters presented in the following are an example of what could be possible from today's knowledge. Further studies should be performed to confirm their validity and to determine the optimum parameter set.

Using the existing pre-accelerator chain, it can be expected that beam parameters at least as good as in the LHC can be achieved. For the moment, the bunch-by-bunch differences observed in LHC operation [13] are neglected. Average bunch parameters measured in the 2013 proton-lead run [15] are taken as a conservative baseline. The assumed beam parameters for the lead and proton beams for heavy-ion operation of the FCC-hh are given in Table 9.1.

For the number of bunches per beam, k_b, given in Table 9.1, one injection per beam from the LHC is assumed. The LHC filling is assumed to be the planned "baseline" filling scheme after LS2 [20]. One shot from the LHC fills only about one quarter of the total circumference of the FCC. This implies that either only one experiment, clusters of experiments or two experiments, placed at opposite positions in the ring, could be provided with collisions. The reason for this choice is related to the turnaround time of the LHC as an injector, which will be explained in the discussion of the luminosity evolution. The β^*-values are the same as during p-p operation.

Intensity losses and emittance growth at injection, during the ramp and while preparing collisions are neglected.

Parameter	Symbol	Unit	Lead	Proton
No. of particles per bunch	N_b	$[10^8]$	1.4	115
Normalised transv. emittance	ϵ_n	$[\mu\text{m}]$	1.5	3.75
RMS bunch length	σ_s	[m]	0.08	0.08
No. of bunches per beam	k_b	-	432	432
β-function at IP	β^*	[m]	1.1	1.1

Table 9.1.: Assumed beam parameters for FCC-hh heavy-ion operation. Discussed operation modes are Pb-Pb and p-Pb.

9.2.4. RF System and Longitudinal Parameters

A RF system similar to the one currently used in the LHC, which has an RF frequency of $f_{\mathrm{RF}} = 400.8\,\mathrm{MHz}$, gives an harmonic number of

$$h = \frac{T_{\mathrm{rev}}}{T_{\mathrm{RF}}} = \frac{C_{\mathrm{ring}}}{c} f_{\mathrm{RF}} = 133692\ (= 2^2 \times 3 \times 13 \times 857) \tag{9.11}$$

in a ring with a circumference of exact $C_{\mathrm{ring}} = 100\,\mathrm{km}$. In reality, the circumference will be adjusted to give an h with more small factors, but this is not important in the following.

Injection

When the beam is injected, assuming bunch to bucket transfer, the longitudinal beam parameters, i.e., the relative RMS momentum spread, σ_p, the RMS bunch length, σ_s, and the longitudinal emittance, ϵ_s, are defined by the previous accelerator. To conserve the beam quality, the RF bucket has to be matched to the arriving beam. Assuming an injected bunch length of $\sigma_s = 0.1\,\mathrm{m}$, the corresponding σ_p and ϵ_s arriving from the LHC can be calculated as

$$\sigma_p = 2\pi \frac{f_s \sigma_s}{c|\eta|} = 1.9 \times 10^{-4}, \tag{9.12}$$

$$\epsilon_s = 4\pi \sigma_p \sigma_s E_b/(Zc) = 2.6\,\mathrm{eVs/charge}, \tag{9.13}$$

where f_s is the synchrotron frequency given by Eq. 2.18, η is the phase-slip-factor of Eq. 2.15, Z is the particles' charge number and E_b is the energy of the synchronous particle. At $E_b = 3.3Z\,\mathrm{TeV}$, an RF voltage of $V_{\mathrm{RF}} = 12\,\mathrm{MV}$ was used in the LHC.

From Eq. (9.13), it follows that ϵ_s is constant, if σ_s and σ_p are constant. If σ_s can be preserved during the transfer, Eq. (9.12) and (2.18) show that for a given lattice the RF voltage is the only free parameter to match the momentum spread.

Because of the preliminary stage of the lattice design, the effect of a varying cell length should be investigated. γ_T is the only parameter in Eq. (9.12) depending on the lattice. From Eq. (9.10), (9.2) and (9.8) follows

$$\gamma_T \propto \frac{1}{L_c} \tag{9.14}$$

$$\Rightarrow \sigma_p \propto \gamma_T \sqrt{V_{\mathrm{RF}}} \propto \frac{\sqrt{V_{\mathrm{RF}}}}{L_c} \tag{9.15}$$

for $\gamma \gg \gamma_T$. To obtain a matched distribution with σ_p equal to the injected value, V_{RF} has to be increased proportionally to the square of the cell length as shown in Fig. 9.1.

We define a baseline FCC-hh lattice with a FODO cell length of $L_c \approx 203\,\mathrm{m}$ for the calculations in the following. With this, Eq. (9.2) and (9.10) estimate $\gamma_T \approx 103$. Figure 9.1 shows that for this baseline lattice, an RF voltage of about $V_{\mathrm{RF}} = 13\,\mathrm{MV}$ is

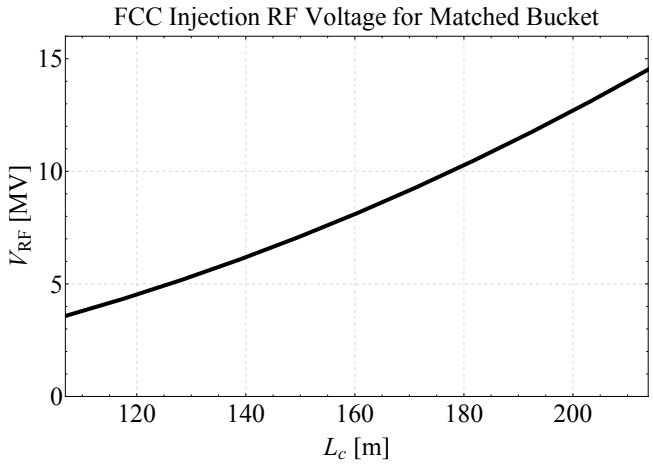

Figure 9.1.: RF voltage dependence on the cell length at injection in the FCC for matched bucket condition.

required at injection in the FCC.

Top Energy

To counteract the adiabatic damping of the bunch length during the energy ramp, white RF noise is applied to keep σ_s at a constant value of 0.08 m. This value is taken from the p-p parameter list and is based on the resolution limits of the experiments, imposing a minimum length of the luminous region.

Using an RF voltage of $V_{RF} = 32\,\mathrm{MV}$, twice the LHC design value [40], at top energy of the FCC-hh, the synchrotron frequency, the relative RMS momentum spread and the longitudinal emittance are

$$f_s = 3.4\,\mathrm{Hz}, \tag{9.16}$$
$$\sigma_p = 0.6 \times 10^{-4}, \tag{9.17}$$
$$\epsilon_s = 10.1\,\mathrm{eVs/charge}. \tag{9.18}$$

The bucket height, $(\Delta p/p)_{\max}$, and area, A_{bucket}, evaluate to [38]

$$\left(\frac{\Delta p}{p}\right)_{\max} = \sqrt{\frac{2ZeV_{\mathrm{RF}}}{\pi h|\eta|\beta_{\mathrm{rel}}E_b}} = 1.8 \times 10^{-4}, \tag{9.19}$$

$$A_{\mathrm{bucket}} = \frac{8C_{\mathrm{ring}}}{h\pi c}\sqrt{\frac{ZeV_{\mathrm{RF}}E_b}{2\pi h|\eta|}} = 28.6\,\mathrm{eVs/charge}. \tag{9.20}$$

At injection energy these values are $(\Delta p/p)_{\max} = 4.5 \times 10^{-4}$ and

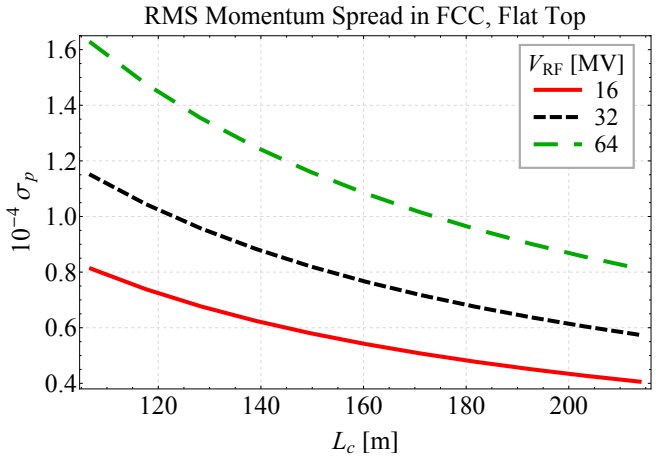

Figure 9.2.: RMS momentum spread dependence on lattice and RF voltage at top energy, as described by Eq. (9.15).

$A_{\text{bucket}} = 4.7\,\text{eVs/charge}$. The calculation is based on the baseline lattice defined in the previous paragraph.

An energy spread of 0.6×10^{-4} seems small and it has to be investigated in detail, if this would cause instabilities. As Eq. (9.15) states and Fig. 9.2 visualises, increasing the RF voltage could be advantageous, but the gain in σ_p is small for L_c on the order of twice the LHC cell length. In the design stage of the machine, it could as well be an option to increase γ_T by decreasing the cell length to obtain a higher σ_p. Nevertheless, the benefit has to be weighed against other design criteria relying on the cell length. For a chosen bunch length, the longitudinal emittance will behave proportionally to the momentum spread.

In general, it seems reasonable to aim for a similar momentum spread as in the LHC, around $\sigma_p = 1.1 \times 10^{-4}$. This however would require an unrealistically high RF voltage of about $V_{\text{RF}} \approx 100\,\text{MV}$.

9.3. Lead-Lead Operation

Based on the assumptions made above, approximations of relevant beam properties and effects are calculated in the following section. Because of the preliminary state of the accelerator design, simplifying assumptions had to be made in several places, therefore the study presented here can only give a first indication of what could be expected from heavy-ion operation of such a machine.

9.3.1. Intra-Beam Scattering

Intra Beam Scattering (IBS) is a dynamic effect within a bunch of charged particles, where multiple small-angle Coulomb scattering leads to particle losses and emittance growth. This effect can become very strong and reduce the potential luminosity. The basic theory of IBS is described in Chapter 2.5.1. To estimate the effect in the FCC-hh, the methods of Piwinski [54, 60] and Wei [59] are used. IBS growth rates in the two transverse and the longitudinal plane are referred to as $\alpha_{\mathrm{IBS},x,y}$ and $\alpha_{\mathrm{IBS},s}$, respectively, in the following.

The large parameter space, originating from the uncertainties of the lattice design, defines a range of IBS growth rates. Equation (9.1) and (9.2) are used to estimate the average dispersion, $\langle D_x \rangle$, and β-functions, $\langle \beta_{x,y} \rangle$, required to approximate the IBS growth rates.

Figure 9.3 shows $1/\alpha_{\mathrm{IBS}}$ as a function of L_c. The plot on the top presents the results at $3.3Z$ TeV (injection energy) and the bottom row at $50Z$ TeV (collision energy) for the initial bunch parameters given in Table 9.1. Only the longitudinal and horizontal plane are shown. IBS in the vertical plane is negligible without coupling, as assumed in the calculations. For the plots at top energy the dependence of σ_p on L_c is taken into account, while σ_p is constant at injection energy. The results are calculated for a set of RF voltages. σ_p can become very small for long cells (Fig. 9.2) and larger RF voltage can mitigate this effect.

Note that the horizontal IBS strength increases (= decreasing $1/\alpha_{\mathrm{IBS}}$) and the longitudinal decreases with increasing L_c at injection, but at top energy both, $\alpha_{\mathrm{IBS},s}$ and $\alpha_{\mathrm{IBS},x}$, become stronger for longer cells. The factors in the IBS calculation depending on the cell length are $\langle D_x \rangle \propto L_c^2$, $\langle \beta_x \rangle \propto L_c$ and $\sigma_p \propto 1/L_c$. With Eq. (2.25) and (2.26) it can be justified that for σ_p independent of L_c (as in the case of the injected beam), $\alpha_{\mathrm{IBS},s}$ only has a weak dependence on the lattice, while $\alpha_{\mathrm{IBS},x}$ features a second term $\propto D_x^2 \propto L_c^4$. At top energy, σ_p is influenced by the lattice conditions and becomes a function of L_c. Thus the strong dependence of $\alpha_{\mathrm{IBS},s}$ on σ_p takes over and the longitudinal IBS growth is enhanced for long cells.

In general, IBS could lead to longitudinal emittance growth at injection energy, while the transverse growth rates are moderate. At collision energy IBS should still be modest, with growth times above 20 h. The situation even improves, if the energy spread could be kept at the LHC design value, see Table 9.2.

However, as will be shown in the next section, this is only true for the initial beam parameters right after arriving at top energy. Because of the strong radiation damping, the beam emittances will shrink and the IBS will become strong enough to balance the damping.

Table 9.2 summarises the IBS growth times for a bunch with initial parameters, assuming (a) $\sigma_p = 0.6 \times 10^{-4}$ (obtained with γ_T of baseline lattice) and (b) $\sigma_p = 1.1 \times 10^{-4}$ (LHC design) at collision energy, $\sigma_p = 1.9 \times 10^{-4}$ at injection energy. The dispersion and β-functions are taken as calculated from the baseline lattice with $L_c = 203$ m. The comparison of the formalisms by Piwinski and Wei shows that Wei

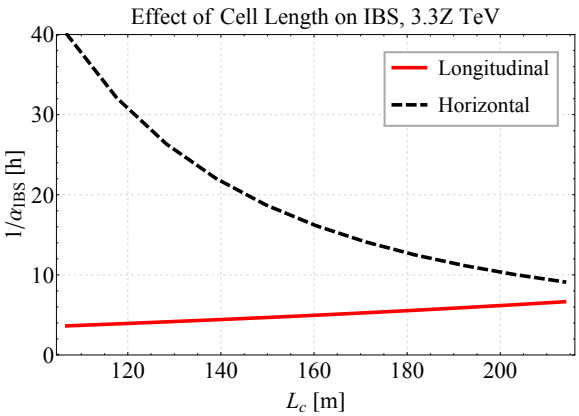

(a) At $3.3Z$ TeV and $V_{RF} = 13\,\text{MV}$.

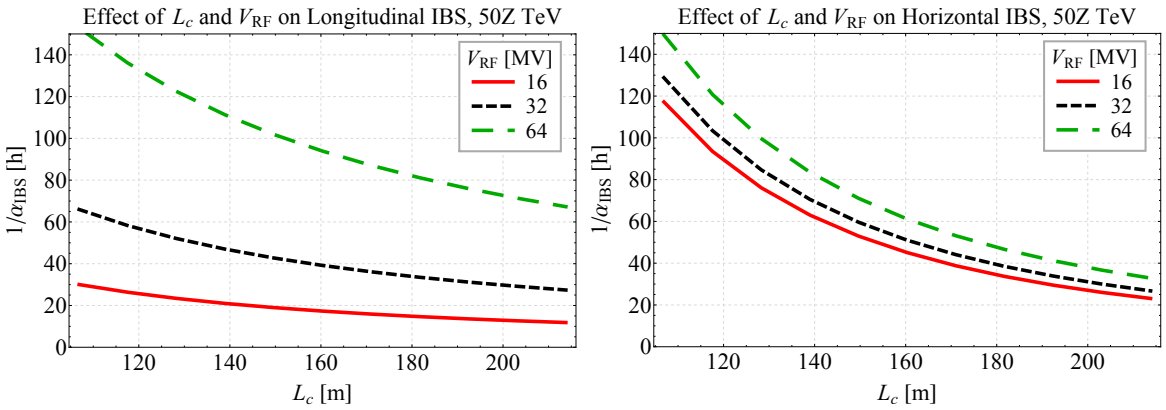

(b) At $50Z$ TeV collision energy.

Figure 9.3.: Range of Pb initial IBS growth times as a function of the cell length, L_c, for FCC-hh at injection (a) and collision (b) energy, evaluated with Piwinski's equations. (b) left: longitudinal, right: horizontal growth times. For given values of the total RF voltage, V_{RF}, in MV. No transverse coupling assumed.

Growth Times	Unit	Injection		Collision			
				(a)		(b)	
		Piwinski	Wei	Piwinski	Wei	Piwinski	Wei
$1/\alpha_{\mathrm{IBS},s}$	[h]	6.3	5.1	29.1	27.3	141.4	132.0
$1/\alpha_{\mathrm{IBS},x}$	[h]	10.0	8.2	30.0	28.0	43.9	41.0
$1/\alpha_{\mathrm{IBS},y}$	[h]	-10^4	-10^3	-10^6	-10^6	-10^6	-10^6

Table 9.2.: Initial IBS growth times for Pb-ions in FCC-hh calculated with the Piwinski [55] and Wei [59] formulae, assuming baseline lattice ($L_c = 203\,\mathrm{m}$) and no transverse coupling. Assumption for momentum spread: injection $\sigma_p = 1.9 \times 10^{-4}$ at $V_{\mathrm{RF}} = 13\,\mathrm{MV}$, collision (a) $\sigma_p = 0.6 \times 10^{-4}$ (obtained with γ_T of baseline lattice), (b) $\sigma_p = 1.1 \times 10^{-4}$ (LHC design) at $V_{\mathrm{RF}} = 32\,\mathrm{MV}$.

estimates a systematically slightly stronger IBS rate. The overall agreement is better than 10% at high energy and 20% at injection energy for the given parameters.

9.3.2. Radiation Damping

A charged particle travelling in a storage ring will radiate energy, when it is bent on its circular orbit. Because of the average energy loss into this synchrotron radiation, the betatron and synchrotron oscillation amplitudes are damped with the radiation damping rates $\alpha_{\mathrm{rad},i}$, where $i = x, y, s$. These quantities do not depend on the beam parameters. The strongest dependence is on the third power of the energy, the machine size and the particle type. Note that the longitudinal damping is twice as fast as the transverse. For a more detailed description of radiation damping see Chapter 2.5.2.

To get an impression how strong the radiation damping will be in the FCC, the damping rates are compared to the LHC design values:

$$\frac{\alpha_{\mathrm{rad,FCC}}}{\alpha_{\mathrm{rad,LHC}}} = \frac{E_{\mathrm{FCC}}^3/(\rho_{0,\mathrm{FCC}} C_{\mathrm{FCC}})}{E_{\mathrm{LHC}}^3/(\rho_{0,\mathrm{LHC}} C_{\mathrm{LHC}})} \approx \frac{E_{\mathrm{FCC}}^3/C_{\mathrm{FCC}}^2}{E_{\mathrm{LHC}}^3/C_{\mathrm{LHC}}^2} \approx \frac{7^3}{4^2} \approx 22. \tag{9.21}$$

This scaling is valid for all planes, because of relation (2.61). The circumference of the accelerator was chosen such that the required dipole field does not exceed the expected technical limits. Therefore, the bending radius can be approximated to be proportional to the circumference, $\rho_0 \propto C_{\mathrm{ring}}$. The new machine will be about a factor 4 longer than the LHC. Moreover, the energy will be increased by about a factor 7 ($= 50Z\,\mathrm{TeV}/7Z\,\mathrm{TeV}$). Table 9.3 quotes the radiation damping times at injection and collision energy. Note that quantum excitation for lead beams is still negligible.

Damping Times	Unit	Injection	Collision
$1/\alpha_{\mathrm{rad},s}$	[h]	852	0.24
$1/\alpha_{\mathrm{rad},x}$	[h]	1704	0.49
$1/\alpha_{\mathrm{rad},y}$	[h]	1704	0.49

Table 9.3.: Emittance radiation damping times for Pb-ions in the FCC.

9.3.3. Luminosity

The quantity that measures the ability of a particle accelerator to produce the required number of interactions is the luminosity (see Chapter 2.4). Using Table 9.1 and Eq. (2.22) the initial luminosity at the beginning of collisions computes to

$$\mathcal{L}_{\mathrm{initial}} = 2.6 \times 10^{27}\,\mathrm{cm}^{-2}\mathrm{s}^{-1}. \tag{9.22}$$

Which is, due to the higher intensity and energy, already 2.6 times higher than the design luminosity for Pb-Pb of the LHC.

The total event cross-section, $\sigma_{c,\mathrm{tot}}$, is given by the sum over the cross-sections of all possible interactions removing particles from the beam in collision (burn-off). Apart from the inelastic hadronic interactions, the effects of Bound Free Pair Production (BFPP) and Electromagnetic Dissociation (EMD) are very important for Pb-Pb collisions (also see Chapter 2.5.4 and 7).

$$\begin{aligned} \sigma_{c,\mathrm{tot}} &= \sigma_{c,\mathrm{BFPP}} + \sigma_{c,\mathrm{EMD}} + \sigma_{c,\mathrm{hadron}} \\ &\approx 354\,\mathrm{b} + 235\,\mathrm{b} + 8\,\mathrm{b} = 597\,\mathrm{b} \end{aligned} \tag{9.23}$$

The numerical values in Eq. (9.23) are estimated for $E_b = 50Z\,\mathrm{TeV}$ with the aid of References [67, 71].

Luminosity Evolution

While the beams are in collision, the instantaneous value of the luminosity will change, through intensity losses and emittance variations,

$$\mathcal{L}(t) = A\frac{N_b^2(t)}{\sqrt{\epsilon_x(t)\epsilon_y(t)}}, \tag{9.24}$$

where all time independent factors are merged in $A = f_{\mathrm{rev}}k_b/(4\pi\beta^*)$. For simplification, equal beam populations and sizes of both beams are assumed. To obtain the beam evolution with time, a system of four differential equations for the intensity, emittances and bunch length evolution has to be solved. The solutions can be inserted

into Eq. (9.24) to obtain the luminosity evolution.

$$\frac{\mathrm{d}N_b}{\mathrm{d}t} = -\sigma_{c,\mathrm{tot}} A \frac{N_b^2}{\sqrt{\epsilon_x \epsilon_y}} \tag{9.25}$$

$$\frac{\mathrm{d}\epsilon_x}{\mathrm{d}t} = \epsilon_x(\alpha_{\mathrm{IBS},x} - \alpha_{\mathrm{rad},x}) \tag{9.26}$$

$$\frac{\mathrm{d}\epsilon_y}{\mathrm{d}t} = \epsilon_y(\alpha_{\mathrm{IBS},y} - \alpha_{\mathrm{rad},y}) \tag{9.27}$$

$$\frac{\mathrm{d}\sigma_s}{\mathrm{d}t} = \frac{1}{2}\sigma_s(\alpha_{\mathrm{IBS},s} - \alpha_{\mathrm{rad},s}) \tag{9.28}$$

The factor 1/2 in Eq. (9.28) was introduced because the emittance growth rates are twice the amplitude growth rates.

The time evolution of the intensity is given again by the event rate of Eq. (2.20), where $\mathcal{L}$ is replaced by Eq. (9.24). A minus sign is introduced, since for each collision event generated one particle is lost: $\mathrm{d}R/\mathrm{d}t = -\mathrm{d}N/\mathrm{d}t$.

The time evolution of the emittances and bunch length is influenced by IBS growth and radiation damping. While the radiation damping rates are constant in time and do not depend on the beam conditions, the IBS growth rates vary along with the decreasing intensity and changing emittances, which change due to radiation damping and IBS itself. Owing to this dynamic behaviour of the emittance growth times, it is impossible to find an analytic solution of this system.

In the following three simplified cases will be discussed; (1) the emittance, or (2) the emittance growth rate is kept constant through the whole fill, (3) IBS and radiation damping are in balance after some time into the fill. To further simplify the situation round beams ($\epsilon = \epsilon_x = \epsilon_y$) and fully coupled transverse motion ($\alpha_{\mathrm{IBS},x,y} = (\alpha_{\mathrm{IBS},x} + \alpha_{\mathrm{IBS},y})/2$) is assumed. In this case, the ordinary differential equation (ODE) system is reduced to three equations, since the horizontal and vertical emittances are equal for all times.

(I) In the first case, $\epsilon(t) = \epsilon_0 = \text{const.}$ should be considered, which is achieved when $\alpha_{\mathrm{IBS}} - \alpha_{\mathrm{rad}} = 0$ and thus $\mathrm{d}\epsilon/\mathrm{d}t = 0$. For zero crossing angle, the bunch length evolution is decoupled from the luminosity. Eq. (9.25) simplifies to

$$\frac{\mathrm{d}N}{\mathrm{d}t} = -\sigma_{c,\mathrm{tot}} A \frac{N_b^2}{\epsilon_0} \tag{9.29}$$

This can easily be solved for the intensity and, in combination with Eq. (9.24), for the luminosity evolution with time:

$$N_b(t) = \frac{N_{b0}}{A N_{b0} \sigma_{c,\mathrm{tot}} t/\epsilon_0 + 1} \tag{9.30}$$

$$\Rightarrow \mathcal{L}(t) = \mathcal{L}_0 \left(\frac{1}{A N_{b0} \sigma_{c,\mathrm{tot}} t/\epsilon_0 + 1} \right)^2 . \tag{9.31}$$

By investigating these equations, it becomes clear that the only non-constant factor is the time t, which appears only in the denominator, i.e. the intensity and with it the luminosity can only decay.

(II) In the second case, where the total emittance damping rate is constant, $\alpha_\epsilon = \alpha_{\mathrm{IBS}} - \alpha_{\mathrm{rad}} = \text{const.}$, with $\alpha_{\mathrm{IBS}} \ll \alpha_{\mathrm{rad}}$. It is implicitly approximated that IBS is independent of the beam parameters, decoupling the bunch length and emittance evolutions. Simultaneously solving the two remaining differential equations (9.25) and (9.26) gives

$$\epsilon_n(t) = \epsilon_0 \exp[-\alpha_\epsilon t] \tag{9.32}$$

$$N_b(t) = \frac{N_{b0}\epsilon_0}{\epsilon_0 + AN_{b0}\sigma_{c,\mathrm{tot}}(\exp[\alpha_\epsilon t] - 1)/\alpha_\epsilon} \tag{9.33}$$

$$\Rightarrow \mathcal{L}(t) = \mathcal{L}_0 \frac{\epsilon_0^2 \exp[\alpha_\epsilon t]}{(\epsilon_0 + AN_{b0}\sigma_{c,\mathrm{tot}}(\exp[\alpha_\epsilon t] - 1)/\alpha_\epsilon)^2}. \tag{9.34}$$

Again t is the only non-constant parameter. As expected, Eq. (9.32) and (9.33) can only decay. However, the combination of both, the luminosity evolution (Eq. (9.34)), features the exponentially growing factor $\exp[\alpha_\epsilon t]$ in the numerator and denominator. This means, as long as the numerator $\epsilon_0^2 \exp[\alpha_\epsilon t]$ predominates the denominator $(\epsilon_0 + AN_{b0}\sigma_{c,\mathrm{tot}}(\exp[\alpha_\epsilon t] - 1)/\alpha_\epsilon)^2$ a growth of the initial luminosity to a higher peak is possible. It should be noted that the assumption of a constant damping leads to emittances asymptotically approaching zero, which is non-physical. Because of this effect, the luminosity peak computed with Eq. (9.34) is overestimated.

(III) In reality the IBS growth rate changes dynamically with the intensity and emittance, thus it will become stronger, while the emittances shrink due to radiation damping. Since the total emittance growth rate is given by $\alpha_\epsilon = \alpha_{\mathrm{IBS}} - \alpha_{\mathrm{rad}}$, the emittance will approach a value where the growth from IBS balances the damping. This balance is not a real equilibrium, where the emittance and bunch length would be constant. But the IBS strength keeps decreasing due to intensity burn-off, leading to a slowly shrinking emittance and bunch length to maintain the balance.

An analytical expression for the balance value of the emittance and bunch length can be derived from Wei's IBS formalism given by Eq. (2.34) and (2.35). Even in this simplified form, the transverse growth rate shows a rather complicated dependence on ϵ, providing only a numerical solution. Both factors under the square root in the denominator of Eq. (2.34) depend on evolving beam properties. $\epsilon \propto 10^{-6}/\gamma \approx 10^{-11}$ and $C_2\sigma_p^2 \approx D_x^2/\beta_x(10^{-4})^2 \propto 10^{-10}$ are in the same order of magnitude, therefore we approximate $\sqrt{\epsilon + C_2\sigma_p^2} \longrightarrow \sqrt{2C_2\sigma_p^2}$. Eq. (2.34) can be set equal to $\alpha_{\mathrm{rad},x}$ to satisfy the balance condition and be solved for the emittance $\epsilon_B = \epsilon_{n,B}/\gamma$:

$$\epsilon_{n,B} \cong \gamma \sqrt{\frac{C_1 N_b}{\sqrt{2C_2}\alpha_{\mathrm{rad},x} D_p \sigma_{s,B}^2}}. \tag{9.35}$$

D_p is the proportionality factor between the momentum spread and the bunch length

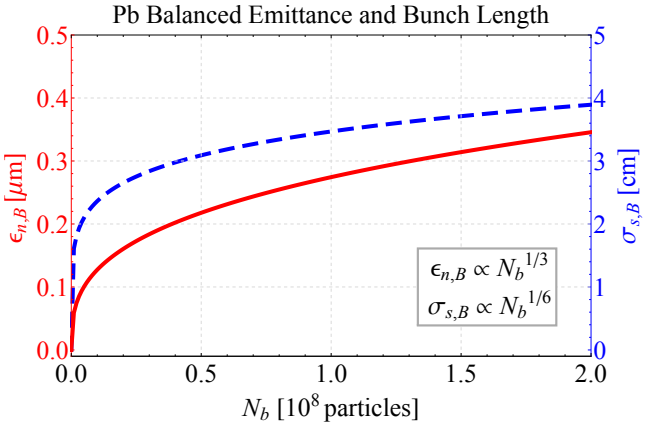

Figure 9.4.: Normalised emittance (red) and bunch length (blue) for balanced IBS and radiation damping.

given by Eq. (9.12). $\epsilon_{n,B}$ still depends on the balance value of the bunch length, $\sigma_{s,B}$, which is determined by replacing $\epsilon \longrightarrow \epsilon_{n,B}/\gamma$ in Eq. (2.35) and applying $\alpha_{\mathrm{IBS},s} = \alpha_{\mathrm{rad},s}$:

$$\sigma_{s,B} \cong \left(\frac{C_3 \sqrt{C_1 N_b \alpha_{\mathrm{rad},x}}}{D_p^{5/2} (2C_2)^{1/4} \alpha_{\mathrm{rad},s}} \right)^{1/3} \propto N_b^{1/6}. \tag{9.36}$$

Inserting $\sigma_{s,B}$ into Eq. (9.35) leads to an equivalent equation for the normalised emittance:

$$\epsilon_{n,B} \cong \gamma \left(\frac{C_1 N_b D_p \alpha_{\mathrm{rad},s}}{C_3 \sqrt{2C_2} \alpha_{\mathrm{rad},x}^2} \right)^{1/3} \propto N_b^{1/3}. \tag{9.37}$$

When a balance between IBS and radiation damping is reached, the emittance and bunch length depend only on the bunch intensity. The higher the number of particles, the larger the beam dimensions as shown in Fig. 9.4. The balanced normalised emittance (red) and the bunch length (blue) are plotted as a function of the intensity. The plot shows that these quantities become small in the expected range of bunch charge. Longitudinal, and potentially transverse, blow-up might become necessary to keep the beam sizes in a reasonable range.

The intensity evolution, where $\alpha_{\mathrm{IBS}} = \alpha_{\mathrm{rad}}$, can be obtained by inserting Eq. (9.37) into Eq. (9.25):

$$N_{b,B}(t) \cong 3\sqrt{3} N'_{b0} \left(3 + 2^{5/6} A \sigma_{\mathrm{c,tot}} {N'_{b0}}^{2/3} t \left[\frac{C_3 \sqrt{C_2} \alpha_{\mathrm{rad},x}^2}{C_1 D_p \alpha_{\mathrm{rad},s}} \right]^{1/3} \right)^{-3/2}. \tag{9.38}$$

Note that $N'_{b0} \neq N_{b0}$ is not the initial intensity at the beginning of the fill, but should

be the number of particles left when the balanced regime is reached. The luminosity evolution can then be calculated by inserting Eq. (9.38) and (9.37) into (9.24).

Figure 9.5 shows the beam and luminosity evolution for case (II) and (III) as discussed above in comparison with tracking simulations done with the CTE program [77]. The results are displayed for two colliding lead bunches featuring the beam parameters given in Table 9.1. One experiment is taking data. The black line shows the calculations with Eq. (9.32)-(9.34) for the approximation where $\alpha_\epsilon = \text{const.}$ and $\alpha_{\text{IBS}} \ll \alpha_{\text{rad}}$. The dashed green line shows the calculations done with Eq. (9.36)-(9.38) in the regime where IBS and radiation damping balance each other ($\alpha_{\text{IBS}} = \alpha_{\text{rad}}$). The two red lines are CTE simulations with (solid) and without (dashed) IBS coupling. The simulations are based on the assumption of a smooth lattice (Section 9.2.2) and the Piwinski's IBS formalism.

It is clearly visible that the bunch length and emittances of the analytical calculations for $\alpha_{\text{IBS}} \ll \alpha_{\text{rad}}$ (black) asymptotically approach zero, which is non-physical, leading to a strong over-estimation of the luminosity. While the simulation with uncoupled planes (dashed red line) shows a realistic horizontal and longitudinal behaviour, the vertical emittance still damps to zero. In the coupled simulation (solid red lines) all three beam dimensions settle at a balanced value above zero. The transverse normalised emittance reaches around $0.2\,\mu$m, corresponding to a beam size of $\sigma^* \approx 3\,\mu$m at the IP for $\beta^* = 1.1\,$m. The bunch length damps twice as fast as the transverse planes, before IBS kicks in and stabilises the bunch length around $\sigma_s \approx 3\,$cm. The derivation of the balanced state equations (green dashed) assumes as well coupled transverse motion. The calculation is in very good agreement with the corresponding simulation.

Because of the small beam sizes, problems with instabilities might appear, apart from the fact that it could become difficult to find the collisions. Blow-up might become necessary in the longitudinal but maybe also in the transverse planes. A transverse emittance blow-up could also act as a luminosity levelling method.

Without further approximations it is not possible to solve the differential equation system of Eq. (9.25)-(9.28) analytically. But by using Wei's analytic IBS expressions the system can be solved numerically. Figure 9.6 presents numerical solutions of the ODE system (dashed lines) obtained with *Mathematica*. Coupled transverse motion and round beams are assumed. The solid red line indicates again the CTE simulation shown in Fig. 9.5. The black dashed line shows the corresponding solution of the ODE system. The agreement between the numerical solution and the tracking result is excellent. Hence, the analytical calculation (with coupling) in the balanced regime is in excellent agreement with the ODEs. The small differences, are explained by the difference in IBS growth rates calculated with Piwinski's and Wei's algorithms for the same beam conditions. To prevent the bunch length from shrinking to too low values and to model the evolution under longitudinal blow-up, the ODEs are solved for constant bunch length ($\mathrm{d}\sigma_s/\mathrm{d}t = 0$, green dashed line). This enhances the intensity burn-off and the luminosity peak, since the IBS is weakened, reducing further the balance value of the emittance. Introducing an additional constant term in Eq. (9.26) can constrain the emittance above a certain value, ϵ_{min}, similar to the equilibrium

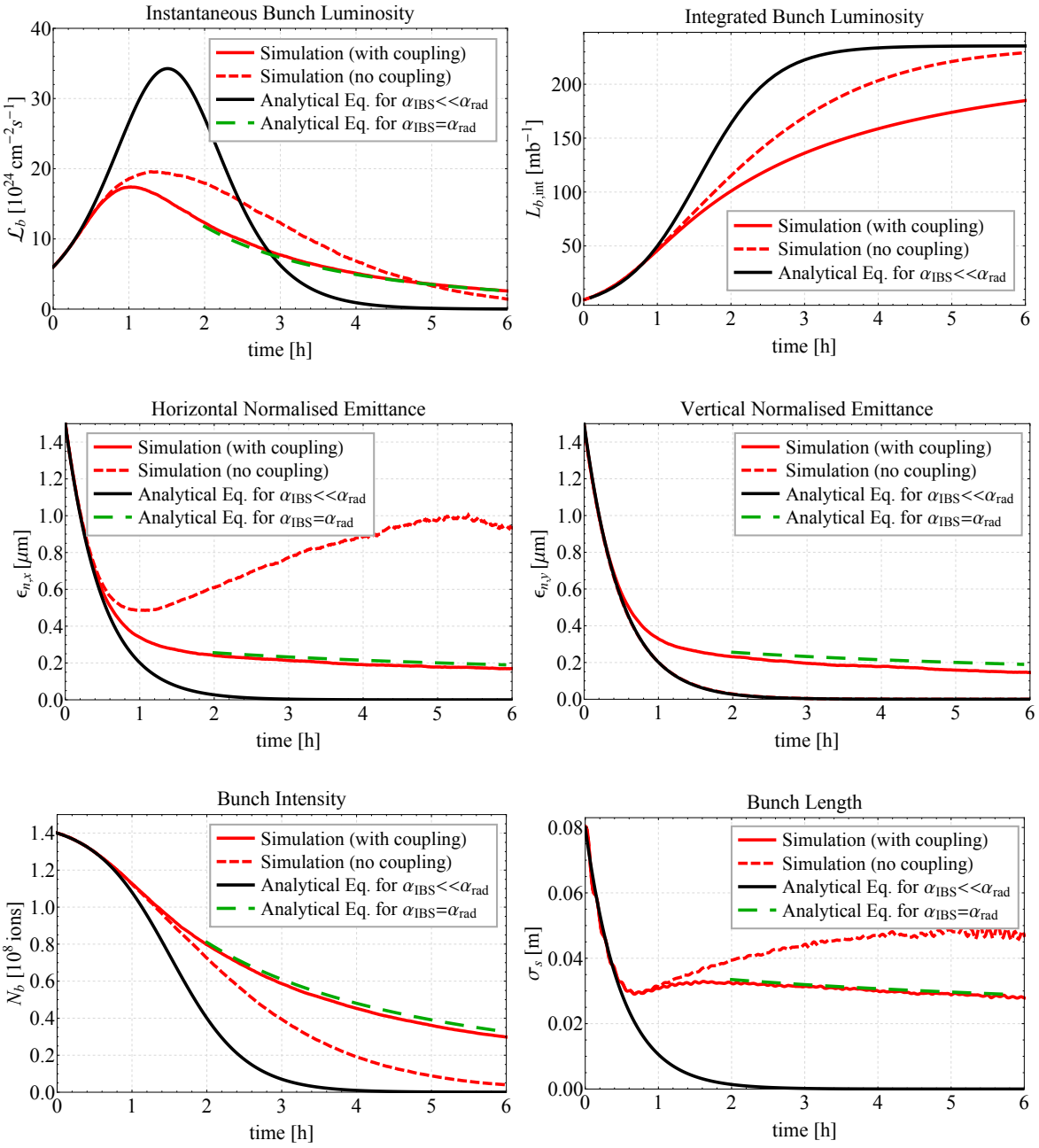

Figure 9.5.: Pb-Pb beam and luminosity evolution. Top: instantaneous (left) and integrated luminosity (right), middle: horizontal (left) and vertical (right) normalised emittance, bottom: intensity (left) and bunch length (right). One experiment is in collisions. The black lines show the calculations done with Eq. (9.32)-(9.34) for $\alpha_{\mathrm{IBS}} \ll \alpha_{\mathrm{rad}}$, the dashed green lines show the calculations done with Eq. (9.36)-(9.38) in the regime where IBS and radiation damping balance each other ($\alpha_{\mathrm{IBS}} = \alpha_{\mathrm{rad}}$), the two red lines are CTE simulations with (solid) and without (dashed) IBS coupling.

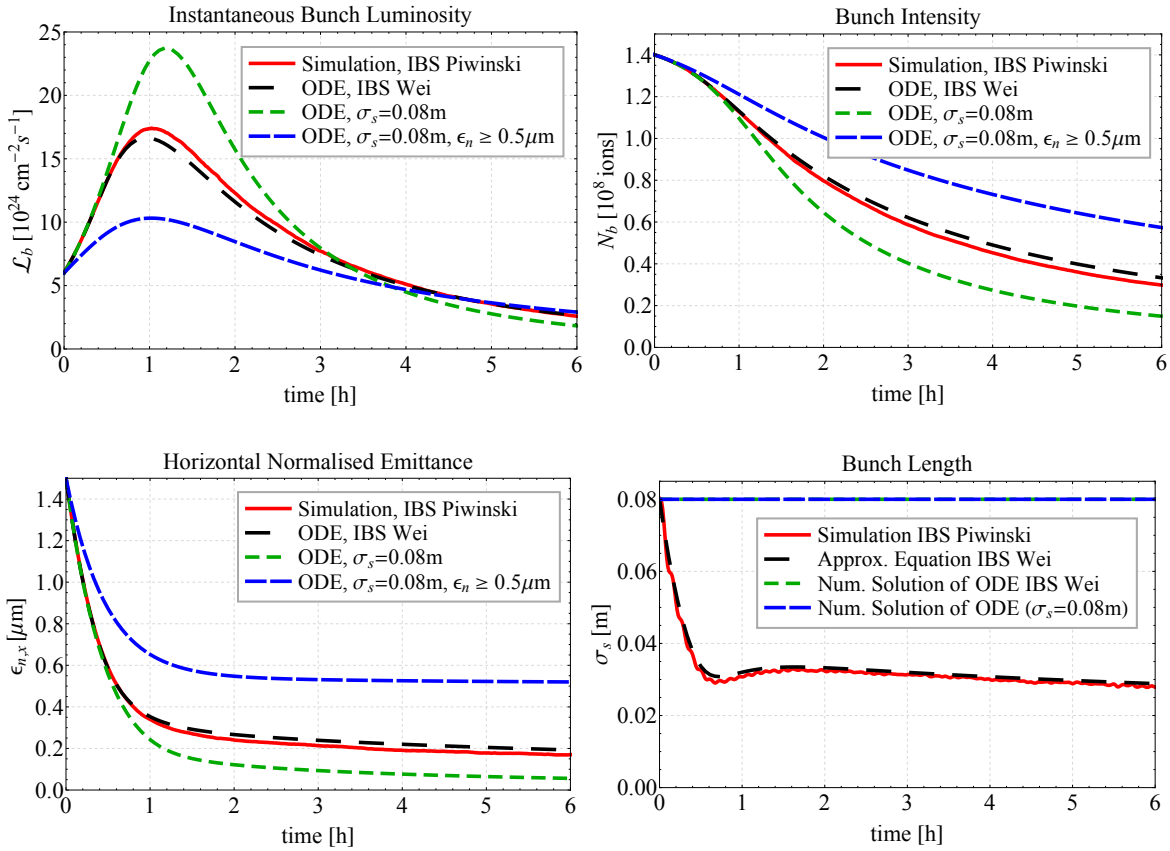

Figure 9.6.: Pb-Pb beam evolution derived from ODE in comparison with simulation result. Top: Luminosity (left) and intensity (right), bottom: normalised emittance (left) and bunch length (right).

between radiation damping and quantum excitation in lepton machines [38]:

$$\frac{\mathrm{d}\epsilon}{\mathrm{d}t} = \alpha_{\mathrm{IBS},x}\,\epsilon - \alpha_{\mathrm{rad}}(\epsilon - \epsilon_{\mathrm{min}}). \tag{9.39}$$

Solving the equations for both, constant bunch length and a minimum emittance of e.g. $\epsilon_{\mathrm{min}} = 0.5\,\mu$m, results in the blue dashed-dotted curve. As intended, the emittance stops decaying at about $0.5\,\mu$m, naturally coming along with a luminosity reduction.

As an other method for luminosity levelling, it could be considered to increase the value of β^*. Figure 9.7 compares CTE simulations for three different values. The solid red line shows the same simulation as the solid red line in Fig. 9.5 and 9.6 with $\beta^* = 1.1\,$m. The dashed black and green lines display the results for $\beta^* = 5\,$m and 10 m, respectively. As expected, the initial and peak luminosity is reduced. Moreover, the decay after passing the peak is slowed down, lengthening the fill for higher β^*. Consequently, the intensity burn-off is slowed down, such that >60% of the beam is left after 6 h similar to the current situation in the LHC.

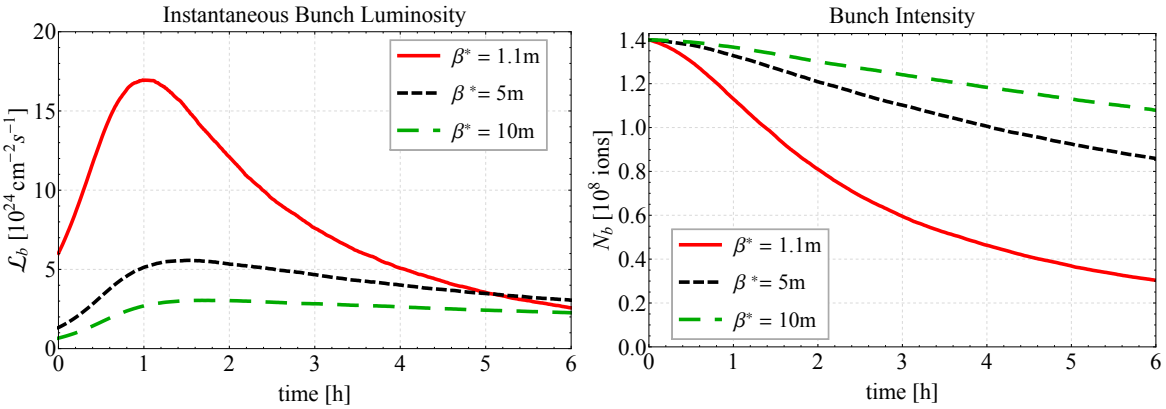

Figure 9.7.: Instantaneous luminosity (left) and intensity (right) evolution for different values of β^* in Pb-Pb operation.

Looking back at Fig. 9.5, the intensity decay is very fast, because of the high burn-off rates going along with the small emittances. In the analytical case (black) the total beam intensity is converted into luminosity in about 4 h. In the simulation the finite emittances reduce the peak luminosity and spread out the luminosity events over a longer period, however, the event production is still very efficient: only about 20% of the initial particles are left after 6 h collision time.

For comparison, in a normal LHC fill, the natural cooling from radiation damping is much weaker and not sufficient to increase the luminosity above its initial value. After about 6 h, the luminosity has decayed so much that it is necessary to refill. At that time, the beam population has only decreased to 40 or 50% of its initial value. These particles have to be thrown away to be replaced with fresh beam. To optimise the integrated luminosity, the time in collisions has to be maximised.

For the operation of a new very high energy hadron collider this attitude will change. The event production efficiency will be close to its optimum, where all particles are converted into luminosity. Under equal operational conditions, this will lead to a constant fill length. In this regime the integrated luminosity per fill is given by

$$\mathcal{L}_{\text{int}} = \frac{N_b k_b}{\sigma_{c,\text{tot}}}. \tag{9.40}$$

The simulations show that the luminosity evolution is not symmetric to the maximum, but it drops rather slowly once the balanced regime is reached. Depending on the turnaround time, t_{ta}, it is advantageous to dump the beams before all particles are burned-off and refill. The turnaround time is the time required to go back into collision

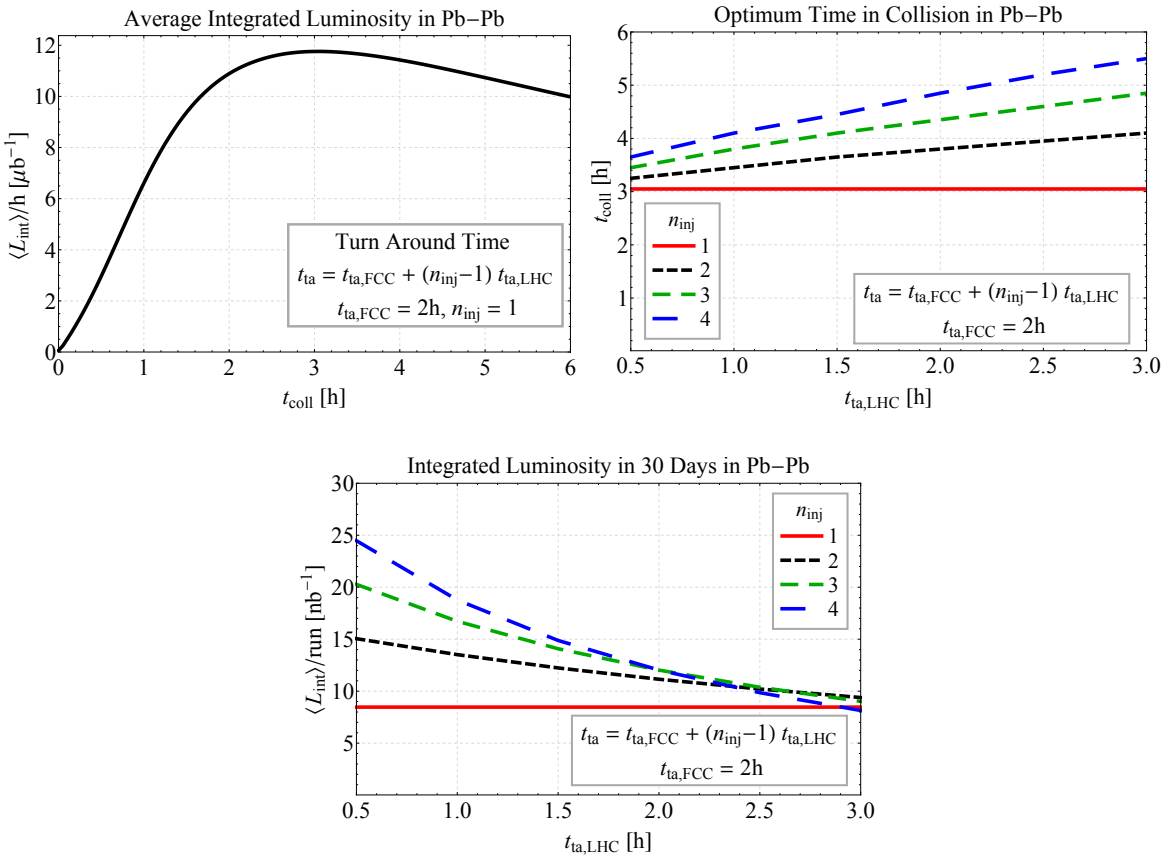

Figure 9.8.: Top: Average integrated luminosity per hour (left), optimal time in collision, assuming different number of LHC injections, n_{inj}, (right). Bottom: Optimised integrated luminosity.

after a beam abort. The average integrated luminosity defined as

$$\langle \mathcal{L}_{\mathrm{int}} \rangle = \frac{1}{t_{\mathrm{coll}} + t_{\mathrm{ta}}} \int_0^{t_{\mathrm{coll}}} \mathcal{L}_{\mathrm{int}}(t)\mathrm{d}t \tag{9.41}$$

can be used to estimate the luminosity outcome per hour, depending on the expected turnaround time and time in collision, t_{coll}. In fact, for a given t_{ta} this equation can be used to find the duration t_{coll} for which $\langle \mathcal{L}_{\mathrm{int}} \rangle$ is maximized. The left upper plot in Fig. 9.8 shows $\langle \mathcal{L}_{\mathrm{int}} \rangle$/h as a function of t_{coll}. For $t_{\mathrm{ta}} = 2\,\mathrm{h}$ the maximum is reached after around $t_{\mathrm{coll}} = 3\,\mathrm{h}$, which is about the time when the luminosity has decreased back to its initial value. Under optimal running conditions, without failures and early beam aborts, from this point on it is more efficient to dump and refill, rather than collecting at low rates. As the bottom plot of the figure displays, around $8\,\mathrm{nb}^{-1}$ (red solid line) could be collected during such an idealised 30 days Pb-Pb run. It is assumed that only one injection with two beams of 432 bunches each is taken from the LHC.

In general, a maximum of four injections would fit into the FCC. The total turnaround time consists of two components,

$$t_{\mathrm{ta}} = t_{\mathrm{ta,FCC}} + (n_{\mathrm{inj}} - 1)t_{\mathrm{ta,LHC}} \tag{9.42}$$

firstly $t_{\mathrm{ta,FCC}}$, including everything done in the FCC (cycling to go back to injection energy, ramp, preparing collisions etc.), and secondly $t_{\mathrm{ta,LHC}}$, being the time between injections. n_{inj} is the number of LHC injections. The current LHC turnaround time is on average about $t_{\mathrm{ta,LHC}} = 3\,\mathrm{h}$. Consequently, the already injected bunches would have to wait many hours at the FCC injection plateau. At this energy, the Pb bunches lose about $R_{\mathrm{loss}} = 5\%$ of their intensity per hour from IBS. For more intense bunches, the loss rate is enhanced. Approximating the intensity loss at the injection plateau as linear and neglecting losses during $t_{\mathrm{ta,FCC}}$, the total colliding beam intensity can be estimated with

$$N_{\mathrm{beam}} = k_b N_b \sum_{i=1}^{n_{\mathrm{inj}}} (1 - R_{\mathrm{loss}} t_{\mathrm{ta}}(i-1)). \tag{9.43}$$

Dividing this by the injected beam intensity, $n_{\mathrm{inj}} k_b N_b$, gives the fractional part of the intensity surviving until collision. Taking into account that $\mathcal{L} \propto N^2$, one can approximate that the potential luminosity is reduced by a factor $(N_{\mathrm{beam}}/n_{\mathrm{inj}} k_b N_b)^2$ due to IBS at the injection plateau.

Multiplying $\langle \mathcal{L}_{\mathrm{int}} \rangle$ by this factor leads to the estimates of $\langle \mathcal{L}_{\mathrm{int}} \rangle$/run shown on the bottom of Fig. 9.8 for up to $n_{\mathrm{inj}} = 4$. The top right plot of Fig. 9.8 displays the corresponding optimal time in collision. The total luminosity per run is shown as a function of the LHC turnaround time. This in an essential quantity to be improved for FCC, as it significantly influences the operation strategy. $t_{\mathrm{ta,FCC}} = 2\,\mathrm{h}$ is assumed. The plot makes clear, that the longer $t_{\mathrm{ta,LHC}}$ the less attractive it becomes to inject more than once. It has to be considered that the larger n_{inj}, the higher the risk of losing an LHC fill during the injection process. This would lengthen the injection plateau by several hours and hence reduce the achievable luminosity. Moreover, for shorter $t_{\mathrm{ta,FCC}}$, the crossing point of the curves shifts to the left, meaning that even for faster LHC cycles the potential luminosity outcome might be higher for fewer injections per fill. The unknown turnaround time imposes a large uncertainty on the estimates of $\langle \mathcal{L}_{\mathrm{int}} \rangle$ per hour and run. Any operational problems leading to delays will reduce the overall efficiency and reduce the estimated performance.

Table 9.4 collects the numerical values for the initial, peak and integrated luminosity per fill in Pb-Pb operation. The values quoted are taken from the simulation including coupling, to treat the most realistic case. The optimisation is taken into account and the values are given for $n_{\mathrm{inj}} = 1$, $t_{\mathrm{coll}} = 3\,\mathrm{h}$, $t_{\mathrm{ta}} = 2\,\mathrm{h}$ and $t_{\mathrm{run}} = 30\,\mathrm{days}$. The initial luminosity value is already 2.6 times over the nominal LHC, the peak could go up to around 7 times nominal LHC, which would be of the order of the requested LHC Pb-Pb luminosity for Run 3.

	Unit	per Bunch	k_b Bunches
$\mathcal{L}_{\text{initial}}$	[Hz/mb]	0.006	2.6
$\mathcal{L}_{\text{peak}}$	[Hz/mb]	0.017	7.3
$\mathcal{L}_{\text{int,fill}}$	$[\mu\text{b}^{-1}]$	0.13	57.8
$\mathcal{L}_{\text{int,run}}$	$[\text{nb}^{-1}]$	0.02	8.3

Table 9.4.: Pb-Pb luminosity in the FCC-hh. The maximum integrated luminosity per bunch calculated with Eq. (9.40) is $\mathcal{L}_{\text{int,fill}} = 0.235\,\mu\text{b}^{-1}$.

Luminosity Lifetime

The luminosity lifetime is defined as the time at which the luminosity has decreased to $1/e$ of its initial value. This time can easily be extracted from the simulated data:

$$\tau_{\mathcal{L}} = 6.2\,\text{h}, \tag{9.44}$$

with one experiment in collisions including burn-off, radiation damping and IBS. In case of two exactly opposite experiments, taking data under the same conditions, the luminosity lifetime will decrease accordingly, since the particle losses per turn are doubled.

9.3.4. Beam-Beam Tune Shift

The beam-beam tune shift (see Chapter 2.5.3) can be a limiting factor for the luminosity, since, if it becomes too large, the particles could cross resonances and get lost. If this is the case, the intensities have to be reduced, the emittances blown-up or a crossing angle introduced to force the tune shift below its limit, consequently the luminosity will be reduced simultaneously. N_b and ϵ_n change during the fill and thus the beam-beam tune shift. This is especially important in the case discussed here, since with the damped emittance, the tune shift increases. From the simulation results displayed in Fig. 9.5 the intensity and emittance evolutions are combined to determine the variation of the beam-beam tune shift during a fill with one experiment in collisions, see Fig. 9.9.

The peak value reaches $\xi \approx 1.4 \times 10^{-3}$. If more than one experiment is taking data, this tune shift should be multiplied by the number of experiments. However, this is not exactly true for the curve in Fig. 9.9, since it was obtained from the simulated beam evolution considering one active IP. The curve would change slightly (to lower values), due to the faster intensity burn-off and thus the beam evolution for two or more experiments would be different.

Only during operation it does become certain where the beam-beam limit of a collider exactly is. For the p-p operation in the LHC, for instance, a beam-beam limit of 0.015 was expected, based on Sp$\bar{\text{p}}$S experience. Nevertheless, the tune shifts achieved in p-p in dedicated experiments exceeded the nominal value by almost a factor of 5 and the

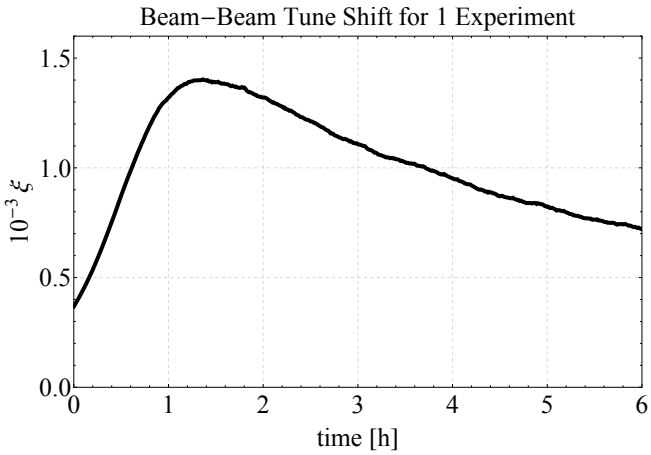

Figure 9.9.: Evolution of the beam-beam tune shift for one experiment in collision.

value reached in normal operation by already a factor of 2 [62].

Comparing to those factors, and taking into account that the usual tune stability in the LHC is in the order of 10^{-3}, the beam-beam tune shift in Pb-Pb operation for FCC is not negligible, but probably also not at the limit.

9.3.5. Bound-Free Pair Production Power

Ultraperipheral electromagnetic interactions dominate the total cross-section during heavy-ion collisions, see Eq. (9.23), and cause the initial intensity to decay rapidly [65]. The most important interactions in Pb collisions are BFPP and EMD. These interactions create secondary beams emerging from the collision point, which impact in a localised position (depending on the lattice) around a superconducting magnet downstream of the IP. More details can be found in Chapter 2.5.4 and 7.

The production rate of these processes is proportional to the instantaneous luminosity. Already under LHC conditions, the risk of quenching a superconducting magnet due to these losses is high [66]. In the FCC the peak luminosity could be an order of magnitude higher, increasing the risk even further. The power, P, in these secondary beams can be calculated with Eq. 2.70.

Figure 9.10 shows the power evolution of the BFPP1 beam ($^{208}\mathrm{Pb}^{81+}$ ions, capture of one e^-), which has the highest cross-section and accordingly the highest intensity and damage potential. For the calculation the total BFPP cross-section, $\sigma_{\mathrm{BFPP}} = 354\,\mathrm{b}$ at $50Z\,\mathrm{TeV}$, estimated with [67], was used. The probability of higher order interaction, i.e., capturing two or more electrons and leading to a charge state of $\leq 80^+$ is much smaller and ignored for the purpose of estimating the upper limit of the stored power.

For the computation of the beam power, the simulated luminosity, shown in Fig. 9.5,

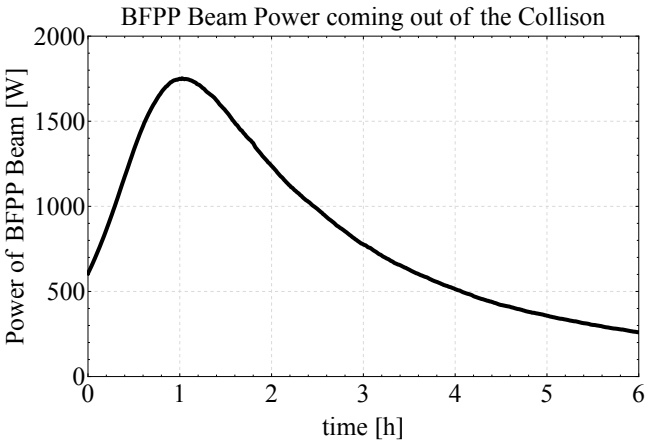

Figure 9.10.: BFPP1 beam ($^{208}Pb^{81+}$ ions) power evolution in Pb-Pb operation in FCC.

was used. The maximum power goes up to $P \approx 1.7\,\mathrm{kW}$, but already the initial value of 600 W would lead to quenches and prevent from operating the machine. Depending on the aperture and optics in the FCC, the EMD1 beam ($^{207}Pb^{82+}$ ions, emission of one neutron) might as well hit the beam screen, depositing additional energy. For comparison, the BFPP1 beam power in the nominal LHC is about 26 W, which is already expected to cause operational problems and long-term damage. Countermeasures would definitely be required to absorb these particles before they can impact on the superconducting magnets. It has to be studied, if a highly resistant collimator in the dispersion suppressor region, as discussed for HL-LHC heavy-ion operation (see Chapter 7.4 and [21, 145]), would be sufficient to stop the beams produced in the collisions at the highest energy of the FCC.

9.4. Proton-Lead Operation

9.4.1. Beam and Luminosity Evolution

IBS approximately scales with $r_0^2 \propto (Z^2/A_{\mathrm{ion}})^2$ and is therefore weaker for protons than for lead ions. In fact, IBS is negligible for the (initial) proton beam parameters used in p-Pb operation at top energy. The radiation damping rates in Eq. (2.25) to (2.27) show a dependence on the particle type as $(EZ)^3 r_0/m_{\mathrm{ion}}^3 \propto Z^5/A_{\mathrm{ion}}^4$. Calculating this ratio shows that the radiation damping for lead is about twice as fast as for protons at the same equivalent energy. Thus, the emittances of both beams evolve with different time constants. Consequently, eight differential equations, four per beam, have to be solved simultaneously to describe the beam and luminosity evolution for p-Pb collisions. These could be reduced to six equations by assuming fully coupled transverse motion

and round beams, in this case $\epsilon(t) = \epsilon_x(t) = \epsilon_y(t)$ holds at all times. Rewriting Eq. (2.21) under this approximation leads to the instantaneous luminosity for p-Pb

$$\mathcal{L} = A\frac{N_b(\mathrm{p})N_b(\mathrm{Pb})}{\epsilon(\mathrm{p}) + \epsilon(\mathrm{Pb})}, \tag{9.45}$$

with $A = f_{\mathrm{rev}}k_b/(2\pi\beta^*)$. With this, the differential equation system follows

$$\frac{\mathrm{d}N_b(i)}{\mathrm{d}t} = -\sigma_{c,\mathrm{tot}}A\frac{N_b(j)N_b(i)}{\epsilon(j) + \epsilon(i)} \tag{9.46}$$

$$\frac{\mathrm{d}\epsilon(i)}{\mathrm{d}t} = \epsilon(i)(\alpha_{\mathrm{IBS},x,y}(i) - \alpha_{\mathrm{rad},x,y}(i)) \tag{9.47}$$

$$\frac{\mathrm{d}\sigma_s(i)}{\mathrm{d}t} = \frac{1}{2}\sigma_s(i)(\alpha_{\mathrm{IBS},s}(i) - \alpha_{\mathrm{rad},s}(i)), \tag{9.48}$$

where only the three equations of beam i (either Pb or p) are noted. The equations for beam j have an equivalent form with different initial conditions and growth rates. The dependences of the IBS growth rates on N_b, ϵ and σ_s couple the three equations for each beam. The dependence of the luminosity on both beams' emittances and intensities couple the Pb and p beam evolution. An exact analytic solution of this coupled differential equation system does not exist. Unfortunately, the CTE program does not feature simulations with different particle species, so only approximated analytical and numerical solutions of the ODE system are available to perform estimates.

At the beginning of the fill, $\alpha_{\mathrm{IBS}} \ll \alpha_{\mathrm{rad}}$ and it can be approximated that $\alpha_\epsilon = \alpha_\epsilon(Pb) = 2\alpha_\epsilon(p) = \text{const.}$ in all three planes. This constant emittance decay rate, neglects the dynamically changing IBS with damped emittance. As seen in the Pb-Pb analysis, the peak and integrated luminosity estimates done under these assumptions will be overestimated, due to the emittances asymptotically approaching zero.

In general, the proton beams are more intense compared to lead. In the LHC proton-proton operation, bunches with 10^{11} particles are regularly used. Lead bunches have in the order of 10^8 particles. In proton-lead operation, it is possible to increase the initial luminosity by increasing the proton intensity (the lead intensity is assumed to be at the limit). Nevertheless, the higher the proton intensity, the stronger the beam-beam effects in these strong-weak interactions. Therefore, it was chosen for the LHC proton-lead run in 2013 to use proton intensities around 10% of the nominal value used in p-p operation. This should also be the baseline for p-Pb collision mode in FCC-hh.

In each collision of a proton with a lead ion, these two particles are removed from their beams. Therefore, the maximum integrated luminosity is reached, when each lead ion has found a collision partner in the higher intense proton beam. The number of lead ions is only about 1% of the number of protons. In the limit of burning-off all the lead, the proton intensity is hardly changed and could be considered as roughly constant through the whole fill.

To find an approximated analytical equation for the proton-lead luminosity evolution,

the following assumptions are made:

$$N_b(\mathrm{Pb}) \ll N_b(\mathrm{p}) = N_{b0}(\mathrm{p}) = \text{const.} \tag{9.49}$$
$$\alpha_\epsilon = \alpha_\epsilon(\mathrm{Pb}) = 2\alpha_\epsilon(\mathrm{p}) \approx -\alpha_{\mathrm{rad}}(\mathrm{Pb}) \tag{9.50}$$
$$\alpha_{\mathrm{rad},s} = 2\alpha_{\mathrm{rad},x,y} \tag{9.51}$$

where Eq. (9.50) is assumed for all three planes and Eq. (9.51) follows from Eq. (2.61). Applying these constraints to the differential equations (9.46) - (9.48) leads to an exponential behaviour of the emittance and bunch length of both beams with related time constants

$$\epsilon(\mathrm{Pb}, t) = \epsilon_0(\mathrm{Pb}) \exp[\alpha_\epsilon t] \tag{9.52}$$
$$\sigma_s(\mathrm{Pb}, t) = \sigma_{s0}(\mathrm{Pb}) \exp[\alpha_\epsilon t] \tag{9.53}$$
$$\epsilon(\mathrm{p}, t) = \epsilon_0(\mathrm{p}) \exp[\alpha_\epsilon t/2] \tag{9.54}$$
$$\sigma_s(\mathrm{p}, t) = \sigma_{s0}(\mathrm{p}) \exp[\alpha_\epsilon t/2], \tag{9.55}$$

where the emittance growth rate of the Pb beam is taken as the reference, $\alpha_\epsilon \approx -\alpha_{\mathrm{rad},x,y}(\mathrm{Pb})$. This value is negative, hence these are exponential decays. The proton intensity was assumed to be time independent, thus

$$N_b(\mathrm{p}, t) = N_{b0}(\mathrm{p}). \tag{9.56}$$

To solve the last equation for the Pb intensity evolution, Eq. (9.52), (9.54) and (9.56) are inserted into Eq. (9.46), followed by applying the method of separation of variables. The solution of the arising integral

$$\ln\left(N_b(\mathrm{Pb}, t)\right) = \int \frac{\mathrm{d}x}{x^2(ax+b)} = -\frac{1}{bx} + \frac{a}{b^2} \ln\left(\frac{ax+b}{x}\right) \tag{9.57}$$

with $x = \exp[\alpha_\epsilon t/2]$ can be found, e.g., in [146]. The final result is

$$N_b(\mathrm{Pb}, t) = N_{\mathrm{Pb}} e^{-\frac{2\sigma_{c,\mathrm{tot}} A N_{\mathrm{p}}}{\alpha_\epsilon \epsilon_{\mathrm{p}}^2} \left(\epsilon_{\mathrm{p}}(\exp[-\alpha_\epsilon t/2]-1) + \epsilon_{\mathrm{Pb}} \ln[\epsilon_{\mathrm{p}}+\epsilon_{\mathrm{Pb}}] - \epsilon_{\mathrm{Pb}} \ln[\epsilon_{\mathrm{p}} \exp[-\alpha_\epsilon t/2]+\epsilon_{\mathrm{Pb}}]\right)}. \tag{9.58}$$

The equations for the evolution of the emittance and intensity are inserted into Eq. (9.45) to obtain the p-Pb luminosity evolution. Figure 9.11 presents the results. The above derived analytical approximation is shown as the solid lines, while the dashed lines correspond to the numerical solution of the ODE system. The evolution of the intensity (middle left), beam size at the IP (middle right) and bunch length (bottom) are displayed in black for the proton and in red for the lead beam.

The peak luminosity is shifted to later times compared to Pb-Pb operation, due to the slower radiation damping for protons, leading to longer fills. The Pb intensity burn-off is very fast, while the proton intensity hardly changes. This arises form the fact that in one collision one Pb nucleus is lost per proton. A free knob to adjust the

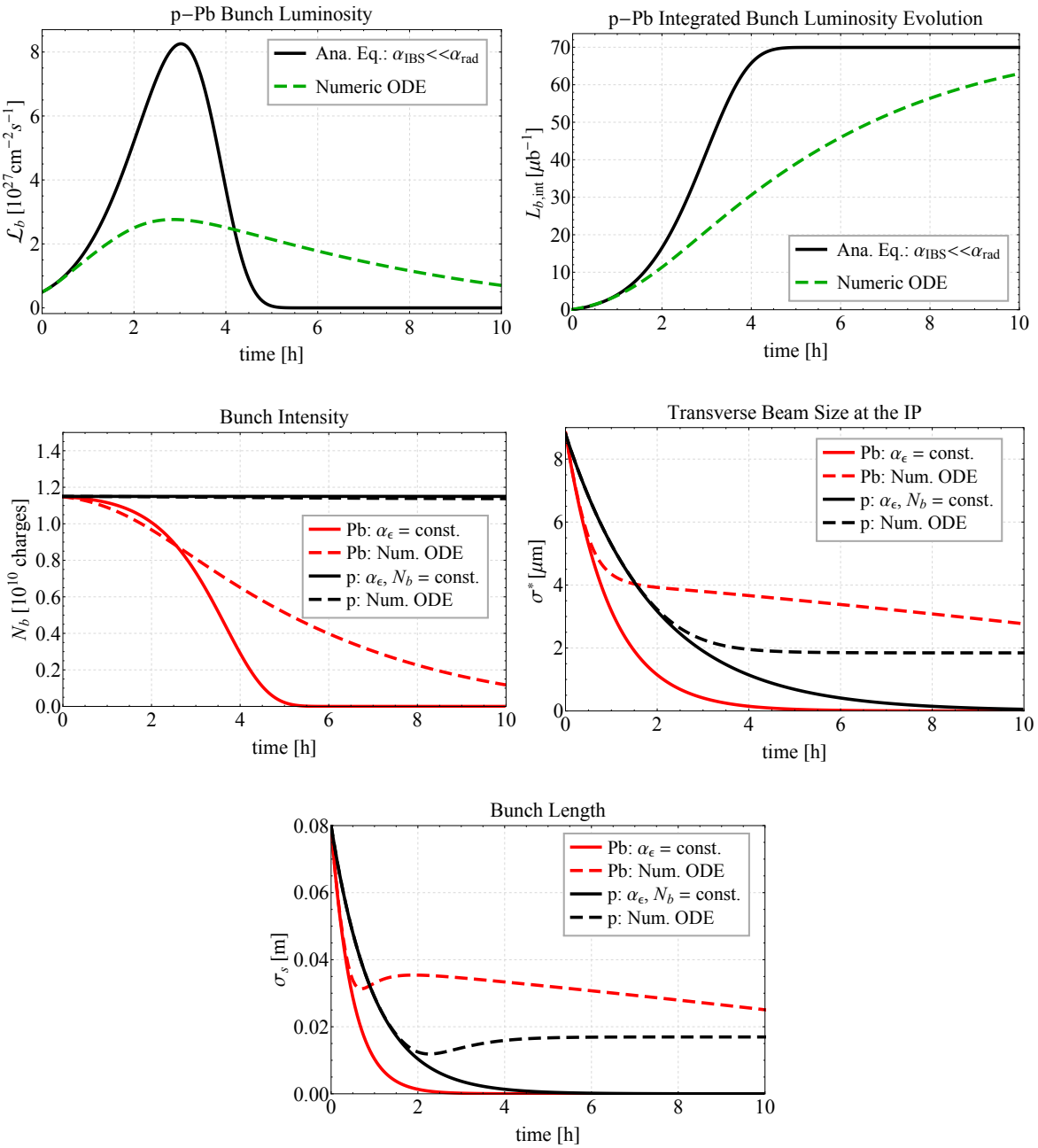

Figure 9.11.: p-Pb beam and luminosity evolution for one experiment in collisions. Top: instantaneous (left) and integrated (right) bunch luminosity, middle: intensity (left) and beam size at the IP (right), bottom: bunch length for the proton (black) and lead (red) beam. Approximated analytic calculations (solid lines), neglect the dynamically changing IBS, leading to unrealistically small beam sizes. The numerical ODE solution is shown as dashed lines, giving more realistic estimates.

luminosity peak and evolution is the proton intensity. Increasing N_b(p) would lead to higher initial and peak rates followed by an even faster Pb burn-off and shorter fills. Decreasing N_b(p) would distribute the achievable luminosity over a longer period with reduced peak rates.

The $1/e$-luminosity lifetime, extracted from the numerical solution of the ODE system shown in Fig. 9.11, determines to

$$\tau_{\mathcal{L}} = 14.0\,\text{h}. \tag{9.59}$$

9.4.2. Optimising the Integrated Luminosity

Because of the weaker IBS for protons, their intensity losses at injection are smaller and the proton beam can wait in the machine without deteriorating significantly. Therefore, the proton beam is injected first, followed by the lead. Depending on the number of injections, either both LHC rings are filled with the same species, or the filling is shared between the species and each LHC beam is injected in opposite directions in the FCC. In this way the number of particles surviving until top energy is maximised.

From the numerical solution of the ODE system, which provides the best estimate of the beam and luminosity evolution available today, the average luminosity per hour is determined. Similar to Pb-Pb, an expression for the total available p and Pb beam intensity in collision is derived, taking into account the different waiting times and loss rates at the injection plateau. The average luminosity per hour is then calculated as in Eq. (9.41) reduced by the factor $(N_{\text{beam}}(\text{Pb})/n_{\text{inj}}k_bN_b(\text{Pb}))(N_{\text{beam}}(\text{p})/n_{\text{inj}}k_bN_b(\text{p}))$ for losses during injection.

Figure 9.12 shows the results for the average integrated luminosity (top left) and the corresponding time in collisions (top right) to archive the optimised integrated luminosity per 30 days run (bottom). For $n_{\text{inj}} = 1$ the maximal luminosity of $1.7\,\text{pb}^{-1}$/run is reached for a fill length of 6.5 h. This does not take into account any delays or early aborted fills changing the assumed optimised statistics. Again it becomes clear that the longer the LHC turnaround time, the less attractive it becomes to wait for more injections before colliding. The collectible luminosity decreases, due to particle losses on the lengthened injection plateau. Moreover, the optimal fill length becomes longer, enhancing the risk to be aborted ahead of schedule, potentially decreasing the predicted luminosity further. Table 9.5 summarises the initial, peak and integrated luminosity values in p-Pb operation.

9.4.3. Beam Current Lifetime

As mentioned, the ion beam is naturally weak, while proton beams can be produced with much higher intensities. In the collision the lead beam loses $Z = 82$ charges per lost proton. Thus, the ion beam will in general have the smaller beam current lifetime, i.e., faster intensity decay. Consequently, the ion beam lifetime determines the length of the fill in p-Pb operation.

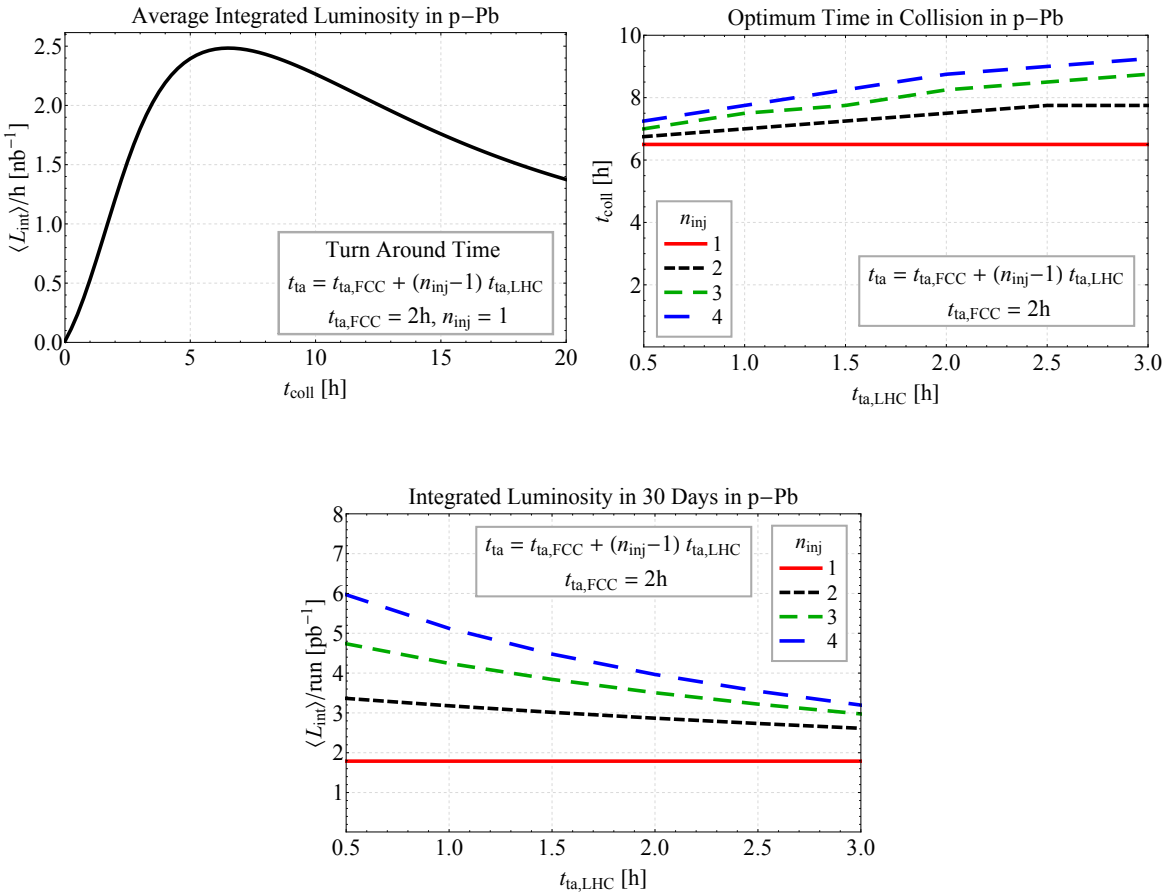

Figure 9.12.: Top: Average integrated luminosity per hour (left), optimal time in collision (right). Bottom: Optimised integrated luminosity for p-Pb operation.

The beam current lifetime is given by

$$\frac{1}{\tau_N} = -\frac{1}{N}\frac{\mathrm{d}N}{\mathrm{d}t} = -\frac{1}{N}\sigma_{c,\mathrm{tot}}\mathcal{L},$$

with $N = k_b N_b$ and $N_b = N_b(\mathrm{Pb})$. Inserting Eq. (9.45) for the luminosity, the Pb beam current lifetime in p-Pb collisions is

$$-\tau_N(\mathrm{Pb}, t) = \frac{2\pi\beta^*}{\sigma_{c,\mathrm{tot}} n_{\mathrm{exp}} f_{\mathrm{rev}} N_b(\mathrm{p})}(\epsilon(\mathrm{p}, t) + \epsilon(\mathrm{Pb}, t)). \tag{9.60}$$

The first factor is constant for $N_b(\mathrm{p}) \gg N_b(\mathrm{Pb})$. Hence, the lifetime only varies in time proportionally to the convoluted emittance of the two beams. As expected, $\tau_N(\mathrm{Pb})$ decreases with increasing proton intensity, because of the higher interaction probability.

	Unit	per Bunch	k_b Bunches
$\mathcal{L}_{\text{initial}}$	[Hz/mb]	0.5	213
$\mathcal{L}_{\text{peak}}$	[Hz/mb]	2.8	1192
$\mathcal{L}_{\text{int,fill}}$	$[\mu\text{b}^{-1}]$	48.7	21068
$\mathcal{L}_{\text{int,run}}$	$[\text{nb}^{-1}]$	4.1	1784

Table 9.5.: p-Pb luminosity in the FCC. $\sigma_{c,tot} = 2\,\text{b}$ was used. The maximum integrated luminosity per fill calculated with Eq. (9.40) is $\mathcal{L}_{\text{int}} = 30\,\text{nb}^{-1}$.

The initial value evaluates to

$$\tau_N(\text{Pb}, t = 0) = 39.3\,\text{h} \tag{9.61}$$

for $n_{\text{exp}} = 1$. Owing to the damping of the emittances, these values will decrease exponentially during the fill and lead to a much shorter fill durations. It is interesting to note that Eq. (9.60) is independent of the lead beam current.

9.4.4. Beam-Beam Tune Shift

With Eq. (2.62) the beam-beam tune shift ξ can be calculated for weak-strong beam-beam interactions as in the case of p-Pb collisions. The initial beam parameters in Table 9.1 are such that the number of charges and the beam sizes of both beams are approximately equal, resulting in the same tune shift, $\xi(\text{p}) \approx \xi(\text{Pb}) = 3.7 \times 10^{-4}$, at the beginning of the fill. However, the proton and lead beam properties evolve differently with time, changing the force exerted from one to the other during the fill. Figure 9.13 shows the calculation of ξ based on the numerical solution of the ODE system. The effect on the proton (black) beam is small ($\xi(\text{p}) < 2 \times 10^{-3}$). The increase of $\xi(\text{p})$ due to the shrinking emittances is negated by the rapid Pb intensity losses. Owing to the almost constant proton intensity but damping emittances, the tune shift to the Pb beam becomes significant and approaches a value of $\xi(\text{Pb}) = 8.3 \times 10^{-3}$ in the regime where IBS and radiation damping start to balance each other. This value is close to the assumed beam-beam limit of $\xi = 0.01$ for p-p operation.

9.5. Proton-Proton Operation

In the following the derived tools are applied to p-p operation in the FCC. In p-p operation two scenarios are under investigation, namely bunches spaced by 25 or 5 ns with different beam properties. The proton beam parameters are listed in Table 9.6.

Radiation damping is negligible for protons at injection energy. At 50 TeV the transverse and longitudinal emittance radiation damping times are $1/\alpha_{\text{rad},x,y} = 1.0\,\text{h}$ and $1/\alpha_{\text{rad},x,y} = 0.5\,\text{h}$, respectively. As already explained in Section 9.3.1, depending on

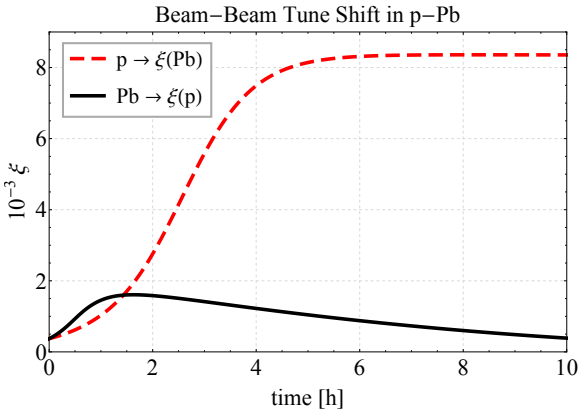

Figure 9.13.: p-Pb beam-beam tune shift for 1 IP in collision.

the lattice choice, the IBS growth rates can be rather different. Figure 9.14 shows the IBS growth times as a function of the FODO cell length, L_c, at injection (left) and top energy (right). The same behaviour as for Pb is observed, whereas the rates are lower. For the chosen baseline lattice with $L_c \approx 203\,\mathrm{m}$ and $\gamma_T \approx 103$, the initial growth times calculated with Piwinski's algorithm are listed in Table 9.7. IBS is in general small for the initial proton beam parameters. Only the horizontal growth time at injection is below 10 h, which might lead to transverse emittance growth, if the time spend on the injection plateau becomes too long.

In Fig. 9.15 the luminosity and beam evolution in p-p operation is displayed. The solid lines show the free beam evolution without any artificial blow-up, obtained by solving an ODE system of the form (9.25)-(9.28) for two experiments in collision. The

Parameter	Symbol	Unit	25 ns	5 ns
No. of particles per bunch	N_b	$[10^{11}]$	1.0	0.2
Normalised transv. emittance	ϵ_n	$[\mu\mathrm{m}]$	2.2	0.44
RMS bunch length	σ_s	[m]	0.08	0.08
No. of bunches per beam	k_b	-	10600	53000
β-function at IP	β^*	[m]	1.1	1.1
Total cross section	$\sigma_{c,\mathrm{tot}}$	[mb]	153	153
No. of main IPs	-	-	2	2

Table 9.6.: Assumed beam parameters for FCC proton-proton operation [29].

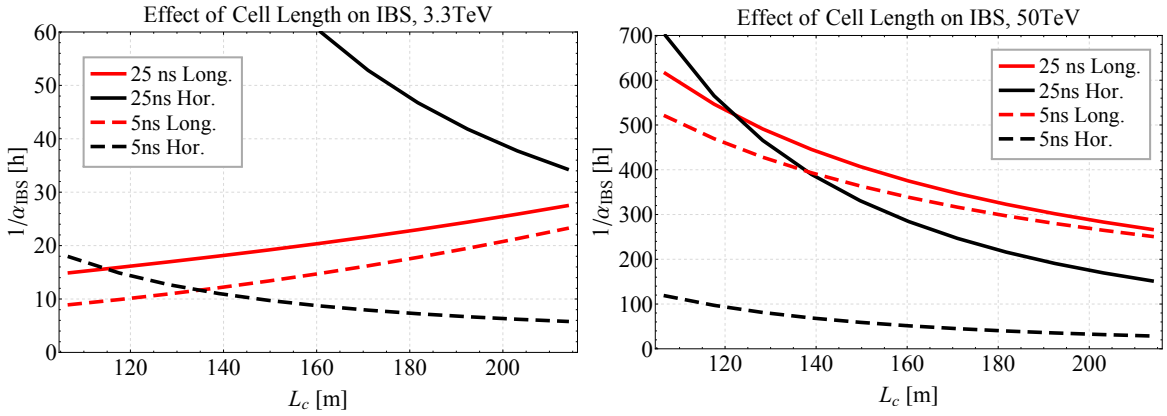

Figure 9.14.: Initial IBS growth times and their dependence on the FODO cell length, L_c, at injection (left) and top energy (right) for p-p operation in the FCC.

Growth Times	Unit	Injection		Collision			
				(a)		(b)	
		25 ns	5 ns	25 ns	5 ns	25 ns	5 ns
$1/\alpha_{\mathrm{IBS},s}$	[h]	25.9	21.3	283.1	264.7	1467	1534
$1/\alpha_{\mathrm{IBS},x}$	[h]	37.7	6.2	169.5	31.7	265.4	55.5
$1/\alpha_{\mathrm{IBS},y}$	[h]	-10^5	-10^4	-10^7	-10^7	-10^8	-10^7

Table 9.7.: Initial IBS growth times for protons in FCC-hh calculated with Piwinski's formalism, assuming the baseline lattice ($L_c = 203\,\mathrm{m}$). Assumption for momentum spread: injection $\sigma_p = 1.5\times10^{-4}$, collision (a) $\sigma_p = 0.5\times10^{-4}$ (obtained with γ_T of baseline lattice), (b) $\sigma_p = 1.1\times10^{-4}$ (LHC design).

dashed lines represent the solution of the following differential equations:

$$\frac{\mathrm{d}N_b}{\mathrm{d}t} = -\sigma_{c,\mathrm{tot}} A \frac{N_b^2}{\epsilon} \tag{9.62}$$

$$\frac{\mathrm{d}\epsilon}{\mathrm{d}t} = \alpha_{\mathrm{IBS},x}\ \epsilon - \alpha_{\mathrm{rad},x}(\epsilon - \frac{N_b}{N_{b0}}\epsilon_0) \tag{9.63}$$

$$\frac{\mathrm{d}\sigma_s}{\mathrm{d}t} = 0, \tag{9.64}$$

here a constant bunch length and a transverse emittance blow-up designed to keep the beam-beam parameter ξ at its initial value is implemented. For the FCC study it is assumed that the peak luminosity is limited by a maximum beam-beam tune shift of $\xi = 0.01$, from which the initial beam parameters were derived. Leaving the beams to evolve freely leads to an increase of up to ~ 5 times this value, as shown in the bottom right plot of Fig. 9.15. In this case, the bunch length shrinks to about

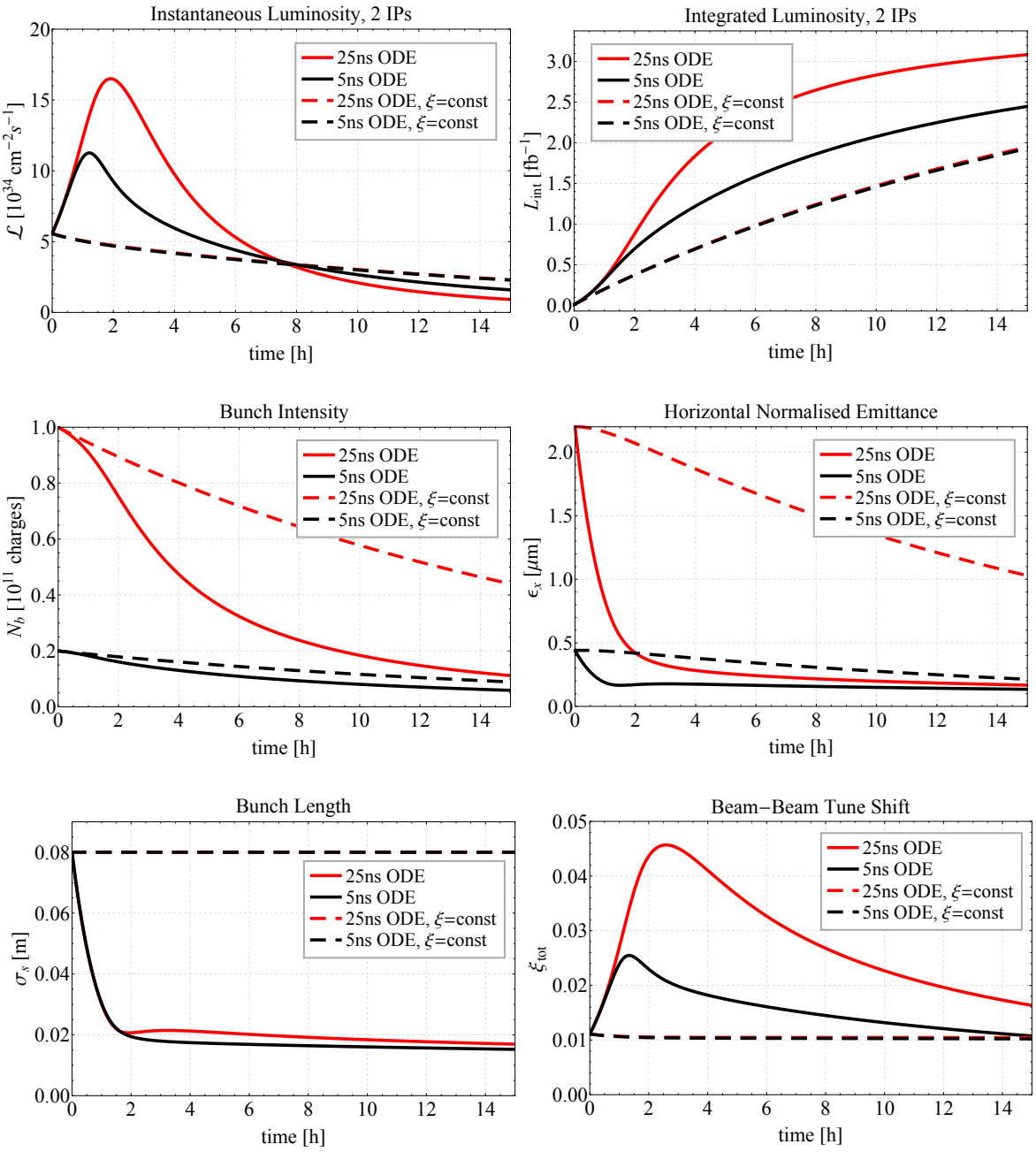

Figure 9.15.: p-p beam and luminosity evolution for two experiment in collisions. Top: instantaneous (left) and integrated (right) luminosity, middle: intensity (left) and normalised emittance (right), bottom: bunch length (left) and total beam-beam tune shift (right). Solid lines show free beam evolution without artificial blow-up, dashed lines show situation with constant bunch length and transverse emittance blow-up such $\xi =$ const. Beams for 25 (red) and 5 ns (black) bunch spacing are investigated.

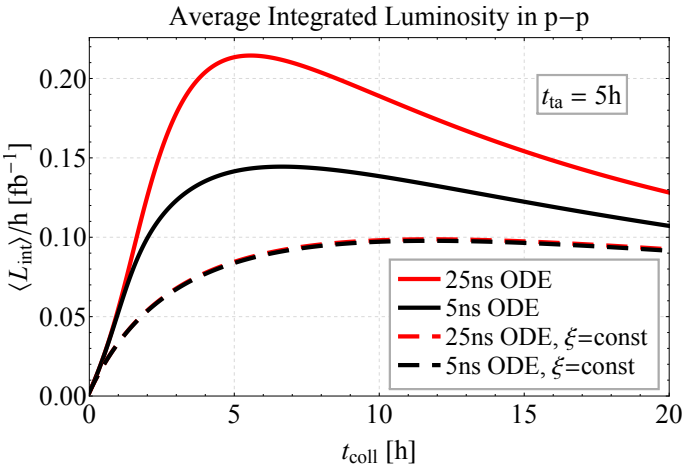

Figure 9.16.: Average integrated luminosity per hour in p-p operation.

2 cm, which is not feasible for the experiments. The transverse normalised emittances balance around 0.2 μm. The peak luminosity reaches $16 \times 10^{34}\,\mathrm{cm}^{-2}\mathrm{s}^{-2}$ for 25 ns and to $11 \times 10^{34}\,\mathrm{cm}^{-2}\mathrm{s}^{-2}$ for the 5 ns scenario. Since the beam-beam parameter is proportional to N_b/ϵ, the luminosity will decay exponentially, if ξ = const. This luminosity decay could be mitigated by β^*-levelling. The minimum β^* is constrained by the aperture in the triplet, thus β^* could be lowered proportionally to the shrinking emittance, resulting in an about constant luminosity as long as the damping is strong enough.

Figure 9.16 shows the average integrated luminosity as a function of the time in collisions, assuming a total turnaround time of $t_{\mathrm{ta}} = 5$ h (as in [29]), evaluated with Eq. (9.41) and the results shown in the upper right plot of Fig. 9.15. The four cases discussed in the previous paragraph are displayed. The particle losses of proton bunches on the LHC injection plateau are small and thus neglected. The optimum time in collisions calculates to 5.6 h and 6.7 h for the 25 ns and 5 ns case of free beam evolution (solid lines), respectively. Under optimised conditions, 5.1 fb^{-1} (25 ns) and 3.4 fb^{-1} (5 ns) could be (on average) collected per day. Considering ξ = const., the two options are very similar. The integrated luminosity is maximised for 11.8 h collision time, delivering on average 2.3 fb^{-1}/day. If the beam-beam limit is higher than expected and the beams could be left to evolve freely, the luminosity outcome could potentially be doubled.

9.6. Summary Tables for Heavy-Ion Operation

In Table 9.8-9.10 all calculated and assumed parameters for Pb-Pb, p-Pb and p-p operation at $E_b = 50Z$ TeV in the FCC-hh are collected. In case of p-Pb operation the Pb beam is assumed to be the same as for Pb-Pb, therefore the corresponding column only quotes the proton beam parameters. The Pb beam parameters at injection are

listed as well as the LHC Pb-Pb design parameters [40]. The p-p luminosity parameters given in Table 9.10 are based on the case where the beam-beam tune shift is kept constant to its initial value. The "/" separates the results of the two beam options.

	Unit	LHC Design	FCC Injection	FCC Collision
Geometry and Main Magnets				
Circumference	[km]	26.659	100	
Field of main bends	[T]	8.33	1.0	16
Bending radius	[m]	2803.95	10424	
Example Lattice				
Cell length	[m]	106.9	203	
Gamma transition γ_T		55.7	103	
RF System				
Revolution frequency	[kHz]	11.245	2.998	
RF frequency	[MHz]	400.8	400.8	
Harmonic number		35640	133692	
Total RF Voltage	[MV]	16	13	32
Synchrotron frequency	[Hz]	23.0	8.4	3.4
Bucket height ($\Delta E/E$)	[10^{-4}]	3.56	4.5	1.8
Bucket area	[eVs/charge]	8.0	4.7	28.6

Table 9.8.: FCC-hh storage ring parameters.

9.7. Conclusions

The FCC will enter a new regime of hadron collider operation. Strong radiation damping will lead to small emittances and very efficient intensity burn-off. The emittances and bunch length become so small that artificial blow-up might be necessary to avoid instabilities. An artificial blow-up might also be used as a way of luminosity levelling. Because of the small beam dimensions, the peak Pb-Pb luminosity can expected to be about 7 times the nominal LHC design value. The absolute integrated luminosity maximum per fill, when all particles are converted into luminosity, comes into reach, again because of the natural cooling from radiation damping. It is estimated that an integrated luminosity of about $8\,\mathrm{nb}^{-1}$ could be expected per run of 30 days.

If the LHC is used as the last pre-accelerator, its cycle time has to be drastically improved. Otherwise, the time between two injections into the FCC will be in the same order as the expected time in collisions per fill. To optimise the run time, the LHC could be re-filled in parallel to physics operation, maximising the time in physics and the integrated luminosity, while filling only one fourth of the FCC.

In p-Pb operation, is the fill length determined by the burn-off of the lead beam. The

	Unit	LHC Design	FCC Injection	FCC Collision		
General Beam Parameters						
Operation mode	-	Pb-Pb	Pb	Pb-Pb	p-Pb	p-p (25 ns/5 ns)
Beam energy	[TeV]	574	270	4100	50	
Relativistic γ-factor		2963.5	1397	21168	53290	
No. of bunches	-	592	432			10600/53000
No. of particles per bunch	[10^8]	0.7	1.4		115	1000/200
Transv. norm. emittance	[μm.rad]	1.5	1.5		3.75	2.2/0.44
RMS bunch length	[cm]	7.94	10.0	8.0		
RMS energy spread	[10^{-4}]	1.1	1.9	0.6		
Long. emittance (4σ)	[eVs/charge]	2.5	2.6	10.1		
Circulating beam current	[mA]	6.12	2.38			509.14
Stored beam energy	[MJ]	3.8	2.6	39.8		8491.5
Intra Beam Scattering						
Long. IBS emit. growth time	[h]	7.7	6.2	29.2	4×10^3	283.1/264.7
Hor. IBS emit. growth time	[h]	13	10.0	30.0	4×10^3	169.5/31.7
Synchrotron Radiation						
Long. emit. rad. damping time	[h]	6.3	852	0.24	0.5	
Hor. emit. rad. damping time	[h]	12.6	1704	0.49	1.0	
Power loss per ion	[W]	2.0×10^{-9}	1.1×10^{-11}	5.7×10^{-7}	3.4×10^{-9}	
Power loss per metre in main bends	[W/m]	0.005	1.0×10^{-5}	0.53	0.26	55.4
Energy loss per ion per turn	[MeV]	1.12	0.01	775.3	4.7	
Synchrotron radiation power per ring	[W]	83.9	0.7	34389	17016	3.6×10^6
Critical photon energy	[eV]	2.77	0.08	269.3	4300	

Table 9.9.: Beam parameter summary for FCC.

	Unit	LHC Design	FCC Collision		
Luminosity					
Operation mode	-	Pb-Pb	Pb-Pb	p-Pb	p-p (25 ns/5 ns)
β-function at the IP	[m]	0.5	1.1		
Initial RMS beam size at IP	[μm]	15.9	8.8		6.7/3.0
Number of IPs in collision	-	1	1		2
Crossing-angle	[μrad]	0			
Initial luminosity	[10^{27}cm^{-2}s^{-1}]	1	2.6	213	5.6×10^7
Peak luminosity	[10^{27}cm^{-2}s^{-1}]	1	7.3	1192	5.6×10^7
Integrated luminosity per fill	[μb^{-1}]	<15	57.8	21068	1.65×10^6
Integrated luminosity per hour	[μb^{-1}]	-	11.5	2478	98.2×10^3
Optimum time in collision	[h]	-	3.0	6.5	11.8
Assumed turnaround time	[h]	-	2.0	2.0	5.0
Overall operation cycle	[h]	-	5.0	8.5	16.8
Initial bb tune shift per IP	[10^{-4}]	1.8	3.7	3.7	55.5
Total cross-section	[b]	515	597	2	0.153
Peak BFPP beam power	[W]	26	1705	0	0
Initial beam current lifetime	[h]	<11.2 (2 exp.)	10.9	39.3	17.3 (2 exp.)
Luminosity lifetime ($\mathcal{L}_0/e$)	[h]	<5.6 (2 exp.)	6.2	14.0	17.0

Table 9.10.: Luminosity summary for FCC.

longer radiation damping time and weaker IBS of the proton beam, lead to longer fills in p-Pb operation. However, by adjusting the proton beam intensity the luminosity peak and time distribution could be levelled.

The formalisms developed for the heavy-ion operation have also been applied to p-p operation. First prediction of the p-p beam and luminosity evolution, under the assumption of constant bunch length and an emittance blow-up, designed to keep the beam-beam tune shift ξ = const., could be presented. Furthermore, IBS calculations show that transverse emittance growth for long injection plateaus could become an issue for high intensity, low emittance protons.

The benefit of an heavy-ion programme in this new energy regime, should be investigated by the physics community. Nevertheless, the first estimates from the accelerator physics point of view look very promising and no show stoppers have been found.

10. Summary and Outlook

This thesis has addressed the performance of the LHC as a heavy ion collider and its luminosity optimisation. The results compiled in this work are summarised in three categories: performance of the past and current LHC, the future HL-LHC and the, today still hypothetical, FCC.

Performance Analysis of the Past Runs Heavy-ion beams in the LHC show a large spread in the single bunch properties, which is imprinted mostly on the SPS and LHC injection plateau by strong dynamic effects like IBS, space charge and RF noise. This spread in the bunch parameters introduces an even stronger deviation in the single bunch luminosities and lifetimes. A statistical analysis of the 2011 run showed that bunches with lower intensities deliver the highest contribution to the total instantaneous and integrated luminosity, since they are more numerous. Bunches with very high intensities, and thus high luminosities, are rare. Bunches with low intensity show longer decay times than high intensity bunches, due to the reduced collision rate. Therefore, it is advantageous for the overall luminosity production to distribute the available total beam current among many bunches with moderate intensity rather than to a few highly intense bunches.

Because of the large cross-sections for electromagnetic processes, compared to inelastic interactions, intensity and luminosity burn off very rapidly. These ultraperipheral electromagnetic interactions change the charge or mass state of the ion involved and produce secondary beams emerging from the collision point. The modified magnetic rigidity leads to a different bending compared to the primary beam and they impact in a localised position in the downstream dispersion suppressor on each side of the IP. The intensity carried by these secondary beams is proportional to the luminosity. Observations of highly luminosity correlated losses around the IPs in collision and in IR3 (momentum collimation) were made and could be identified as originating from the BFPP and EMD processes. While in 2011, these losses could not yet quench superconducting magnets, the luminosity is subject of continuous upgrades and the risk of quenches and, possibly, long term damage will increase soon.

A test of the previously proposed bump technique for temporary loss mitigation was performed on the right side of IP5. The experiment successfully moved the losses deposited in the superconducting dipole to the connecting cryostat by introducing a small orbit bump. An algorithm was developed to calculate the impacting secondary beam distributions in the beam screen and applied to investigate the impact properties for a set of potential optics for the next run. Particle distributions were used as

input for FLUKA simulations, which could reproduce the BLM measurements with and without the bump and estimate the heat load around the impact point during the experiment. Preliminary simulations for a beam energy of $6.5Z$ TeV could further show that, according to the peak energy deposition in the magnet coils, the risk of quench is low for the expected luminosities after LS1, if the mean BFPP1 impact position lies at the beginning of the empty cryostat, i.e., outside the dipole. As soon as the decision on the final optics configuration for the 2015 run is taken, a FLUKA study can help to find the best bump settings. After the foreseen upgrades in LS2, the mitigation by orbit bumps is unlikely to be sufficient and dedicated collimators are required. Positions for these collimators were proposed.

The so-called Collider Time Evolution (CTE) program can be used to track two bunches of macro-particles in time in a collider. In the scope of this thesis, the program was improved, by correcting several bugs, leading to more precise results. A routine for β^*-levelling was implemented and the original treatment of stochastic cooling was reimplemented. The simulation results obtained are in very good agreement with the measured bunch and luminosity evolution in the LHC. It was found that, using average bunch parameters, the simulation describes well the total beam behaviour in Pb-Pb operation. Since, p-Pb is now a standard operation mode of the LHC, it could be considered to extent the simulation program to treat colliding bunches of different species.

A semi-empirical model was developed, to describe the total beam and luminosity evolution in Pb-Pb collisions in the LHC, while taking into account the spread between bunches. The model combines a parametrisation of the observed bunch-by-bunch differences at the beginning of collisions in 2011 and a set of CTE simulations covering the full spectrum of expected bunch properties colliding at the desired energy and β^*. The results strongly depend on the initial bunch parameter distribution. The experience of Pb-Pb collisions in the LHC is so far limited to two runs. In the first run in 2010, injection schemes with only one to maximum eight bunches per SPS train [10] were used, which is not representative to predict future performance. Predictions made with this model, based on the bunch spread as observed in 2011, likely underestimate the real future performance, since great improvements were already achieved in the 2013 p-Pb run. By gaining more experience and readjusting the parametrisation at the beginning of each run, the luminosity model will gradually improve and the estimates for current and future runs become more and more precise.

Predictions for Future Runs In the upcoming LHC heavy-ion run in 2015, Pb-Pb collisions will be provided. Compared to 2011, a new filling scheme, fitting more bunches into one LHC ring, higher bunch intensities, comparable with those achieved in 2013, and a beam energy of $E_b = 6.5Z$ TeV are foreseen. With these parameters, peak luminosities in the order of three to four times the design value can be expected. Nevertheless, before the ALICE detector upgrade during LS2, ALICE has to be levelled to the design peak luminosity of $\mathcal{L} = 1 \times 10^{27}\,\mathrm{cm}^{-2}\mathrm{s}^{-1}$ to avoid event pile up during the drift time in the time projection chamber (TPC) [110]. ATLAS and CMS are not

limited and could run at the highest available luminosities. However, at the expected peak rates the BFPP beam intensity will be high enough that quenches become more likely. This might enforce levelling also in IP1 and 5.

By making simplified but realistic assumptions, analytic equations were derived to describe the luminosity and beam evolution for a varying number of levelled and non-levelled IPs. Performance estimates for potential scenarios with levelling were analytically calculated and found to be in good agreement with CTE simulations based on the same conditions.

Upgrades foreseen in the LHC Injector Upgrade (LIU) project to enhance the LHC heavy-ion luminosity by improving the injector complex were summarised and detailed performance predictions for Run 3 and beyond were made, using the developed semi-empirical luminosity model. Only the full upgrade (including a new SPS injection kicker, bunch splitting and batch compression in the PS, and slip stacking in the SPS) brings the requested $10\,\mathrm{nb}^{-1}$, to be integrated during the HL-LHC period, into reach.

As mentioned, because of the high burn-off rates and with three experiments in collisions, the fills will be very short and the ratio of physics to turnaround time will decrease. Stochastic cooling in the LHC could shrink the emittances, collide beams more efficiently and thereby reduce the fraction of the beam which has to be dumped at the end of the fill. First simulation results showed an improvement in integrated luminosity, with a full 3D cooling system, approaching 50% per experiment. More dedicated work on the system design is required to confirm that the assumed properties are feasible. In particular, the compatibility with high intensity proton-proton operation, hardware development, tunnel space and manpower availability are to be clarified. The setup and expected performance for a proof of principle experiment was presented. Because of the narrow bandwidth of the test arrangement with only a single cooling cavity, the cooling effect is expected to be small and might be difficult to observe. For this reason, the outcome of a feasibility experiment of the presented form is considered to be of low value for the project. However, a first stage 1D cooling system could be considered to gain experience, reduce the initial cost and commissioning time, but quickly benefit from the cooling.

Performance of the Future Circular Collider With the view to high energy physics after the LHC era, the Future Circular Collider (FCC) project was launched to study the possibilities of a new circular collider reaching a center-of-mass energy of $100Z\,\mathrm{TeV}$ in hadron collisions. In the scope of this thesis, the very first performance estimates for Pb-Pb, p-Pb and p-p collisions could be made. At these high energies, radiation damping and IBS dominate the beam and luminosity evolution in all operation modes. At the time of writing, the lattice design is still progressing and a smooth (average) lattice was used in the calculations. The effect of a varying FODO cell length and RF voltage was investigated and reference lattice parameters were chosen.

Analytic equations for the beam and luminosity evolution were derived under certain conditions. The results were compared with CTE simulations and the numerical

solution of a system of ordinary differential equations (ODE). With the ODEs, special cases including artificial longitudinal and transverse emittance blow-up could be studied. Moreover, luminosity estimates depending on the LHC (as an injector) and FCC turnaround time are given. The beam losses due to BFPP can be dealt with by incorporating suitable collimators and absorbers into the initial lattice design. It was found that even with the reduced emittances due to radiation damping, the beam-beam tune shift in Pb-Pb collisions is small. However, it can become significant for the Pb beam in p-Pb operations.

The work presented here is intended to be an initial study, setting the scope of an potential heavy-ion program in the FCC. The ODE model should be extended to include more detailed calculations and take more effects like quantum excitation, beam-beam and RF noise into account. The calculations should be repeated once a full lattice design is available. The FCC study has just begun. If a heavy-ion programme is desired, one has to learn from the LHC experience and ensure that the lattice design and other machine parameters are compatible with heavy-ion operation, e.g., include BFPP collimators in the original design.

Acknowledgement

Firstly, I would like to greatly thank my supervisor Prof. Dr. Achim Stahl for his constant support through the different stages of my scientific career and as well during the process of writing this thesis. I am thankful for his encouragement and the interesting discussions we had over the years.

I owe deepest gratitude to my CERN supervisor Dr. John M. Jowett for his precious advice during my whole PhD. He was the one to channel my efforts in the right direction, help me with ideas when I was stuck, and provide feedback for my work.

Great support was given by the LHC Operations group. I would like to thank you for the kind assistance during dedicated measurement periods and continuously taking measurements, which were an essential contribution to the analysis of my thesis. Especially, I am indebted to Dr. Reyes Alemany-Fernandez, who encouraged me to do a PhD and assisted me in operational questions and requests.

A big "Thank you" goes to the people involved with the heavy-ion injector complex: I owe deep gratitude to Dr. Django Manglunki, who always patiently answered my questions and did his best to provide me with the information and data I needed. I am also grateful to Dr. Michael A. Bodendorfer, Dr. Heiko Damerau, Dr. Simone Gilardoni, Dr. Steven Hancock and others for the fruitful discussions concerning the performance of the heavy ions in the injectors.

I wish to thank, my colleague Dr. Reine Versteegen for the great collaboration and the BE/BI group for the assistance in understanding the uncertainties on the given measurement devices, especially I would like to thank Dr. Federico Roncarolo, Dr. Mariusz Sapinski and Georges Trad.

It is a pleasure to thank Dr. Roderik Bruce for his help in getting started with the CTE simulation program and his suggestions on the implementation of new features, even though he committed to new task. Also, in any question concerning the collimation system of the LHC, he, Pascal Hermes and Dr. Stefano Redaelli offered great support.

The study of stochastic cooling presented here required the expertise of many people: I deeply thank Dr. Mike Blaskiewicz from the Brookhaven National Laboratory for teaching me the required simulation techniques and giving me the opportunity to get direct experience with their operating cooling system at RHIC. During my stay at BNL, I have also learnt a lot from Dr. Mike J. Brennan and Dr. Kevin Mernick. I am grateful to them for their precious time. I would like to thank Dr. Fritz Caspers for his discussions and constructive criticism, which pointed us to important issues to be considered. Dr. Lars Thorndahl's enthusiasm to the project was encouraging

and a great help in the development of new ideas. Thank you to Dr. Benoit Salvant, Dr. Silvia Verdú-Andrés and Dr. Manfred Wendt for providing their expert knowledge on impedance, cavity design and Schottky signals.

I am indebted to the CERN FLUKA team (EN/STI), in particular to Dr. Anton Lechner, Dr. Francesco Cerutti, Dr. Nikhil Shetty and Dr. Leftheris Skordis, who prepared and ran the FLUKA simulations presented in this thesis. They provided instantaneous support and results on very short term. Thanks a lot.

I would also like to acknowledge Dr. Andrea Dainese, Dr. Silvia Masciocchi and Dr. Urs Wiedemann for the opportunity to present my results in their collaboration meetings, providing a discussion background on the physics potential of nuclear beams at the FCC. I am also grateful to Dr. Daniel Schulte for discussions.

I like to express my gratitude to Claudia Cüster-Weiger and Ruth Jansen from the physics institute III B of the RWTH Aachen and to Delphine Rivoiron from CERN, who always helped me with administrative processes and bureaucratic problems. And not to forget, thanks to my office mates for the always good atmosphere in our office.

Several people were helpful in shaping this manuscript and proof reading. For this I thank: Dr. John M. Jowett, Dr. Moritz Guthoff, Dr. Regina Kwee-Hinzmann, Dr. Tom Mertens, Dr. Mike Blaskiewicz and Dr. Fritz Caspers.

I thank the Wolfgang-Gentner-Programme of the Bundesministerium für Bildung und Forschung for the financial support and Dr. Michael Hauschild, the coordinator of the programme, for his assistance and advice.

I am grateful to my friends and family, especially Moritz Guthoff, for the moral support during these exciting, but stressful times. Zuletzt möchte ich mich bei meinen Eltern, Claudia und Detlef, bedanken. Ohne ihre uneingeschränkte Unterstützung während meines bisherigen Lebensweges wäre ich nicht da wo ich heute bin.

Appendix

A. Collider Time Evolution Program

A general introduction to CTE and its capabilities is given in Chapter 3.1.1. Here, a more technical description of the input requirements and options is given.

A.1. The Input File

The input file defines the conditions of a given simulation run. It is composed of sections grouping the input parameters to the corresponding processes. In the following all input parameters are listed with a short explanation of their meaning and units.

A.1.1. Processes

The switches listed in this section provide the possibility to activate (1) or deactivate (0) the implemented processes for the current simulation run.

- *RFswitch*, activates synchrotron motion and debunching losses.
- *betatronSwitch*, activates betatron motion.
- *raddampSwitch*, activates radiation damping and quantum excitation.
- *IBSswitch*, activates intra beam scattering (IBS).
- *collimationSwitch*, activates losses on aperture cuts.
- *collisionSwitch*, activates collisions between two individual bunches.
- *stochCoolSwitch*, activates stochastic cooling.
- *levellingSwitch*, activates β^*-levelling.

A.1.2. Ring, General Parameters

Here the properties of the accelerator and other general parameters are defined.

- *nturns*, number of simulation turns.
- *nMacro*, number of macro-particles per bunch.
- *eqTime*, fill length in the real machine in hours.
- *nwirte*, every *nwirte* turns output is written (to reduce the outputfile size).

- *writeAllCoordSwitch*, activates (1) output (one file per beam) of all particle coordinates every *nwirte* turns.
- *writeMountSwitch*, activates (1) mountain range output of distribution profile in the three planes.
- *iseed*, random number seed.
- *gammat*, gamma transition.
- *circ*, ring circumference.
- *gamma0*, relativistic Lorentz factor.
- *vrf*, voltage of the first RF system in Volts.
- *nharm*, harmonic number of the first RF system.
- *vrf2*, voltage of a second RF system in Volts.
- *nhamr2*, harmonic number of the second RF system.
- *tunx* and *tuney*, horizontal and vertical tune.
- *chromx* and *chromy*, horizontal and vertical chromaticity.
- *dqmin*, linear coupling term between transverse planes.
- *aatom*, mass number of the ion species.
- *qatom*, charge number of the ion species.
- *thib*, bucket length, particles with $|t| > thib/2$ are considered lost.
- *twissFile*, path to the MADX lattice file with the column structure as (NAME, S, L, BETX, BETY, ALFX, ALFY, DX, DPX, DY, DPY, ANGLE, K1L), for the definition of these MADX variables see [41].

A.1.3. Starting Conditions

The initial beam conditions of two real bunches and how the longitudinal coordinates should be generated is defined in this section. The transverse coordinates are generated under the assumption of a Gaussian profile.

- *emix1* and *emiy2*, initial horizontal and vertical geometric RMS emittance of bunch 1 in metres.
- *pnumber1*, initial number of particles of bunch 1.
- *emix2*, *emiy2*, *pnumber2*, initial emittances and intensity of bunch 2.
- *longCoordMethod*, switch to generate initial longitudinal coordinates. Possible values:
  - 0: generates parabolic distribution with smokering,
  - 1: reads distribution form file (file paths are given in last two lines of this section, one file per beam is required)
  - 2: generates bi-Gaussian distribution with given energy spread and bunch length, only matched in small-angle approximation.

  - 3: generates pseudo-Gaussian distribution, exactly matched phase-space.

  for more information on a specific routine see Section A.2.3.
- *rmsBunchLen1*, *rmsBunchLen2*, RMS bunch length of bunch 1 and 2 in metres.
- *rmsDelta1*, *rmsDelta2*, $\Delta p/p_0$ for bunch 1 and 2.
- *tauhat1*, *tauhat2*, half bucket length of the RF system with shortest wavelength for beam 1 and 2 in seconds. For single RF $tauhat = thib/2$.
- *bunchLenPrecis*, precision in sampling of the bunch length, e.g. 0.01 gives 1% accuracy.
- *power*, bunch shape parameter, only used for *longCoordMethod* = 0.
- *alint*, smoke ring parameter, only used for *longCoordMethod* = 0.

A.1.4. Radiation Damping

In this section the method to calculate the radiation damping times and corresponding variables are specified.

- *radMethod*, method used to determine radiation damping times. Possible values:
  - manual : uses pre-calculated values given in next input line,
  - lattic : uses radiation integrals calculated over the lattice. MADX lattice file required (path given in second section),
  - approx : uses smooth approximation of the lattice.

  for more information on a specific routine see Section A.2.3.
- *tradlong, tradperp, siglong, sigperp*, parameters for *radMethod = manual*.
- *rho0*, dipole bending radius in metre.

A.1.5. Intra-Beam Scattering

Several methods to calculate emittance growth rates due to IBS are provided, *ibsMethod* can have the following values:

- *nagaitsev*, uses the full lattice information,
- *piwiSmooth*, uses a smooth lattice approximation,
- *piwLattice*, uses the full lattice information,
- *modPiwLatt*, uses the full lattice information,
- *baneApprox*, approximation for high-energy, uses full lattice information,
- *interpolat*, interpolation of pre-calculated growth times, requires external file (given in second last line of this section),

for more information on a specific routine see Section A.2.3. Additionally required parameters:

- *coupleIBS*, switch for total transverse IBS coupling (0 gives separated growth rates, 1 gives the same average growth rates in x and y).

- *coulombLog*, coulomb logarithm, only used in *nagaitsev* IBS method.
- *fracibstot*, fraction of IBS strength that should be used.
- *nBins*, number of bins used for longitudinal IBS calculation.

A.1.6. Stochastic Cooling

Only if *stochCoolSwitch = 1*, the parameters in this section are used. In case the effect of stochastic cooling should be studied, it is necessary to split one turn into fractions in order to save the particle coordinates at the position of each of the three (horizontal, vertical, longitudinal) pickups. A kick, corresponding to the pickup measurement, is given at the position of the kicker.

In order to simulate the correct cooling time, the number simulation turns has to be scaled with the ratio of the number of macro-particles to the number of real-particles and compared to the number of real turns. For a given equivalent time and number of macro-particles, real-particles and simulation turns will be recalculated after the start of the simulation to obtain the required relation. Since the number of real-particles can be different for both beams, the number of macro-particles in the second beam will be adjusted, so that the equivalent time is the same for both beams.

The following input parameters are required for stochastic cooling.

- *fimpedx0* and *fimpedx1*, lower and upper frequency of the horizontal cooling system in nano seconds.
- *gainx0* and *gainx1*, gains for the lower and upper frequency of the horizontal cooling system.
- *fracx*, pickup - kicker distance for horizontal system as a fraction of total circumference.
- *fimpedy0* and *fimpedy1*, lower and upper frequency of the vertical cooling system in nano seconds.
- *gainy0* and *gainy1*, gains for the lower and upper frequency of the vertical cooling system.
- *fracy*, pickup - kicker distance for vertical system as a fraction of total circumference.
- *fimpeds0* and *fimpeds1*, lower and upper frequency of the longitudinal cooling system in nano seconds.
- *gains0* and *gains1*, gains for the lower and upper frequency of the longitudinal cooling system.
- *fracs*, pickup - kicker distance for longitudinal system as a fraction of total circumference.
- *nextra*, extra turns with cooling off.
- *ntdelay*, *0* for one turn delay, *1* for cascaded one turn delays.
- *nturnon*, number of turns to turn on nonlinear RF and longitudinal wakes.

- *ampbtf*, *phibtf* and *harmbtf*, amplitude, phase and carrier harmonic for beam transfer function kick.
- *nresamp*, number of samples used for Fast Fourier Transformations.
- *coffsetx* and *coffsety*, closed orbit offset in horizontal and vertical plane inside the pickup.
- *snrinv*, ratio of RMS noise to RMS signal (inverse signal-to-noise ratio) for transverse pickup.
- *taupart*, equivalent length of a macro-particle.
- *writeStochCoolSwitch*, switch to write special stochastic cooling output every *nwrite* turns.

A.1.7. Collimation

This section is responsible for particle losses due to aperture restrictions. *refEmxy* and *cutoffAmpl* are used while generating the initial particle distributions. *emitMethod* defines the value of the emittance written in the output.

- *refEmxy*, reference geometric transverse emittance used for the collimation/aperture cuts in betatron space (in metres).
- *cutoffAmpl*, number of reference sigma at which initial transverse distribution is cut due to aperture restrictions.
- *collimAvgSwitch*, set to *1* to collimate the maximum amplitude over all phases and set to *0* to collimate only horizontal plane (accounting for the betatron phase).
- *emitMethod*, method used to calculate transverse emittance. Possible values:
  - *stdev*: uses standard deviation of the coordinates.
  - *stcal*: takes into account that the tails of the distribution might be cut.
  - *exfit*: uses exponential fit to betatron actions.

  for more information on a specific routine see Section A.2.3.
- *nSigCutBeta*, number of reference sigma at which the betatron collimator is placed.
- *nSigCutMom*, number of reference sigma at which the momentum collimator is placed.
- *betaxMom*, horizontal beta function at momentum collimator in metres.
- *dispxMom*, horizontal dispersion at momentum collimator in meters.

A.1.8. Collisions

Only if *collisionSwitch = 1*, the parameters in this section are used.

- *collRoutine*, collision model to be used. Possible values:

  - *1d*: slow routine, makes no assumptions on beam profiles.
  - *6a*: fast routine, assumes transverse Gaussian beam distributions.

  for more information on a specific routine see Section A.2.3.
- *nIPs*, number of interaction points with different parameters.
- *sigI*, total interaction cross section in collisions in barn.
- *nbunches*, number of (identical) bunches per beam.
- *longIntBins*, number of bins for numeric integration of hourglass effect.
- *angleSwitch*, switch to change crossing angle plane in odd turns (*1* alternating crossing plane, *0* fixed plane).
- *betaS*, minimal β^* in metres.
- *theta*, half crossing angle in rad.
- *IPmult*, number of IPs with this β^* and crossing angle.
- *lumimax*, maximum luminosity allowed for this IP, if levelling is switched on.
- *levIPSwitch*, switch to level this IP, *1* for levelling to *lumimax*.

The last line including *betaS*, *theta*, *IPmult* and *levIPSwitch* should be repeated for *nIPs* times to define those parameters for the different IPs.

A.2. Detailed Simulation Settings

This section gives more detailed information about some specific settings and available methods. The simulation program is based on three types of input parameters: firstly, the ones defining the initial beams and storage ring properties. Secondly, the ones responsible for the precision and speed of the simulation itself. And finally, the ones controlling the calculation for given process.

A.2.1. Beam and Machine Parameters

The parameters of this category define the purpose of the simulation code; the study of a particle beam with given or expected initial parameters in an existing or potential storage ring. These parameters are the subject of study in order to estimate the accelerator performance.

A.2.2. Simulation Speed and Accuracy

When building a simulation program one usually has to make a compromise between the speed of the simulation and how close the simulation can image the reality.

CTE is a simulation code which works on a turn-by-turn basis. This means, in general, each routine describing a certain beam process is called once per turn and applies its effect integrated over the full turn. In order to speed up the time required

for the simulation, CTE combines a certain number of real turns in one simulation turn. The ratio between real and simulation turns can be adjusted by setting the input parameter *nturns*, specifying the number of simulation turns to be performed for the requested equivalent real time *eqTime*. The time needed for one simulation run scales linearly with the number of simulation turns, since the main loop of the code runs *nturns* times. Of course, the closer *nturns* is to the number of real turns, the more accurate the simulation becomes.

The effect of a process is applied on a single particle basis, thus the single particle coordinates are changed one by one in each routine. Therefore, the simulation time is also significantly affected by the number of particles to be treated. CTE merges all real particles, given in *pnumber*, into *nmacro* macro-particles to speed up the simulation.

The program intrinsically makes no assumption on the shape of the longitudinal profile. For the IBS calculations, the bunches are split into longitudinal slices (*nBins*) and calculations are performed separately on each slice. A similar binning is used for the hourglass effect (*longIntBins* slices). In general, the number of longitudinal slices has a small effect on the simulation (provided the they are not too small), and $nBins = 500$ and $longIntBins = 100$ can be used as a default.

A.2.3. Processes with redundant Methods

In order to keep the program as general as possible and to be able to use it for any machine and beam, the computation of certain process is implemented in several alternative methods. The user can choose the optimal method for his purpose. The input information required for redundant methods varies, so that one method might be chosen above another due to the availability of the additional input parameters. On the other hand, some methods give higher accuracy and/or faster performance than others. There are five variables, for which a the way of calculation can be chosen:

- *longCoordMethod*: defined in section A.1.3. Four methods to generate the initial longitudinal particle coordinates are available:
  - 0: requires the additional input variables *power* and *alint*. A smooth but non-Gaussian bunch profile is generated. With the right parameter choice it could, however, approximate a Gaussian profile. Nevertheless, this method should only be used if more exotic bunch profiles are required.
  - 1: reads in (longitudinal) particle coordinates from a separate file. The paths to two files containing the particle coordinates for bunch 1 and 2 are required. These files should have *nmacro* lines, each line defining the initial coordinates for one macro-particle as (d, d, d, d, t, pt), whereas, the d is only a dummy variable and not used, only the longitudinal coordinates in column 5 and 6 are saved. The transverse coordinates are calculated in a separate method and restricted to be Gaussian, while the longitudinal plane can be of any distribution.
  - 2: generates a bi-Gaussian distribution with given energy spreads

(*rmsDelta1* and *rmsDelta2* for beam 1 and 2, respectively) and bunch lengths (*rmsBunchLen1* and *rmsBunchLen2*). The generated coordinates are only matched in the small-angle approximation, leading to bunch length oscillations in time, due to the the small mismatch to the bucket.

  - 3: preferred method for longitudinal Gaussian profiles. Generation of a pseudo-Gaussian distribution with an exact phase-space matching, which does not filament. The variable *bunchLenPrecis* defines the precision to which the generated distribution fits the RMS value given as *rmsBunchLen*.

- *radMethod*: defined in section A.1.4. Three methods to calculate the radiation damping times and equivalent emittances are available:
  - manual: uses pre-calculated values that are given in the input variables *tradlong, tradperp, siglong* and *sigperp*, corresponding to the longitudinal and horizontal emittance damping times and equivalent emittances, respectively.
  - lattic: damping times and equivalent emittances are calculated from the radiation integrals [38] over the lattice. The lattice file given in *twissFile* (section A.1.2) is required. In case a lattice file is available, this should be the preferred option.
  - approx: calculates a smooth lattice, assuming average β-functions and horizontal dispersion. The vertical dispersion is assumed to be zero. The smooth approximation of the radiation integrals $I_2 = 2\pi/\rho_0$ and $I_{4x} = I_{4y} = 0$ is used, where ρ_0 is the bending radius of the dipoles.
- *ibsMethod*: IBS growth rates can be calculated with six different methods, different input information is required for each:
  - *piwiSmooth*: uses the Piwinski formalism [54] in the smooth lattice approximation. The horizontal dispersion and the β-functions are approximated as $\langle D_x \rangle = C_{\text{ring}}/(2\pi\gamma_T^2)$ and $\langle \beta_{xy} \rangle = C_{\text{ring}}/(2\pi Q_{xy})$, respectively, where C_{ring} is the circumference of the accelerator, γ_T is the relativistic Lorentz factor at transition energy and Q_{xy} is the horizontal or vertical tune.
  - *piwLattice*: in addition to *piwiSmooth* the variations of the optical functions in the lattice are taken into account. The lattice file given in *twissFile* (section A.1.2) is required.
  - *modPiwLatt*: uses a modified version of Piwinski's formalism used in *piwLattice*, where the horizontal IBS growth rate is calculated by using the $\mathcal{H}$-function ($\mathcal{H} = [D_x^2 + (\beta_x D'_x - \frac{1}{2}\beta'_x D_x)^2]/\beta_x$), which is more accurate.
  - *baneApprox*: uses a high-energy approximation derived by K.L.F Bane [57]. This routine should not be used at small energies, e.g. injection energy. It uses the full lattice information similar to *piwLattice* and *modPiwLatt*. An external file containing tabulated values of Bane's g-functions is required.
  - *interpolate*: uses an interpolation of pre-calculated IBS growth times in emittance-space provided in tabulated external file.
  - *nagaitsev*: uses the formalism derived by Nagaitsev [58]. This routine is

much faster compared to the others using Piwinski's and Bane's formalisms with comparable results, while using the full lattice information in *twissFile*. An input value of the Coulomb logarithm (*coulombLog*) is required for the calculation. This is the default used for LHC.

- *emitMethod*: the transverse emittances can be calculated out of the particle coordinates with three methods defined in Section A.1.7.
  - *stdev*: calculates the emittances out of the standard deviations of the particle coordinates. Default function used for LHC.
  - *stcal*: takes into account that the tails of the particle distribution could be cut. After the calculation of the standard deviation, a Gaussian with cut tails is assumed. From the cut Gaussian, the standard deviation of the uncut Gaussian is calculated. In case the tails of the distribution are not cut *stcal* and *stdev* should be equivalent.
  - *exfit*: calculates the betatron actions for all particles and does an exponential fit to get the emittance.
- *collRoutine*: two functions are available to simulate the collision between the two bunches.
  - *1d* (slow routine): integrates interaction probability for every particle by sorting particles in opposing beam in discrete bins. No assumptions on the shape of the beam distribution are made.
  - *6a* (fast routine): assumes Gaussian transverse distribution and calculates interaction probability from transverse distribution analytically and uses global reduction factor (hourglass and crossing angle) for all particles. No assumptions on longitudinal distribution are made.

B. Batch Compression to 100 ns in the PS

During a machine development session in the PS in 2013 [17], the batch compression of heavy-ions to 100 ns bunch spacing was demonstrated. The principle of the procedure was discussed in Chapter 2.3.3. Unfortunately, a report about this experiment was not written. Thanks to H. Damerau, Fig. B.1 shows the results of the experiment. The spacing between two bunches is displayed on the x-axis, while the time through the experiment is shown along the y-axis. The colours correspond to the measured amplitude of the bunch profiles ($\propto N_b$): blue shows low, red high amplitude. The bunch centres are separated by 200 ns at the beginning of the measurement, with progressing time they move closer together, such that after 40 s the desired spacing of 100 ns is achieved [147].

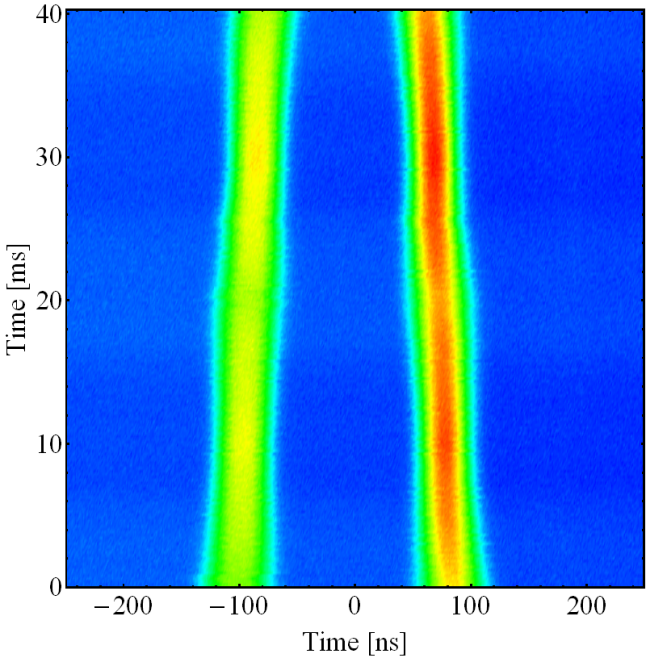

Figure B.1.: Batch Compression of heavy-ion bunches to 100 ns spacing in the PS. Courtesy of H. Damerau.

C. Additional Material: Secondary Beams

Figure C.1 to C.3 show the horizontal beam envelopes of the main (10σ) and secondary (1σ) beams in IP1, 2 and 5 as discussed in Chaper 7. The beams cross in the vertical plane in IP1 and 2, but in the horizontal plane in IP5. The crossing angle bump in IP5 is visible on the excursion of the main and secondary beams in the first 200 m behind the IP in Fig.C.3, while for IP1 (Fig. C.1) and 2 (Fig. C.2), the trajectories lie on the central orbit. The observable small deflections here are introduced by the D1 and D2 bending magnets, responsible for separating the beams out of the common beam pipe back into their single pipes. The possible position of the collimators to be installed in the dispersion suppressor, are marked as black bars from the top of the plots, the preferred collimator location is highlighted in green.

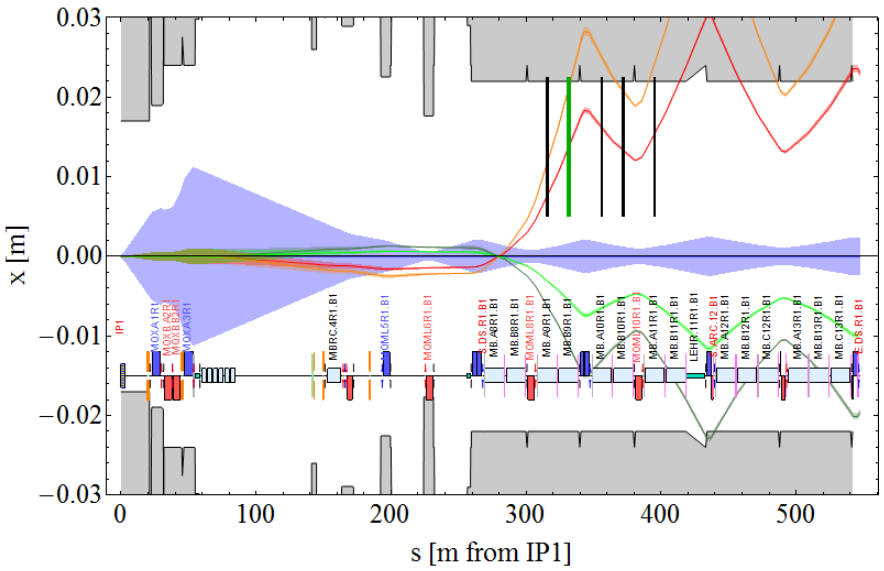

Figure C.1.: Horizontal beam envelopes to the right of IP1. Same structure and colour code as in Fig. 2.11a. The potential collimator positions are indicated as black bars, the preferred location is highlighted in green.

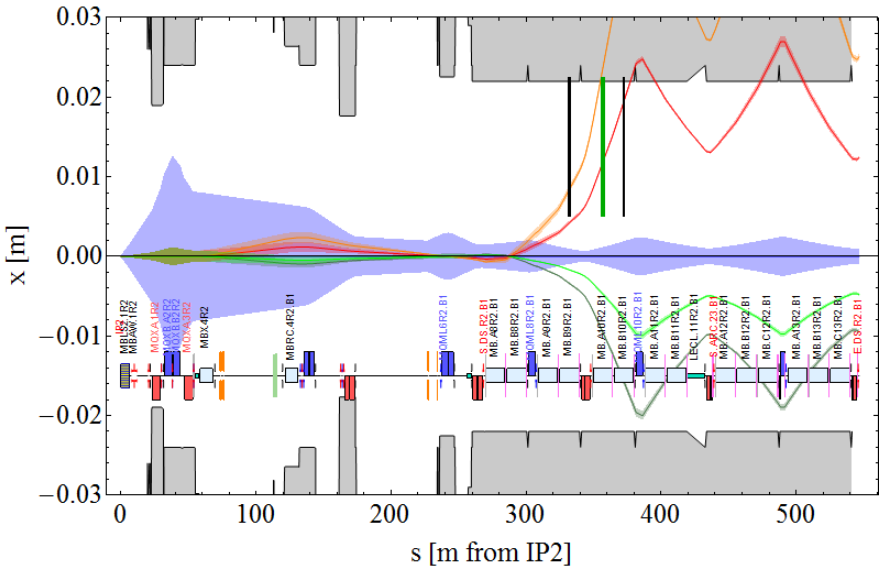

Figure C.2.: Horizontal beam envelopes to the right of IP2. Same structure and colour code as in Fig. 2.11a. The potential collimator positions are indicated as black bars, the preferred location is highlighted in green.

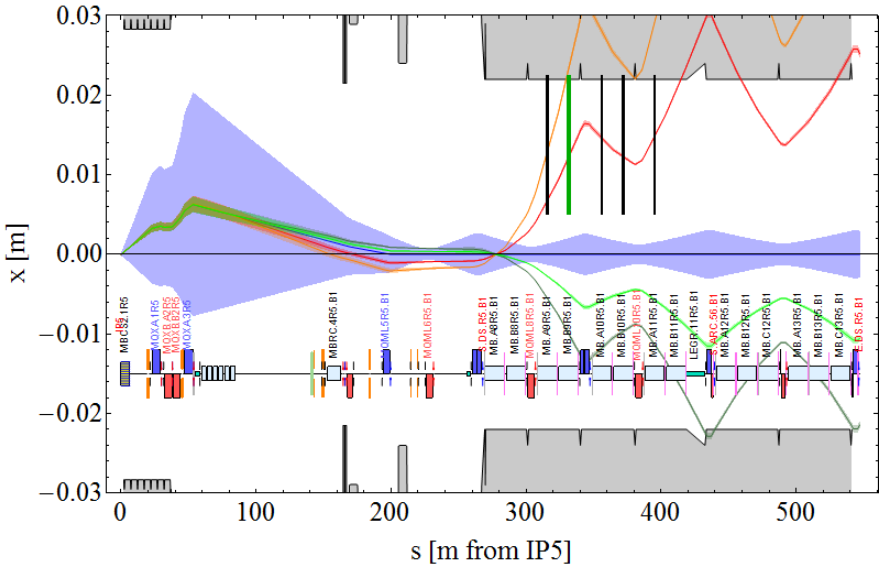

Figure C.3.: Horizontal beam envelopes to the right of IP5. Same structure and colour code as in Fig. 2.11a. The potential collimator positions are indicated as black bars, the preferred location is highlighted in green.

List of Figures

List of Tables

List of Symbols

A_{ion}	Mass number of an ion.
α_c	Momentum compaction factor.
α_{IBS}	Inter-beam scattering growth rates.
α_{rad}	Radiation damping rates.
α, β, γ	Courant-Snyder parameters, Twiss parameters.
A_x, A_y	Transverse beam pipe or beam screen aperture.
Au-Au	Gold-gold collisions.
B	Magnetic field strength in Tesla [T].
β_x, β_y, β_{xy}	β-function.
β_{rel}	Relativistic $\beta = v/c$, v is the velocity of the particle, c the speed of light.
β^*	β-function at IP.
$B\rho$	Beam rigidity.
c	Speed of light.
C_{ring}	Accelerator circumference.
C_{FCC}	Circumference of the FCC.
C_{LHC}	Circumference of the LHC.
$\mathcal{D}$	BLM signal for a given monitor at a given time.
D_x, D_y	Horizontal and vertical dispersion.
d_x, d_y	Local, single-pass dispersion.
$e^{\pm}$, e^-, e^+	Electron ($-$) or positron ($+$).
ϵ, ϵ_x, ϵ_y, ϵ_{xy}	Geometric transverse emittance.
ϵ_n, $\epsilon_{n,x}$, $\epsilon_{n,y}$, $\epsilon_{n,xy}$	Normalised transverse emittance.
$\tilde{\varepsilon}_n$	Effective normalised transverse emittance; calculated from the luminosity, intensity and bunch length measurements.
ϵ_s	Longitudinal emittance.
E_b	Beam energy.
η	Phase-slip-factor.

f_{rev}	Revolution frequency.
f_{RF}	RF frequency.
γ	Relativistic Lorentz factor.
γ_T	Relativistic γ-factor at transition energy.
h	Harmonic number.
$\mathcal{I}$	Radiation integrals.
J_x, J_y, J_s	Damping partition numbers.
k_b	Number of colliding bunches.
$\mathcal{L}$	Total instantaneous luminosity.
$\mathcal{L}_b$	Instantaneous bunch luminosity.
$\mathcal{L}_{\mathrm{int}}$	Total integrated luminosity.
$\mathcal{L}_{b,\mathrm{int}}$	Integrated bunch luminosity.
$\mathbf{M}$	Transfer matrix.
m_{ion}	Mass of an ion.
N	Number of particles per beam.
n	Neutron.
N_b	Number of particles per bunch.
n_b	Number of bunches per beam.
n_{PS}	Number of PS batches per SPS train.
p	Proton.
Pb	Chemical symbol for the element lead.
Pb-Pb	Lead-lead collisions.
p	Total momentum of an ion.
p_x, p_y	Horizontal or vertical component of the momentum.
p-p	Proton-proton collisions.
p-Pb	Proton-lead collisions.
$\Delta p/p$	RMS relative momentum spread.
q	$q = Ze$; charge of an ion.

r_0	Classical particle radius.
r_{p0}	Classical proton radius.
ρ_0	Horizontal bending radius.
ρ_{corr}	Correlation coefficient.
s	Longitudinal position within the co-moving coordinate system relative to the central orbit; s runs from $s = 0$ (in IP1) to $s = C_{\text{LHC}}$.
σ, σ_x, σ_y	RMS beam size.
σ_c	Interaction cross-section in Barn [b].
$\sigma_{c,\text{BFPP}}$	Total interaction cross-section for all BFPP reactions.
$\sigma_{c,\text{BFPP1}}$	Interaction cross-section for BFPP1 reaction.
$\sigma_{c,\text{BFPP2}}$	Interaction cross-section for BFPP2 reaction.
$\sigma_{c,\text{EMD}}$	Total interaction cross-section for all EMD reactions.
$\sigma_{c,\text{EMD1}}$	Interaction cross-section for EMD1 reaction.
$\sigma_{c,\text{EMD2}}$	Interaction cross-section for EMD2 reaction.
$\sigma_{c,\text{hadron}}$	Inelastic (hadronic) interaction cross-section.
$\sigma_{c,\text{tot}}$	Total interaction cross-section, including all processes removing particles from the beam.
σ_p	RMS relative momentum spread.
σ_s	RMS bunch length.
$\sqrt{s_{\text{NN}}}$	Centre-of-mass energy per nucleon.
θ_c	Half crossing angle.
U-U	Uranium-uranium collisions.
V_{RF}	RF voltage.
x	Horizontal position within the co-moving coordinate system relative to the central orbit.
ξ	Linear beam-beam parameter.
y	Vertical position within the co-moving coordinate system relative to the central orbit.
Z	Charge number of an ion.

List of Abbreviations and Acronyms

ALICE	A Large Ion Collider Experiment; the LHC experiment dedicated to heavy-ion physics, located in IP2.
ATLAS	A Toroidal LHC ApparatuS; one of the multi-purpose LHC experiments, located in IP1.
B1	LHC Beam 1; rotating clockwise.
B2	LHC Beam 2; rotating counter-clockwise.
BFPP	Bound Free Pair Production.
BFPP1	BFPP of first order; one of the participating ions captures one electron.
BFPP2	BFPP of second order; one of the participating ions captures two electrons.
BLM	Beam Loss Monitor; ionization chamber measuring beam losses.
BNL	Brookhaven National Laboratory; in Upton, New York, USA.
BPM	Beam Position Monitor; pickup measuring transverse beam position.
BQM	Beam Quality Monitor, instrument to measure the longitudinal bunch profile.
BSRT	Beam Synchrotron Light Telescope; continuous measurement of transverse beam size.
BTF	Beam Transfer Function.
CERN	Organisation Européenne pour la Recherche Nucléaire; in Genava, Switzerland.
CMS	Compact Muon Solenoid; one of the multi-purpose LHC experiments, located in IP5.
CTE	Collider Time Evolution; program for tracking simulations of colliding bunches.
DS	Dispersion Suppressor; first section of the arc, which suppresses the dispersion to be zero at the IP.

EM	Electromagnetic.
EMD	Electromagnetic Dissociation.
EMD1	EMD of first order; one of the participating ions emits one neutron.
EMD2	EMD of second order; one of the participating ions emits two neutrons.
FBCT	Fast Beam Current Transformer, instrument to measure the bunch or beam intensity.
FCC	Future Circular Collider; recently started circular collider study in the Geneva area.
FLUKA	FLUktuierende KAskade; particle physics MonteCarlo simulation package for calculations of particle transport and interactions with matter.
FWHM	Full Width Half Maximum.
HL-LHC	High Luminosity Large Hadron Collider.
IBS	Intra Beam Scattering.
IP	Interaction Point; can be followed by a number between 1 and 8 specifying the location inside the LHC ring.
IR	Interaction Region; can be followed by a number between 1 and 8 specifying the location inside the LHC ring.
ISR	Intersection Storage Ring, CERN.
LEIR	Low Energy Ion Ring; first circular pre-accelerator for heavy-ions.
LHC	Large Hadron Collider.
LHCb	Large Hadron Collider beauty; the LHC experiment specialised to b-physics, located in IP8.
LINAC	LINear ACcelerator.
LS	Long Shutdown; can be followed by the number of the corresponding LS since the start of the LHC.
LSS	Long straight section.
MB	Main bending magnet, dipole.
MQ	Main quadrupole magnet.
n	Neutron.

ODE	Ordinary Differential Equation.
p	Proton.
Pb	Chemical symbol for the element lead.
PS	Proton Synchrotron, first common pre-accelerator for protons and heavy-ions.
PSB	Proton Synchrotron Booster; first circular pre-accelerator for protons.
Q11	Short form for the eleventh main quadrupole after the given IP, could also any other number.
QCD	Quantum ChromoDynamics.
QGP	Quark Gluon Plasma.
RF	Radio Frequency.
RFQ	Radio Frequency Quadrupole.
RHIC	Relativistic Heavy Ion Collider; collider at BNL.
SPS	Super Proton Synchrotron; last pre-accelerator before the LHC.
TCP	Target Collimator Primary.
TE	Transverse Electric.
TM	Transverse Magnetic.
TPC	Time Projection Chamber, used as tracker for the ALICE experiment.
VdM	Van der Meer Scan; performed for luminosity calibration.
WS	Wire Scanner; measurement of transverse beam size.
ZDC	Zero Degree Calorimeters, forward detector of the ALICE experiment.
Z TeV	Energy unit TeV including the charge number, Z, of the ion; specifies the total energy of the nucleus in proton equivalent values.

Bibliography

[1] ATLAS Collaboration. Observation of a new particle in the search for the Standard Model Higgs boson with the ATLAS detector at the LHC. *Physics Letters B*, 716(1):1 – 29, 2012.

[2] CMS Collaboration. Observation of a new boson at a mass of 125 GeV with the CMS experiment at the LHC. *Physics Letters B*, 716(1):30 – 61, 2012.

[3] Fischer, W. and Jowett, J.M. Ion Colliders. *Reviews of Accelerator Science and Technology*, 7, 2014. to be published.

[4] Jacob, M. and Johnsen, K. A review of accelerator and particle physics at the CERN Intersecting Storage Rings. Technical report, CERN 84-13, CERN, Geneva, Switzerland, 1984.

[5] Hahn, H. et al. The RHIC design overview. *Nuclear Instruments and Methods in Physics Research Section A: Accelerators, Spectrometers, Detectors and Associated Equipment*, 499(2–3):245 – 263, 2003.

[6] Esumi, S. Heavy Ion results from RHIC-BNL. In *HCP 2012 – Hadron Collider Physics Symposium 2012*, EPJ Web of Conferences 49, 02007 (2013), Kyoto, Japan, 2012.

[7] Jacak, B. and Müller, B. The exploration of hot nuclear matter. *Science*, 337(6092):310–314, 2012.

[8] Andronic, A. An overview of the experimental study of quark-gluon matter in high-energy nucleus-nucleus collisions, 2014. to apprear as an invited review in Int. J. Mod. Phys. A.

[9] Muller, B., Schukraft, J. and Wyslouch, B. First Results from Pb+Pb collisions at the LHC. Technical report, arXiv:1202.3233, CERN-OPEN-2012-005, CERN, Geneva, Switzerland, 2012. To appear in Annual Review of Nuclear and Particle Science.

[10] Jowett, J.M. et al. First Run of the LHC as a Heavy-ion Collider. In *Proceedings of the 2011 International Particle Accelerator Conference*, TUPZ016, pages 1837–1839, San Sebastian, Spain, 2011.

[11] Jowett, J.M., Bruce, R. and Mertens, T. Luminosity and Beam Parameter Evolution for Lead Ion Beams in the LHC. In *Proceedings of the 2011 International Particle Accelerator Conference*, TUPZ017, pages 1840–1842, San Sebastian, Spain, 2011.

[12] Mertens, T. Intrabeam scattering in the LHC. Master's thesis, Universidade do Porto, Porto, Portugal, 2011.

[13] Schaumann, M. and Jowett, J.M. Bunch-by-Bunch Analysis of the LHC Heavy-Ion Luminosity. In *Proceedings of the 2013 International Particle Accelerator Conference*, TUPFI025, CERN-ACC-2013-0136, pages 1391–1393, Shanghai, China, May 2013.

[14] Alemany, R. et al. First proton-nucleus collisions in the LHC: the p-Pb pilot physics fill. Technical report, CERN-ATS-Note-2012-094 MD, CERN, Geneva, Switzerland, Nov 2012.

[15] Jowett, J.M. et al. Proton-nucleus Collisions in the LHC. In *Proceedings of the 2013 International Particle Accelerator Conference*, MOODB201, CERN-ACC-2013-0057, pages 49–51, Shanghai, China, May 2013.

[16] ALICE Collaboration. Upgrade of the ALICE Experiment: Letter Of Intent. CERN-LHCC-2012-012, LHCC-I-022, Geneva, Switzerland, 2012.

[17] Manglunki, D. et al. Planes for the Upgrade of CERN's Heavy Ion Complex. In *Proceedings of the 2013 International Particle Accelerator Conference*, WEPEA060, pages 2645–2647, Shanghai, China, 2013.

[18] Garoby, R. et al. Status and Plans for the Upgrade of the LHC Injectors. In *Proceedings of the 2013 International Particle Accelerator Conference*, THPWO077, pages 3936–3938, Shanghai, China, 2013.

[19] Hanke, K. et al. Status of the LIU project at CERN. In *Proceedings of the 2014 International Particle Accelerator Conference*, THPME070, pages 3397–3399, Dresden, Germany, 2014.

[20] Schaumann, M. Semi-Empirical Model for Optimising Future Heavy-Ion Luminosity of the LHC. In *Proceedings of the 2014 International Particle Accelerator Conference*, TUPRO014, CERN-ACC-2014-0084, pages 1033–1035, Dresden, Germany, Jun 2014.

[21] Jowett, J.M., Schaumann, M. and Versteegen, R. Heavy Ion Operation from Run 2 to HL-LHC. In *Proceedings of RLIUP: Review of LHC and Injector Upgrade Plans*, CERN-2014-006, Archamps, France, Oct 2013.

[22] Blaskiewicz, M. and Brennan, J.M. Bunched beam stochastic cooling in a collider. *Phys. Rev. ST Accel. Beams*, 10:061001, Jun 2007.

[23] Blaskiewicz, M., Brennan, J.M. and Severino, F. Operational Stochastic Cooling in the Relativistic Heavy-Ion Collider. *Phys. Rev. Lett.*, 100:174802, May 2008.

[24] Blaskiewicz, M., Brennan, J.M. and Mernick, K. Three-Dimensional Stochastic Cooling in the Relativistic Heavy Ion Collider. *Phys. Rev. Lett.*, 105:094801, Aug 2010.

[25] Fischer, W. et al. Measurement of the total cross section of uranium-uranium collisions at $\sqrt{s_{NN}} = 192.8$ GeV. *Phys. Rev. C*, 89:014906, Jan 2014.

[26] Blaskiewicz, M., Brennan, J.M. and Mernick, K. RHIC Luminosity Increase with Bunched Beam Stochastic Cooling. In *Proceedings of the COOL2013 Workshop*, MOAM1HA02, Murren, Switzerland, 2013.

[27] Schaumann, M. and Jowett, J.M. Potential for Stochastic Cooling of Heavy-Ions

in the LHC. In *Proceedings of the COOL2013 Workshop*, TUPM1HA02, Murren, Switzerland, 2013.

[28] Schaumann, M. et al. Studies on Stochastic Cooling of Heavy-Ions in the LHC. In *Proceedings of the 2014 International Particle Accelerator Conference*, TUPRO013, Dresden, Germany, 2014.

[29] Ball, A. et al. Future Circular Collider Study, Hadron Collider Parameters. Technical report, FCC-ACC-SPC-0001, CERN, Geneva, Switzerland, 2014.

[30] Official website of the Future Circular Collider Study. `https://espace2013.cern.ch/fcc/Pages/default.aspx`, 2014. Accessed 15/12/2014.

[31] Schaumann, M. Potential performance for Pb-Pb, p-Pb, and p-p collisions in a future circular collider. 2014. Submitted to Physical Review Special Topics - Accelerators and Beams.

[32] Schaumann, M., Jowett, J.M. and Bruce, R. Intra-beam Scattering and Luminosity Evolution for HL-LHC Proton Beams. Technical report, CERN-ATS-2012-290, CERN, Geneva, Switzerland, Dec 2012.

[33] Schaumann, M., Jowett, J.M. and Bruce, R. Influence of the Ats Optics on Intra-Beam Scattering for HL-LHC. In *Proceedings of the 2013 International Particle Accelerator Conference*, TUPFI024, pages 1388–1390, Shanghai, China, May 2013.

[34] Metral, E. et al. Beam intensity limitations. Technical report, HILUMILHC-Del-D2-4-v1.0, CERN-ACC-2014-0297, CERN, Geneva, Switzerland, Oct 2014. HILUMI LHC - Deliverable Report D2.4.

[35] Wiedemann, H. *Particle Accelerator Physics*. Springer, 3 edition, 2007.

[36] Lee, S.Y. *Accelerator Physics*. World Scientific, 3 edition, 2012.

[37] Wille, K. *The Physics of Particle Accelerators - an introduction*. Oxford University Press, 2005.

[38] Chao, A. et al, editors. *Handbook of Accelerator Physics and Engineering*. World Scientific, second edition, 2013.

[39] Official CERN website. `http://www.cern.ch`. Status 12/2014.

[40] LHC Design Report Volume I - The LHC main ring. CERN-2004-003-V-1, Geneva, Switzerland, 2004.

[41] Official MADX website. `http://www.cern.ch/madx`. Status 12/2014.

[42] LHC Design Report Volume I - The LHC main ring, Chapter 21 "The LHC as Lead Ion Collider". CERN-2004-003-V-1, Geneva, Switzerland, 2004.

[43] Bailey, R. and Collier, P. Standard Filling Schemes for Various LHC operation Modes. Technical report, LHC-Project-Note-323, CERN, Geneva, Switzerland, 2003.

[44] LHC Design Report Volume III - The LHC Injector Chain. CERN-2004-003-V-3, Geneva, Switzerland, 2004.

[45] Poth, H. Electron cooling: Theory, experiment, application. *Physics Reports*,

196(3–4):135–297, 1990.

[46] RF gymnastics in *Fifty years of the CERN Proton Synchrotron : Volume 1*. CERN-2011-004, Geneva, Switzerland.

[47] Garoby, R. RF gymnastics in synchrotrons. In *CAS - CERN Accelerator School: Specialised Course on RF for Accelerators*, CERN-2011-007, pages 431–446, Ebeltoft, Denmark, Sept 2010.

[48] Manglunki, D. Private communication, 2014.

[49] Carli, C. et al. Commissioning and Performance of LEIR. In *Proceedings of the COOL2007 Workshop*, THM1I01, Kreuznach, Germany, 2007.

[50] Bodendorfer, M. et al. LEIR model: A plan for understanding/upgrading the LEIR performance limitations. In *LIU Day 2014*, CERN, Geneva, Switzerland, 2014.

[51] Alemany-Fernandez, R., Lamont, M. and Page, S. Functional specification LHC modes. Technical report, LHC-OP-ES-0005, CERN, Geneva, Switzerland, Nov 2007.

[52] Herr, W. Beam-Beam Interactions. In *CAS - CERN Accelerator School: Intermediate Course on Accelerator Physics*, CERN-2006-002, pages 379–410, Zeuthen, Germany, Sept 2003.

[53] ALICE Collaboration. ALICE Zero-Degree Calorimeter (ZDC): Technical Design Report. ALICE-TDR-3, CERN-LHCC-99-005, Geneva, Switzerland, 1999.

[54] Piwinski, A. Intra-beam Scattering. In *CAS - CERN Accelerator School: Accelerator Physics*, CERN-1987-003-V-1.402, pages 402–415, Oxford, UK, Sept 1985.

[55] Piwinski, A. Intra-beam Scattering. In *Proc. 9th Int. Conf. on High Energy Accelerators*, page 405, Stanford, 1974.

[56] Bjorken, J. and Mtingwa, S. Intrabeam Scattering. *Part. Accel.*, 13:115, 1983.

[57] Bane, K. A Simplified Model of Intrabeam Scattering. Technical report, SLAC-PUB-9226, SLAC, Stanford, CA94309, USA, Jun 2002.

[58] Nagaitsev, S. Intrabeam scattering formulas for fast numerical evaluation. *Phys. Rev. ST Accel. Beams*, 8:064403, 2005.

[59] Wei, J. Evolution of Hadron Beams under Intrabeam Scattering. In *Proceedings of the 1993 Particle Accelerator Conference*, pages 3651–3653, Washington, DC, 1993.

[60] Chao, A. et al, editors. *Handbook of Accelerator Physics and Engineering*. World Scientific, first edition, 1999.

[61] Bruce, R. Emittance increase caused by core depletion in collisions. arXiv:0911.5627v1, 2013.

[62] Schaumann, M. Beam-Beam Interaction Studies at LHC. Master's thesis, RWTH Aachen University, Aachen, Germany, 2011.

[63] Demtröder, W. *Experimentalphysik 3 - Atome, Moleküle und Festkörper*.

Springer, third edition, 2005.

[64] Jackson, J. *Classical Electrodynamics*. Wiley, 3 edition, 1998.

[65] Baltz, A.J., Rhoades-Brown, M.J. and Weneser, J. Heavy-ion partial beam lifetimes due to Coulomb induced processes. *Phys. Rev. E*, 54:4233–4239, Oct 1996.

[66] Bruce, R. et al. Beam losses from ultraperipheral nuclear collisions between $^{208}Pb^{82+}$ ions in the Large Hadron Collider and their alleviation. *Phys. Rev. ST Accel. Beams*, 12:071002, Jul 2009.

[67] Meier, H. et al. Bound-Free Electron-Positron Pair Production in Relativistic Heavy Ion Collisions. *Phys. Rev. A*, 63:032713, 2001.

[68] Artemyev, A.N., Serbo, V.G. and Surzhykov, A. Double lepton pair production with electron capture in relativistic heavy-ion collisions. *The European Physical Journal C*, 74:2829, 2014.

[69] ALICE Collaboration. ALICE - Technical Proposal for A Large Ion Collider Experiment at the CERN LHC. CERN-LHCC-95–71, LHCC-P3, Geneva, Switzerland, 1995.

[70] Ferrari, A. et al. FLUKA : A multi-particle transport code (program version 2005). Technical report, CERN Report No. CERN-2005-010, CERN, Geneva, Switzerland, 2005.

[71] Braun, H. et al. Hadronic and electromagnetic fragmentation of ultrarelativistic heavy ions at LHC. *Phys. Rev. ST Accel. Beams*, 17:021006, 2014.

[72] Oppedisano, C. et al. Measurements of the electromagnetic dissociation cross section of Pb nuclei at $\sqrt{s_{NN}} = 2.76\,\text{TeV}$. *Journal of Physics G: Nuclear and Particle Physics*, Proceedings of Quark Matter 2011, 2011.

[73] Klein, S.R. Localized beam pipe heating due to e- capture and nuclear excitation in heavy ion colliders. *Nucl.Instrum.Meth.*, A459:51–57, 2001.

[74] Jowett, J.M. Ions in the LHC ring: Status of what has been done and what has to be done on LHC. In *Proceedings of the LHC Performance Workshop, Chamonix XII*, CERN-AB-2003-008-ADM, pages e–proc. 2–6–JJ, Chamonix, France, 2003.

[75] Jowett, J.M., Jeanneret, J. and Schindl, K. Heavy ion beams in the LHC. In *Proceedings of the 2003 Particle Accelerator Conference*, PAC03-TPPB029, CERN-LHC-PROJECT-REPORT-642, page 1682, Portland, Oregon, 2003.

[76] Jowett, J.M. et al. Limits to the performance of the LHC with ion beams. In *Proceedings of the 2004 European Particle Accelerator Conference*, EPAC-2004-MOPLT020, CERN-LHC-PROJECT-REPORT-772, Lucerne, Switzerland, 2004.

[77] Bruce, R. et al. Time evolution of the luminosity of colliding heavy-ion beams in BNL Relativistic Heavy Ion Collider and CERN Large Hadron Collider. *Phys. Rev. ST Accel. Beams*, 13:091001, 2010.

[78] Blaskiewicz, M. et al. Stochastic Cooling of a High Energy Collider. In *Proceedings of the 2011 International Particle Accelerator Conference*, TUYA03, San Sebastian, Spain, 2011.

[79] *CAS - CERN Accelerator School: Beam Diagnostics*, CERN-2009-005, Dourdan, France, 2008.

[80] Forck, P. Lecture Notes on Beam Instrumenteation and Diagnostics. In *JUAS*, Archamps, France, 2011.

[81] Tomás, R. et al. Record low beta beating in the LHC. *Phys. Rev. ST AB*, 15(9):091001, 2012.

[82] Aiba, M. et al. First β-beating measurement and optics analysis for the CERN Large Hadron Collider. *Physical Review Special Topics - Accelerators and Beams*, 12(8):081002, August 2009.

[83] Jones, O. Commissioning and First Performance of the LHC Beam Instrumentation. Technical report, CERN-BE-2010-007 BI, CERN, Geneva, Switzerland, 2010.

[84] Roncarolo, F. *Accuracy of the Transverse Emittance Measurements of the CERN Large Hadron Collider*. PhD thesis, EPFL, Lausanne, Switzerland, 2005.

[85] Jung, R. et al. The LHC 450 GeV to 7 TeV Synchrotron Radiation Profile Monitor using a Superconducting Undulator. Technical report, CERN-SL-2002-015 BI, CERN, Geneva, Switzerland, 2002.

[86] Fisher, A.S. et al. First Beam Measurements with the LHC Synchrotron Light Monitor. Technical report, CERN-BE-2010-019 BI, CERN, Geneva, Switzerland, 2010.

[87] Roncarolo, F. Can we get a reliable on-line measurement of the transverse beam size? In *LHC Evian Workshop*, Evian, France, 2010.

[88] Papotti, G. et al. Longitudinal Beam Measurements at the LHC: The LHC Beam Quality Monitor. In *Proceedings of the 2011 International Particle Accelerator Conference*, TUPZ022, pages 1852–1854, San Sebastian, Spain, 2011.

[89] Holzer, E.B. et al. Beam Loss Monitoring for LHC Machine Protection. *Physics Procedia*, 37(0):2055 – 2062, 2012. Proceedings of the 2nd International Conference on Technology and Instrumentation in Particle Physics (TIPP 2011).

[90] Lechner, A. et al. Power deposition in LHC magnets with and without dispersion suppressor collimators downstream of the betatron cleaning insertion. In *Proceedings of the 2014 International Particle Accelerator Conference*, MOPRO021, pages 112–115, Dresden, Germany, 2014.

[91] Verweij, A. and Auchmann, B. Quench limits: extrapolation of quench tests to 7 TeV. In *LHC Collimation Review 2013*, Geneva, Switzerland, 2013.

[92] Granieri, P. Steady-state cable quench limits: what we know and what we don't. In *172nd LHC Collimation Working Group Meeting*, Geneva, Switzerland, 2014.

[93] Granieri, P. Steady-state cable quench limit of the 11T dipole. In *35th LHC ColUS Meeting*, Geneva, Switzerland, 2014.

[94] Caspers, F. et al. The 4.8 GHz LHC Schottky Pick-Up System. In *Proceedings of the 2007 Particle Accelerator Conference*, FRPMN068, Albuquerque, New Mex-

ico, USA, 2007.

[95] Antoniou, F. et al. Performance of SPS Low Transition Energy Optics for LHC Ion Beams. In *Proceedings of the 2013 International Particle Accelerator Conference*, TUPME046, pages 1667–1669, Shanghai, China, 2013.

[96] Piwinski, A. The Touschek Effect in Strong Focusing Storage Rings. Technical report, DESY 98-179, arXiv:physics/9903034, DESY, Hamburg, Germany, 1999.

[97] Baud, G. et al. Performance Assessment of Wire-Scanners at CERN. In *Proceedings of the 2013 International Beam Instrumentation Conference*, TUPF03, Oxford, UK, 2013.

[98] Gilardoni, S. and Hancock, S. Private communication, 2014.

[99] Tranquille, G. Performance of the Electron Cooler. In *LIU-ION LEIR internal review*, CERN, Geneva, Switzerland, 2014.

[100] Kuhn, M. Emittance Preservation at the LHC. Master's thesis, University of Hamburg, Hamburg, Germany, 2013.

[101] Baudrenghien, P. and Mastoridis, T. Longitudinal emittance blowup in the large hadron collider. *Nuclear Instruments and Methods in Physics Research Section A: Accelerators, Spectrometers, Detectors and Associated Equipment*, 726:181–190, 2013.

[102] Bodendorfer, M. et al. Lead performance throughout the injector chain with focus on LEIR. In *MSWG Group Meeting 04/06/2013*, CERN, Geneva, Switzerland, 2013.

[103] Manglunki, D. Performance of the injectors with ions after LS1. In *Proceedings of RLIUP: Review of LHC and Injector Upgrade Plans*, CERN-2014-006, Archamps, France, Oct 2013.

[104] J. M. Jowett, M. Schaumann, R.V. Heavy-Ion Operation of HL-LHC in *High Luminosity LHC*. To be published as a special issue of Int. Journal of Modern Physics A, 2014.

[105] HL-LHC: Preliminary Design Report. To be published, 2014.

[106] LIU-SPS 50 ns Injection System for Pb Ions Review. Geneva, Switzerland, 2013. website visited 12/2014.

[107] B.Goddard et al. A New Lead Ion Injection System for the CERN SPS with 50ns Rise Time. In *Proceedings of the 2013 International Particle Accelerator Conference*, MOPFI052, pages 398–400, Shanghai, China, 2013.

[108] Argyropoulos, T. et al. Slip Stacking in the SPS. In *LIU Day 2014*, CERN, Geneva, Switzerland, 2014.

[109] Bartosik, H. et al. Low Gamma Transition Optics for the SPS: Simulation and Experimental Results for High Brightness Beams. In *Proceedings of the 2012 High Brightness Workshop*, WEO1B01, Beijing, China, 2012.

[110] Morsch, A. ALICE Luminosity and Beam Requirements. Technical report, ALICE-INT-2001-10 version 2.0, CERN, Geneva, Switzerland, 2001.

[111] F. Cerutti and A. Lechner and N.V. Shetty and E. Skordis and G. Steele. The CERN FLUKA team (EN/STI) responsible for heavy-ion studies, 2013 and 2014.

[112] Blobel, V. and Lohrmann, E. *Statistische und numerische Methoden der Datenanalyse*. Teubner Stuttgart, 1998.

[113] Hermes, P.D. et al. Studies on Heavy Ion Losses from Collimation Cleaning at the LHC. In *Proceedings of the 2014 High Brightness Workshop*, MOPAB43, East Lansing, MI, USA, Nov 2014.

[114] Bruce, R. et al. Energy deposition with and without cryo-collimators in IR2 (ions) and IR7. In *3rd Joint HiLumi LHC-LARP Annual Meeting*, Daresbury Laboratory, UK, Nov 2013.

[115] F. Cerutti and A. Lechner and N.V. Shetty and E. Skordis. The CERN FLUKA team (EN/STI) responsible for heavy-ion studies, 2014.

[116] Lechner, A. Private communication, 2014.

[117] Luo, Y. et al. RHIC Performance for FY2012 Heavy Ion Run. In *Proceedings of the 2013 International Particle Accelerator Conference*, TUPFI082, Shanghai, China, 2013.

[118] Kolomenski, A. and Lebedev, A. The Effect of Radiation on the Motion of Relativistic Electrons in Synchrotrons. In *Proc. CERN Symposium 1956*, page 447, 1956.

[119] Nagaitsev, S. et al. Experimental Demonstration of Relativistic Electron Cooling. *Phys. Rev. Lett.*, 96:044801, Jan 2006.

[120] Möhl, D. *Stochastic Cooling of Particle Beams*. Lecture Notes in Physics 866. Springer, 2013.

[121] Phillips, W.D. Nobel Lecture: Laser cooling and trapping of neutral atoms. *Rev. Mod. Phys.*, 70:721–741, Jul 1998.

[122] Rubbia, C. et al. Beam cooling with ionization losses. *Nuclear Instruments and Methods in Physics Research Section A: Accelerators, Spectrometers, Detectors and Associated Equipment*, 568(2):475 – 487, 2006.

[123] Neuffer, D. Principles and Applications of Muon Cooling. In *Part. Accel. 14*, FERMILAB-FN-378, pages 75–90, 1983.

[124] Mikhailichenko, A.A. and Zolotorev, M.S. Optical stochastic cooling. *Phys. Rev. Lett.*, 71:4146–4149, Dec 1993.

[125] Litvinenko, V. et al. Present Status of Coherent Electron Cooling Proof-of-Principle Experiment. In *Proceedings of the 2014 International Particle Accelerator Conference*, MOPRO013, pages 87–90, Dresden, Germany, Jun 2014.

[126] Litvinenko, V. CeC Overview. In *C-AD Machine Advisory Committee Meeting (MAC-11)*, BNL, Upton, NY, USA, 2014.

[127] Litvinenko, V.N. and Derbenev, Y.S. Coherent Electron Cooling. *Phys. Rev. Lett.*, 102:114801, Mar 2009.

[128] Möhl, D. Beam Cooling. In *CAS - CERN Accelerator School: Introduction to*

Accelerator Physics, CERN-2005-004, Loutraki, Greece, 2000.

[129] Betts, A. *Signal Processing and Noise*. English Universities Press, London, 1970.

[130] Verdú-Andrés, S. Private communication, 2014.

[131] Jensen, E. RF Cavity Design. In *CAS - CERN Accelerator School: Intermediate Course on Accelerator Physics*, Chios, Greece, Sept 2011.

[132] Pozar, D.M. *Microwave Engineering*. John Wiley & Sons, Inc., 4 edition, 2012.

[133] Shapiro, J. Lecture notes: Electricity and Magnetism, 2011.

[134] Lide, D.R., editor. *Electrical Resistivity of Pure Metals, in CRC Handbook of Chemistry and Physics, Internet Version 2005*. CRC Press, Boca Raton, FL, 2005.

[135] Brennan, M.J. Private communication, 2014.

[136] Caspers, F. Private communication, 2014.

[137] Angerth, B. et al. The LHC beam screen: specification and design. In *Proceedings of the 1994 European Particle Accelerator Conference*, CERN-LHC-Note-283, London, UK, 1994.

[138] LHC Design Report Volume I - The LHC main ring, Chapter 5 "Collective Effects". CERN-2004-003-V-1, Geneva, Switzerland, 2004.

[139] Ng, K.Y. Impedances of Bellows Corrugations. In *Proceedings of the 1987 Particle Accelerator Conference*, Fermilab Report FN-449, Washington, DC, 1987.

[140] Mounet, N. *The LHC Transverse Coupled-Bunch Instability*. PhD thesis, EPFL, Lausanne, Switzerland, 2012.

[141] Thorndahl, L. Private communication, 2014.

[142] Dominguez, O. and Zimmermann, F. Beam Parameters and Luminosity time Evolution for an 80-km VHE-LHC. In *Proceedings of European Coordination for Accelerator Research & Development (EuCARD) Workshop 2013*, EuCARD-CON-2013-010, Geneva, Switzerland, 2013.

[143] Armesto, N. et al. Heavy-ion physics studies for the Future Circular Collider. In *Proceedings of Quark Matter 2014*, submitted to Nucl. Phys., arXiv:1407.7649, Darmstadt, Germany, 2014.

[144] Alemany Fernandez, R. and Holzer, B. First Considerations on Beam Optics and Lattice Design for the Future Hadron-Hadron Collider FCC. Technical report, CERN-ACC-NOTE-2014-0065, CERN, Geneva, Switzerland, Sep 2014.

[145] Zlobin, A. et al. Status of 11T 2-in-1 Nb3Sn diople development for LHC. In *Proceedings of the 2014 International Particle Accelerator Conference*, WEPRI097, pages 2722–2724, Dresden, Germany, Jun 2014.

[146] Bronstein, I.N. et al. *Taschenbuch der Mathematik*. Harri Deutsch, 7 edition, 2008.

[147] Damerau, H. Private communication, 2014.